Title
Some New Directions in Spectroscopy

Author
Cole, William Thomas Shaw

Publication Date
2019

Peer reviewed|Thesis/dissertation

Some New Directions in Spectroscopy

By

William Thomas Shaw Cole

A dissertation submitted in partial satisfaction of the

requirements for the degree of

Doctor of Philosophy

In

Chemistry

in the

Graduate Division

of the

University of California, Berkeley

Committee in charge:

Professor Richard J. Saykally, Chair
Professor Daniel M. Neumark
Professor David B. Graves

Spring 2019

Abstract

Some New Directions in Spectroscopy

by

William Thomas Shaw Cole

Doctor of Philosophy in Chemistry

University of California, Berkeley

Professor Richard J. Saykally, Chair

The work presented in this thesis comprised two major projects. The first, a spectroscopic study of water clusters in the Terahertz vibrational region revealed a dramatic enhancement of tunneling motions involved in breaking and reforming hydrogen bonds. The second project involved constructing a second harmonic scattering (SHS) experiment which was used to probe buried interfaces.

The study of water clusters provides a useful route towards unraveling the many body terms of the water potential. High-resolution vibrational-rotational-tunneling (VRT) spectroscopy is a particular sensitive measure of the repulsive walls of the water potential. While this method is extremely powerful, the major challenge is assigning the complex spectra that is output from the experiment. To that end, the major contribution of this thesis is an automated pattern matching algorithm based on the symmetric-top, rigid rotor model. Using this algorithm, transitions of the water dimer, pentamer, hexamer, and octamer were identified and assigned from a back log of experimental data. These assignments revealed a dramatic enhancement of tunneling motions in the librational (300 – 600 cm^{-1}) region. These enhancements were most dramatic for motions involved in breaking and reforming the hydrogen bond in the clusters, adding to the evidence that understanding this region is essential to understanding hydrogen bond breaking dynamics.

The use of 2nd order, nonlinear spectroscopy to probe surfaces is a well-established technique. Employing second harmonic generation in a scattering geometry enables probing buried interfaces in colloidal samples; these samples provide an appealing path forward towards studying real world polymers such as water purification membranes. We show that SHS can be used to probe resonant and non-resonant molecules at a polymer interface, and we extract free energies of adsorption from a variety of organic molecules. In the future, we plan to extend this technique to ionic species to supplement our existing studies of ion adsorption via sum frequency generation in reflection geometry.

Table of Contents

For Fritzi and Geoff

Acknowledgements

I will never be able to fully acknowledge and thank the wonderful people I have had the pleasure to work with in my time at Cal. I want to start by thanking the entire Saykally group who has been a constant source of encouragement and inspiration.

I am grateful to Tony for his many kind words and patience with my many questions, and for playing golf with a scrub like me. Remember your star burns bright. Royce and I had many lunches discussing science and life, or at least that was our justification for 2-hour lunches. Sumana and Chris have been the most helpful and patient people I could imagine helping me to transition into non-linear spectroscopy, and I am truly grateful for their help. The younglings: Hikaru, Shane, and Frank have revitalized the group, and I am confident the group is in excellent hands going forward. It is important to thank the most important member of the Saykally group, Ivette, without whom no work would get done. The other former members of the group: Deb, Jacob, Akber, Scott, Haoyun, and others have all helped me throughout my graduate career and for that I am most appreciative. I also owe a huge thank you to group alumni Ray Fellers who collected the data that is assigned herein, without his efforts this thesis would be much shorter.

I owe a debt of gratitude to Dr. Jared Anderson and Dr. Tien Ho for introducing me to chemistry research and the setting me on a path that has led me here. You inspired me to ask the difficult questions.

I have had the incredible pleasure to have met many incredible people in my time here who have made the past 5 years enjoyable. In no particular order, I want to thank Jeremy, Robinson, Erin, Victor, Allison, Peter, Mary, Jessalyn, Brad, Alex, and Brett for being wonderful friends. I want to especially thank my roommates, Luke and Michael, who have kept me sane these past 4 years. I probably wouldn't have made it to the end without you two.

My parents, Fritzi, and Geoff, and my sister, Casey, have done so much for me I would never be able to put my gratitude into words. Thank you, I love you.

And lastly, I want to thank Rich. I came to Cal to work for you and I am happy I did. I know I can be stubborn and difficult but I thank you for sticking with me and challenging to think critically about science. Thank you for all you have done for me, except for trying to make me sing.

Chapter I: Terahertz Vibration – Rotation – Tunneling (VRT) Spectroscopy of Clusters

Introduction to Terahertz Spectroscopy

Study of Water Clusters

The challenge in developing a predictive molecular-scale description of water is essentially that of correctly describing its extended and highly dynamic hydrogen-bonded network [1–6]. Spectroscopic study of water clusters provides accurate benchmarks for detailed characterization of the complex pairwise and many-body forces that operate in bulk water phases, which have proven difficult to adequately capture through bulk experiments or from theory [2,3,7,8]. The need to accomplish this goal is underscored by recurring controversies surrounding the fundamental intermolecular structure and dynamics of water [2,9,10].

Early studies of water clusters were conducted in the microwave region and revealed a rich rotational structure characterized by permutational tunneling pathways [11–13]. These pathways became more pronounced and elaborate when excitation into the intermolecular vibrational degree of freedom was achieved [14–16]. Due to the high barriers of these permutational tunneling pathways, only high resolution techniques could accurately measure the detailed spectra of these species, although studies in solid and liquid noble gases were important for their ability to measure the band origins of intermolecular vibrations over a range much broader than those accessible from any specific high resolution technique [17–20]. Clusters ranging from dimer through octamer [3,6,21–24], as well as nonamer and decamer [25] have been studied in detail by high precision microwave and terahertz spectroscopy [2,3,7,26,27]. Some of the measured clusters and their structures are shown in Figure 1.

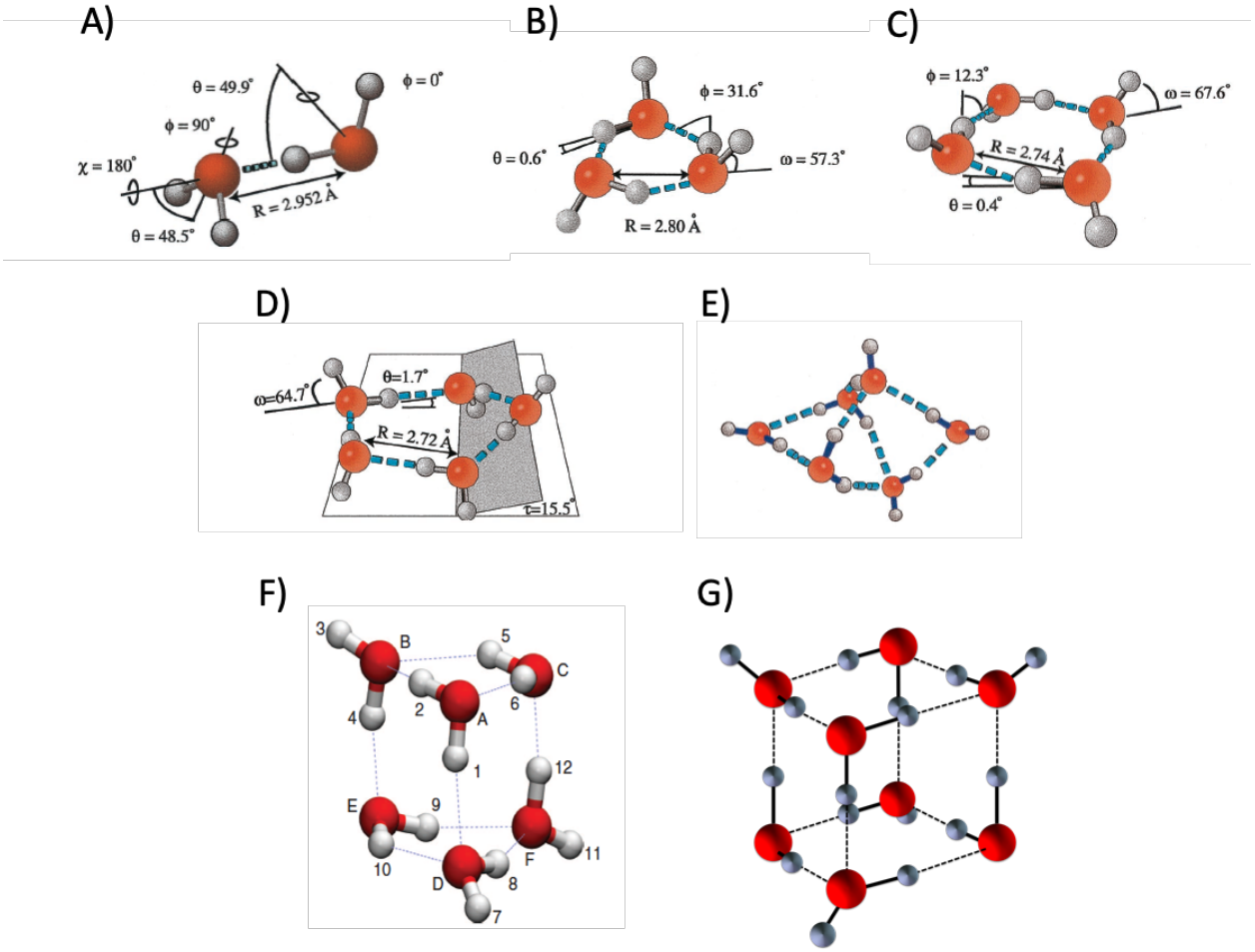

Figure 1: The structures of various water clusters measured in the gas phase. Oxygens are shown in red and hydrogen in grey or white. The shown structures are for: A) the dimer, B) trimer, C) tetramer, D) pentamer, E) the cage isomer of the hexamer, F) the prism isomer of the hexamer, and G) the octamer. This figure is adapted with permission from reference [2].

Study of these clusters was driven by a desire to develop more accurate water potential energy surfaces [28,29]. Water cluster were particularly useful in elucidating the 2 and 3 body terms in the many-body expansion of water potentials[30–32]. Several early potential models were developed by fitting experimental water cluster transitions to parameterize terms in the model [16,33,34]. These models were successful in predicting some properties of the bulk; notably, the VRT(ASP-W) model was able to correctly predict the water dimerization equilibrium constant [35–37]; however, these lacked the desired universality. The inherit limitation in developing a universal water model was the inadequate *ab initio* model for the water dimer and trimer, which in theory, should encompass complete information about the 2 and 3 body terms. These models required 12 and 21 dimensional treatments for the dimer and trimer, respectively, which has only recently become feasible for the dimer [8,38–40]. This breakthrough for the water dimer has led to a question of what use accurate water cluster spectra can be if not to parameterize and calibrate improved water models.

From discussions about the such models with its developers, it seems one important limitation of these type of models is the inability to predict intermolecular VRT transitions in the librational region (300 – 600 cm^{-1}). This region is of particular interest due to theoretical studies which suggest that hydrogen bond breaking motions occur primarily through excitation of librational degrees of freedoms [41–44]. Therefore, it remains of general interest to measure spectra in this vital frequency range. Additionally, there will always be a role for water cluster spectra in benchmarking newly developed theories. Due to the molecular motions which comprise VRT features, these transitions provide a very sensitive test of the short-range repulsive forces of water clusters [45–48]. More recent theoretical endeavors have focused on water – halide clusters and water self-ions ($OH^- \bullet (H_2O)_n$), and it is expected that existing knowledge of water cluster interactions will be very useful in this context.[49,50]

Tunneling Dynamics of Water Clusters

While benchmarking theory is clearly an important endeavor, it is possible that there is additional insight that measured water cluster transitions can provide. It is well-known that the famous remarkable properties of water result from the intricacies of the hydrogen bond network (HBN) connecting the individual water monomers [3,41,42,51–54]. Understanding details of the processes by which the HBN rearranges is thus essential to understanding and accurately modeling water. Various experimental techniques have addressed these rearrangement dynamics, but these have generally required extensive interpretation to rationalize the measured properties [55–61]. In contrast, molecular dynamics (MD) simulations have provided a detailed microscopic picture of many aqueous systems, but are limited in that they depend explicitly on the model potentials used in the simulation [41,42,52,62]. For example, recent work has again indicated that nuclear quantum effects are important for correctly describing hydrogen bond behavior [63,64].

Incoherent neutron scattering experiments on both H_2O and D_2O demonstrate evidence of relaxation processes with two distinct timescales [56]. Similar experiments performed by Cabral et al. on mixtures of H_2O with DMSO showed good agreement with the theoretical results of Luzar and Chandler [56,65], viz. that the "residence" time, defined as the average time in which a molecule remains in a narrow geometric domain wherein a hydrogen bond could form, is 1.8 ± 0.4 ps for pure water and is 6 ± 2ps in the mixture. These neutron scattering experiments

supported the theoretical contention that librational motions (hindered rotations) are the primary means of breaking and forming hydrogen bonds in the liquid. Subsequent experiments using coherent quasielastic neutron scattering have provided further refinement of these deductions and also demonstrated that the temperature dependence of hydrogen bond dynamics is curiously weak compared to that of other transport properties of liquid water [56,66,67].

More recently, mid-IR femtosecond pump-probe spectroscopy experiments and photon echo experiments have yielded additional insight into the intramolecular modes associated with HBNR dynamics. Pump-probe spectroscopy experiments on the O-H stretch in HDO:D_2O solutions demonstrate that consideration of the coupling between the intramolecular OH stretch and a translational intermolecular vibration is essential to understanding the vibrational relaxation in the liquid [55,61,68–71]. Further studies employing femtosecond mid-IR spectroscopy demonstrated coupling between intra- and inter-molecular modes, and also identified two distinct time domains for relaxation processes, viz. sub-picosecond and picosecond [58,72–75]. In photon echo experiments, Stenger et al. demonstrated that there may also be an even longer (5-15 ps) timescale process occurring, which must be connected to the hydrogen bond rearrangement, indicating that these dynamics may be much slower than previously thought [76]. Huse et al. then performed ultrafast pump probe experiments on the O-H bending mode and showed that explicit consideration of the librational excitations is necessary to rationalize ultrafast vibrational relaxation [70].

While the proceeding experiments have provided significant insight into aqueous hydrogen bond dynamics, some authors have argued that they possess a common weakness [42,54], viz. lack of a conclusive connection between the relaxation processes observed and the detailed hydrogen bond dynamics occurring in the bulk. While some measured properties, such as the "residence time" obtained in neutron scattering experiments, have been shown to agree well with the predicted hydrogen bond lifetimes, the connections of other properties to actual bulk phase dynamics is less transparent. Motivated by this history, and mindful of the ambiguities, our group has endeavored to explore the relation of our high-precision terahertz spectroscopy measurements of water cluster intermolecular vibrational modes to the HBNR dynamics of bulk water.

We draw attention to studies suggesting that the behavior of other small water clusters can provide additional insight into the hydrogen bond dynamics of the bulk [77–80]. In the aforementioned theoretical studies by Luzar and Chandler, the authors found that the dynamics of a particular hydrogen bond were not affected by the neighboring hydrogen bonds [42,62,69,71], i.e. the local environment of a hydrogen bond does not significantly affect the dynamics of the hydrogen bond itself. Furthermore, more recent studies show that even static correlations are insignificant, and this result holds regardless of temperature [80]. Additionally, the spectra of clusters comprising 10-100 molecules resemble the spectra of bulk [59,81]. Later is this thesis, we will show an example of using measured tunneling splittings for different water clusters to calculate the hydrogen bond "lifetime" in these clusters and relate these lifetimes to the bulk.

Theoretical Description of VRT Transitions in Clusters

The measured water cluster transitions presented in this thesis were found in the wavelength range near 500 cm^{-1}. This is in the middle of the librational region of liquid water which spans from approximately 300 – 900 cm^{-1} [78]. The motions associated with this region are

hindered, intermolecular vibrations of the hydrogen bond axis, which can occur either in or out of the plane defined by the two oxygens and one hydrogen that form the hydrogen bond. These motions are predicted to play an central role in the breaking and reforming of hydrogen bonds, and thus understanding the details of such motions of water clusters in this region can enhance our understanding of the nature of such motions in bulk phases [42,43].

For clusters in this experimental region, the vibrational degree of freedom are intermolecular in nature. The simple equation for estimating vibrational degrees of freedom still works for cluster species; therefore, for a nonlinear cluster such as the water pentamer, we expect a total of 3N – 6 vibrational modes. We can find the number of *intermolecular* modes by using the fact that each individual water molecule has 3 *intramolecular* modes.

$$\#\ inter.vib. = (3N - 6) - 3(\#water\ molecules) \qquad (\mathbf{1})$$

For the water pentamer, we thus expect 24 intermolecular vibrations and 15 intramolecular vibrations. Due to the large number of intermolecular degrees of freedom and their inherent nonrigidity, it is typical to forgo modeling these vibration explicitly and instead to use a constant term to represent a the band origin (v), which simply corresponds to the energy difference between two intermolecular modes.

To model the observed rotational structure of the transitions, the typical assumption is that the(vibrationally averaged) water clusters behave as either a near-prolate or near oblate symmetric rotor, which enables the use of simple energy level models for those species. The classification of a molecule or cluster as prolate or oblate depends on the specific moments of inertia of the species of interest. A prolate molecule (cigar shaped) is defined as a species with $I_a < I_b = I_c$ where a, b, and c refer to the 3 axes of a coordinate system defined with its origin at the center of mass of the molecule or cluster. Similarly, an oblate molecule (frisbee disc-shaped) is a molecule or cluster where $I_a = I_b < I_c$. Importantly, it is convention that axes are labelled a to c in order of increasing moment of inertia, as the above relationship would imply. It has been commonplace to categorize water clusters into either of these type in order to simplify analysis [16,82–84]. However, the water hexamer transitions presented in Chapter 2 of this thesis were found to deviate significantly from this simple model and a more detailed asymmetric top model had to be utilized. For the purposes of this section we will use a simple oblate top molecule as an example.

Equation 2 gives the expected energy levels of an oblate rotor (such as the vibrationally averaged) water pentamer) with respect to the total angular momentum quantum number, J, and its projection along the principal axis, K:

$$E(J,K) = v + B * J(J+1) + (C - B) * K^2 - D_J[J(J+1)]^2 - D_{JK} * [J(J+1)K^2] - D_K * K^4 \qquad (\mathbf{2})$$

Here v is the band origin discussed above (v is defined as 0 for the ground sate). B and C are rotational constants for axes b and c respectively, and are related to the moment of inertia by: $X = \frac{\hbar^2}{2I_x}$, *where x labels the axis*, and D_J, D_{JK}, and D_K are centrifugal distortion constants which help to account for deviations from a symmetric top model [16]. The typical selection rules associated with rotational spectroscopy are $\Delta J = \pm 1, 0$ and likewise $\Delta K = \pm 1$; $\Delta K = 0$ is also possible, but only if $\Delta J \neq 0$. These selection rules give rise to the classical P ($\Delta J = -1$), Q ($\Delta J = 0$), and R ($\Delta J = +1$) branches associated with vibration – rotation spectroscopy.

Additional spectral structure arises from permutational tunneling of cluster species, which further splits these energy level. To understand these tunneling motions, it is useful to utilize complete nuclear permutation inversion (CNPI) groups, which represent the class of symmetry operations which either permute two identical nuclei or perform an inversion on the overall complex. The use of CNPI groups to understand permutational tunneling is a well-established idea dating back to the original formulations of Longuet-Higgins and Coudert and Hougen, among others [12,13,85]. The interested reader is directed to the above references on the subject, but a simplified explanation will be given here.

For a given water cluster, the CNPI group consists of the union of the group of all permutation of the oxygen (S_O), the group of all permutation of the hydrogens (S_H), and the inversion group operation. The size of this group is O! * H! * 2, where O and H are the number of oxygens and hydrogens, respectively. Even for the smallest water cluster species, viz. the dimer, there are 96 group elements; if all of these group elements lead to an observable tunneling splitting, the resultant spectrum would be challenging to interpret. Fortunately, in practice, we only need to consider the "feasible" tunneling elements, which are defined here as the elements which do not break or reform a chemical bond. This definition will serve as long as the excitations in the experiment are below the threshold for bond breaking. The number of elements to be considered for a particular water cluster is given by n! * 2^n * 2, where n is the number of water molecules in the cluster. As a note, this formula represents an upper bound; it is possible that not all of the group elements actually need to be considered; put another way, not all of the group elements may lead to a splitting which is experimentally observable (i.e. too small in magnitude). For example, the expected number of "feasible" elements for the water pentamer is 7680, but it was found experimentally that a group of size 320 accurately represented the observed spectra. This reduction reduces the 96 elements of the water dimer down to 16, and for a larger cluster like the pentamer simplifies 870912000 elements to 96.

Glossing over how to obtain the actual group elements for a given cluster (the interested reader is again referred to References [12,13,85]), the group can be used to find irreducible representation (irrep) of the resultant energy levels. Once these representations are known, Fermi's Golden Rule can be applied to determine what transitions are actually possible. The relevant form of Fermi's Golden Rule is:

$$\Gamma_f \otimes \Gamma_\mu \otimes \Gamma_i \in A_1 \qquad (3)$$

Here Γ_f and Γ_i are the irreps of the final and initial state, respectively, Γ_μ is the irrep of the dipole moment, and A_1 is the totally symmetric representation. An example, how tunneling splitting can be labelled by irreps are shown in Figure 2.

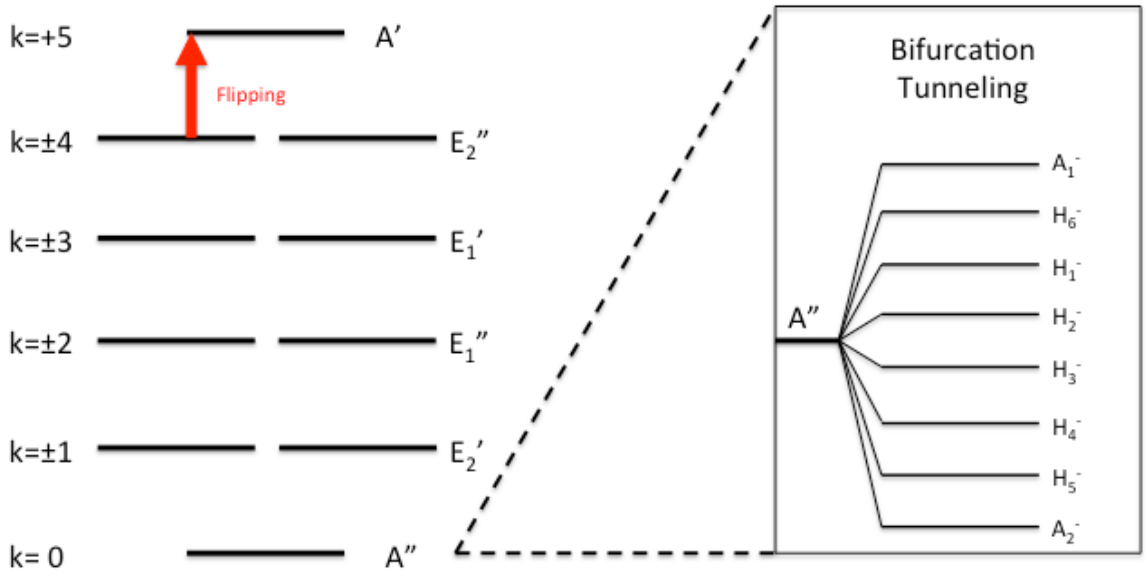

Figure 2: Pseudorotational manifold of the water pentamer. The diagram on the left shows the result of the "flipping" motion, shown as a red arrow, which generates a manifold of 10 energy levels, labeled by the irreducible representations of the C_{5h} point group. A pseudo-quantum number, k, defined in the text, also labels the levels. On the right, the splitting caused by bifurcation tunneling is shown for a single pseudorotational level. These states can be labeled by the irreducible representations of G_{320}, as shown by Wales et al [86]. The reader is referred to Wales et al for a detailed discussion of the relevant group theory [86].

In Figure 2, we can see the effects of two types of tunneling motion on the the energy level expression in Equation 2. First, a flipping motions splits each E(J,K) level into 10 levels comprising 4 pairs of doubly degenerate states and two singlet states. Each of these levels is then in turn split into 8 singlet states; importantly, only the symmetry levels of the final states (those shown on the right in Figure 2) need to be subjected to Fermi's Golden Rule, as the symmetry of the originally split lines is implicitly considered. While this tunneling does lead to an increase in the density of states, it also leads to more levels of symmetry, which can be exploited during assignment to distinguish transitions of one symmetry from another.

Experimental Systems

The work conducted in this chapter consists of analyzing data from an old lead-salt diode laser spectrometer, as well as an attempt to incorporate a novel quantum cascade laser (QCL) into the design in order to access new spectral regions. A brief description of the diode laser setup will be given in addition to a detailed report on the incorporation of the QCL.

Lead-Salt Diode Laser Spectrometer

The Berkeley supersonic beam/diode laser spectrometer used for the measurements reported in this thesis has been described in detail elsewhere [87–89] and only a short description will be provided here.

A helium-cooled diode laser spectrometer (Spectra Physics) using lead-salt diodes (Laser Photonics) was used to produce infrared radiation from 515-528 cm^{-1} ,(which corresponds roughly to 15 THz). The beam was multipassed 18-22 times through a pulsed planar supersonic expansion of a mixture of H_2O and He using a Herriot cell and detected using a helium-cooled (Si:B) photoconductive detector (IR Labs). The supersonic expansion is produced by bubbling pure He gas, with a backing pressure of 1-2 atm, through liquid H_2O, and then expanding it through a 101.6 mm long slit at a repetition rate of 35 Hz into a vacuum chamber maintained at ~200mTorr by a Roots blower (Edwards 4200) backed by two rotary pumps (E2M 275). The cooling in the supersonic beam was sufficient for the cluster species to reach a rotational temperature of 4 - 10K. Simultaneously, the fringe spacing of a vacuum-spaced etalon and an OCS reference gas spectrum are detected with a liquid He cooled (Cu:Ge) detector (Santa Barbara Research Center) and recorded to enable precise frequency calibration. The observed linewidths of ~ 30 MHz full-width half maximum (FWHM) are slightly larger than the Doppler-limited linewidths extrapolated form earlier experiments. Typical frequency accuracy is 10-20 MHz, which was limited by linewidths of the cluster absorptions and laser drift.

Spectra are detected in direct absorption using a time-gated phase-sensitive signal processing approach. The sensitivity of the experiment has been previously discussed by Keutsch et al [90]: briefly, the signal-to-noise ratio of the Q-branches was about 200:1 compared to 8000:1 for the most intense vibrations observed in lower frequency THz experiments performed in the same group. The sensitivity of the diode laser experiment (10-100ppm) is about 2 orders of magnitude lower than that of the THz sideband lase experiments, indicating that the observed transitions are very intense.

Accessing the 500 cm^{-1} region of the electromagnetic spectrum has been notoriously difficult. The first observation of a librational vibration in the region was report in 1987 by von Puttkamer and Quack for $(HF)_2$ [91]. The spectra reported here required the use of 10 separate laser diodes, each scanned across several modes to cover the specified spectral range. However, large laser gaps are nevertheless present in the spectra, which causes considerable difficulty in the assignment. It is relevant to note that Keutsch et al. have previously assigned a portion of the measured raw experimental spectrum to out-of-plane librations of the H_2O trimer [90]. Recent matrix isolation results from the Lund group prompted a reinvestigation of the remaining unassigned lines in that region [17–20].

A Terahertz VRT spectrometer employing quantum cascade lasers

The full details of this section can be found in: Cole, W.T.S., Hlavacek, N.C., Lee, A.W.M., Kao, T.-Y., Hu, Q., Reno, J.L., Saykally, R.J., Chem. Phys. Lett., ***638****, 144 (2015).*

Introduction

The use of high resolution Terahertz spectroscopy radiation sources for spectroscopy of jet cooled expansions of ions, clusters, and molecules has engendered important advances in the understanding of intermolecular forces and molecular structure. Of particular interest to our group is the study of water clusters, as these are a route to a more detailed understanding of bulk water [2,3,82,83]. However, the paucity of Terahertz sources operating above 3 THz, and increasing

constraints on laser safety have stifled progress in this field [92]. Recently emerging frontiers in space, atmospheric, and defense-related research have driven the development of new Terahertz laser source technologies that are having a broad impact on the Terahertz region in general [93–96]. One notable advance has been the development of Quantum Cascade Lasers (QCLs) that function in the low Terahertz regime (1.2-5 THz). These devices offer many attractive features for spectroscopy, such as high power, narrow bandwidth, and continuous tunability over a broad spectral range [97–100]. While the advent of QCLs has greatly impacted infrared spectroscopy [101], only recently have commercial Terahertz QCLs become available to the general scientific community, and these have primarily been employed for imaging technologies [102–105].

The principal motivations for using a Terahertz QCL as the laser source for high resolution VRT spectroscopy include the desire to simplify the experimental design and to increase the sensitivity and the operating frequency. Prior to the Terahertz QCL, uW power levels were generated with microwave sidebands on Schottky diode mixers pumped with high-power CO_2 laser-pumped gas lasers. These systems are difficult to operate, unstable, have diminishing amounts of power at frequencies > 3 THz, and are constrained in operating frequency to regions around the discrete gas lines of the gas laser. The new QCL source offers much higher powers than previous solid state sources (mWs compared to 10s of μWs) . QCLs are available in a continuous range of frequencies, where the emission can be engineered coarsely by adjusting the band structure, and finely by design of the optical cavity. Additionally, the operation of this commercial device is safe and relatively simple, allowing facile integration into an experimental setup and straightforward operation. As a field test of these performance features, the EASY-QCL was integrated into the Berkeley Terahertz VRT spectroscopy setup and used to measure absorptions in a supersonic expansion of methanol/Ar.

Terahertz VRT Spectrometer Design

The EASY-QCL system provided by LongWave Photonics comprises two main components: the Stirling cycle He cryocooler and the fabricated QCL semiconductor chip based on MIT group's design, mounted inside a vacuum cell mounted on the cooler. The chip itself consists of distributed feedback (DFB) laser array using a metal-metal waveguide and has been described in detail in [104,106] to achieve better efficiency and beam divergence. The fabricated QCL chip contains 20 independent devices, each capable of lasing at center frequencies separated by a few GHz. The emitting power is around 1 to 1.5 mW depends on the laser frequency. A chip similar to that used in this study is shown in Figure 3.

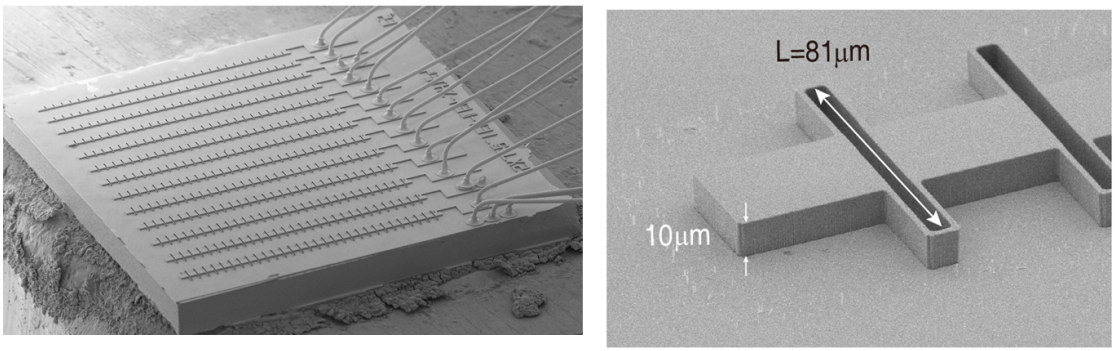

Figure 3: A portion of the DFB QCL chip; the individual devices can be seen on the left hand side of the figure. The right hand side shows the design of the antenna-coupled DFB laser and dimensions of the multiple quantum well (MQW) stack.

The QCL system is integrated into the Berkeley VRT spectrometer as shown in Figure 4
.

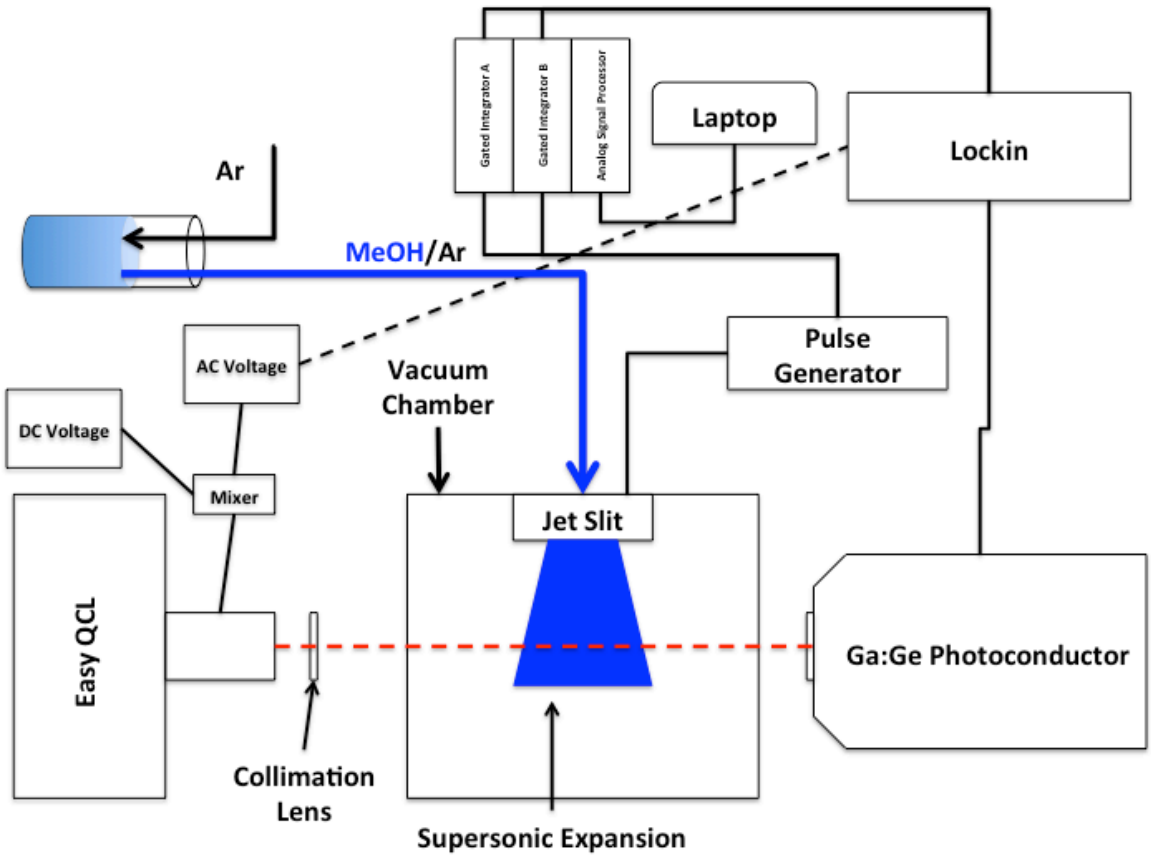

Figure 4: Diagram of the apparatus for Terahertz VRT spectroscopy of supersonic jets using the EASY-QCL system.

Briefly, a DC power source (Keithley, Model 2230-30-1) provides a DC voltage which is mixed with a 0.5 mV, 50 kHz sine wave AC voltage, provided by the lockin(Stanford Research Systems, Model 830), in a bias tee (ThorLabs, Model T1G), the resultant of which is then applied to the QCL device. The laser output is collimated by a concave-hemispherical HRFZ-Si lens treated with an anti-reflectivity coating (Tydex, St. Petersburg, RN) and directed through a Zenor window to a vacuum chamber maintained at 70 mTorr by a Roots blower (Edwards EH4200) backed by two rotary pumps (Edwards E2M275). The laser beam passes through the chamber and a second window to the detector, a stressed Ge:Ga photoconductor mounted in a side-looking IR Labs dewar which is cooled to 4 K with LHe. Signal from the detector is amplified by a transimpedance preamplifier (IRLabs, LN-8) before being sent to the lockin and detected at twice the modulation frequency (2f). For scans of ambient pressure methanol, the signal was digitized and sent directly to the computer. For scans of the pulsed supersonic jet, the signal was routed to two boxcar integrators (Stanford Research Systems, Model SR250) operating with delays of 300 μs and 1.3 ms with respect to the supersonic pulse trigger. The gate width on both integrators was set at 150 μs; a 100-point running average was sent to an analog processor (Stanford Research Systems, Model SR 235) where the signals were subtracted from each other before being digitized and sent to the computer. The entire system was controlled by an in-house Labview program.

The demodulated signal from the scan has a second derivative shape with respect to a traditional absorbance feature. The reason that 2f detection is so useful for this type of spectroscopy is that it effects both high(ca. 1 ppm) absorption sensitivity and suppression of baseline due to systematic power variation of the source with a relatively simple and convenient configuration. In combination with a lockin at kilohertz frequencies drastic noise reduction further increases the sensitivity [107].

Ambient Methanol Measurements

Spectroscopic grade methanol (Sigma Aldrich) vapor was introduced into the chamber at a pressure of ca. 400 mTorr and then the chamber was sealed. Laser scan conditions were as follows: voltage swept from 16.3 to 17.8 V in 1mV steps, time between steps was 0.5 seconds, sine wave modulation at 50 kHz with 0.5 mV amplitude. The stressed photoconductor detector was biased at 40 mV via the preamplifier and the resulting signal was amplified 10x. The signal was detected by the lockin at 100 kHz with a time constant of 300 ms and the output was sent directly to the computer for analysis.

Several pressures were tested in the range 100-2000mTorr. The reported pressure was chosen empirically as a compromise between good signal to noise ratio and insuring that pressure broadening was not causing consecutive peaks to overlap.

Supersonic Methanol/Ar jet measurements

Planar supersonic beams of Ar and methanol/Ar were produced as follows. For the Ar jet, pure Ar gas was fed directly to the jet input at a backing pressure of 1-2 atm. The methanol/Ar jet was created by bubbling Ar gas through a flask containing spectroscopy grade methanol at a backing pressure of 1-2 atm. The jet operation has been described in detail elsewhere [89]. In brief, the gas is expanded through a 4” x 0.005” slit nozzle pulsed at a rate of 40

Hz, as controlled by a pulse generator (Stanford Research Systems, Model DG535). The planar supersonic beam was overlapped with the laser beam at a distance of 1" below the slit and parallel to the slit direction to maximize signal and minimize residual Doppler broadening; rotational temperature are expected to be ~4 K in the jet [89]. Laser scan conditions were as follows: the laser DC voltage was swept from 16.3 to 17.8 V in 1 mV steps, time between steps was 1 second, modulation was at 50 kHz with an amplitude of 0.5 mV. The detector was biased with 40 mV supplied by the preamplifier and the signal was amplified 10x. The lockin demodulated the signal at 100 kHz with a time constant of 100 μs. Observed peaks were optimized by fixing the laser frequency on the peak and adjusting the lockin phase until the peak completely disappeared, and then switching the phase by 90 degrees.

Results

Ambient Pressure Methanol

A 2f absorption spectrum of a gas cell containing methanol at a pressure of approximately 400 mTorr was taken as an initial test of the setup. The spectrum is shown in Figure 5, the frequency of the laser was determined as described in the following section.

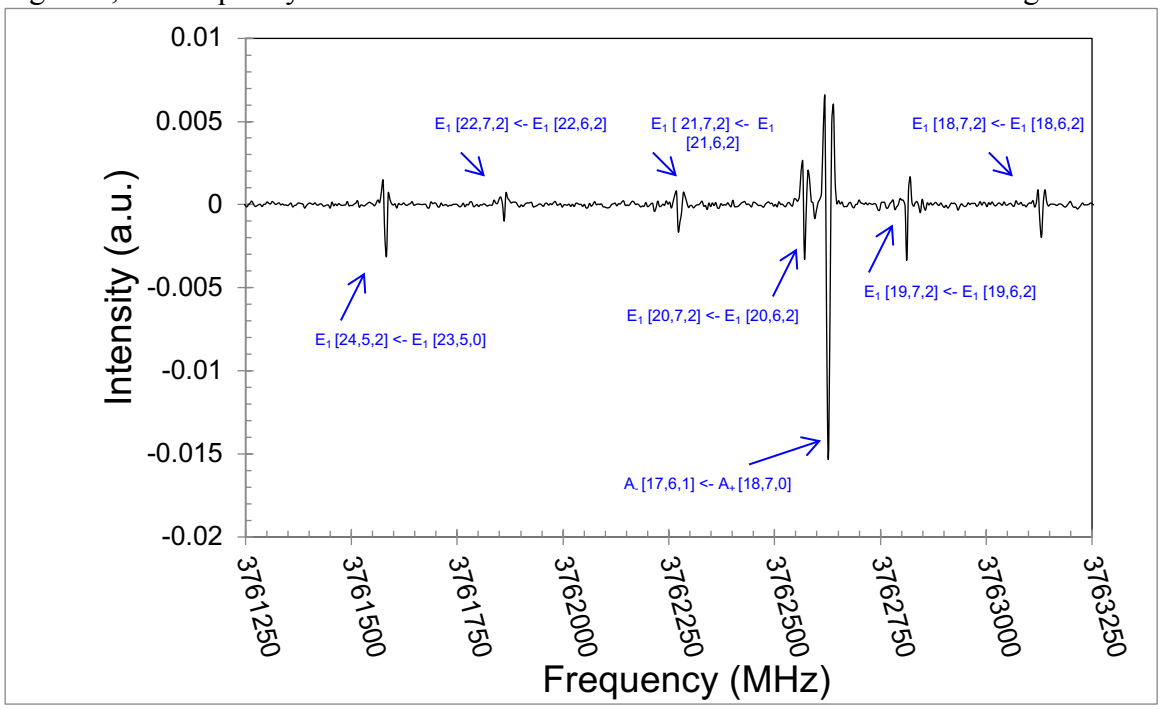

Figure 5: 2f absorption spectrum of methanol at a pressure of 400 mTorr. All transitions are assigned to the JPL methanol line catalog. The format for the assignments is (Symmetry of upper state) (J',K',v') <- (Symmetry of lower state) (J",K",v"). FWHM linewidths range from 8 to 13 MHz. Calibration of the initial QCL voltage to the frequency domain was accomplished by a linear fit to the JPL methanol line catalog (a cubic fit was also performed by did not yield significantly different results).

The spectrum shows well-defined absorptions of methanol in the roughly 2 GHz operating window of the specific QCL device. FWHM linewidths are measured to be 8-13 MHz, in reasonable agreement with the linewidths predicted by the methanol self-broadening coefficient of 30.5 MHz/Torr [98]. Doppler broadening for the ambient methanol scans are expected to be negligible (< 1 MHz) compared to pressure broadening (~10 MHz).

Calibration of QCL Frequency

The observed peaks in the ambient methanol spectrum were used to calibrate the frequency tuning of the QCL by fitting to the JPL catalog frequencies of methanol lines, using the spectral assignment shown in Figure 3. This resulted in a linear fit with a start frequency of 3761245 MHz and a voltage tuning of 1321.4080 MHz/V. Other functions (e.g. cubic) were used to calibrate the data, but showed no significant improvement over the linear calibration. This result is encouraging as it demonstrates that the frequency tuning of the laser based on voltage alone for a single device is significant (a ca. 2 GHz total range) and quite linear over this range. Although the effect of operating temperature on the frequency tuning was not investigated here due to time constraints, the total (temperature and frequency) tuning for similar devices have been shown to be several times what we have measured [104]. The minimum estimate then for total frequency coverage provided by the 20 devices on the chip would be 40 GHz (electrical tuning only), but given the above, it is likely that the actual tuning of the QCL array is closer to 160 GHz, if thermal tuning were included. It should be noted that while this calibration procedure gives a relative constraint on the frequency of the laser, improvements must be made in order to achieve suitable frequency accuracy better than 1 MHz for high resolution spectroscopy applications.

VRT spectroscopy of supersonic expansions

Application of the QCL system to a supersonic expansion of methanol/Ar was accomplished and the results are presented in Figure 6. A scan of the same frequency region in an expansion of pure argon showed no spectra.

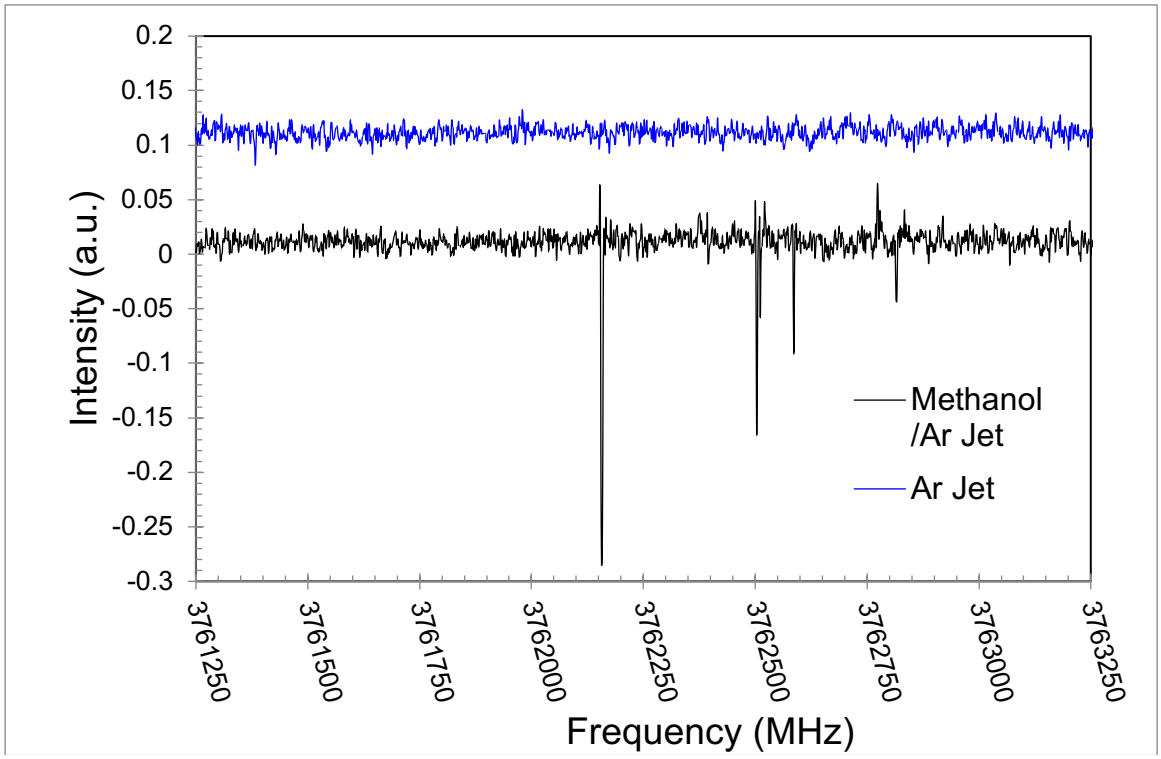

Figure 6: Comparison of 2f absorption spectra of Ar and Methanol/Ar supersonic jets. Supersonic jet produced by bubbling Ar, at a pressure of 1-2 atm, through methanol into a chamber maintained at 70 mTorr by a roots blower through a 4" by 0.005" slit nozzle at a pulse rate of 40 Hz. The 50kHz FM modulated laser beam was passed once through the sample and collected by a stressed Ge:Ga photodetector. Detector output was demodulated, averaged, and background subtracted using a lockin and boxcar integrators. Significant peaks in the methanol spectrum do not belong to the methanol monomer transitions in the JPL catalog. Linewidths are between 2-3MHz with the exception of the most intense line, which has a linewidth of 5.5 MHz, which could be explained by multiple transitions overlapping.

The spectrum was obtained from the same device used to capture the ambient methanol data and thus represents the same frequency window. When attempting to assign the measured transitions to the JPL catalog it was determined that the lines do not correspond to any known or predicted methanol monomer lines. From results obtained with the pure Ar expansion, it is clear the lines originate from a methanol-containing cluster, most likely CH_3OH-Ar or $(CH_3OH)_2$. Definitive assignment of the cluster cannot be accomplished with the current limited frequency window. However, the spectrum clearly illustrates the exciting potential of the QCL device for VRT spectroscopy of supersonic expansions, which will soon permit access to a frequency domain that has never been explored previously by a high-resolution spectroscopy technique.

Without a spectral assignment, no explicit determination of the rotational temperature can be made, but we expect it to be similar (4 K) to that observed in previous experiments using this same supersonic jet system [89]. The FWHM linewidths of peaks were measured to be 2-3 MHz with the exception of the most intense line, which had a linewidth of 5.5 MHz, as shown in Figure 7.

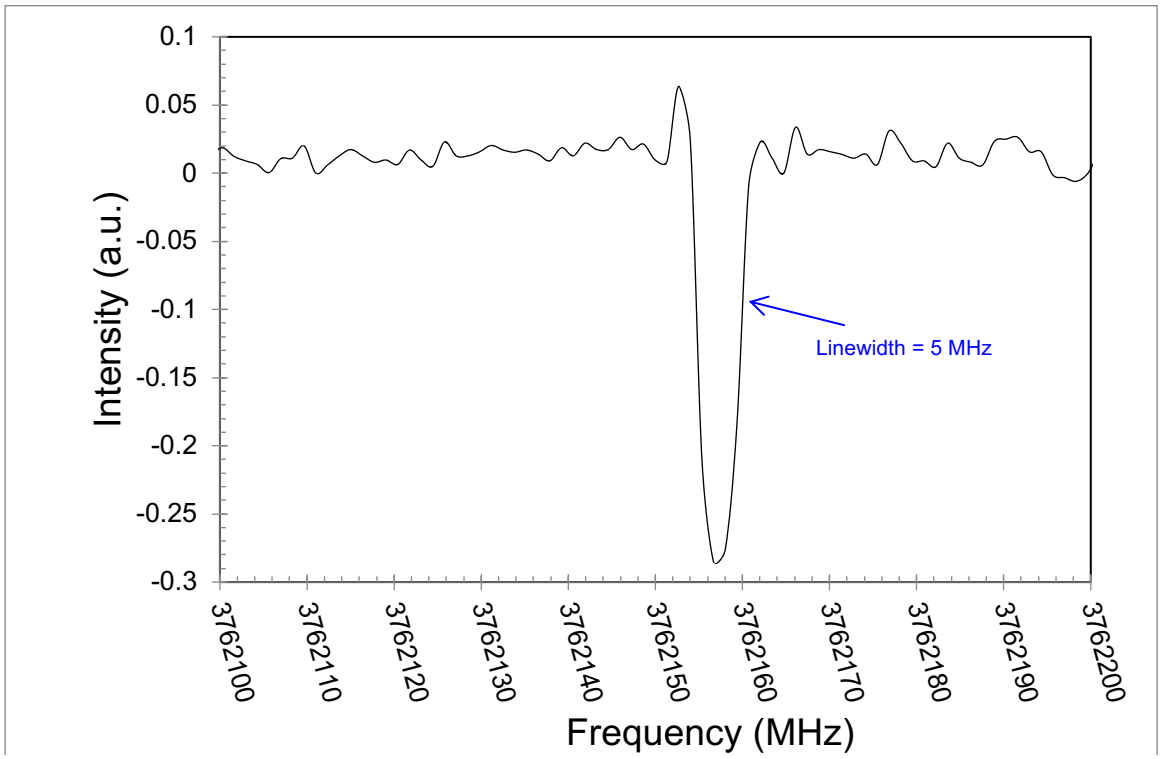

Figure 7: Expanded spectrum of the most intense Methanol/Ar supersonic jet peak at 3762156.8 MHz. The peak shape is not a perfect 2nd derivative shape, but the laser may have been undermodulated, which could explain the irregularity.

This larger linewidth is most likely explained by the presence of two unresolved lines separated by a frequency smaller than the experimental resolution. The other linewidths are slightly larger than the expected 4 K Doppler broadening of ca. 1 MHz. An explanation for this is that the voltage steps of the scans, 1 mV/step or 1.321 MHz/step, contributed an instrumental broadening to each peak. This could clearly be eliminated by using smaller frequency steps; however doing so greatly increased the scan time of the experiment, which was problematic due to the length of the current laser loan period. However, the currently employed experimental parameters clearly effect high-resolution scans.

Based on the measured spectra, we are able to determine the minimum fractional absorption sensitivity of the QCL spectrometer, defined as

$$\frac{\Delta P}{P} = \frac{N}{S/\sqrt{B}}$$

where N is the rms noise with the laser on and S is the maximum laser signal before amplification by the system with no methanol present in the spectrometer. Both quantities are adjusted for system amplification, and amplitude modulation/lockin detection. B is the detection bandwidths for the scan. The values we obtained from experiment were as follows: 115mV laser signal, the detection bandwidth was 2.5 Hz, and the rms noise of the laser on the detector was 0.293 $\mu V/\sqrt{Hz}$. The fractional sensitivity determined in this way is $4.03*10^{-6}$, which is comparable to the far infrared laser sideband system, previously utilized for this experiment [87,88]. This is very promising, considering that the previous designs utilized some form of multipass optics in the vacuum chamber [87–89], whereas the current setup employs only a single pass. Additionally, the stressed Ge:Ga photocondutor used for this experiment was likely to have been saturated by the high power (>1mW) provided by the QCL; thus, it is likely that incorporation of multipass optics into the system will produce considerably higher signal to noise ratios that our previous designs. More evidence for the presence of saturation is the fact that the ultimate sensitivity limit of the detector, which can be regarded and the quantum, or "shot noise" limit, is given by:

$$Q_L = 2.8 * 10^{-10} \left(\frac{v}{\eta P \tau M^2}\right)$$

Here v is laser frequency (in cm^{-1}), η is the detector quantum efficiency, P is the laser incident power, τ is the integration time, and M is the modulation index ($0 < M < 1$). Using typical values of 1s for the integration time, 0.3 for M, 1 mW for P, and 0.1 for quantum efficiency we get a shot noise limited fractional absorption sensitivity of $3.51*10^{-8}$ for light at a wavelength of 125.4 cm^{-1}; this is fully 2 orders of magnitude better than our measured value.

Conclusions

We have described the first results reported from integrating a commercial Terahertz QCL system into a supersonic beam VRT spectroscopy apparatus. Moreover, his result is the first known example of a laser source access this frequency range for high-resolution spectroscopy experiments of supersonic expansions. Given that progress in the field of high-resolution terahertz spectroscopy has stalled in the past years due to lack of available sources, this advance represents a promising means of accessing the important but totally unexplored frequency domain above 5 Thz.

Comparing this system to our previously used laser sideband spectrometer, the sensitivity of this technique (ca. 1 ppm fractional absorption) is comparable without using any multipassing optics, which considerably simplifies the operation. A hundredfold improvement is likely to be realized with incorporation of a multipass cell [89]. The measured continuous tuning range is also encouraging, as it can be regarded as only a fraction of the possible tuning range for a single device when temperature tuning is included. The biggest hurdle that needs to be overcome before the device can be effectively used for routine high resolution VRT spectroscopy is that of establishing a convenient means to accurately determine the laser frequency. Efforts are underway to phase lock the laser to high harmonics of a microwave source, which would provide the requisite frequency accuracy [108].

References

(1) Clary, D. C. Quantum Dynamics in the Smallest Water Droplet. *Science (80-.).* **2016**, *351* (6279), 1267–1268.

(2) Keutsch, F. N.; Saykally, R. J. Water Clusters: Untangling the Mysteries of the Liquid, One Molecule at a Time. *Proc. Natl. Acad. Sci.* **2001**, *98* (19), 10533–10540.

(3) Mukhopadhyay, A.; Cole, W. T. S.; Saykally, R. J. The Water Dimer I: Experimental Characterization. *Chem. Phys. Lett.* **2015**, *633*, 13–26.

(4) Babin, V.; Paesani, F. The Curious Case of the Water Hexamer: Cage vs. Prism. *Chem. Phys. Lett.* **2013**, *580*, 1–8.

(5) Paesani, F. Getting the Right Answers for the Right Reasons: Toward Predictive Molecular Simulations of Water with Many-Body Potential Energy Functions. *Acc. Chem. Res.* **2016**, *49* (9), 1844–1851.

(6) Cole, W. T. S.; Farrell, J. D.; Wales, D. J.; Saykally, R. J. Structure and Torsional Dynamics of the Water Octamer from THz Laser Spectroscopy near 215 Um. *Science (80-.).* **2016**, *352* (6290), 1194–1197.

(7) Liu, K.; Cruzan, J. D.; Saykally, R. J. Water Clusters. *Science (80-.).* **1996**, *271* (5251), 929–933.

(8) Babin, V.; Leforestier, C.; Paesani, F. Development of a "First Principles" Water Potential with Flexible Monomers: Dimer Potential Energy Surface, VRT Spectrum, and Second Virial Coefficient. *J. Chem. Theory Comput.* **2013**, *9* (12), 5395–5403.

(9) Fellers, R. S.; Leforestier, C.; Braly, L. B.; Brown, M. C.; Saykally, R. J. Spectroscopic Determination of the Water Pair Potential. *Science (80-.).* **1999**, *284* (5416), 945–948.

(10) Wang, Y.; Babin, V.; Bowman, J. M.; Paesani, F. The Water Hexamer: Cage, Prism, or Both. Full Dimensional Quantum Simulations Say Both. *J. Am. Chem. Soc.* **2012**, *134* (27), 11116–11119.

(11) Coudert, L. H.; Lovas, F. J.; Suenram, R. D.; Hougen, J. T. New Measurements of Microwave Transitions in the Water Dimer. *J. Chem. Phys.* **1987**, *87* (11), 6290–6299.

(12) Coudert, L. H.; Hougen, J. T. Analysis of the Microwave and Far Infrared Spectrum of the Water Dimer. *J. Mol. Spectrosc.* **1990**, *277*, 259–277.

(13) Coudert, L. H.; Hougen, J. T. Tunneling Splittings in the Water Dimer: Further Development of the Theory. *J. Mol. Spectrosc.* **1988**, *130* (1), 86–119.

(14) Dyke, T. R. Group Theoretical Classification of the Tunneling–Rotational Energy Levels of Water Dimer. *J. Chem. Phys.* **1977**, *66* (492), 492–497.

(15) Hu, T. A.; Dyke, T. R. Water Dimer Coriolis Resonances and Stark Effects. *J. Chem. Phys.* **1989**, *91* (12), 7348–7354.

(16) Goldman, N.; Keutsch, F. N.; Saykally, R. J.; Leforestier, C.; Harker, H. A. Complete Characterization of the Water Dimer Vibrational Ground State and Testing the VRT(ASP-W)III, SAPT-5st, and VRT(MCY-5f) Surfaces. *Mol. Phys.* **2004**, *101* (23–24), 3477–3492.

(17) Ceponkus, J.; Uvdal, P.; Nelander, B. Intermolecular Vibrations of Different Isotopologs of the Water Dimer: Experiments and Density Functional Theory Calculations. *J. Chem. Phys.* **2008**, *129* (19), 1–7.

(18) Ceponkus, J.; Nelander, B. Water Dimer in Solid Neon. Far-Infrared Spectrum. *J. Phys. Chem. A* **2004**, *108* (31), 6499–6502.

(19) Ceponkus, J.; Engdahl, A.; Uvdal, P.; Nelander, B. Structure and Dynamics of Small

Water Clusters, Trapped in Inert Matrices. *Chem. Phys. Lett.* **2013**, *581*, 1–9.
(20) Ceponkus, J.; Uvdal, P.; Nelander, B. Far-Infrared Band Strengths in the Water Dimer: Experiments and Calculations. *J. Phys. Chem. A* **2008**, *112* (17), 3921–3926.
(21) Cole, W. T. S.; Saykally, R. J. Hydrogen Bond Network Rearrangement Dynamics in Water Clusters: Effects of Intermolecular Vibrational Excitation on Tunneling Rates. *J. Chem. Phys.* **2017**, *147* (6), 064301–064308.
(22) Cole, W. T. S.; Yönder, Ö.; Sheikh, A. A.; Fellers, R. S.; Viant, M. R.; Saykally, R. J.; Farrell, J. D.; Wales, D. J. Terahertz VRT Spectroscopy of the Water Hexamer-H12 Cage: Dramatic Libration-Induced Enhancement of Hydrogen Bond Tunneling Dynamics. *J. Phys. Chem. A* **2018**, *122* (37), 7421–7426.
(23) Cole, W. T. S.; Fellers, R. S.; Viant, M. R.; Saykally, R. J. Hydrogen Bond Breaking Dynamics in the Water Pentamer: Terahertz VRT Spectroscopy of a 20 μ m Libration. *J. Chem. Phys.* **2017**, *146* (1), 014306–014316.
(24) Cole, W. T. S.; Fellers, R. S.; Viant, M. R.; Leforestier, C.; Saykally, R. J. Far-Infrared VRT Spectroscopy of the Water Dimer: Characterization of the 20 μ m out-of-Plane Librational Vibration. *J. Chem. Phys.* **2015**, *143* (15), 154306–154324.
(25) Pérez, C.; Shields, G. C.; Temelso, B.; Zaleski, D. P.; Seifert, N. A.; Pate, B. H.; Kisiel, Z. Hydrogen Bond Cooperativity and the Three-Dimensional Structures of Water Nonamers and Decamers. *Angew. Chemie Int. Ed.* **2014**, *53* (52), 14368–14372.
(26) Pérez, C.; Muckle, M. T.; Zaleski, D. P.; Seifert, N. A.; Temelso, B.; Shields, G. C.; Kisiel, Z.; Pate, B. H. Structures of Cage, Prism, and Book Isomers of Water Hexamer from Broadband Rotational Spectroscopy. *Science (80-.).* **2012**, *336* (6083), 897–901.
(27) Keutsch, F. N.; Cruzan, J. D.; Saykally, R. J. The Water Trimer. *Chem. Rev.* **2003**, *103* (7), 2533–2577.
(28) Millot, C.; Stone, A. J. Towards an Accurate Intermolecular Potential for Water. *Mol. Phys.* **1992**, *77* (3), 439–462.
(29) Hodges, M. P.; Stone, A. J.; Xantheas, S. S. Contribution of Many-Body Terms to the Energy for Small Water Clusters: A Comparison of Ab Initio Calculations and Accurate Model Potentials. *J. Phys. Chem. A* **1997**, *101* (48), 9163–9168.
(30) Xantheas, S. S. Ab Initio Studies of Cyclic Water Clusters (H 2 O) n , n =1–6. II. Analysis of Many-body Interactions . *J. Chem. Phys.* **2002**, *100* (10), 7523–7534.
(31) Xantheas, S. S. Ab Initio Studies of Cyclic Water Clusters (H2O)n, n = 1-6. III. Comparison of Density Functional with MP2 Results. *J. Chem. Phys.* **1995**, *102* (11), 4505–4517.
(32) Xantheas, S. S.; Dunning, T. H. Ab Initio Studies of Cyclic Water Clusters (H2O)n, N=1-6. I. Optimal Structures and Vibrational Spectra. *J. Chem. Phys.* **1993**, *99* (11), 8774–8792.
(33) Goldman, N.; Fellers, R. S.; Brown, M. G.; Braly, L. B.; Keoshian, C. J.; Leforestier, C.; Saykally, R. J. Spectroscopic Determination of the Water Dimer Intermolecular Potential-Energy Surface. *J. Chem. Phys.* **2002**, *116* (23), 10148–10163.
(34) Goldman, N.; Leforestier, C.; Saykally, R. J. A "first Principles" Potential Energy Surface for Liquid Water from VRT Spectroscopy of Water Clusters. *Philos. Trans. R. Soc. A Math. Phys. Eng. Sci.* **2005**, *363* (1827), 493–508.
(35) Goldman, N.; Leforestier, C.; Saykally, R. J. Water Dimers in the Atmosphere II: Results from the VRT(ASP-W)III Potential Surface. *J. Phys. Chem. A* **2004**, *108* (5), 787–794.
(36) Scribano, Y.; Goldman, N.; Saykally, R. J.; Leforestier, C. Water Dimers in the

Atmosphere III: Equilibrium Constant from a Flexible Potential. *J. Phys. Chem. A* **2006**, *110* (16), 5411–5419.
(37) Goldman, N.; Fellers, R. S.; Leforestier, C.; Saykally, R. J. Water Dimers in the Atmosphere : Equilibrium Constant for Water Dimerization from The. *J. Phys. Chem. A* **2001**, *105* (3), 515.
(38) Babin, V.; Medders, G. R.; Paesani, F. Development of a "First Principles" Water Potential with Flexible Monomers. II: Trimer Potential Energy Surface, Third Virial Coefficient, and Small Clusters. *J. Chem. Theory Comput.* **2014**, *10* (4), 1599–1607.
(39) Babin, V.; Leforestier, C.; Paesani, F. Erratum: Development of a " First-Principles " Water Potential with Flexible Monomers: Dimer Potential Energy Surface, VRT Spectrum, and Second Virial Coe Ffi Cient. *J. Chem. Theory Comput.* **2013**, *9* (4), 5395–5403.
(40) Medders, G. R.; Babin, V.; Paesani, F. Development of a "First-Principles" Water Potential with Flexible Monomers. III. Liquid Phase Properties. *J. Chem. Theory Comput.* **2014**, *10* (8), 2906–2910.
(41) Luzar, A.; Chandler, D. Structure and Hydrogen Bond Dynamics Mixtures by Computer Simulations. *J. Chem. Phys.* **1993**, *98* (10), 8160–8173.
(42) Luzar, A. Resolving the Hydrogen Bond Dynamics Conundrum. *J. Chem. Phys.* **2000**, *113* (23), 10663–10675.
(43) Luzar, A.; Chandler, D. Hydrogen-Bond Kinetics in Liquid Water. *Nature* **1996**, *379*, 55–57.
(44) Wang, X. G.; Carrington, T. Using Monomer Vibrational Wavefunctions to Compute Numerically Exact (12D) Rovibrational Levels of Water Dimer. *J. Chem. Phys.* **2018**, *148* (7).
(45) Leforestier, C.; Liu, K.; Elrod, M. J.; Saykally, R. J.; Braly, L. B. Fully Coupled Six-Dimensional Calculations of the Water Dimer Vibration-Rotation-Tunneling States with a Split Wigner Pseudo Spectral Approach. II. Improvements and Tests of Additional Potentials. *J. Chem. Phys.* **2002**, *106* (20), 8527–8544.
(46) Leforestier, C.; Szalewicz, K.; Van Der Avoird, A. Spectra of Water Dimer from a New Ab Initio Potential with Flexible Monomers. *J. Chem. Phys.* **2012**, *137* (1).
(47) Paesani, F. Water: Many-Body Potential from First Principles (From the Gas to the Liquid Phase). *Handb. Mater. Model.* **2018**, 1–25.
(48) Nguyen, T. T.; Székely, E.; Imbalzano, G.; Behler, J.; Csányi, G.; Ceriotti, M.; Götz, A. W.; Paesani, F. Comparison of Permutationally Invariant Polynomials, Neural Networks, and Gaussian Approximation Potentials in Representing Water Interactions through Many-Body Expansions. *J. Chem. Phys.* **2018**, *148* (24).
(49) Egan, C. K.; Paesani, F. Assessing Many-Body Effects of Water Self-Ions. I: OH-(H2O)n Clusters. *J. Chem. Theory Comput.* **2018**, *14* (4), 1982–1997.
(50) Bajaj, P.; Riera, M.; Lin, J. K.; Montijo, Y. E. M.; Gazca, J.; Paesani, F. Halide Ion Micro-Hydration : Structure , Energetics , and Spectroscopy of Small Halide – Water Clusters. *J. Phys. Chem. A* **2019**, 1–23.
(51) Ohmine, I.; Tanaka, H. Fluctuation, Relaxations, and Hydration in Liquid Water. Hydrogen-Bond Rearrangement Dynamics. *Chem. Rev.* **1993**, *93* (7), 2545–2566.
(52) Stillinger, F. H. Water Revisited. *Science (80-.).* **1980**, *209* (4455), 451–457.
(53) Richardson, J. O.; Pérez, C.; Lobsiger, S.; Reid, A. A.; Temelso, B.; Shields, G. C.; Kisiel, Z.; Wales, D. J.; Pate, B. H.; Althorpe, S. C. Concerted Hydrogen-Bond Breaking by

Quantum Tunneling in the Water Hexamer Prism. *Science (80-.).* **2016**, *351* (6279), 1310–1313.
(54) Teixeira, J.; Luzar, A. Series A: Life Sciences - HYdration Processes in Biology. In *Physics of Liquid Water. Structure and Dynamics*; 1999; p 35.
(55) Bakker, H. J.; Woutersen, S.; Nienhuys, H. K. Reorientational Motion and Hydrogen-Bond Stretching Dynamics in Liquid Water. *Chem. Phys.* **2000**, *258* (2–3), 233–245.
(56) Cabral, J. T.; Luzar, A.; Teixeira, J.; Bellissent-Funel, M. C. Single-Particle Dynamics in Dimethyl-Sulfoxide/Water Eutectic Mixture by Neutron Scattering. *J. Chem. Phys.* **2000**, *113* (19), 8736–8745.
(57) Conde, O.; Teixeiraj, J. Depolarized Light Scattering of Heavy Water, and Hydrogen Bond Dynamics. *Mol. Phys.* **1984**, *53* (4), 951–959.
(58) Fecko, C. J.; Loparo, J. J.; Roberts, S. T.; Tokmakoff, A. Local Hydrogen Bonding Dynamics and Collective Reorganization in Water: Ultrafast Infrared Spectroscopy of HOD/D 2O. *J. Chem. Phys.* **2005**, *122* (5), 0–18.
(59) Goss, L. M.; Brault, J. W.; Blake, T. A.; Sharpe, S. W.; Vaida, V. Direct Absorption Spectroscopy of Water Clusters. *J. Phys. Chem. A* **2002**, *103* (43), 8620–8624.
(60) Lankhorst, D.; Schriever, J.; Leyte, J. C. Determination of the Rotational Correlation Time of Water by Proton NMR Relaxation in H$_2$17O and Some Related Results. *Ber. Bunsenges. Phys. Chem.* **1982**, *86*, 215–221.
(61) Nienhuys, H.; Woutersen, S.; Santen, R. A. Van; Bakker, H. J.; Woutersen, S. Mechanism for Vibrational Relaxation in Water Investigated by Femtosecond Infrared Spectroscopy Mechanism for Vibrational Relaxation in Water Investigated by Femtosecond Infrared Spectroscopy. *J. Chem. Phys.* **2017**, *1494* (1999), 1494–1500.
(62) Luzar, A.; Chandler, D. Effect of Environment on Hydrogen Bond Dynamics in Liquid Water. *Phys. Rev. Lett.* **1996**, *76* (6), 928–931.
(63) Habershon, S.; Markland, T. E.; Manolopoulos, D. E. Competing Quantum Effects in the Dynamics of a Flexible Water Model. *J. Chem. Phys.* **2009**, *131* (2), 1–36.
(64) Michaelides, A. Quantum Nature of the Hydrogen Bond. *Acta Crystallogr. Sect. A Found. Crystallogr.* **2015**, *67* (a1), C195–C195.
(65) Luzar, A. Water Hydrogen-Bond Dynamics Close to Hydrophobic and Hydrophilic Groups. *Faraday Discuss.* **1996**, *103*, 29–40.
(66) Teixeira, J.; Bellissent-Funel, M. C.; Chen, S. H.; Dianoux, A. J. Experimental Determination of the Nature of Diffusive Motions of Water Molecules at Low Temperatures. *Phys. Rev. A* **1985**, *31* (3), 1913–1917.
(67) Teixeira, J.; Luzar, A.; Longeville, S. Dynamics of Hydrogen Bonds: How to Probe Their Role in the Unusual Properties of Liquid Water. *J. Phys. Condens. Matter* **2006**, *18* (36).
(68) Woutersen, S.; Emmerichs, U.; Bakker, H. J. Femtosecond Mid-IR Pump-Probe Spectroscopy of Liquid Water: Evidence for a Two-Component Structure. *Science (80-.).* **1997**, *278* (5338), 658–660.
(69) Auer, B. M.; Skinner, J. L. Water: Hydrogen Bonding and Vibrational Spectroscopy, in the Bulk Liquid and at the Liquid/Vapor Interface. *Chem. Phys. Lett.* **2009**, *470* (1–3), 13–20.
(70) Huse, N.; Ashihara, S.; Nibbering, E. T. J.; Elsaesser, T. Ultrafast Vibrational Relaxation of O-H Bending and Librational Excitations in Liquid H2O. *Chem. Phys. Lett.* **2005**, *404* (4–6), 389–393.
(71) Ni, Y.; Skinner, J. L. IR and SFG Vibrational Spectroscopy of the Water Bend in the Bulk

Liquid and at the Liquid-Vapor Interface, Respectively. *J. Chem. Phys.* **2015**, *143* (1), 0–12.
(72) Cowan, M. L.; Bruner, B. D.; Huse, N.; Dwyer, J. R.; Chugh, B.; Nibbering, E. T. J.; Elsaesser, T.; Miller, R. J. D. Ultrafast Memory Loss and Energy Redistribution in the Hydrogen Bond Network of Liquid H2O. *Nature* **2005**, *434* (7030), 199–202.
(73) De Marco, L.; Thämer, M.; Reppert, M.; Tokmakoff, A. Direct Observation of Intermolecular Interactions Mediated by Hydrogen Bonding. *J. Chem. Phys.* **2014**, *141* (3).
(74) Ramasesha, K.; De Marco, L.; Mandal, A.; Tokmakoff, A. Water Vibrations Have Strongly Mixed Intra- and Intermolecular Character. *Nat. Chem.* **2013**, *5* (11), 935–940.
(75) Fecko, C. J.; Eaves, J. D.; Loparo, J. J.; Tokmakoff, A.; Geissler, P. L. Ultrafast Hydrogen-Bond Dynamics in the Infrared. *Science (80-.).* **2003**, *301* (September), 1698–1702.
(76) Stenger, J.; Madsen, D.; Hamm, P.; Nibbering, E. T. J.; Elsaesser, T. A Photon Echo Peak Shift Study of Liquid Water. *J. Phys. Chem. A* **2002**, *106* (10), 2341–2350.
(77) Buckingham, A. D.; Del Bene, J. E.; McDowell, S. A. C. The Hydrogen Bond. *Chem. Phys. Lett.* **2008**, *463* (1–3), 1–10.
(78) Keutsch, F. N.; Fellers, R. S.; Brown, M. G.; Viant, M. R.; Petersen, P. B.; Saykally, R. J. Hydrogen Bond Breaking Dynamics of the Water Trimer in the Translational and Librational Band Region of Liquid Water. *J. Am. Chem. Soc.* **2001**, *123* (25), 5938–5941.
(79) Keutsch, F. N.; Saykally, R. J.; Wales, D. J. Bifurcation Tunneling Dynamics in the Water Trimer. *J. Chem. Phys.* **2002**, *117* (19), 8823–8835.
(80) Luzar, A. Extent of Inter-Hydrogen Bond Correlations in Water. Temperature Effect. *Chem. Phys.* **2000**, *258* (2–3), 267–276.
(81) Wang, Y.; Huang, X.; Shepler, B. C.; Braams, B. J.; Bowman, J. M. Flexible, Ab Initio Potential, and Dipole Moment Surfaces for Water. I. Tests and Applications for Clusters up to the 22-Mer. *J. Chem. Phys.* **2011**, *134* (9).
(82) Braly, L. B.; Cruzan, J. D.; Liu, K.; Fellers, R. S.; Saykally, R. J. Terahertz Laser Spectroscopy of the Water Dimer Intermolecular Vibrations. I. (D2O)2. *J. Chem. Phys.* **2000**, *112* (23), 10293–10313.
(83) Braly, L. B.; Brown, M. G.; Keutsch, F. N.; Fellers, R. S.; Saykally, R. J. Terahertz Laser Spectroscopy of the Water Dimer Intermolecular Vibrations. II. (H2O)2. *J. Chem. Phys.* **2000**, *112* (23), 10314–10326.
(84) Liu, K.; Brown, M. G.; Cruzan, J. D.; Saykally, R. J. Terahertz Laser Spectroscopy of the Water Pentamer: Structure and Hydrogen Bond Rearrangement Dynamics. *J. Phys. Chem. A* **1997**, *101* (48), 9011–9021.
(85) Longuet-Higgins, H. C. The Symmetry Groups of Non-Rigid Molecules. *Mol. Phys.* **2002**, *100* (1), 11–20.
(86) Wales, D. J.; Walsh, T. R. Theoretical Study of the Water Pentamer. *J. Chem. Phys.* **1996**, *105* (16), 6957–6971.
(87) Blake, G. A.; Laughlin, K. B.; Cohen, R. C.; Busarow, K. L.; Gwo, D. H.; Schmuttenmaer, C. A.; Steyert, D. W.; Saykally, R. J. Tunable Far Infrared Laser Spectrometers. *Rev. Sci. Instrum.* **1991**, *62* (7), 1693–1700.
(88) Blake, G. A.; Laughlin, K. B.; Cohen, R. C.; Busarow, K. L.; Gwo, D. H.; Schmuttenmaer, C. A.; Steyert, D. W.; Saykally, R. J. The Berkeley Tunable Far Infrared Laser Spectrometers. *Rev. Sci. Instrum.* **1991**, *62* (7), 1701–1716.

(89) Liu, K.; Fellers, R. S.; Viant, M. R.; McLaughlin, R. P.; Brown, M. G.; Saykally, R. J. A Long Path Length Pulsed Slit Valve Appropriate for High Temperature Operation: Infrared Spectroscopy of Jet-Cooled Large Water Clusters and Nucleotide Bases. *Rev. Sci. Instrum.* **1996**, *67* (2), 410–416.
(90) Keutsch, F. N.; Fellers, R. S.; Viant, M. R.; Saykally, R. J. Far-Infrared Laser Vibration-Rotation-Tunneling Spectroscopy of Water Clusters in the Librational Band Region of Liquid Water. *J. Chem. Phys.* **2001**, *114* (9), 4005–4015.
(91) Von Puttkamer, K.; Quack, M. High Resolution Interferometric FTIR Spectroscopy of (HF)2: Analysis of a Low Frequency Fundamental near 400 Cm-1. *Mol. Phys.* **1987**, *62* (5), 1047–1064.
(92) Chamberlain, J. M.; Kimmiti, M. F.; Crompton, A.; Havenith, M.; Smith, G.; Mittleman, D. M. Where Optics Meets Electronics: Recent Progress in Decreasing the Terahertz Gap. *Philos. Trans. R. Soc. A Math. Phys. Eng. Sci.* **2004**, *362* (1815), 199–213.
(93) Williams, B. S. Terahertz Quantum-Cascade Lasers. *Nat. Photonics* **2007**, *1*, 517–525.
(94) Heugen, U.; Bergner, A.; Schwaab, G.; Haller, E. E.; Chamberlin, D. R.; Bründermann, E.; Havenith, M. New P-Ge THz Laser Spectrometer for the Study of Solutions: THz Absorption Spectroscopy of Water. *Rev. Sci. Instrum.* **2005**, *76* (6), 063110.
(95) Siegel, P. H. THz Technology: An Overview. *Int. J. High Speed Electron. Syst.* **2003**, *13* (2), 351–394.
(96) M. Tonouchi. Cutting-Edge Terahertz Technology. *Nat. Photonics* **2007**, 97–105.
(97) Hübers, H.-W.; Mahler, L.; Pavlov, S. G.; Tredicucci, A.; Ritchie, D. A.; Köhler, R.; Beere, H. E.; Semenov, A. D.; Linfield, E. H. Terahertz Quantum Cascade Laser as Local Oscillator in a Heterodyne Receiver. *Opt. Express* **2005**, *13* (15), 5890.
(98) Hübers, H. W.; Pavlov, S. G.; Richter, H.; Semenov, A. D.; Mahler, L.; Tredicucci, A.; Beere, H. E.; Ritchie, D. A. High-Resolution Gas Phase Spectroscopy with a Distributed Feedback Terahertz Quantum Cascade Laser. *Appl. Phys. Lett.* **2006**, *89* (6), 2013–2016.
(99) Hübers, H. W.; Eichholz, R.; Pavlov, S. G.; Richter, H. High Resolution Terahertz Spectroscopy with Quantum Cascade Lasers. *J. Infrared, Millimeter, Terahertz Waves* **2013**, *34* (5–6), 325–341.
(100) Hu, Q.; Gao, J. R.; Cui, M.; Shi, S. C.; Hovenier, J. N.; Reno, J. L.; Kao, T.-Y.; Ren, Y.; Klapwijk, T. M.; Hayton, D. J. Frequency Locking of Single-Mode 3.5-THz Quantum Cascade Lasers Using a Gas Cell. *Appl. Phys. Lett.* **2012**, *100* (4), 041111.
(101) Zhang, L.; Tian, G.; Li, J.; Yu, B. Applications of Absorption Spectroscopy Using Quantum Cascade Lasers. *Appl. Spectrosc.* **2014**, *68* (10), 1095–1107.
(102) Kao, T.-Y.; Hu, Q.; Lee, A. W. M.; Cai, X.; Reno, J. L. Antenna Coupled Photonic Wire Lasers. *Opt. Express* **2015**, *23* (13), 17091.
(103) Kunsch, J.; Faist, J.; Scalari, G.; Mechold, L.; Havenith, M.; Giovannini, M.; Bründermann, E.; Abraham, M. Turn-Key Compact High Temperature Terahertz Quantum Cascade Lasers: Imaging and Room Temperature Detection. *Opt. Express* **2006**, *14* (5), 1829.
(104) Burghoff, D.; Hu, Q.; Reno, J. L.; Kao, T.-Y.; Wei Min Lee, A. Terahertz Tomography Using Quantum-Cascade Lasers. *Opt. Lett.* **2012**, *37* (2), 217.
(105) Curl, R. F.; Capasso, F.; Gmachl, C.; Kosterev, A. A.; McManus, B.; Lewicki, R.; Pusharsky, M.; Wysocki, G.; Tittel, F. K. Quantum Cascade Lasers in Chemical Physics. *Chem. Phys. Lett.* **2010**, *487* (1–3), 1–18.
(106) Hu, Q.; Kao, T. Y.; Cui, M.; Vercruyssen, N.; Reno, J. L.; Ren, Y.; Gao, J. R.; Hovenier,

J. N. Beam and Phase Distributions of a Terahertz Quantum Cascade Wire Laser. *Appl. Phys. Lett.* **2013**, *102* (11), 111113.
(107) Silver, J. A. Frequency-Modulation Spectroscopy for Trace Species Detection: Theory and Comparison among Experimental Methods: Errata. *Appl. Opt.* **2009**, *31* (24), 4927.
(108) Hayton, D. J.; Khudchencko, A.; Pavelyev, D. G.; Hovenier, J. N.; Baryshev, A.; Gao, J. R.; Kao, T. Y.; Hu, Q.; Reno, J. L.; Vaks, V. Phase Locking of a 3.4 THz Third-Order Distributed Feedback Quantum Cascade Laser Using a Room-Temperature Superlattice Harmonic Mixer. *Appl. Phys. Lett.* **2013**, *103* (5).

Chapter II: Untangling the Librational Spectra of Water Clusters in the 15 Terahertz(20 Micron) Region

Summary

A major endeavor of this thesis work was the assignment and analysis of a large collection of water cluster diode laser spectra measured in the 500 cm^{-1} region by previous group members. A small portion of these data had been previous assigned by Keutsch et al[1] to the H_2O trimer; however, over 600 H_2O transitions and ~1000 D_2O transitions had heretofore eluded assignment. The major challenges in assigning these transitions were the large and numerous laser gaps in the experimental region, which hindered traditional assignment protocol employing combination differences of transitions. An initial approach was to use a computational brute force method(viz. calculating combination differences for a given set of input parameters (which could be uniquely chosen for a given water cluster size) and comparing those to the experimental data. This approach proved successful, and was subsequently refined to include more rigorous criteria for comparisons, ultimately permitting assignment of ~400 H_2O transitions and ~900 D_2O transitions. The following sections elaborate on the details of these assignments, as reported in the literature [2–7].

In addition, we present in this section the results of a study of the water h_{16}-octamer by terahertz vibration-rotation-tunneling (VRT) spectroscopy in the 215 micron region, involving the measurement of a very low frequency torsional vibration in two low-lying isomers(D_{2d} and S_4). Nearly 100 individual vibration-rotation transitions have been measured to ppm accuracy and fit to a standard semi-rigid symmetric rotor model, producing rotational constants, which, when combined with theoretical values, characterize the structures and vibrational distortions of the cluster. The results are in good agreement with recent theoretical predictions of the hydrogen bond rearrangement tunneling rates [8] and cluster structures

Far-infrared VRT spectroscopy of the water dimer: Characterization of the 20 μm out-of-plane librational vibration

The full details of this section can be found in: Cole, W.T.S., Fellers, R.S., Viant, M.R., Leforestier, C., Saykally, R.J., J. Chem. Phys. ***143****, 154306 (2015).*

Introduction

The study of water clusters with high-resolution spectroscopic methods has facilitated the determination of accurate potential energy surfaces for the water dimer, and more detailed models for bulk water [9–17]. A central objective of this research, and one which is actually nearing fruition, is the determination of a "predictive universal water model" capable of describing water in all its forms over wide ranges of conditions, based on the combination of high precision spectroscopic results and state-of-the-art *ab initio* calculations for small water clusters [9,14,15,18–23]. The most important step in this process is to obtain a "perfect" water dimer potential surface, since two-body forces account for ~90% of the total cohesive energy of solid and liquid water [11,14,24], and the

dominant many-body interactions (induction) are actually contained in the tensorial description of dimer polarization [11,13]. Three-body interactions will then be refined via similar procedures for the trimer, tetramer, etc.

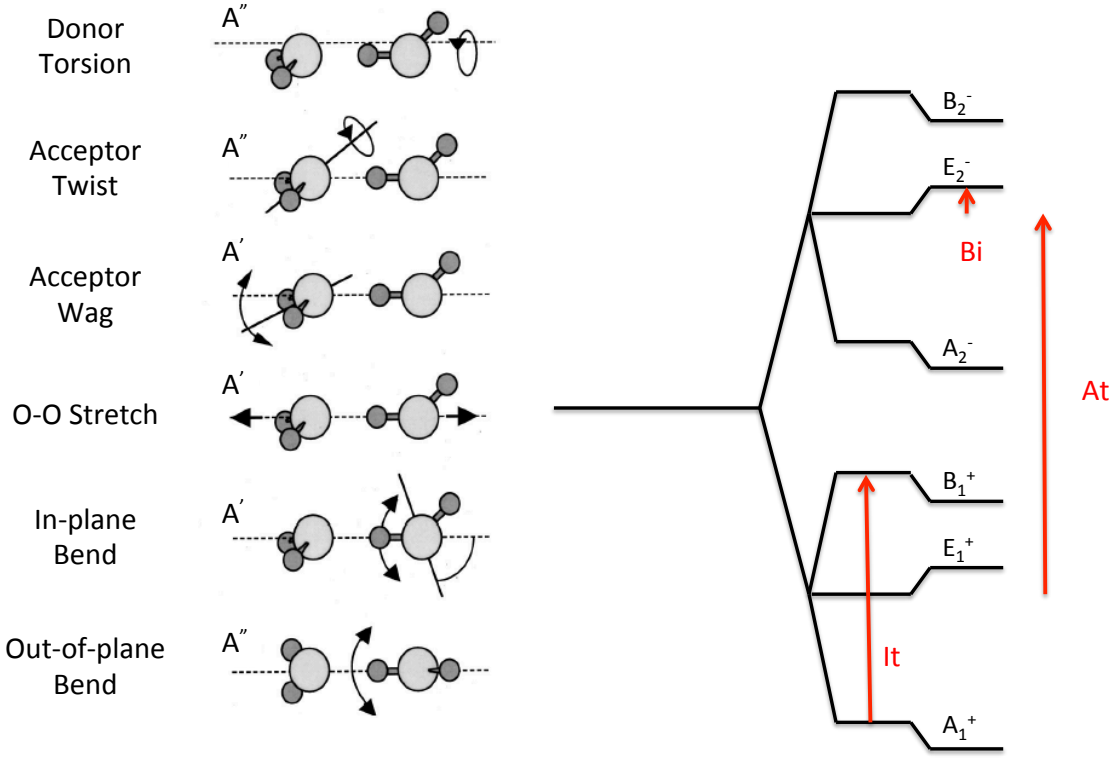

Rep.	E	(12)(34) (ab)(13)(24) (ab)(14)(23)	(ab)(1324) (ab)(1423)	(12)(34)	E*	(12)(34)	(ab)(13)(24) (ab)(14)(23)	(ab)(1324) (ab)(1423)	(12)(34)
A_1^+	1	1	1	1	1	1	1	1	1
A_2^+	1	-1	-1	1	1	-1	-1	1	1
B_1^+	1	1	-1	-1	1	1	-1	-1	1
B_2^+	1	-1	1	-1	1	-1	1	-1	1
E^+	2	0	0	0	-2	2	0	0	-2
A_1^-	1	1	1	1	1	-1	-1	-1	-1
A_2^-	1	-1	-1	1	1	-1	1	-1	-1
B_1^-	1	1	-1	-1	1	-1	-1	1	-1
B_2^-	1	-1	1	-1	1	-1	1	1	-1
E^-	2	0	0	0	-2	-2	0	0	2

Figure 1: (Top Left) The six intermolecular vibrations of $(H_2O)_2$. The labels by the molecules represent the symmetry of the vibration with respect to the molecular plane of symmetry. (Top Right) A representative energy level for a state with $K_a = 0$, J=0 and A' vibrational symmetry. The symmetry of the energy levels are given by their representation in the group G_{16} as shown by Dyke [25]. The results of the three tunneling motions on the energy levels are also shown. Acceptor switching tunneling (At) splits a $|J,K_a>$ level in to a set of two levels (denoted as 1's triplet and 2's triplet depending on the subscript of the symmetry label). Interchange tunneling (It) splits each of these two levels into a triplet. Bifurcation tunneling (Bi) further perturbs the levels but does not result in additional energy levels. (Bottom) The character table for the G_{16} symmetry group which characterizes the energy levels of the water dimer.

Accurate description of water dimer spectra ultimately requires the solution of a 12-dimensional dynamics problem, comprising the six strongly coupled large- amplitude intermolecular motions and six intramolecular vibrations [15,16,26,27]. The experimentally determined "trans-linear" structure of the water dimer [25,28–31] is widely recognized as the archetype of hydrogen bonding [32].

Figure 1 depicts the 6 intermolecular vibrations along with the rotation-tunneling energy level diagram for a representative $(H_2O)_2$ $|J,K_a>$ state. The complicated energy level diagram is a result of the 3 low-barrier tunneling pathways that connect the 8 degenerate minima on the 12-Dimensinal water dimer potential energy surface [33–35]. Acceptor switching tunneling (At) is the lowest barrier pathway (estimated at 157cm^{-1} from the VRT(ASP-W) potential [10]) and is interpreted as the exchange of the two hydrogens in the acceptor molecule. (At) tunneling splits the initial energy level of the dimer into two new levels, conventionally labeled A_1 and A_2. The second tunneling pathway, interchange (It), comprises the exchange of the donor and acceptor molecules. Several pathways exist for this form of tunneling, but the lowest barrier path (207 cm^{-1}) is the "Geared" interchange. (It) tunneling further splits each A_1 or A_2, level into a triplet. The new energy levels are labeled by their representation in the G_{16} group. A final tunneling pathway, bifurcation (Bi), is represented by the exchange of the hydrogens on the donor molecule. This pathway has the highest barrier (394 cm^{-1}), and results in an additional shift of the energy levels, but no new splittings. All of these tunneling motions are strongly coupled with the intermolecular vibrations, and can produce non-trivial shifts/splittings(> a few cm^{-1})accounting for the considerable complexity in the H_2O dimer spectra [36–40]. These tunneling motions, especially the (Bi) pathway, can be used to obtain dynamical information about the hydrogen bond [41].

As we described in a recent review [28], extensive high precision spectra have now been measured for all of these degrees of freedom-except two, which are actually the most important motions to fully characterize: the in-plane and out-of-plane librations. A short collection of the salient experimental results and recent theoretical predictions is given in Table 1. Both librations are thought to be important in hydrogen bond dynamics, but the lack of laser sources at frequencies above 5 THz has limited progress. Both librations comprise motions that initiate the hydrogen bond breaking/formation processes in the condensed phases. Several theory groups have examined the importance of librations in the dynamics of the water hydrogen bond network, and studies of the H_2O trimer and larger clusters have provided considerable insight [42–46]. In this paper we present the first detailed experimental study of a libration in the $(H_2O)_2$ dimer, made in the librational band region of the liquid via far-infrared VRT spectroscopy.

Table 1: Previously Measured and Calculated VRT levels and Tunneling Splittings of $(H_2O)_2$[a]

			Experiment	HBB2	CCpol-8s/f	MB-pol		Experiment	HBB2	CCpol-8s/f	MB-pol
OO	-	(2)	153.62(1.88)	148.57(1.14)	149.63(1.23)	154.31(2.41)	(1)		152.50(1.12)	152.07(1.48)	156.60(2.71)
	-	(1)		145.00(3.48)	143.20(3.27)	149.44(1.97)	(2)		150.52(1.04)	153.54(2.54)	152.69(4.13)
AT	-	(1)		128.91(0.74)	132.10(1.48)	129.44(0.24)	(1)		142.25(4.33)	142.42(4.04)	143.68(4.87)
	-	(2)	120.19(9.39)	121.01(8.41)	117.50(8.67)	119.07(10.15)	(2)		136.24(5.31)	136.52(4.66)	137.04(5.95)
AW	-	(2)	108.89(0.02)	105.78(0.03)	107.82(0.10)	108.87(0.13)	(2)	123.56(3.41)	122.25(2.48)	123.12(3.16)	123.65(3.83)
	-	(1)	107.93(2.95)	105.35(1.99)	109.23(3.29)	108.38(3.24)	(1)	109.98(5.24)	108.95(4.55)	108.28(4.76)	109.65(5.89)
DT	-	(1)		116.54(4.84)	113.35(5.91)	113.83(5.61)	(2)		94.25(2.66)	92.18(3.34)	91.22(3.47)
	-	(2)	64.52(2.54)	67.18(2.03)	61.33(2.48)	61.31(2.54)	(1)	87.75(1.11)	89.55(0.54)	86.37(1.32)	85.63(1.00)
GS	-	(2)	11.18(0.65)	10.16(0.60)	12.75(0.61)	12.05(0.69)	(1)	14.39(0.70)	14.00(0.64)	15.45(0.67)	15.04(0.77)
	-	(1)	0.00(0.75)	0.00(0.68)	0.00(0.72)	0.00(0.81)	(2)	11.66(0.54)	11.50(0.49)	12.36(0.51)	12.18(0.48)
			$K_a = 0$					**$K_a = 1$**			

a: The observed and predicted values of the VRT levels of the intermolecular vibrations of $(H_2O)_2$. Ground State (GS), Donor Torsion (DT), Acceptor Wag (AW), Acceptor Twist (AT), intermolecular stretch (OO) intermolecular energy levels are shown. The labels (1) and (2) correspond to the energies (cm^{-1}) of the origin of the intermolecular vibration's 1's triplet or 2's triplet respectively (See figure 1). The values in parenthesis are the interchange tunneling splittings of the corresponding triplet. This table is reproduced with permission from J. Chem. Theory Comput. 9, 5395 (2013).

Experimental

The Berkeley supersonic beam/diode laser spectrometer used in this study has been described in detail elsewhere [47–49] and only a short description will be provided here.

A helium-cooled diode laser spectrometer (Spectra Physics) using lead-salt diodes (Laser Photonics) was used to produce infrared radiation from 515-528 cm^{-1}. The beam was multipassed 18-22 times through a pulsed planar supersonic expansion of a mixture of H_2O and He using a Herriot cell and detected using a helium cooled (Si:B) photoconductive detector (IR Labs). The supersonic expansion is produced by bubbling pure He gas, with a backing pressure of 1-2 atm, through liquid H_2O, and then through a 101.6 mm long slit at a repetition rate of 35 Hz into a vacuum chamber maintained at ~200mTorr by a Roots blower (Edwards 4200) backed by two rotary pumps (E2M 275). The cooling in the supersonic beam was sufficient for the cluster species to reach a rotational temperature of 4K. Simultaneously, the fringe spacing of a vacuum-spaced etalon and an OCS reference gas spectrum are detected with a liquid He cooled (Cu:Ge) detector (Santa Barbara Research Center) and recorded to enable precise frequency calibration. The observed linewidths of ~ 30 MHz full-width half maximum (FWHM) are slightly larger than the Doppler limited linewidths extrapolated form earlier experiments. Typical frequency accuracy is 10-20 MHz, which was limited by linewidths of the cluster absorptions and laser drift.

Spectra are detected in direct absorption using a time-gated phase sensitive signal processing approach. The sensitivity of the experiment has been previously discussed by Keutsch et al [1]: briefly, the signal-to-noise ratio of the Q-branches was about 200:1 compared to 8000:1 for the most intense vibrations observed in THz experiments performed in the same group. The sensitivity of the diode laser experiment (10-100ppm) is about 2 orders of magnitude lower than that of the THz experiments, indicating that the observed transitions are intense.

Accessing the 500 cm^{-1} region of the electromagnetic spectrum has been notoriously difficult. The first observation of a libration in the region was report in 1987 by von Puttkamer and Quack [50]. The spectra reported here required the use of 10 separate laser diodes, each scanned across several modes to cover the specified spectral range. However, large laser gaps are nevertheless present in the spectra, which causes considerable difficulty in the assignment. It is relevant to note that Keutsch et al. have previously assigned a portion of the measured raw experimental spectrum to librations of the H_2O trimer [1]. Recent matrix isolation results from the Lund group prompted a reinvestigation of the remaining unassigned lines in that region [51–54]. Figure 2 shows the region of the experimental study with respect to the librational band of liquid water, along with the assigned dimer transitions, and the remaining unassigned lines. Figure 3 presents actual spectra observed in a small region, wherein the dimer lines assigned in this regions are much weaker than the dominant trimer lines assigned in [1].

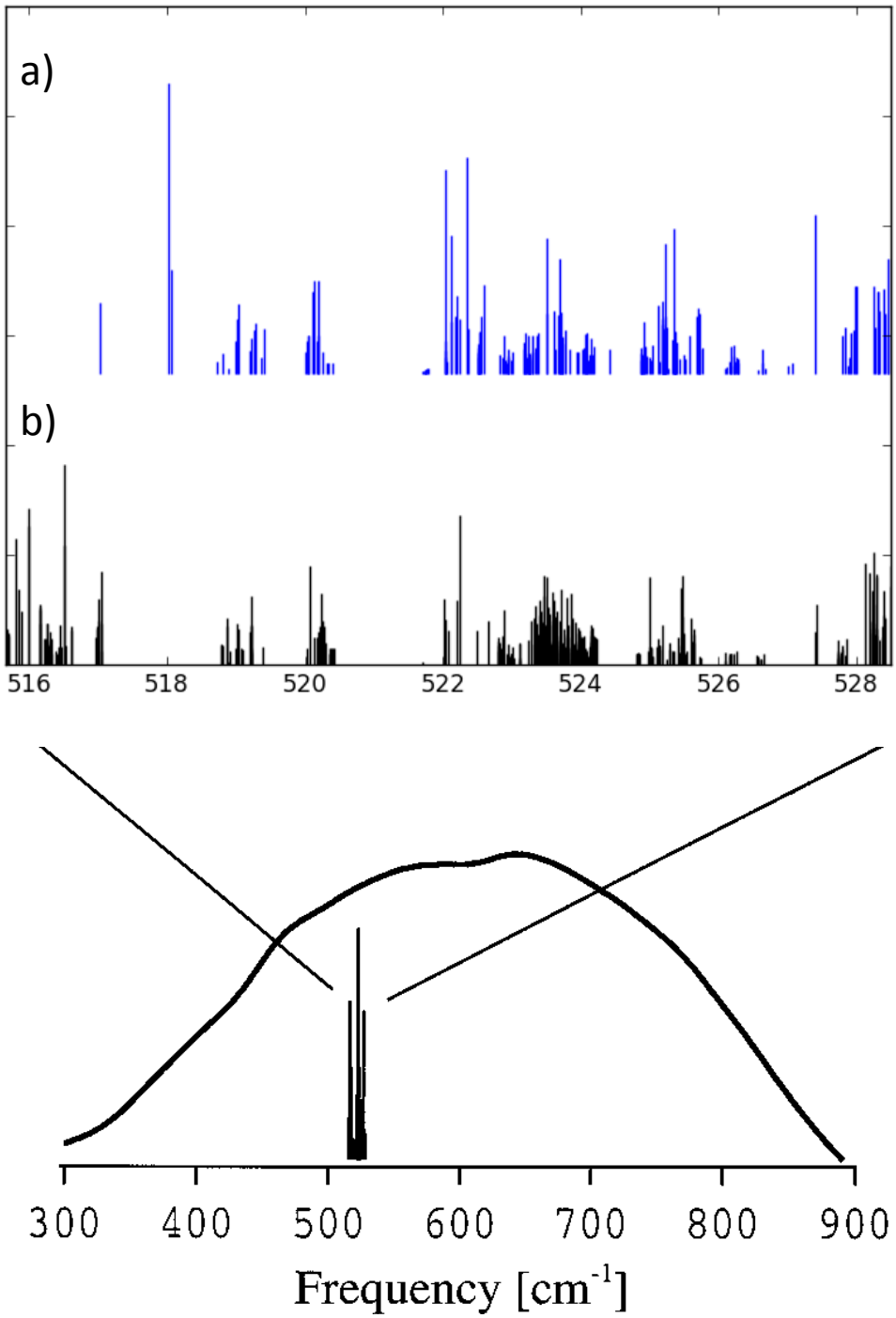

Figure 2: The librational band of liquid water is shown along with the measured dimer transitions. a) Shows the assigned lines presented in this study. b) The remaining unassigned transitions in the region. The spectrum has significant laser gaps, which cause difficulty in the assignment. Spectra were collected from a He:H_2O expansion in a pulsed, supersonic jet. Linewidths are ca. 30 MHz, and frequency accuracy is 10-20 MHz.

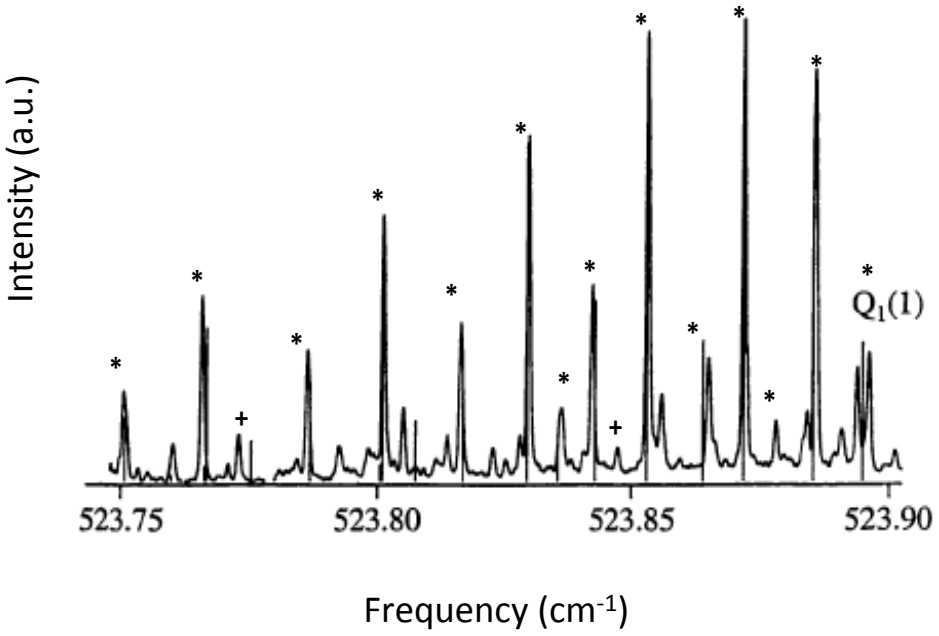

Figure 3: A small portion of the spectral region covered in this study. Asterisks indicate transitions previously assigned to the much stronger out-of-plane libration of the H_2O trimer [1]. The + labels represent the two dimer transitions observed in the region.

Results

Assignment

189 transitions comprising the experimentally observed spectrum have been assigned to an excited vibrational state with A" symmetry; the transitions terminate in three distinct subbands designated by their K_a value; the upper state subbands observed here involve K_a=0, 1, and 2. 55 Transitions are assigned as a-type (ΔK_a=0), 110 transitions are assigned to b-type (ΔK_a=+1), 23 are assigned to "c"-type transitions (ΔK_a=-1), and one transition is assigned to an H_2O monomer. As a note, the labeling of transitions as "c"-type is merely one of convenience to separate those transitions from the rest of the b-type transitions. The selection rules that dictate the assignment are conventional. One of the following must hold: $\Delta J \neq 0$, $\Delta K_a \neq 0$, $\Delta K_c \neq 0$, and additionally, transitions from a state with a given symmetry label must terminate in a level with the same symmetry but with a change in parity (i.e. $A_2^+ \rightarrow A_2^-$). These selection rules dictate the possible observable transitions [25].

Transitions were assigned through the use of pattern recognition algorithms and ground state combination differences. Intensity patterns were also compared to predictions using the spin statistical weights of each symmetry species, but as the power output of the diode laser was quite variable, they could not be used in every case. The presence of Q-branches was used to confirm the results, along with the agreements of the rotational constants from the fit. Some missing transitions hindered assignment of more transitions due to the significant laser gaps in the spectrum.

A Brief Discussion of Notation

For the sections that follow, a description of the notation that will be used is helpful. For Table 1, the transitions are grouped into "sets" which represent transitions to the same "frequency location" in the upper state, referring to the energy level diagram for the H_2O dimer (Figure 1). For example, the A_2^-/B_2^+ "set" refers to the transitions which originate in an eigenstate with symmetry A_2^- or B_2^+ and terminate in one with symmetry A_2^+ or B_2^- respectively. The first symmetry in the label of each "set" corresponds to the symmetry of the lowest possible eigenstate for a given set, noting that this depends on the type of transition. For example, if the transition type is K_a=1<-1 and one considers the set A_2^-/B_2^+, this means that the lowest energy ground state is labeled A_2^-, and that the labels alternate with increments of 1 in J. The reason we group transition in this manner is because the sets originate and terminate in the same relative frequency locations in a given triplet. Returning to our example of the K_a=1<-1 transition in the set A_2^-/B_2^+, the transitions originate in the lowest level of the ground state triplet and terminate in the top level of the upper state triplet. This system greatly simplifies not only the assignment procedure, but also the fitting process.

Analysis

The measured K_a subbands were fit to the following near-prolate top energy expressions as described previously [38,55]:

K_a=0

$$E(A^{\pm} \; or \; B^{\pm}) = v^{(0)} \pm \left(\frac{It^{(0)}}{2}\right) - v_{Bi}^{(0)} + B^{(0)}J(J+1) - D^{(0)}\big(J(J+1)\big)^2 \qquad (\mathbf{1})$$

$$E(E^{\pm}) = v^{(0)} + v_{Bi}^{(0)} + B^{(0)}J(J+1) - D^{(0)}\big(J(J+1)\big)^2 \qquad (\mathbf{2})$$

K_a=1

$$E(A^{\pm}\ or\ B^{\pm}) = v^{(1)} \pm \left(\frac{It^{(1)}}{2}\right) + v_{Bi}^{(1)} + B^{(1)}(J(J+1)-1) - D^{(1)}(J(J+1)-1)^2 \pm \left[\left(\frac{B-C}{4}\right)^{(1)} - d^{(1)}J(J+1)\right]J(J+1) \qquad (\mathbf{3})$$

$$E(E^{\pm}) = v^{(1)} - v_{Bi}^{(1)} + B^{(1)}(J(J+1)-1) - D^{(1)}(J(J+1)-1)^2 \pm \left[\left(\frac{B-C}{4}\right)^{(1)} - d^{(1)}J(J+1)\right]J(J+1) \qquad (\mathbf{4})$$

K_a=2

$$E(A^{\pm}\ or\ B^{\pm}) = v^{(2)} \pm \left(\frac{It^{(2)}}{2}\right) - v_{Bi}^{(2)} + B^{(2)}(J(J+1)-4) - D^{(2)}(J(J+1)-4)^2 \pm \left[\left(\frac{B-C}{4}\right)^{(2)}\right]J(J+1)(J-1)(J+2) \qquad (\mathbf{5})$$

$$E(E^{\pm}) = v^{(2)} + v_{Bi}^{(2)} + B^{(2)}(J(J+1)-4) - D^{(2)}(J(J+1)-4)^2 \pm \left[\left(\frac{B-C}{4}\right)^{(2)}\right]J(J+1)(J-1)(J+2) \qquad (\mathbf{6})$$

In these expressions, $v^{(i)}$, B, D, and (B-C)/4 have their usual meanings. The constant $d^{(1)}$ is an additional centrifugal distortion constant previously shown to improve fitting of the K_a=1 levels, and is a manifestation of the non-rigidity of the complex. The tunneling splittings are defined as shown in Figure 1. Interchange tunneling (It) is the separation of the $A^{\pm}$ and $B^{\pm}$ levels in a particular triplet, and bifurcation (v_{Bi}) is a shift of each energy level in the triplet. Acceptor switching splitting is not determined explicitly from the fit, but can easily be obtained when the origins of the $E^{\pm}$ for both the 1's and 2's triplets are known by:

$$Acceptor\ Switching\ (AS)^{(i)} = \left|v_{1's}^{(i)}(E^{\pm}) - v_{2's}^{(i)}(E^{\pm})\right| \qquad (\mathbf{7})$$

The assigned transitions are shown in Table 2 along with the differences between the observed transitions frequencies and those calculated from the constants obtained from the fit. Table 3 shows the constants obtained from a nonlinear least squares fit of all

the transitions to the expressions given in Equations 1-6 along with the 1σ deviations. The root mean squared deviation of the fit is found to be ~12 MHz, which is well within the frequency accuracy of the experiment. The fit was performed holding the known ground state parameters fixed to calculate the lower state energy. One fit was performed without the parameters fixed, and showed good agreement with the known ground state constant values, indicating that the transitions originated in the vibrational ground state. Results of the fit including correlation matrices are provided in the Supplementary Information.

Table 2: Assigned experimental transitions. All values are given in MHz. The symmetry labels represent the lower state symmetry. The type of transition is shown along with the transition frequency and the difference between observed and calculated transition frequencies. The explicit upper (J') and lower (J") J quantum numbers are shown.

K=1 < - 0

			A_1^+/B_1^-		E_1^+/E_1^-		B_1^+/A_1^-	
Transition type	J'	J"	Frequency	Obs - Calc	Frequency	Obs - Calc	Frequency	Obs - Calc
R(6)	7	6			15754572.8	0.3		
R(3)	4	3			15715103.6	0.0		
R(2)	3	2			15702326.3	2.4		
R(0)	1	0			15677366.1	0.5		
P(2)	1	2			15640633.4	-1.8		
P(6)	5	6			15592917.1	-1.5		
P(9)	8	9			15559477.4	0.0		

			A_2^-/B_2^+		E_2^-/E_2^+		B_2^-/A_2^+	
Transition type	J'	J''	Frequency	Obs - Calc	Frequency	Obs - Calc	Frequency	Obs - Calc
R(0)	1	0	15750564.6	-2.9	15748926.0	-5.2	15679580.0	-10.0
R(2)	3	2	15775602.9	-1.4	15773810.0	-2.5	15704545.1	-8.6
R(3)	4	3	15788407.1	-2.2	15786438.9	-1.6		
R(4)	5	4	15801295.9	-3.3	15799208.3	-1.4		
R(5)	6	5					15742698.1	-8.2
R(6)	7	6	15828089.2	-14.8	15825747.1	-8.5	15756185.8	-10.6
R(7)	8	7	15841336.0	-19.2	15839040.3	-11.4		
Q(1)	1	1	15737611.4	3.3	15735784.7	2.9	15664927.8	-7.7
Q(2)	2	2	15737247.6	9.0	15735561.9	7.1	15664878.2	-6.9
Q(3)	3	3	15736875.8	15.8	15735486.8	10.8	15664847.3	-5.9
Q(4)	4	4	15736354.4	25.0	15735367.3	15.8	15664700.7	-4.7
Q(5)	5	5	15735927.4	30.8			15664514.8	-3.9
P(2)	1	2	15713557.5	-2.9	15712190.4	-7.8	15642750.7	-1.0
P(3)	2	3	15701333.9	-1.9	15700004.3	-7.3		
P(4)	3	4	15689410.9	-2.8				
P(5)	4	5	15677487.0	-2.9	15675832.8	-5.3		
P(6)	5	6	15665946.3	-6.2	15664355.5	-9.0	15594831.1	-8.2
P(7)	6	7	15654757.3	-12.5	15652694.5	-10.0		
P(8)	7	8			15641331.7	-13.1	15571664.1	-1.1
P(9)	8	9					15560163.6	-14.5

K = 1 < - 1

			A_2^-/B_2^+		E_2^-/E_2^+		B_2^-/A_2^+	
Transition type	J'	J"	Frequency	Obs - Calc	Frequency	Obs - Calc	Frequency	Obs - Calc
R(9)	10	9					15753818.4	25.5
R(8)	9	8	15837385.9	-11.6	15840653.3	-11.5	15740516.3	9.1
R(7)	8	7	15824326.9	8.5	15826791.1	12.4		
R(6)	7	6	15811272.5	-6.3			15714101.7	18.9
R(5)	6	5					15701175.4	21.5
R(4)	5	4					15688318.2	21.3
R(3)	4	3	15772309.4	2.9	15774399.1	6.9		
R(2)	3	2	15759746.4	-2.4				
R(1)	2	1	15747330.1	-3.9	15749418.1	0.4	15650663.8	19.4
P(2)	1	2	15698247.7	-9.3	15700298.7	-4.3	15601381.0	1.9
P(3)	2	3	15686055.4	-4.9	15688103.4	-0.2		
P(4)	3	4	15674001.0	-8.4				
P(5)	4	5					15565354.7	2.1
P(6)	5	6	15650333.3	-9.8	15652772.0	-8.4		
P(7)	6	7			15641190.5	6.3		
P(8)	7	8					15530889.3	1.7

			B_2^+/A_2^-		E_2^+/E_2^-		A_2^+/B_2^-	
Transition type	J'	J''	Frequency	Obs - Calc	Frequency	Obs - Calc	Frequency	Obs - Calc
R(9)	10	9	15842745.8	0.0	15842869.4	0.0	15750087.9	4.5
R(8)	9	8	15829080.9	14.6	15828609.8	3.3		
R(7)	8	7					15721674.1	-13.5
R(6)	7	6					15707891.5	0.0
R(5)	6	5			15789415.5	-0.1	15694142.9	-17.9
R(4)	5	4	15777453.7	1.2	15776722.3	2.6		
R(2)	3	2	15752316.7	0.9				
R(1)	2	1	15739942.6	4.4	15739155.8	-1.2	15641477.8	-11.9
P(2)	1	2	15690947.8	-1.5	15689757.2	-0.2	15590663.7	-0.9
P(3)	2	3	15678765.8	-0.7	15677531.4	1.4		
P(4)	3	4	15666802.3	-3.0			15565602.3	0.2
P(5)	4	5	15655013.8	-1.3			15553293.1	16.3
P(6)	5	6			15641637.6	-2.6		
P(7)	6	7					15529855.5	23.2
P(10)	9	10	15599103.7	-14.7	15595341.1	-3.3		

K = 0 < - 1

			A_1^+/B_1^-		E_1^+/E_1^-		B_1^+/A_1^-	
Transition type	J'	J"	Frequency	Obs - Calc	Frequency	Obs - Calc	Frequency	Obs - Calc
R(10)	11	10					15762015.3	-3.2
R(8)	9	8			15777584.0	3.6		
R(6)	7	6			15751154.7	5.4	15709915.7	-7.8
R(5)	6	5	15838541.2	-24.6				
R(3)	4	3			15711967.3	6.0		
R(2)	3	2			15699305.3	4.3	15659376.1	-4.4
R(1)	2	1	15787937.9	-11.4	15686891.2	1.0		
Q(2)	2	2	15760894.9	12.3				
Q(4)	4	4	15760674.4	17.1				
Q(6)	6	6	15760462.2	16.4				
Q(8)	8	8	15760024.2	3.5				
P(1)	0	1	15750273.0	-7.0	15650150.4	-5.7		
P(2)	1	2					15596676.9	5.4
P(5)	4	5	15700772.0	-0.6				
P(6)	5	6			15590454.5	-4.4		
P(7)	6	7	15676366.2	-5.7				
P(8)	7	8			15567303.4	-3.6		
P(9)	8	9			15555922.3	-6.6		
P(10)	9	10					15500205.9	10.1

K = 2 < - 1

			A_2^-/B_2^+		E_2^-/E_2^+		B_2^-/A_2^+	
Transition type	J'	J''	Frequency	Obs - Calc	Frequency	Obs - Calc	Frequency	Obs - Calc
R(9)	10	9					15760674.4	-0.4
R(8)	9	8					15746844.1	-17.2
R(6)	7	6	15838543.5	-4.1	15775891.9	-3.5		
R(5)	6	5	15825488.9	-29.8			15707184.1	3.0
R(4)	5	4			15749526.1	-1.0	15694202.9	-2.6
R(1)	2	1	15774243.4	-12.2	15711420.7	-11.7	15656398.1	-0.9
Q(2)	2	2	15746176.3	21.0	15684814.1	7.1		
Q(3)	3	3	15746115.5	22.1	15684702.1	4.7		
Q(4)	4	4	15746021.7	16.3	15684661.5	-20.5		
Q(6)	6	6	15745594.0	20.0				
Q(7)	7	7	15745144.8	4.7				
P(3)	2	3	15712865.1	-12.2	15650085.5	-12.0	15594734.6	2.1
P(4)	3	4	15700643.7	-20.3				
P(6)	5	6	15676745.2	-22.4			15558912.2	-5.4
P(7)	6	7	15665086.1	-20.5				
P(8)	7	8			15590090.8	-3.4		
P(9)	8	9	15642440.9	-12.1				
P(10)	9	10			15567527.9	-8.9		

			B_2^+/A_2^-		E_2^+/E_2^-		A_2^+/B_2^-	
Transition type	J'	J"	Frequency	Obs - Calc	Frequency	Obs - Calc	Frequency	Obs - Calc
R(8)	9	8					15749638.8	0.0
R(6)	7	6	15836359.2	-32.2	15776419.7	-13.4		
R(5)	6	5	15823020.9	-12.2			15710644.5	3.4
R(4)	5	4			15750132.0	-11.7	15697736.6	0.0
R(1)	2	1	15772550.6	-17.7	15712009.0	-3.7	15660008.2	1.1
Q(2)	2	2	15745019.0	12.6	15686817.7	3.5		
Q(3)	3	3	15744987.5	16.5	15686790.7	-0.8		
Q(4)	4	4	15744864.0	27.1	15686419.9	8.9		
Q(5)	5	5	15744680.3	29.5	15685858.9	0.4		
Q(6)	6	6			15685227.0	29.8		
Q(8)	8	8	15743640.8	18.3				
P(3)	2	3	15711240.2	-21.4	15650478.8	-5.1	15598580.3	-1.1
P(5)	4	5	15686988.7	-14.7				
P(6)	5	6	15674973.0	-5.7				
P(7)	6	7					15551154.9	-3.4
P(8)	7	8			15592349.9	-12.3		
P(10)	9	10			15570108.0	4.3		

Table 3: Results from least squares fit of assigned transitions. All values are given in MHz. The symmetry labels indicate the lower state symmetry.

K = 0

A_1^+/B_1^-			E_1^+/E_1^-			B_1^+/A_1^-		
Constant	Value	1σ error	Constant	Value	1σ error	Constant	Value	1σ error
B	6209.573	0.563	B	6236.608	0.494	B	6169.874	0.405
D	0.911	0.008	D	0.211	0.006	D	0.144	0.003

Origin	15939224.0	5.2
Interchange tunneling	119086.9	12.7
Bifurcation Tunneling	-15553.0	5.2
RMS of Fit	9.2	

Number of Transitions in fit	23

K = 1

E_1^+/E_1^-		
Constant	Value	1σ error
B	6200.3538	0.28
D	-0.3622	0.0042
(B-C)/4	-9.2627	0.18
d	-0.1821	0.0032

Origin	15510412.4	1.3
Interchange tunneling	n/a	
Bifurcation Tunneling	n/a	

A_2^-/B_2^+			E_2^-/E_2^+			B_2^-/A_2^+		
Constant	Value	1σ error	Constant	Value	1σ error	Constant	Value	1σ error
B	6217.946	0.235	B	6221.564	0.228	B	6270.691	1.805
D	0.064	0.031	D	0.057	0.029	D	2.141	0.019
(B-C)/4	4.557	1.414	(B-C)/4	5.255	0.144	(B-C)/4	11.126	0.119
d	0.161	0.023	d	0.028	0.022	d	1.027	0.016

Origin	15890455.7	1.9
Interchange tunneling	61510.0	4.4
Bifurcation Tunneling	-19983.6	1.9

Acceptor Tunneling	380043.3

B_2^+/A_2^-			E_2^+/E_2^-			A_2^+/B_2^-		
Constant	Value	1σ error	Constant	Value	1σ error	Constant	Value	1σ error
B	6196.223	0.776	B	6178.346	0.500	B	6133.107	0.987
D	-0.019	0.007	D	-0.163	0.005	D	-2.150	0.016
(B-C)/4	-40.026	0.427	(B-C)/4	-17.946	0.316	(B-C)/4	-88.450	0.774
d	-0.333	0.004	d	-0.078	0.003	d	-1.673	0.014

Origin	15876498.2	5.2
Interchange tunneling	83884.9	12.6
Bifurcation Tunneling	-23807.2	5.2
RMS of Fit	10.1	

Number of Transitions in fit	108

K = 2

A_2^-/B_2^+			E_2^-/E_2^+			B_2^-/A_2^+		
Constant	Value	1σ error	Constant	Value	1σ error	Constant	Value	1σ error
B	6105.144	1.086	B	6197.430	1.292	B	6195.007	1.020
D	-1.566	0.018	D	5.763	0.109	D	-0.090	0.010
(B-C)/4	-0.442	0.004	(B-C)/4	-5.660	0.111	(B-C)/4	-0.111	0.002

Origin	15892966.0	9.0
Interchange tunneling	100704.6	21.2
Bifurcation Tunneling	-2895.4	9.0

B_2^+/A_2^-			E_2^+/E_2^-			A_2^+/B_2^-		
Constant	Value	1σ error	Constant	Value	1σ error	Constant	Value	1σ error
B	6268.086	1.139	B	6128.279	0.708	B	6166.044	1.369
D	1.732	0.022	D	-0.322	0.017	D	-0.554	0.022
(B-C)/4	-0.329	0.007	(B-C)/4	0.499	0.013	(B-C)/4	-0.410	0.008

Origin	15894035.5	7.3
Interchange tunneling	94285.6	19.3
Bifurcation Tunneling	-2529.2	7.3
RMS of Fit	14.3	

Number of Transitions in fit	57

The c-type K_a=0<-1 Subband

23 lines were assigned to transitions originating in K_a=1 of the ground state and terminating in the K_a=0 excited state. These transitions represent only the 1's triplet of the K_a=0 stack, and thus render it impossible to determine the acceptor switching splitting of the upper state. Significant laser gaps hindered assignment of the B_1^+/A_1^- set (for example, the region where the Q-branch is expected to reside falls in a large gap), however, sufficient transitions were assigned to unambiguously ascribe the spectra to a state with A" vibrational symmetry. The results of the fit are shown in Table 2. Transitions from the ground state K_a=1 2's triplet to the 2's triplet of the upper state K_a=0 stack were also searched for but were not found. A possible explanation for this is that the transitions lie outside the experimental range due to the presumed large acceptor switching tunneling of the upper state; this will be elaborated in a later section.

The b-type K_a=1<-0 Subband

A total of 53 lines were assigned to transitions originating in the K_a=0 ground state and ending in K_a=1 excited state. Complete assignment of the excited state K_a=1, 2's triplet was accomplished and, in combination with the transitions assigned in the following section, allowed a detailed characterization of this manifold. The resulting energy level diagram shown in Figure 4 for all observed transitions confirms the vibrational symmetry of the upper state as A". Additionally, the $E^{\pm}$ levels of the 1's triplet were found. While this may appear arbitrary without accompanying $A_1^{\pm}$ and $B_1^{\pm}$ transitions, the assignment was confirmed by ground state combination differences. Also, the fingerprint of the $A_1^{\pm}$ and $B_1^{\pm}$ transitions was found, however significant laser gaps precluded the observation of a suitable number of transitions for an unambiguous assignment. Nevertheless, the assignment of the $E^{\pm}$ transitions provides valuable insight into the acceptor switching in the upper state K_a=1 stack. A full discussion of the observed tunneling splittings will be presented below.

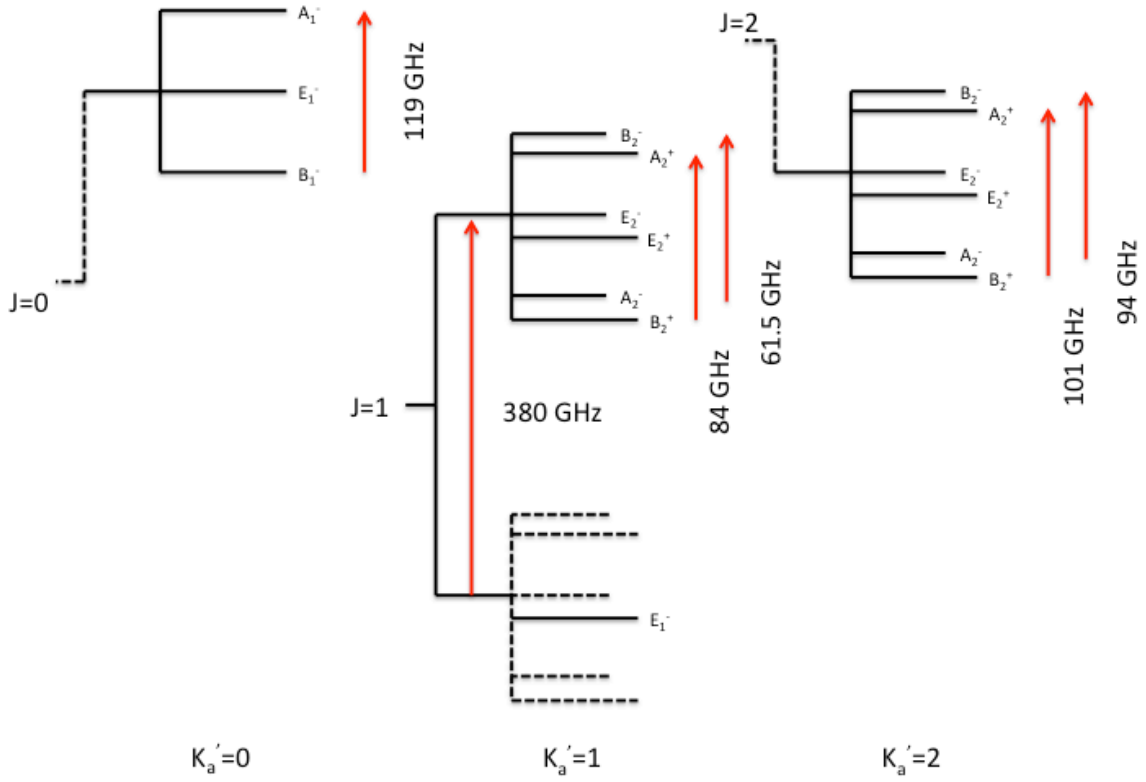

Figure 4: Energy level diagram for the assigned transitions. Determined interchange and acceptor switching tunneling values are shown. Dashed lines represent the group theoretical structure for energy levels not determined from the current study. The energy level structure represents a A" upper state vibration, consistent with the out-of-plane intermolecular libration. The origins of the 2's of the K_a=1 and K_a=2 stack lie in extreme proximity, which suggests that the levels may perturb each other. The bifurcation tunneling is not shown on this figure, however the sign changes from K_a=0 to K_a=1 as expected, and then changes sign from K_a=1 to K_a=2. Drawing not to scale.

The a-type K_a=1<-1 Subband

A total of 55 lines were assigned to a-type transitions originating and terminating in K_a=1 stacks. All assigned transitions correspond to the 2's triplet of the upper state, and in conjunction with the assignments of the previous section, completely characterize the 2's triplet of the upper state K_a=1 subband. This characterization reinforces the assignment of the state as having A" vibrational symmetry. One striking feature of the fit results is the large magnitude of the D and d rotational constants for the B_2^-/A_2^+, which indicates a deviation from the semirigid near-prolate top energy level approximation. Also, the A_2^-/B_2^+ set's asymmetry constant displays an abnormal 1σ value, which may be an indication of some perturbation of that energy level set. Given that the quality of the fit is still very good, a possible explanation for this may engender the close proximity of the 2's of the K_a=1 upper state stack to the 2's of the upper stack K_a=2 stack, which is elaborated in the following section.

The b-type K_a=2<-1 Subband

A total of 57 lines were assigned to transitions from K_a=1 in the ground state to the excited state K_a=2 levels of an A" vibration. The transitions completely characterize the 2's triplet and also reveal an interesting energy level structure between the 2's of the K_a=1 stack and the 2's of the K_a=2 stack. The difference between the origins of the K_a=1 and K_a=2 stacks is less than 1 cm^{-1} for all four stacks (considering the K doublets as separate stacks) and less than 5000 MHz for three of the triplets. This near-degeneracy, in addition with previously mentioned irregularities in the rotational constants, warranted an investigation into the possibility of Coriolis coupling between the levels, as has previously been shown to be significant for certain energy levels [56].

Coriolis coupling is a result of $K_{a/c}$ not being a strictly "good" quantum number for the water dimer, and allows levels of the same symmetry, parity, and J value to mix when brought into close proximity. The interaction generally follows a simple 2-level Coriolis resonance model [38,56]. After extensive investigation, the energy levels were actually found to **not** be strongly Coriolis coupled. An attempt to fit to the standard Coriolis model

$$E = \frac{E^{(i)} + E^{(j)}}{2} \pm \left[\frac{\left(E^{(j)} - E^{(i)}\right)^2}{4} + \frac{\zeta^2 J(J+1)}{2} \right]^{1/2} \qquad (\mathbf{8})$$

wherein the i^{th} and j^{th} energies are obtained from the unperturbed energy expressions from Equations 1-6, produced values for the coupling parameter, $\zeta << 1$ MHz, whereas previously determined values for the parameter have been > 1400 MHz. From this result, we conclude that Coriolis coupling is not a significant effect in the energy levels concerned.

This unusual result can be rationalized by considering the large magnitude of the interchange and bifurcation tunneling splittings, which keep the levels capable of mixing sufficiently isolated from each other. Figure 5 portrays the separation of the six possible sets that are capable of Coriolis interaction for a given J.

The figure illustrates that while the origins of the two stacks are very close, the large tunneling splitting in this state(particularly for the K_a=1 stack) render the levels capable of Coriolis interaction so widely separated that the mixing is insignificant. Even for the sets that lie closest in proximity(the B_2^-/A_2^+ set and the A_2^+/B_2^-set), no appreciable Coriolis perturbation was found.

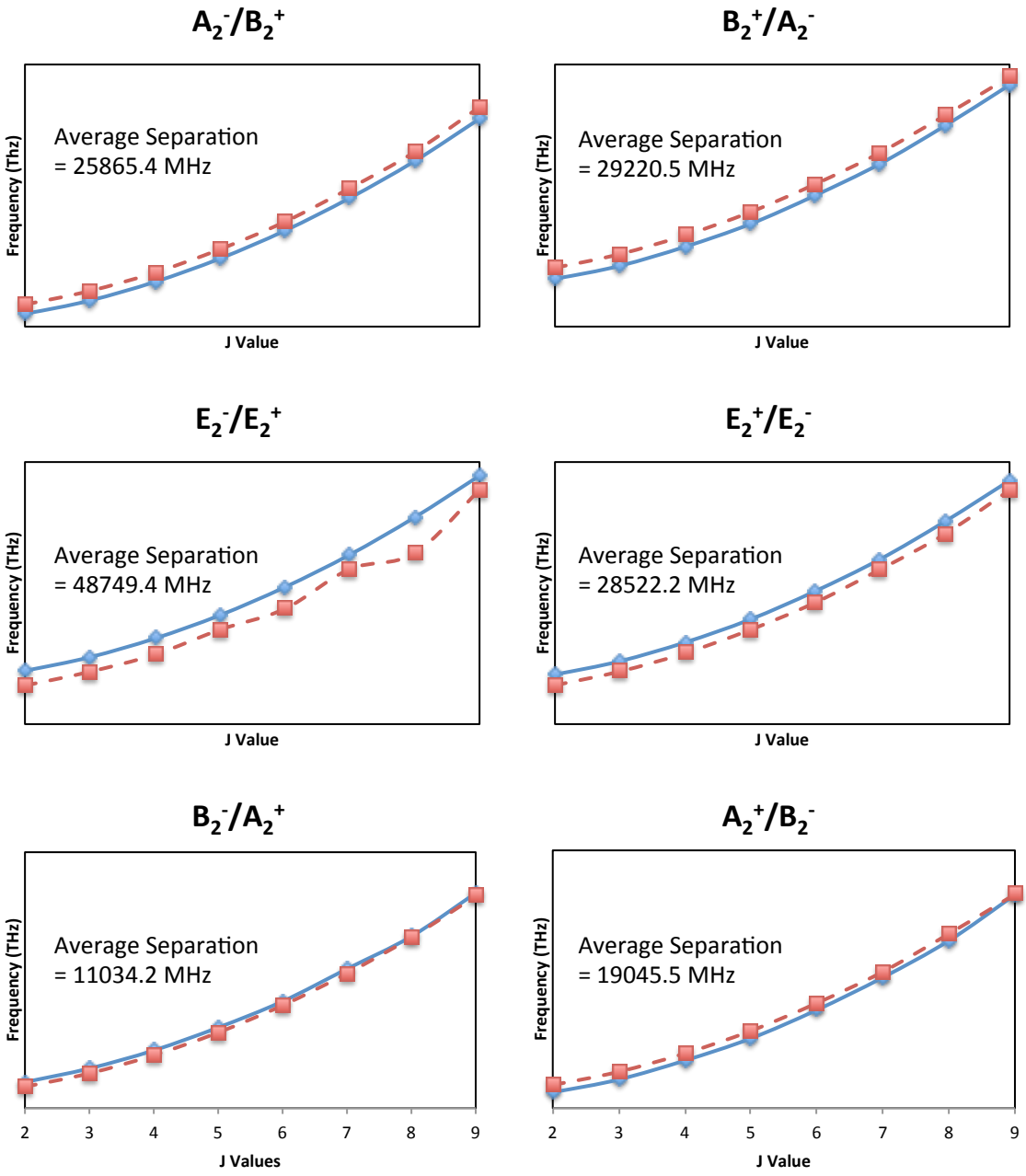

Figure 5: Calculated energy levels for the 2's triplets of the K_a=1 and K_a=2 upper state stacks. Each plot is arranged so that the levels capable of participating in Coriolis coupling are plotted together. The calculated energies for the K_a=1 stack are shown in blue/solid line, and the K_a=2 stack energies are in red/dashed line. The average separation between the levels is given on each plot. The plots that show the closest proximity sets are the B_2^-/A_2^+ and A_2^+/B_2^- sets, corresponding to the lower doublet of the 2's triplet. That large irregularity in the behavior of the K_a=2 E_2^-/E_2^+ set is caused by an extremely large value for both the centrifugal distortion and asymmetry rotational constants and is further discussed later in the paper. The numerical values of the y-axis are arbitrarily removed for clarity of the figure.

Vibrational Assignment

Assignment of the energy level stacks to an A" vibrational symmetry was unambigiously accomplished by observing the resulting diagram for the upper state. Figure 6 is reproduced from [57] and shows the energy level diagram for vibrations with both A' and A" symmetry. It can be seen from the figure that we have observed a 1's triplet at lower energy than the 2's triplet in the K_a=1 stack, which confirms the A" symmetry. Similarly, for the K_a=0 stack, we have observed the ordering of the 1's triplet to be B_1, E, A_1 for the J=0 level, which is also consistent with A" vibrational symmetry. An identical argument was used to justify the A" symmetry for the K_a=2 stack. Together with combination differences, an upper state symmetry of A" is unambiguously assigned.

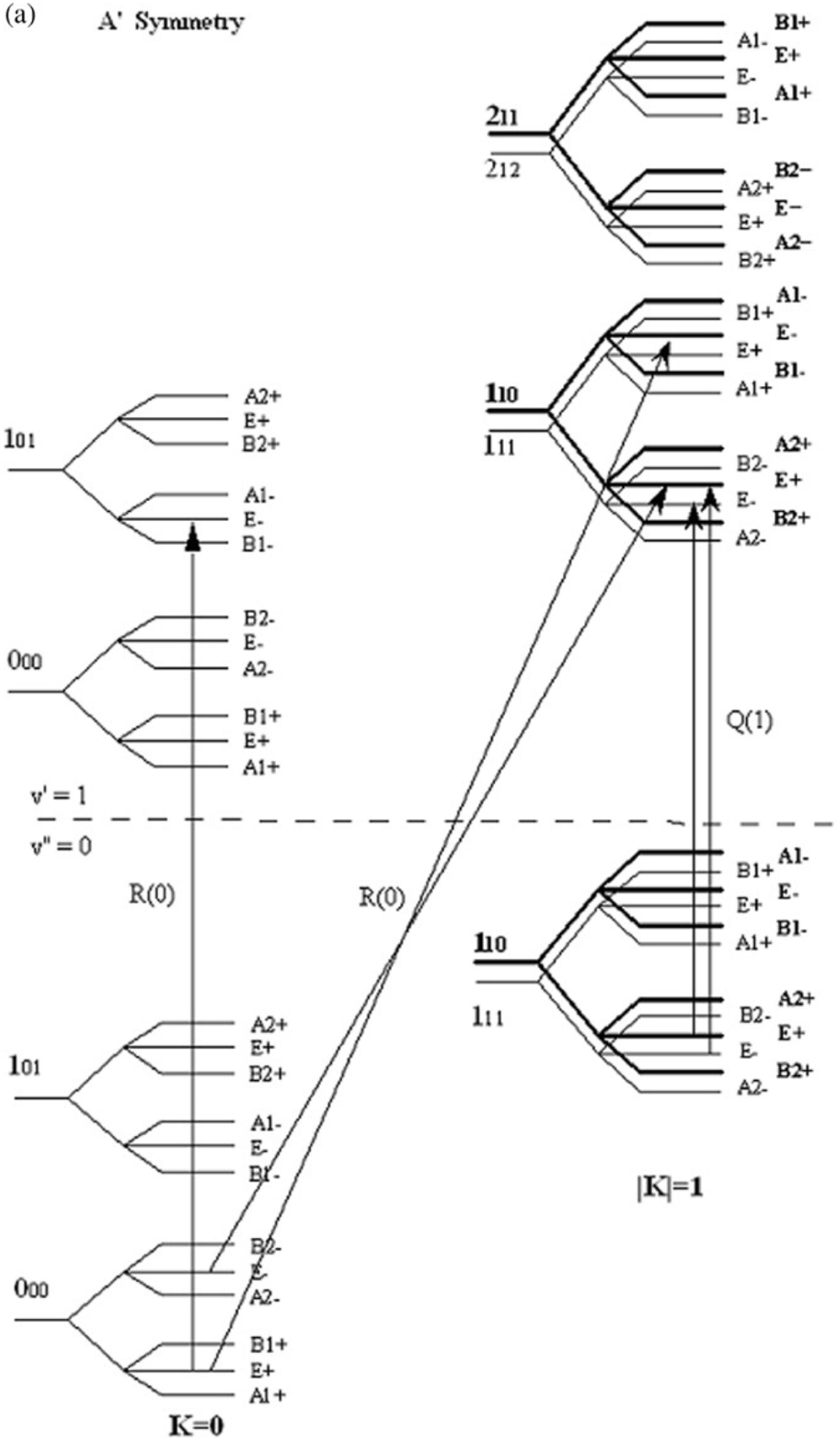
(a)
A' Symmetry
2₁₁
2₁₂
1₀₁
0₀₀
1₁₀
1₁₁
B1+
A1-
E+
E-
A1+
B1-
B2-
A2+
E+
E-
B2+
A2-
A2+
E+
B2+
A1-
E-
B1-
B2-
E-
A2-
B1+
E+
A1+
Q(1)
v' = 1
v" = 0
R(0)
R(0)
K=0
|K|=1

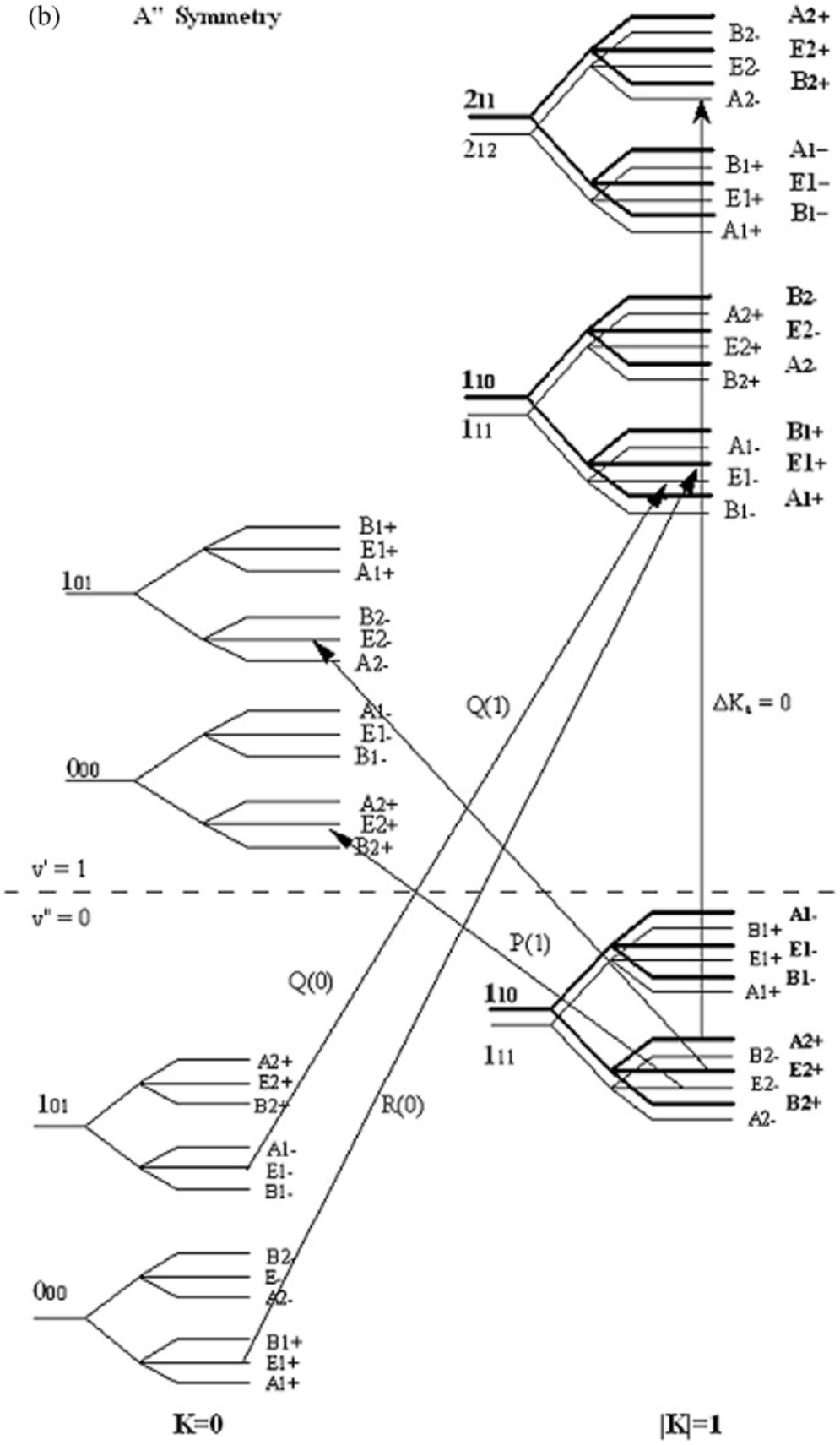
(b) A'' Symmetry
211
212
110
111
101
000
B2-
E2-
A2-
A2+
E2+
B2+
B1+
E1+
A1+
A1-
E1-
B1-
v' = 1
v'' = 0
Q(1)
ΔK = 0
P(1)
Q(0)
R(0)
K=0
|K|=1

Figure 6: Energy level diagram for excited state with A' and A" symmetry. Some possible transitions are shown for each upper state symmetry. Comparisons with Figure 3 provides evidence for the assignment to a vibration with A" symmetry. Reproduced with permission from Molecular Physics. 105, 5-7, (2007). Copyright 2007 Taylor & Francis Group.

For the water dimer, A" vibrational symmetry is consistent with the donor torsion, acceptor twist, and out-of-plane bend intermolecular vibrations. As the former two have been previously measured at frequencies <200 cm^{-1}, it seems clear that the out-of-plane bend is the vibration we are observing here. Additionally, Ceponkus et al. observed the out-of-plane bend in their matrix isolation experiment to lie near 522.4 cm^{-1} which agrees very well with our value for the origin of the K_a=1 stack of 523.7 cm^{-1} [53]. It must be noted, however, that there is a possibility of observing "hot" bands in He expansions due to incomplete vibrational relaxation, which could explain the structure of the remaining unassigned lines. It is unlikely that these "hot" bands affected the present assignment however, as the transitions that were assigned generally correspond to those with highest intensity, and the transitions originating from "hot" bands are expected to be weak.

An estimation of the band origin of the K_a=0 subband can be obtained by considering two facts. The first being that the acceptor switching splitting is generally similar for subbands belonging to the same vibration, and additionally that it tends to decrease as K_a increases. Also, the origin of the K_a=0 subband must be lower than that of the K_a=1 subband, which was experimentally determined herein to be 523.7 cm^{-1}. Based on this the only statement we can confidently make about the origin of the K_a=0 subband is that is lies lower than 523.7 cm^{-1} which would indicate an acceptor switch of at least 15.9 cm^{-1} which would fit the trend of dramatically increased tunneling splitting in the librational manifold observed in this experiment. An estimate of the origin in the 522-523cm^{-1} region seems reasonable and allows some tentative comparisons to theory and matrix isolation experiments, which can be seen in Table 4. If the measurement is to be consistent with previous measurements we would expect the origin of the K_a=0 level to be lower than the matrix isolation result and higher that the B3LYP anharmonic calculation which is a range of 514.9 - 522.4 cm^{-1}, but without verification we cannot definitively assign a band origin.

Analysis

Molecular Constants from the Fit

From the fitted constants given in Table 3, several interesting phenomena are evident. The first is that within a triplet, the B rotational constants are generally quite consistent, whereas the other constants vary considerably, sometimes dramatically. For example, in the K_a=1 stack the B_2^-/A_2^+ set and A_2^+/B_2^- set have greatly increased values of D and d compared to the other sets in this triplet stack. A likely explanation is that these sets are nearly degenerate and may weakly perturb one other, leading to the irregular constants in Table 2. As the constants of the other sets in the triplet have quite typical values for D and d, such a perturbation seems reasonable. Another interesting observation is the behavior of the E_2^-/E_2^+ set of the K_a=2 stack. As seen in Figure 4, the predicted upper state energies for the upper state E_2^-/E_2^+ have a large degree of variability compared to the other plotted upper states. This is a manifestation of the abnormally large D and asymmetry constant for that set compared to the other sets in the stack. The exact cause of this is not obvious, but the most reasonable explanation is that there is

some external perturbation affecting those energy levels, but the source of that perturbation is not yet clear.

Overall, the excited state constants from the fit are larger in magnitude than the corresponding constants in the ground state. Table 4 presents a comparison of the upper state and ground state values, with the ground state constants taken from [38]. The most striking difference between the two states is the dramatic increase in spread of measured constants in the upper state. Such variability in previous analyses has evidenced perturbations, e.g., Coriolis perturbation between the acceptor twist and acceptor wag vibrations as presented by Braly et al [37]. However, as mentioned earlier, the upper states in close proximity showed no evidence of Coriolis perturbations, which indicates that the perturbations must arise from some external levels. Based on calculations on the CC-pol-5s/f PES in the 475-600 cm^{-1} region, there is a large density of states at these energies, and even if the region is filtered by artificially "freezing" the states to 4K, there still exist a large number of possible excited states predicted in the region, as shown in Figure 7. The large number of remaining unassigned transitions in the region constitutes further support for this notion. As the librational band is considered to be essential for understanding the hydrogen bond-breaking dynamics of liquid water, these perturbations clearly warrant further investigation as to their origin.

Table 4: Comparison of the fit constants of the excited state studied here with the water dimer ground state values.

K_a= 0

	Excited State	Ground State
B	6209 - 6236	6158 - 6166
D	0.144 - 0.911	0.036 - 0.050

K_a= 1

	Excited State	Ground State
B	6133 - 6270	6151 - 6167
D	-2.150 - 2.141	0.4895 - 0.542
Asymmetry	-88.450 - 11.126	1.255 - 15.732
d	-0.333 - 1.027	~0.006

K_a= 2

	Excited State	Ground State
B	6105 - 6268	6142 - 6156
D	-1.566 - 5.763	0.039 - 0.051
Asymmetry	-5.660 - 0.499	~0.001

Additional insight into the behavior of the energy levels is obtained from the correlation matrices of the fits. For the K_a=0 upper state, all B constants show a positive correlation with their respective D constants, whereas no correlation was observed between the constants and the tunneling magnitudes (as expected). The correlation for the K_a=1 and K_a=2 upper states the correlations are more interesting. Almost all of the states show the same correlation pattern; that is, the B constant is correlated positively to the D constant and the asymmetry constant is positively correlated to the d constant. In the case of the K_a=2 levels, only the B and D constants are positively correlated. However, the lower triplet level for both K_a=1 and K_a=2 show strong positive correlation between all constants involved in the fit. This could be evidence for some perturbation strongly affecting these levels. Considering that these levels are in near-degeneracy, as shown in Figure 4, this correlation can be again rationalized by an external perturbation. The only other remarkable observation in the correlation matrices is that for the K_a=2, E_2^-/E_2^+ set there is a strong negative correlation between the D constants and the asymmetry constants whereas the B constant is uncorrelated. This is not replicated by any other energy level set in the fit. As we stated above, the K_a=2, E_2^-/E_2^+ set behaves very irregularly compared to the other sets and this correlation pattern serves as still further evidence that something is perturbing these levels.

As a final note, the traditional interpretation of the rotational constants in terms of nuclear coordinates and motions is inapplicable here, given the large magnitude of these constants compared to ground state values. However, this increased magnitude testifies that the water dimer is a highly non-rigid complex and that with excitations into the librational band of water the complex may display a particularly high degree of flexibility. An important conclusion to draw from this observation is that when simulating this region of the bulk (the librational band), flexible monomer models should be used.

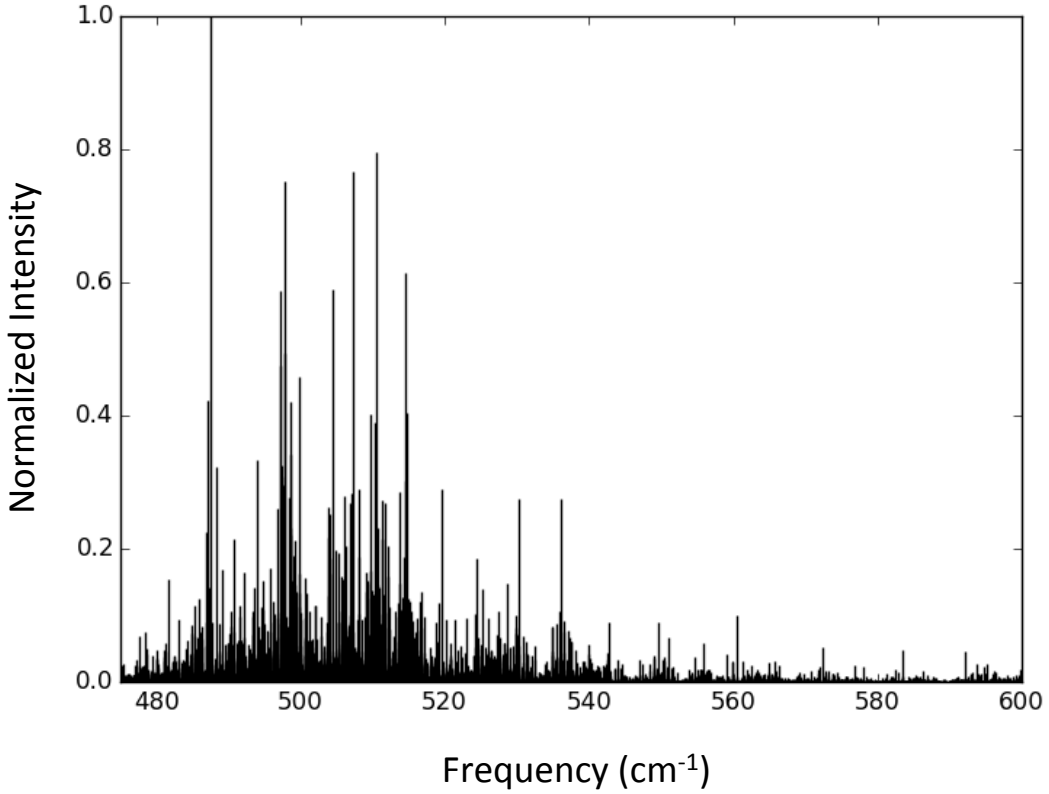

Figure 7: Theoretical spectrum of $(H_2O)_2$ calculated on the CCpol-8s PES at a temperature of 4K.

Tunneling Splittings

As all three tunneling pathways have now been characterized for the librational excitation, a comparison with the ground state values leads to a more complete understanding of the pathways and the associated tunneling barriers. In general, all of the measured values for the tunneling splittings in the librationally excited state show a dramatic increase over their ground state values. This is consistent with the results for previously studied lower energy excitations, however, the increases observed here- particularly for the bifurcation and interchange tunneling pathways- provide interesting new insights. Since only one acceptor switching splitting was measured, comparison to the ground state is tentative, pending further investigation; however, the observed value of ~308 GHz for the K_a=1 stack greatly exceeds the value of ~83 GHz for the K_a=1 stack of the ground state, and is comparable to the value for the K_a=0 ground state stack of 333 GHz. The enhanced acceptor switching is evidence for a reduced potential barrier in the excited state.

The observed interchange tunneling splittings range from 60 to 120 GHz, which again dramatically exceed the ground state values, all of which are less that 23 GHz. As for acceptor switching, the barrier for this pathway is very much less than 500 cm^{-1}; however, an additional factor may lead to the increased splittings. As shown in Figure 8, the tunneling motions closely resemble some of the intermolecular vibrations. Coupling of these vibrational motions to the tunneling pathways would lead to greatly increased splittings/shifts [36,37].

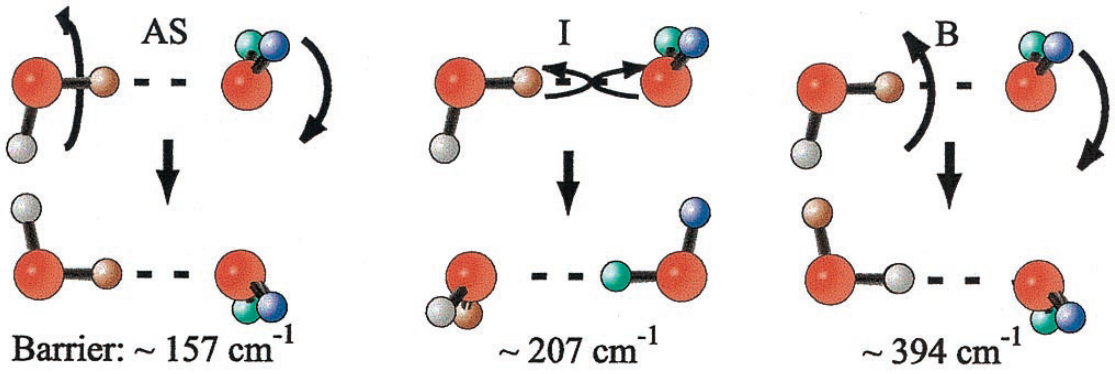

Figure 8: The tunneling pathways of the water dimer along with the potential barriers calculated from the VRT(ASP-W) potential energy surface. The three tunneling pathways are shown: (AS) acceptor switching, (I) interchange tunneling, and (B) bifurcation tunneling. The associated motions of the pathways are also shown. By direct comparison to the motions of the intermolecular vibrations in Figure 1 of this paper, it can be see that some tunneling pathways are analogous to the motions of these vibrations,: coupling of these vibrations to the tunneling motion would produce greatly increased experimental splittings/shifts. This figure is reproduced with permission from PNAS, 98, 19, (2001). Copyright 2001 National Academy of Sciences, USA.

The lowest barrier mechanism for interchange tunneling is the "geared" interchange pathway, consisting of a rotation of the donor molecule about the axis including the hydrogen bond, while the acceptor molecule rotates about its molecular C_2 axis. The donor then rotates about its molecular C_2 axis while the original acceptor rotates into the symmetry plane to become the new donor. The motion of the original donor molecule closely mirrors the motion of the out-of-plane libration, thus, coupling of the two motions is likely to produce an enhanced interchange tunneling. Such an enhancement could lead to increased splitting not consistent with simply transcending the tunneling barrier

For bifurcation tunneling, the pathway is one that results in the exchange of the donor hydrogens. This motion appears to be strongly coupled to the out-of-plane libration. As the observed bifurcation shifts range from 2500-23800 MHz (compared to ground state values estimated to be >750 MHz) this motion produces the most dramatic increase in tunneling effects relative to the ground state yet observed. In fact, the shifts are the highest ever measured for the bifurcation pathway for any water dimer, with the exception of the Coriolis-coupled acceptor wag and acceptor twist levels, where the abnormal shift was effected by the strong Coriolis interaction. Given that the excited state characterized here resides in the librational band region of liquid water, these increased tunneling splittings/shifts deserve further investigation as to their effects on hydrogen bond dynamics in liquid water.

One final intriguing consequence of the large interchange and bifurcation tunneling effects is the permutation of the usual ordering of the energy levels. Figure 9 shows a comparison of the expected and observed eigenstate ordering for two representative levels. The extent of the permutation varies, but is more dramatic in the levels that have larger interchange and bifurcation tunneling perturbations, as would be expected. The effects of this permutation on the hydrogen bond dynamics of liquid and solid water could be interesting.

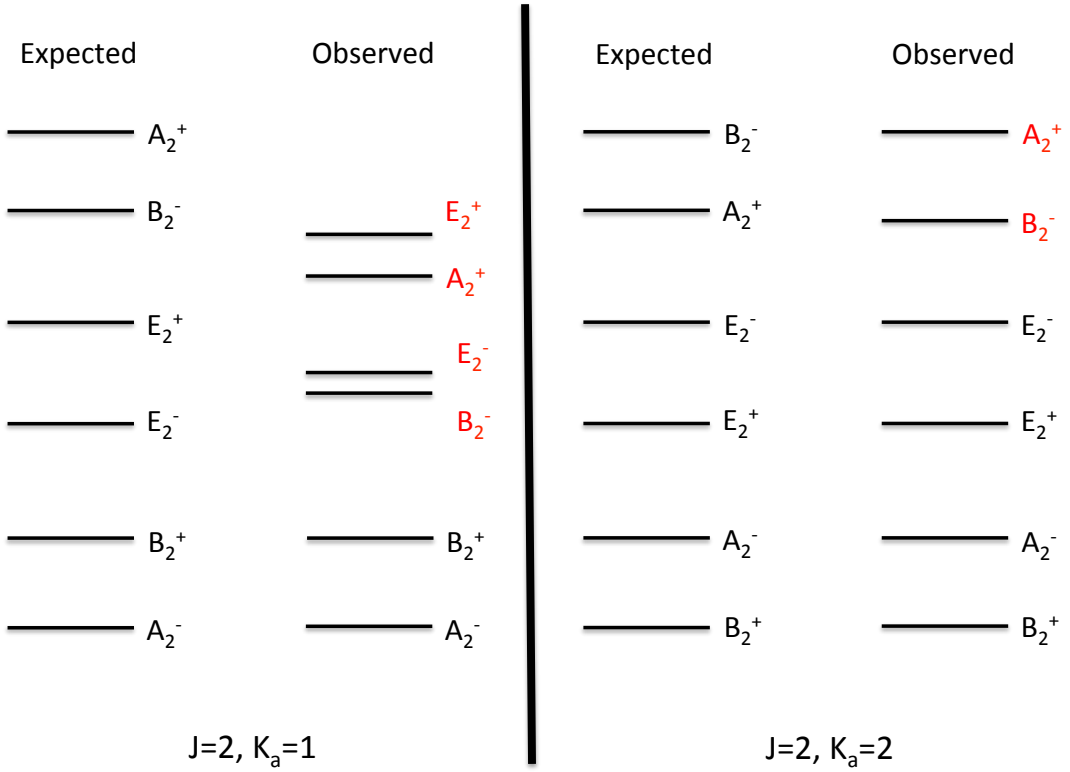

Figure 9: Example of the permutation of energy level order. Drawing is done to relative scale. Levels permuted from their expected order are highlighted in red.

Summary of Water Dimer VRT Studies

We have recently reviewed the experimental studies made for the water dimer[20]. Description of the currently observed VRT levels for $(H_2O)_2$ and $(D_2O)_2$ can be found in papers by Braly et al., the early work in the microwave, the later work by Harker et al., and Keutsch et al.'s complete characterization of the ground state [36–40]. These papers present observations of all the intermolecular vibrations except the in-plane and out-of-plane librations, the latter described herein. Table 5 and Table 6 show the results of the VRT experiments from the Saykally group together with matrix isolation measurements and various theoretical calculations of the intermolecular vibrations for both $(H_2O)_2$ and $(D_2O)_2$.

Table 5: Values for $(H_2O)_2$ intermolecular vibrations. Values shown for VRT experiments correspond to the band origin of the K_a=0 subband, unless otherwise stated (Due to incomplete spectral coverage, some values remain missing). Values for matrix isolation experiments and B3LYP anharmonic DFT calculations are taken from reference [53]. Values for CC-pol-8s/f and MB-pol are taken from reference [9] and correspond to the band origin of the K_a=0 subband. All values are given in cm^{-1}.

Out-of-plane Bend	VRT Exp.	523.7 (K_a=1)[a]	In-plane Bend	VRT Exp.	N/a
	Matrix Isolation Exp.	522.4		Matrix Isolation Exp.	309.1
	B3LYP Anharm.	514.9		B3LYP Anharm.	306.8
	SAPT-5st Harm.	564.7		SAPT-5st Harm.	367.0
	CC-pol-8s/f	N/a		CC-pol-8s/f	N/a
	MB-pol	N/a		MB-pol	N/a
O-O Stretch	VRT Exp.	153.62 (K_a=0, 2's)	Acceptor Twist	VRT Exp.	120.19(K_a=0, 2's)
	Matrix Isolation Exp.	173.0		Matrix Isolation Exp.	150.6
	B3LYP Anharm.	124.4		B3LYP Anharm.	117.7
	SAPT-5st Harm.	186.8		SAPT-5st Harm.	143.7
	CC-pol-8s/f	146.4		CC-pol-8s/f	124.8
	MB-pol	151.9		MB-pol	124.3
Acceptor Wag	VRT Exp.	108.41	Donor Torsion	VRT Exp.	64.52 (K_a=0, 2's)
	Matrix Isolation Exp.	122.2		Matrix Isolation Exp.	116
	B3LYP Anharm.	117.4		B3LYP Anharm.	77.5
	SAPT-5st Harm.	157.9		SAPT-5st Harm.	121.0
	CC-pol-8s/f	108.5		CC-pol-8s/f	87.3
	MB-pol	108.6		MB-pol	87.6

[a] Reported herein

Table 6: Values for $(D_2O)_2$ intermolecular vibrations. Values shown for VRT experiments correspond to the band origin of the K_a=0 subband, unless otherwise stated (Due to incomplete spectral coverage, some values remain missing). Values for matrix isolation experiments and B3LYP anharmonic DFT calculations are taken from reference [53]. Values for CC-pol-8s/f are taken from reference [17] and correspond to the band origin of the K_a=0 subband. All values are given in cm^{-1}. Values for the MB-pol potential are currently being investigated.

Out-of-plane Bend	VRT Exp.	N/a	In-plane Bend	VRT Exp.	N/a
	Matrix Isolation Exp.	393.2		Matrix Isolation Exp.	233.5
	B3LYP Anharm.	396.0		B3LYP Anharm.	246.3
	SAPT-5st Harm.	406.1		SAPT-5st Harm.	274.8
	CC-pol-8s/f	N/a		CC-pol-8s/f	N/a
O-O Stretch	VRT Exp.	N/a	Acceptor Twist	VRT Exp.	91.64
	Matrix Isolation Exp.	166		Matrix Isolation Exp.	123.1
	B3LYP Anharm.	145.0		B3LYP Anharm.	105.1
	SAPT-5st Harm.	172.8		SAPT-5st Harm.	102.8
	CC-pol-8s/f	145.4		CC-pol-8s/f	89.9
Acceptor Wag	VRT Exp.	83.52	Donor Torsion	VRT Exp.	67.49
	Matrix Isolation Exp.	93.3		Matrix Isolation Exp.	87.7
	B3LYP Anharm.	100.0		B3LYP Anharm.	83.3
	SAPT-5st Harm.	118.5		SAPT-5st Harm.	88.1
	CC-pol-8s/f	81.7		CC-pol-8s/f	65.4

With this extensive collection of accurate spectroscopic data, sampling a large range of the dimer potential energy surface, it should now be possible to develop highly accurate potential models through direct inversion methods, and to thereby obtain the two-body interaction term in the many body expansion of bulk water potentials very accurately. Nevertheless, some experimental work remains to be done to completely characterize the fundamental intermolecular vibrations. The region of 300 cm^{-1} is particular interesting due to the observation of the in-plane libration in matrix isolation experiments [53]. The limited availability of suitable radiation sources in the terahertz region has traditionally been the limitation on VRT experiments with water clusters, but emerging technologies may soon mitigate this problem [58]. In any case, the realization of a truly complete characterization of the water dimer clearly near at hand.

Conclusions

We have presented the first high resolution spectroscopy results characterizing the out-of-plane bend intermolecular vibration of $(H_2O)_2$ in the librational band region of liquid water. The excited states exhibit dramatic increases in tunneling splittings compared to the ground state, resulting in a permutation of the energy level ordering. A fit of the assigned transitions yields rotational constants that vary significantly from the ground state values, possibly the result of perturbations from the high density of energy levels that exist in the sampled frequency domain (ca. 500 cm^{-1}).

This work extends the characterization of the hydrogen bond vibrations of the water dimer to encompass five of the six intermolecular modes. Along with the recent measurement of the dimer dissociation energy [59], this will enable rigorous tests of existing and future dimer potential surfaces, and hence, important progress in the determination of a new class of accurate models for solid and liquid water. Further work remains, however, to characterize the predicted 300 cm^{-1} in-plane librational motion.

Hydrogen Bond Breaking Dynamics in the Water Pentamer: Terahertz VRT Spectroscopy of a 20 μm Libration

*The full details of this section can be found in: Cole, W.T.S., Fellers, R.S., Viant, M.R., Saykally, R.J., J. Chem. Phys., **146**, 014306 (2017).*

Introduction

The out-of-plane librational band is the most prominent feature in the intermolecular vibrational spectrum of bulk water, and has important consequences for hydrogen bond dynamics [1,5,41,60]. Excitation of this vibration, which occurs in the 500-800 cm^{-1} region, has been shown to comprise motions that break and reform hydrogen bonds [43,61,62], and the hydrogen bond breaking process has been shown to be highly local, and largely unaffected by hydrogen bond order [44]. Thus, water *clusters* present a convenient route for examining details of these hydrogen bond dynamics [28]. Additionally, analysis of the many-body expansion of the water-water interaction potential has shown that the most significant terms are the 2 and 3 body terms, which comprise ~99% of the interaction energy [63–65]. Towards the development of improved water models, VRT experiments on water clusters have been shown to accurately probe the short-range interactions [9,15]. The key distinctions between water clusters and the bulk are the free hydrogens of the clusters. These hydrogens are predicted to have little effect on the librational motions, as evidenced by low resolution spectroscopy studies of small clusters (n=10-100) [46]. Here we report the high resolution terahertz VRT spectrum of a librational vibration near 500 cm^{-1} for the water pentamer-d_{10}, excitation of which produces a dramatic increase in the bifurcation tunneling rate and consequent hydrogen bond breaking dynamics.

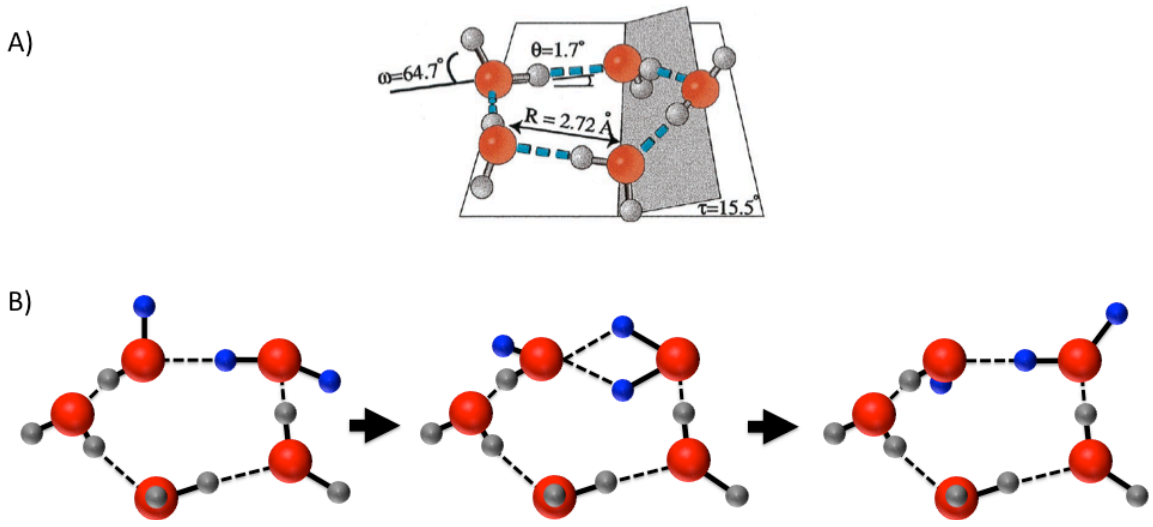

Figure 10: Structure of the water pentamer. A) Oxygen atoms are red and hydrogens grey. The oxygen framework deviates from planarity by 15.5°, but the vibrationally averaged rotational constants have been shown to be well-approximated by a semi-rigid, oblate symmetric top model. **B)** One proposed mechanism of bifurcation tunneling A single monomer switches the hydrogen participating in the hydrogen bond, and an adjacent monomer flips its free hydrogen with respect to the plane. The hydrogens involved in the pathway are colored blue.

As for the water trimer and tetramer, the lowest energy form of the water pentamer is a quasi-planar ring structure (Figure 10A) with all hydrogen bonds directed in the same sense (CW or CCW) [30]. The free hydrogens of each water monomer, directed either above or below the plane of the molecule, are labeled with "u" for up or "d" for down, and the global minimum for the pentamer is labeled (ududd). This structure was predicted by *ab initio* calculations [66–68] and confirmed by Liu et al's observation of the pentamer-d_{10} species in 1996 [69,70]. Liu measured parallel-type transitions of a torsional vibration, and showed that a rigid oblate symmetric rotor model fit the data well; however, parallel transitions can only rigorously determine the B rotational constant and state differences for the corresponding C rotational constant [69,70]. Until the present work, only parallel-type transitions have been measured for the pentamer, limiting the possible structural comparisons with theory [69–73].

The pentamer behaves similarly to the trimer in the way that hydrogen bond tunneling motions affect the energy level structure [74,75]. The most facile process is termed "flipping" and involves a free hydrogen switching from one side of the plane to the other , as shown in Figure 10B. Previous experiments and theory revealed that this motion, in combination with psuedorotation of the ring pucker, results in fast vibrational averaging to a planar, symmetric (C_{5h}) pentamer structure. This process results in a "torsional-puckering" manifold of energy levels, described by Wales et al and Graf et al, and elaborated by Harker et al [66,73,76]. This energy level manifold is shown on the left of Figure 11. The levels of can be labeled by the irreducible representation of the C_{5h} point group. Experiments have shown the separation of these levels to be ca. a few wavenumbers [73].

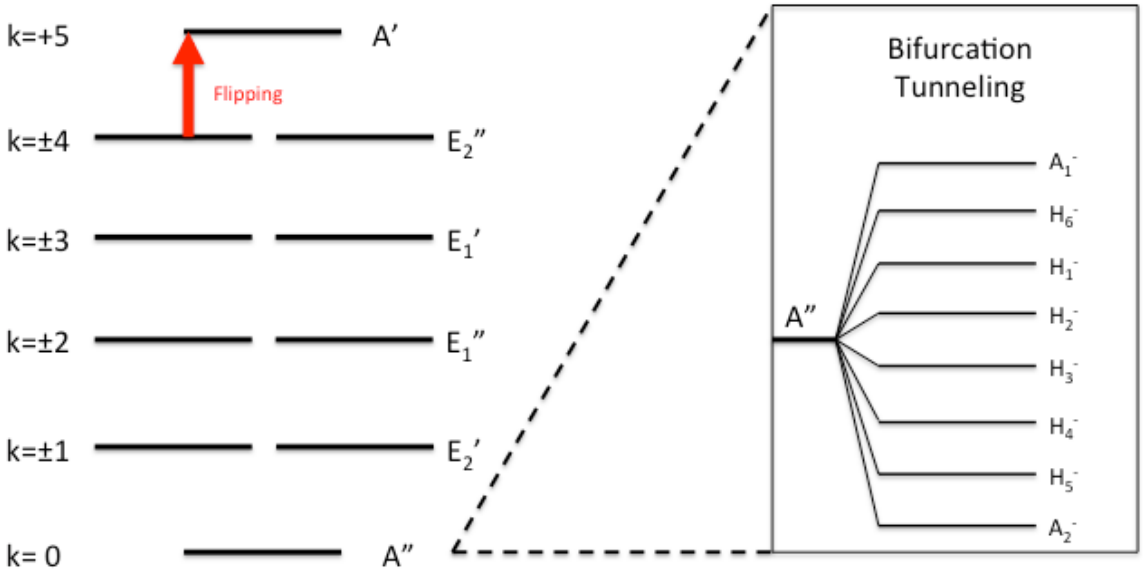

Figure 11: Pseudorotational manifold of the water pentamer. The diagram on the left shows the result of the "flipping" motion, shown as a red arrow, which generates a manifold of 10 energy levels, labeled by the irreducible representations of the C_{5h} point group. A pseudo-quantum number, k, defined in the text, also labels the levels. On the right, the splitting caused by bifurcation tunneling is shown for a single pseudorotational level. These states can be labeled by the irreducible representations of G_{320}, as shown by Wales et al. The reader is referred to Wales et al for a detailed discussion of the relevant group theory [66].

A second tunneling motion, which had previously been observed only in the $(H_2O)_5$ pentamer isotopomer, is "bifurcation", sometimes referred to as "donor tunneling", wherein the hydrogen participating in the hydrogen bond interchanges with the corresponding free hydrogen. This tunneling motion breaks and reforms the hydrogen bond and is of particular interest in studying the effect of cooperativity in water dynamics, as this tunneling path has been characterized experimentally in the dimer , trimer, pentamer, and hexamer, but not for the octamer [1,2,36–38,41,71,72,77–83]. It is currently unclear from recent observations if bifurcation tunneling is observed in the tetramer. This tunneling motion further splits the torsional energy levels, shown on the right of Figure 11, which are now labeled by the irreducible representation of the molecular symmetry group G_{320} [81]. A detailed study by Wales and Walsh elucidated two possible mechanisms for bifurcation tunneling, but determining which one is correct requires experimental study [66]. Further examination by Gregory and Clary predicted tunneling splittings of 220-700 MHz for $(H_2O)_5$ and 70-140 MHz for $(D_2O)_5$ on variants of the ASP potential surface [84]. Brown et al observed bifurcation tunneling in $(H_2O)_5$, of magnitude ~5 MHz, but due to the small number of observed lines, a definitive determination of the tunneling mechanism was not possible [71]. Readers interested in the detailed group theory of the water pentamer are referred to the work of Balasubramanian [81].

Here we report the measurement of 875 VRT transitions belonging to 6 perpendicular subbands originating from $(D_2O)_5$ at ~512 cm^{-1} and the assignment to a librational vibration. The subbands reveal an increase in the bifurcation tunneling splittings of at least 3 orders of magnitude upon single quantum excitation, suggesting strong coupling of the librational motion to the tunneling pathway. Analysis of the fitted constants provides the first characterization of the C rotational constant as well as the D_{JK} and D_K centrifugal distortion terms.

Experimental

Our previous investigations of water dimer and trimer librational motion in the 500 cm^{-1} region prompted us to search for transitions from larger clusters [1,5]. The Berkeley diode laser/supersonic beam spectrometer used in this study has been described in detail elsewhere and only a short description is provided here [1,47–49].

A helium-cooled spectrometer (Spectra Physics) using lead-salt diodes (Laser Photonics) was used to produce infrared radiation from 509-514 cm^{-1}. The beam was multipassed 18-22 times through a pulsed planar supersonic expansion of a mixture of H_2O and He using a Herriot cell and detected using a helium-cooled (Si:B) photoconductive detector (IR Labs). The supersonic expansion was produced by bubbling pure He gas, with a backing pressure of 1-2 atm through liquid D_2O (Cambridge Labs, 99.96% purity), and then expanding through a 101.6 mm long slit at a repetition rate of 35 Hz into a vacuum chamber maintained at ~200mTorr by a Roots blower (Edwards 4200) backed by two rotary pumps (E2M 275). Simultaneously, the fringe spacing of a vacuum-spaced etalon and an OCS reference gas spectra were detected with a liquid He cooled (Cu:Ge) detector (Santa Barbara Research Center) and recorded to enable precise frequency calibration. The observed linewidths of ~ 30-40 MHz full-

width half maximum (FWHM) are somewhat larger than the Doppler-limited linewidths extrapolated from earlier experiments using argon expansions. Typical frequency measurement accuracy is 10-20 MHz, limited by both linewidths of the cluster absorptions and laser drift. Spectra were detected in direct absorption using a time-gated phase sensitive signal processing approach.

Accessing the 500 cm^{-1} region of the electromagnetic spectrum has generally been notoriously difficult. The spectra reported here required the use of 10 separate laser diodes, each scanned across several modes to cover the specified spectral range. Moreover, large laser gaps are present in the spectra, which causes considerable difficulty in the assignment. Additionally, the spectrum reflects several distinct laser intensity fluctuations across different devices that are apparent in the complete spectra shown in Figure 12A. Specifically, between 512.4 cm^{-1} and 513.2 cm^{-1} the intensity is enhanced and between 509.5 cm^{-1} and 510 cm^{-1} the intensity is depressed.

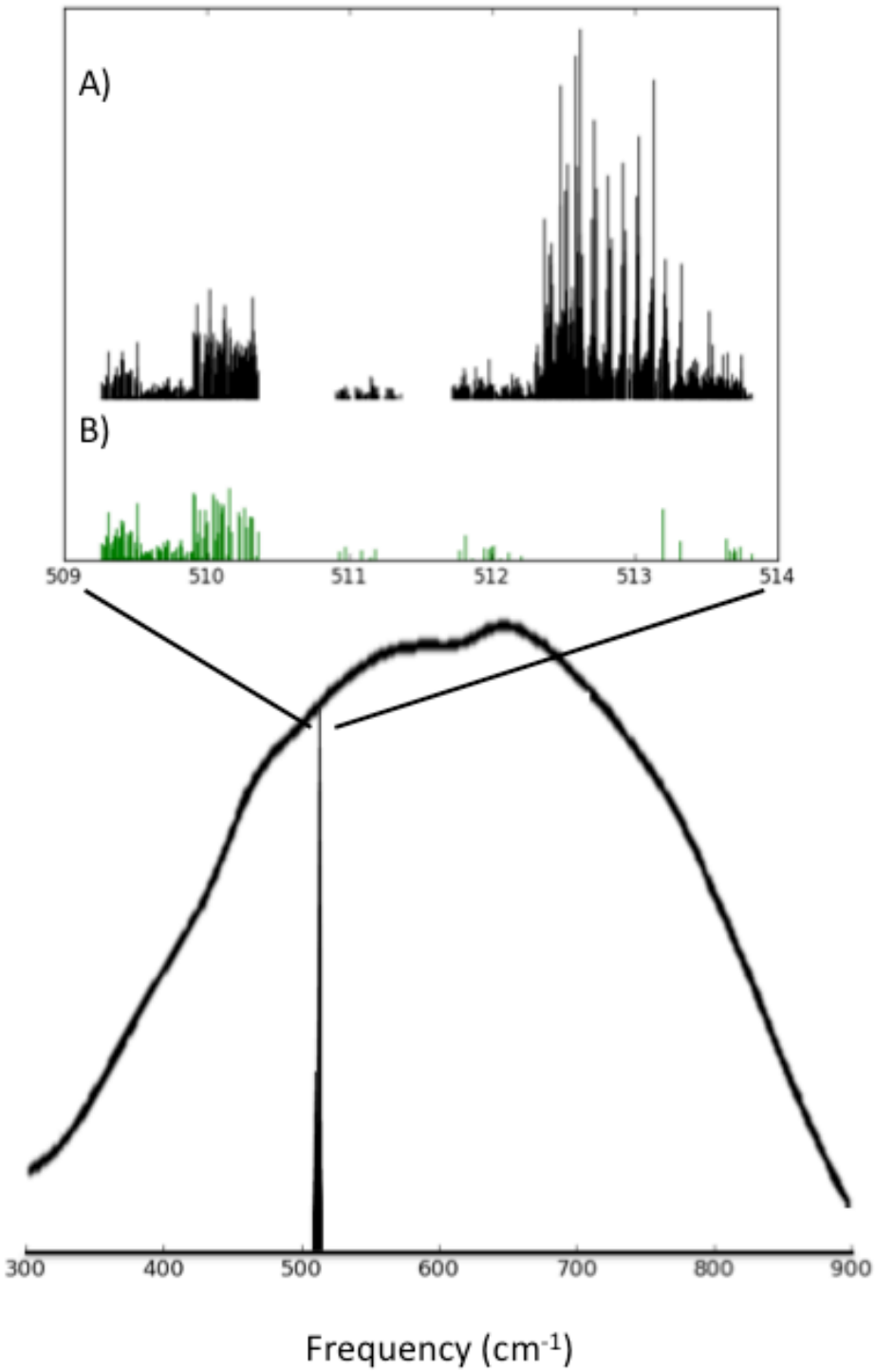

Figure 12: A) All 1063 observed transitions in the experimental range of 509.258 – 513.820 cm^{-1}. There are two major laser gaps in the spectrum: from 510.357 – 510.901 cm^{-1} and 511.360 – 511.719cm^{-1}, as well as several smaller gaps, typically less than 0.01cm^{-1} . The spectrum also shows the drastic intensity fluctuations of the lead salt diode laser, most notably around 509.6 and 512.0 cm^{-1}. **B)** The remaining 188 unassigned transitions. The bottom of the figure shows the experimentally probed region imposed under the libration band of liquid water.

Results and Analysis

Assignment

We were able to assign 875 of the 1063 recorded transitions to the pentamer-d_{10} using a pattern recognition algorithm based on the oblate symmetric top model. A similar program has been used to aid assignment of water dimer and water octamer spectra [2,5]. The above-mentioned intensity fluctuations make it difficult to rely on relative intensities across more than 0.5 cm^{-1}, and complicated the assignment process. The full spectrum, along with the remaining unassigned lines, is shown in Figure 12. Lines were assigned to a total of 6 perpendicular ($\Delta K=\pm 1$) subbands originating from a singly degenerate ground state and terminating in a singly degenerate "torsional-puckering" excited state. A typical band structure is shown in Figure 13. The assigned spectra evidenced a large bifurcation tunneling splitting.

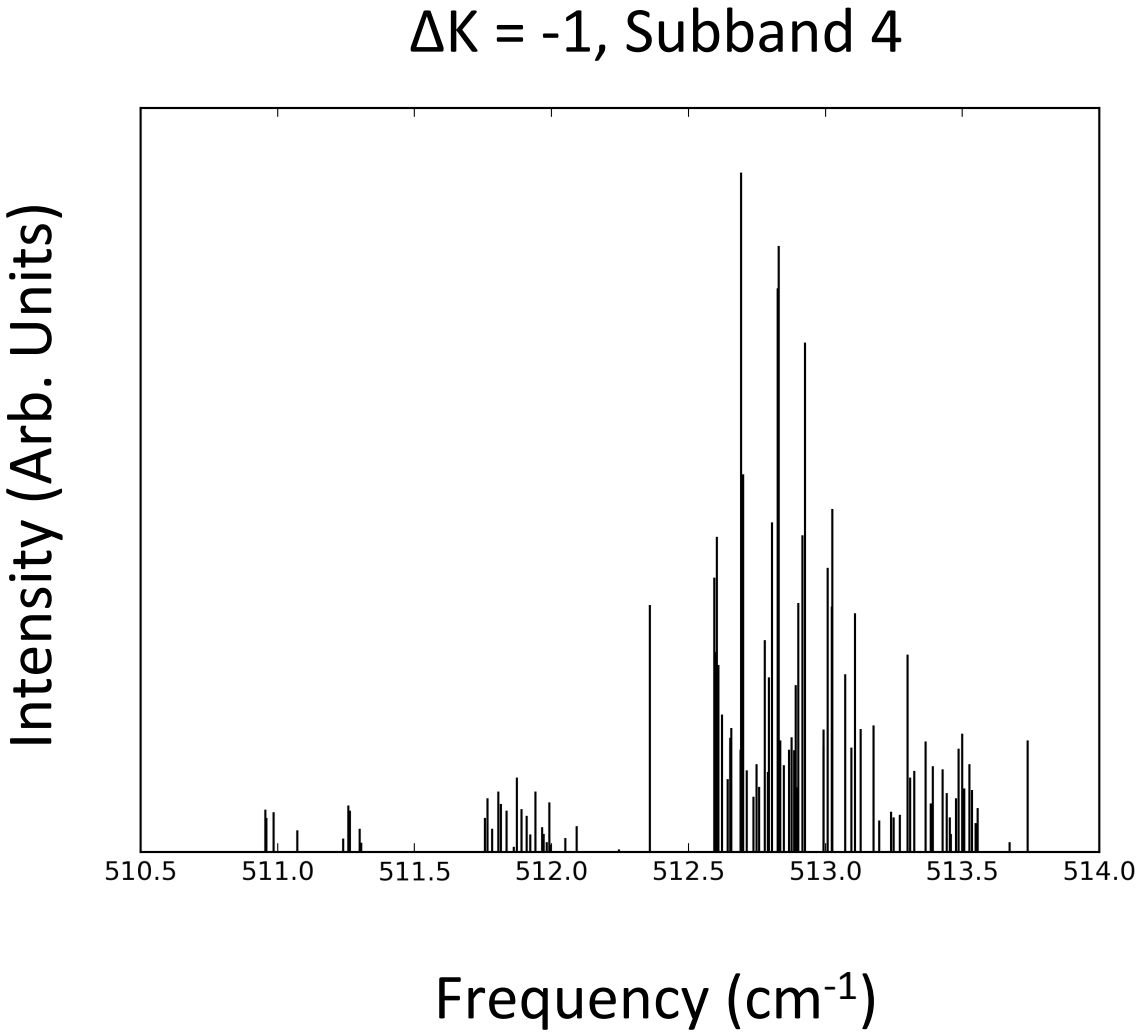

Figure 13: A typical subband structure observed in the experiment. The P branch regions are severely affected by the two large laser gaps described in the text.

Fit results

The assigned transitions were fit to a standard oblate symmetric top energy level expression (Equation 1). This model has been previously shown to correctly model the VRT transitions of the water pentamer by Harker et al [73]. Each subband was fit to a separate expression to simplify the analysis. The average RMS of the 6 subbands was ~8.5 MHz, which is well below the observed linewidths of ~30 MHz and comparable to the wavelength accuracy of ca. 10 MHz.

$$E = B * J(J+1) + (C-B) * K^2 - D_J[J(J+1)]^2 - D_{JK} * [J(J+1)K^2] - D_K * K^4 \quad (\mathbf{1})$$

In Eq. 1, B and C are the usual rotational constants of the structure and D_J, D_{JK}, and D_K are the centrifugal distortion constants. The transitions displayed no Coriolis splitting, suggesting a transition from a singly degenerate state; these states are well-studied by Harker et al, Liu et al, Cruzan et al, and Brown et al and display no Coriolis splittings in the ground state [69–73]. The 6 subbands appear to be evenly spaced with an average separation of ~0.052 cm^{-1}(~1.559 GHz). The results of the fit are shown in Table 7. Correlation matrices and the explicit transition frequencies included in the fit can be found in the Supplemental Material in Appendix A.

Observation of Table 7 shows that the excited state constants for all 6 subbands are in close agreement, indicating that the excited vibrational state is the same for all bands. Likewise, the lower state constants indicate a common vibrational ground state, which is in good agreement with the results of Harker et al and Liu et al for the D_2O pentamer [69,70,73].

Table 7: Results from the fit of all 875 observed transitions to an oblate symmetric top energy level expression. All values are given in MHz, with the exception of the number of transitions. Subbands are labeled 1-6 from low to high frequency to distinguish the 6 subbands. Single-primed values represent the excited state value and double-primed constants are associated with the lower state.

	Subband 1	Subband 2	Subband 3
	Value (MHz)	Value (MHz)	Value (MHz)
v	15361732(9)	15363247(5)	15364722(2)
B'	1767.28(50)	1767.03(29)	1767.36(10)
C'	941.38(76)	941.28(44)	940.99(13)
D_j'	1.10(76)E-02	1.152(65)E-02	1.246(22)E-02
D_{jk}'	1.97(33)E-02	1.66(13)E-02	1.527(42)E-02
D_k'	3.18(31)E-02	3.723(87)E-02	3.521(36)E-02
B"	1750.15(46)	1749.68(28)	1750.020(99)
C"	907.15(79)	906.93(42)	906.72(13)
$D_j"$	7.31(12)E-03	7.09(55)E-03	7.61(21)E-03
$D_{jk}"$	-8.72(32)E-03	1.17(11)E-02	-1.223(42)E-02
$D_k"$	-4.70(41)E-02	-4.054(97)E-02	-4.283(39)E-02
RMS	11.53	9.61	4.21
Number of Transitions	71	137	199

	Subband 4	Subband 5	Subband 6
	Value (MHz)	Value (MHz)	Value (MHz)
v	15366285(2)	15367659(3)	15369321(7)
B'	1767.36(14)	1767.12(21)	1768.25(37)
C'	941.02(19)	941.12(27)	941.47(49)
D_j'	1.205(29)E-02	1.171(46)E-02	1.438(92)E-02
D_{jk}'	1.517(60)E-02	1.60(11)E-02	1.43(17)E-02
D_k'	3.529(42)E-02	3.648(83)E-02	3.55(11)E-02
B"	1750.10(13)	1749.81(20)	1750.65(34)
C"	906.72(18)	906.76(27)	907.03(46)
$D_j"$	7.74(27)E-03	7.57(40)E-03	9.06(75)E-03
$D_{jk}"$	-1.284(57)E-02	-1.140(99)E-02	-1.28(16)E-02
$D_k"$	-4.232(45)E-02	-4.200(99)E-02	-4.26(13)E-02
RMS	6.05	8.42	11.16
Number of Transitions	207	163	98

Tunneling Dynamics

As shown in Figure 11, the tunneling dynamics of the water pentamer lead to a tenfold increase in the number of energy levels; to determine the origin of the 6 observed subbands, we consider the feasible tunneling mechanisms in turn. The most facile tunneling process in the pentamer is "flipping", which leads to the pseudorotation manifold shown in Figure 11. Selection rules for these "flipping" transitions are similar to those for the trimer pseudorotation manifold [74,75]: $\Delta K - \Delta k = 5 + 10n$; here n is a integer and k is the pseudorotation quantum number, shown on the left of Figure 11[66,76,78]. For our observed transitions, ΔK=±1; this implies Δk = ±4, which would result in two subbands in the experimental region instead of the 6 we actually observe. Additionally, the splitting due to flipping in the ground state has been observed to be ca. 1 cm^{-1}, very distinct from the ~0.051 cm^{-1} separation observed for the 6 subbands. Moreover, the bands originating from transitions between pseudorotational level with ΔK=±1 would not be equally spaced [66]. We are thus forced to consider bifurcation tunneling as a second feasible tunneling motion.

Wales and Walsh have shown that there are two possible mechanisms for bifurcation tunneling [66]. The net result of the bifurcation pathway is exchange of the hydrogen bonded and free proton within a single water monomer. In the first pathway, this results in the exchanged free proton localized on the opposite side of the pentamer plane. This pathway was predicted from *ab initio* calculations and two empirical potentials (TIP4P and ASP-W2), and will be referred to as Mechanism A. The second pathway also produces this same result for the exchanged free proton, but this is accompanied by an adjacent monomer flipping its free hydrogen as well. The second pathway was observed for the ASP-W4 potential, and will be referred to as Mechanism B [66]. These two pathways are shown in Figure 14. Both result in an extension of the effective molecular symmetry group to G_{320}; however the spectral intensity pattern changes depending on which mechanism is active. In analyzing our results we considered both mechanisms.

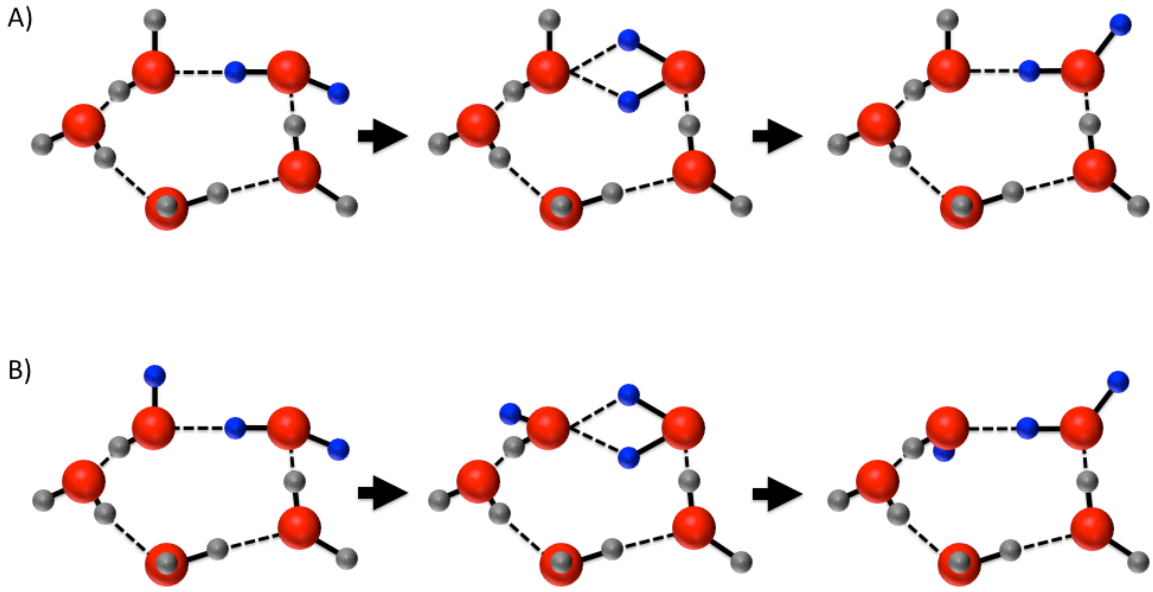

Figure 14: The two proposed mechanisms for bifurcation tunneling in the water pentamer. Oxygens are colored red, and hydrogens are colored grey. Hydrogens involved in the motion are highlighted blue. **A)** In Mechanism A, a single water monomer exchanges its free and hydrogen bonded protons via the transition state (the middle image). The exchanged free proton lies on the opposite side of the plane in the final state shown on the right. **B)** In Mechanism B, a single water monomer exchanges its free and hydrogen bonded protons, with the exchanged free hydrogen again lying on the opposite side of the plane via the transition state shown in the middle image. Additionally, an adjacent water monomer flips its free hydrogen to the opposite side of the plane, as shown in the final state (the right image).

The presence of bifurcation tunneling induces a further splitting of the pseudorotation energy levels, as shown on the right of Figure 11. This splitting pattern for both mechanisms is shown in Table 8 of Wales and Walsh [66]. In the G_{320} MS group notation, the new selection rule for electric dipole transitions indicates that transitions occur between states which change parity with respect to inversion, but which maintain their overall symmetry (i.e. $H_1^+ \rightarrow H_1^-$, $E_1^- \rightarrow E_1^+$, etc.). From the fit, we can assume that the ground state is one of the singly degenerate energy levels (k=0, +5), which we know from the experiments of Harker et al [73], Cruzan et al [72] , and Liu et al [69,70] display no bifurcation tunneling. We refer to the ground state as singly degenerate and neglect the underlying tunneling levels, as these cannot be resolved with current experiments. As a note, we neglect considering higher energy, singly degenerate, pseudorotation manifold levels as Graf et al [76] show that these lie nearly 50 cm^{-1} above k=+5, and are therefore expected not be populated in a supersonic expansion. In G_{320} notation, the energy level label for k=0 or +5 will be $A_1^{\pm} \oplus H_1^{\pm} \oplus H_2^{\pm} \oplus H_3^{\pm} \oplus H_4^{\pm} \oplus H_5^{\pm} \oplus H_6^{\pm} \oplus A_1^{\pm}$, for which the parity can be deduced from Table 8 of Wales and Walsh [66] or from Figure 6a herein. Based on the selection rules, the allowed transitions would be k=0 → ±1,±3,+5 or k=+5 → 0,±2,±4 for either mechanism. To determine which of the above the transitions we are observing, we compare the unique splitting patterns to our experimentally observed pattern.

We can immediately rule out the transitions k=0 → ±1, ±3 and k=5 → ±2, ±4 for two main reasons. The first is that we did not observe Coriolis splitting, which would be expected if the transitions were to terminate in one of the doubly degenerate pseudorotation levels (±1, ±2, ±3, and ±4). It is possible, although unlikely, that the splitting is below the experimental resolution, as previous studies of $(D_2O)_5$ found evidence of Coriolis splitting of ca. 100s of MHz. in these states in a low frequency band (~27 cm^{-1}). The second reason is that a transitions from k=0 or +5 to one of the doubly degenerate states would result in at least 12 subbands appearing, for which we find no evidence in the spectrum.

Considering only k=0 → +5 and k=+5 → 0, we compare the predicted splitting patterns to what is observed experimentally. It is important to note that the group theoretical treatment rigorously predicts there should be 8 separate subbands for any of the singly degenerate → singly degenerate transitions; however, the separation between the 3rd and 4th levels is so small that only a very large bifurcation tunneling splitting would result in the levels separating in the spectrum. The 5th and 6th levels are also closely spaced and not expected to be resolved. In order for the experiment to discern such a splitting, the separation needs to be larger than ca. twice the resolution of 30MHz. That corresponds to a bifurcation magnitude of ~0.154 cm^{-1}, which is 3x larger than the separation of the observed subbands. Thus we expect these closely spaced levels to remain unresolved in the spectrum, similar to what Brown et al observed for $(H_2O)_5$ at 90 cm^{-1} [71]. The exact spacing between these levels predicted by theory can be ascertained from Table 8 of Wales and Walsh [66].

Analysis of the group theoretical treatment of Wales and Walsh shows that there are only two possible bifurcation patterns, distinguished only by opposite intensity variations [66]. For the mechanism B, k=0 → +5 and k=+5 → 0 have the same pattern,

which is also shared by the mechanism A, k=0 → +5, in which the expected ratio of bands from low to high frequency is, 1:10:38:76:76:31. The alternative splitting pattern for mechanism A, k=+5 → 0 is, 31:76:76:38:10:1. Determining the intensity ratio of the observed bands is difficult due to the intensity fluctuations of the laser and the large laser gaps which limit spectral coverage; however we do find a good qualitative agreement between the experimental pattern and that expected from a mechanism A, k=+5 → 0 transition as shown in Figure 15. Based on this assignment, we can extract a value for the bifurcation tunneling of the excited state, 0.06283 cm^{-1}, confirming that the $3^{rd}/4^{th}$ and $5^{th}/6^{th}$ levels would not be resolved separately.

More evidence supporting this assignment can be obtained from comparison to the results of Harker et al, who observed a parallel-type transition at 27.3 cm^{-1} that was assigned to originate in k = +5 of the lowest energy pseudorotational manifold of $(D_2O)_5$ [73]. The authors fit their data to an oblate top model without the D_K term, but we can still compare the B" and D_J" values, since they have no K dependence. Harker et al report a B" value of 1750.870 MHz and a D_J" value of 0.007 MHz, compared to our values of 1750.070 MHz and 0.008 MHz respectively [73]. These values are in excellent agreement with each other suggesting that the lower state is indeed k = +5 of the lowest energy pseudorotational manifold, which would be expected given the rotational cooling effective in the supersonic expansion. Our analysis of the intensity pattern of the 6 observed subbands can then be used to confirm that the excited state is indeed k = 0.

Discussion

Structural Characterization

This study represents the first time a perpendicular-type transition has been measured for the water pentamer (any isotopomer), and it allows us to extract an accurate measure of the C rotational constants. We average the C values from the 6 subbands to give a value of 906.886 MHz for the ground state and 941.211 MHz for the excited state. The ground state value can be compared to that obtained from *ab initio* calculations for $(D_2O)_5$. To our knowledge, the only existing calculations for the $(D_2O)_5$ species are those from Graf et al at the MP2/aug-cc-pVDZ level of theory [76], who obtain a C rotational constant of 922.0 MHz and a B constant value of 1790.9 MHz in the ground state; both of which are in good agreement with our observed values of 906.886 MHz and 1750.070 MHz [76].

Previous water pentamer experiments from Harker et al, Liu et al, and Cruzan et al provide more evidence for the true water pentamer structure [69,70,72,73]. Harker et al recorded 5 low frequency torsional $(D_2O)_5$ parallel subbands which are supplemented by the one parallel $(D_2O)_5$ subband observed by Cruzan et al [72,73], and one other parallel $(D_2O)_5$ subband observed by Liu et al all [69,70]. These studies found ground state B values in the narrow range of 1750.817 – 1751.976 MHz, which yield excellent agreement with our present results. We do notice a marked contrast between our results, and those previously reported with respect to the *change* in rotational constants between ground and excited states, however. The previous rotational constant changes were at most a few MHz, whereas in our present study we report changes of tens of MHz. This dramatic increase is due to the vibrational nature of the excited state; i.e. all previous observations

were due to torsional vibrational modes, whereas the present study observes a libration, which engenders an increased intermolecular motion, as we have previously observed [1,5].

For completeness, Brown et al observed a parallel transition for the $(H_2O)_5$ isotopomer, which yielded a ground state B value of 1992.467 MHz [71]. This value can be compared to the calculations of Graf et al, which predict a value of 2037.0 MHz for the ground state [76].

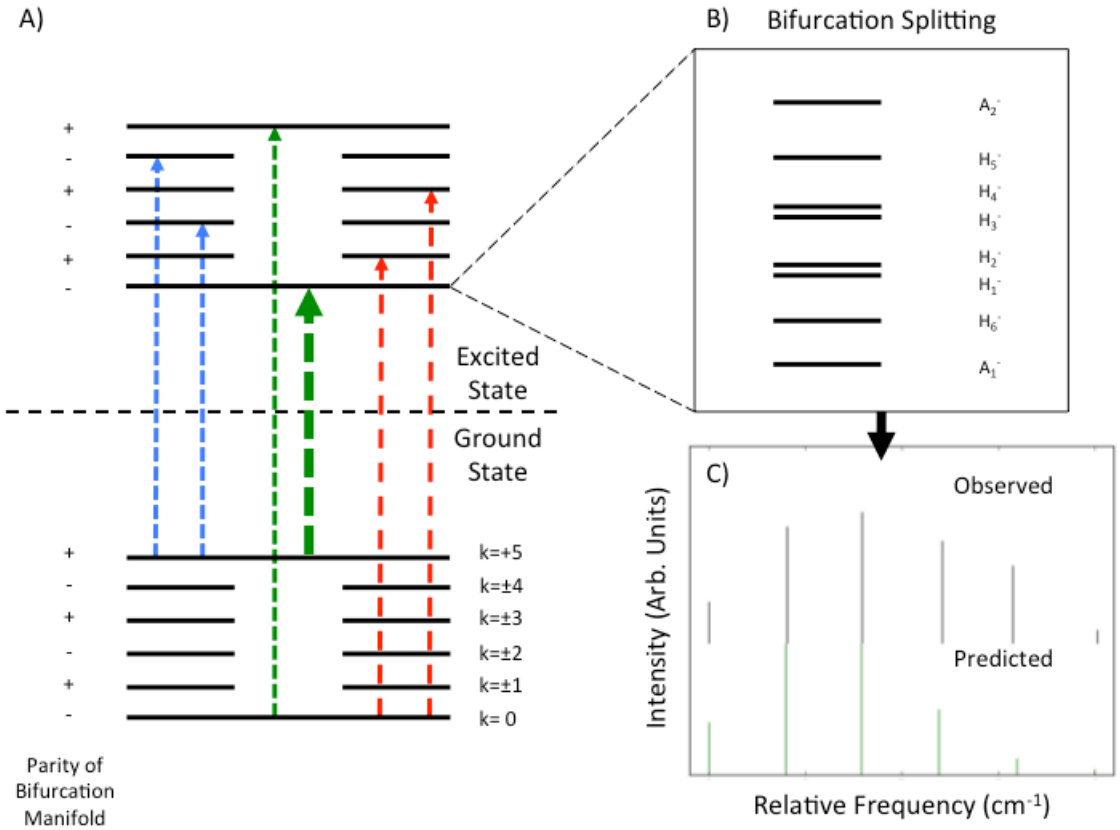

Figure 15: A) The pseudorotational manifold for the ground and a general excited state of the water pentamer. The parity, with respect to the G_{320} inversion operator, is shown to the left of the levels. Blue lines represent possible transitions originating in k=+5 and terminating in a doubly degenerate level. Red lines represent transitions originating in k=0 and terminating in a doubly degenerate level. Green lines show the possible transitions between two singly degenerate levels. The bolded line shows the transition observed in this study. **B)** The bifurcation splitting pattern for the k=0 level, assuming Mechanism A is the bifurcation motion. The labels are for the irreducible representations of G_{320}. The line spacing is not to scale; for the actual spacing see Table 8 of Wales and Walsh [66]. **C)** Comparison of the observed and predicted subband patterns . The first line for the experiment is fixed to be in the same relative position as the first predicted transition. The intensities are scaled such that the most intense transition in both the observed and predicted spectrum has a magnitude of 1.

Vibrational Assignment

The combination of the large number of vibrational modes of the water pentamer (24 intermolecular modes) combined with the inaccuracy of harmonic calculations makes it difficult to establish the exact vibrational mode observed in this study. Nonetheless, we can make some general comparisons with recent harmonic calculations for the $(D_2O)_2$ species. Again, Graf et al have calculated the harmonic intermolecular frequencies and found 10 modes between 300.8 and 712.4 cm^{-1} assigned to librational vibrations [76]. Noting that harmonic calculations overestimate the vibrational frequency, we find two candidate librations, predicted at 572.2 and 577.4 cm^{-1}. Both of these exhibit significant motions both parallel and perpendicular to the principal axis that would account for the relatively large changes observed for both B and C rotational constants.

The intensity of the 577.4 cm^{-1} band is predicted to be ~7x higher than that of the 572.2 cm^{-1} band [76], making the former assignment more likely. And if we are indeed observing the 577.4 cm^{-1} vibration, the weak, unassigned lines at ~509.5 cm^{-1} would comprise evidence for an R branch of the 572.2 cm^{-1} vibration.

Librational Enhancement in Bifurcation Tunneling

Irrespective of the detailed vibrational assignment, a salient result of this study is the observation of a huge enhancement in bifurcation tunneling rates. We have previously observed a large increase in bifurcation tunneling rates for transitions occurring in the 500 cm^{-1} region for both the H_2O dimer and trimer; ca. 40x and 400x respectively [1,5]. As no experiment has yet quantified bifurcation tunneling for the $(D_2O)_5$ ground state, we cannot yet establish the librational enhancement observed herein as precisely. Cruzan et al determined that there was no observable splitting resulting from bifurcation tunneling at the experimental resolution of 450 kHz[82] for $(D_2O)_5$. Taking that resolution as an upper limit to the tunneling splitting, we would then be observing an enhancement of ca. 4000x. Such a large enhancement attests to a strong coupling between the librational motion and the tunneling pathway, as discussed previously for both the dimer and trimer [1,5]. Irrespective of whether the observed vibration is the 577.4 or 572.2 cm^{-1} mode, both are predicted to have a large component of motion in the plane perpendicular to the principal axis [76]. Comparison with Figure 14 suggests that either bifurcation mechanism similarly exhibits significant motion in that plane.

Bifurcation Mechanism

The proposal of two distinct pentamer bifurcation mechanisms from theory provides an opportunity to establish the actual mechanism responsible for the observed splittings [66,84]. As mentioned above, the only previous experimental observation of bifurcation tunneling in the water pentamer was from Brown et al, who observed splitting for the $(H_2O)_5$ species. Fortunately, predicted splitting *pattern* does not change with isotopic substitution, only the absolute splitting *magnitude* and intensity patterns (from the statistical weights). Therefore, combining the results presented herein with those Brown et al will allow a reliable determination of which proposed mechanism is responsible for the observed spectral splittings [71].

First, it is important to note that both the present results and those of Brown et al are consistent with a VRT transition between two singly degenerate pseudorotational states [71]. As discussed in the Results section, the two distinct patterns predicted from group theory engender a single vibration-rotation transition split into an equally spaced sextet [66]. We again note that there are 8 possible transitions, but due to the near-degeneracy of the 3rd/4th and 5th/6th energy levels, only 6 separate transitions will be resolved in the present experiments. This sextet can have two possible intensity patterns for $(D_2O)_5$, viewed from low to high frequency; 31:76:76:38:10:1(Mechanism A) or 1:10:38:76:76:31(Mechanism B), based exclusively on the spin statistical weights of the energy levels. The analogous patterns for $(H_2O)_5$ are and 1:3:18:54:81:51(Mechanism A) and 51:81:54:18:3:1(Mechanism B).

As elaborated in Results, our observed intensity pattern of 3:9:10:7:5:1 qualitatively agrees with the pattern predicted by mechanism A. The difference can be rationalized in terms of the intensity fluctuations of the laser. Brown et al also reported an equally spaced sextet, but their intensity ratio was not explicitly given [71], although they claimed that their measured intensity pattern agreed with the predicted intensity pattern for Mechanism A for $(H_2O)_5$. As a note, the bifurcation mechanism Brown et al report in Figure 1 of their paper does not correspond to mechanism A.

Based on the above information, we conclude that the bifurcation tunneling mechanism observed experimentally is the predicted mechanism A (Figure 14A), as this is the only mechanism that can account for both intensity patterns. This mechanism was found by Wales and Walsh [66] in *ab initio*, TIP4P, and ASP-W2 calculations and additionally by Gregory and Clary [39] on the ASP-P and ASP-NB surfaces. *It is important to note that the bifurcation mechanism was incorrectly reported by Brown et al as mechanism B* [71]. The similarity of mechanism A to the bifurcation mechanism in the water trimer, in addition to the dramatic increase in splittings observed upon excitation to a librational vibration, suggest that detailed examination of the bifurcation tunneling motion would be a promising route to studying hydrogen bond breaking/formation and the effect of cooperativity in both water clusters and in bulk water phases.

Summary

We have observed 6 perpendicular subbands for the $(D_2O)_5$ isotopomer originating from the pseudorotational k=+5 ground state level and terminating in the k=0 level of a librational vibration, split by bifurcation tunneling, . The magnitude of this bifurcation tunneling splitting was found to be 0.06283 cm^{-1} (1884 MHz), which is at least a 4000x enhancement of this tunneling splitting in the ground state. We have also reported the first experimental measurement of the C rotational constant of the water pentamer, and establish the mechanism for bifurcation tunneling. The dramatic increase in bifurcation tunneling observed upon excitation of the librational vibration establishes the pentamer as the third water cluster displaying such large enhancement in this spectral region. Further study of this librational enhancement will provide further insight into details of the hydrogen bond breaking/formation process and effect of cooperatively in both clusters and bulk water. Recent studies question the origin of the bifurcation splitting, and further examination of these spectral features will require consideration of librational vibrations [85].

Combining the results herein with the previous studies of the H_2O pentamer provides a comprehensive data set spanning both torsional and librational bands of liquid water [69–73]. Additionally, bifurcation tunneling has now been definitively observed in the water dimer [5,36–38], trimer [1,36,41,74], pentamer [69–73], and hexamer [77–80]; but not for the tetramer or octamer [2]. Measurements of water tetramer spectra [82,83] may possibly show bifurcation tunneling, but it appears to be dramatically quenched, relative to the trimer and pentamer.

Terahertz VRT Spectroscopy of the Water Hexamer-d_{12} Prism: Dramatic Enhancement of Bifurcation Tunneling upon Librational Excitation

The full details of this section can be found in: Cole, W.T.S., Farrell, J.D., Sheikh, A.A., Yönder, Ö., Fellers, R.S., Viant, M.R., Wales, D.J., Saykally, R.J., J. Chem. Phys., ***148*** *094301 (2018).*

Introduction

The challenge in developing a general predictive molecular-scale description of water is essentially that of correctly describing its extended and dynamic hydrogen-bonded network [2,28,30,63–65,86–88]. High-resolution spectroscopy of water clusters provides a means of systematically untangling its complexities. In this context, the water hexamer is of particular interest, as it is the smallest cluster exhibiting a 3-D hydrogen bond network [77,87,89–101]. Previous studies have revealed the existence of low energy cage, prism, and book hexamer isomers within a supersonic expansion [77–80,102]. It has been established that the cage isomeric structure is the global minimum energy structure for the all-H_2O isomer [77,103], although the prism isomer lies in close energetic proximity, and is actually the lowest energy isomer for the all D_2O isomer [79,87,103–111]. Additionally, cyclic hexamer clusters have been observed in frozen rare gas matrices [112,113].

The first detailed experimental study of a water hexamer cluster was reported by Liu et al, who observed and characterized Terahertz spectra of the cage isomer in a supersonic expansion [77,78]. More recently, Perez et al observed the cage, prism, and book isomers (in addition to heptamer and nonamer clusters) in a supersonic expansion using broadband microwave spectroscopy [79,114]. This study characterized the ground state structures of these isomers at high resolution and provided critical insight into the associated hydrogen bond network tunneling motions. A subsequent study by Richardson et al provided an in-depth description of the tunneling motions of the prism, revealing a pathway which simultaneously breaks two hydrogen bonds [80]. The structure of the water prism is shown in Figure 16.

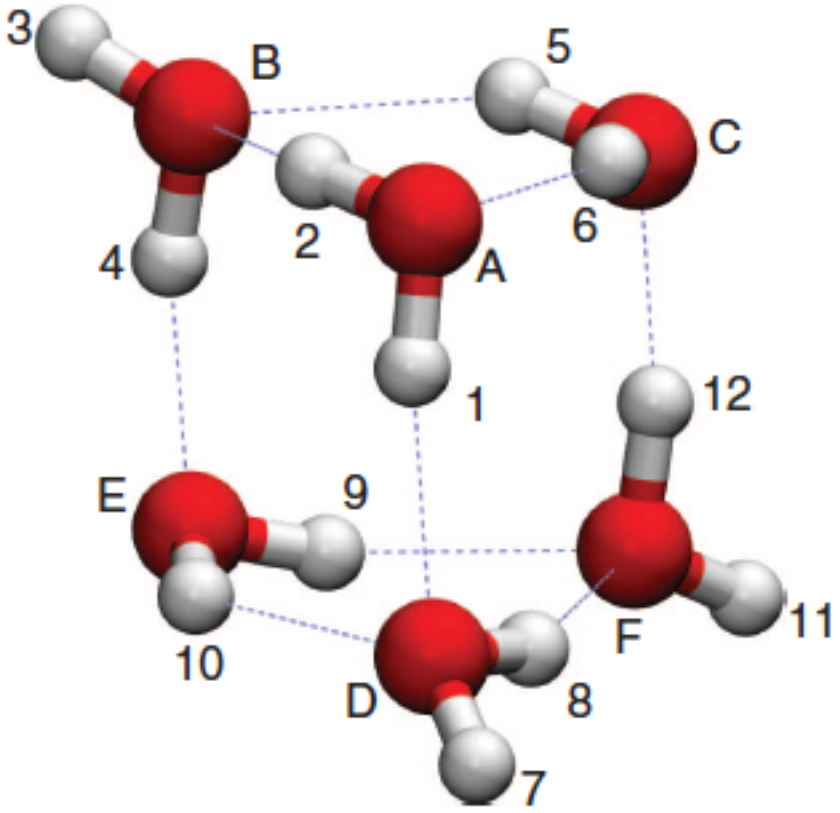

Figure 16: The lowest energy structure of the water hexamer prism. Oxygens are labeled by A – F and hydrogens are labeled 1 – 12. Reproduced with permission from Reference 91 [80].

Here we report the measurement of a parallel vibration-rotation-tunneling (VRT) librational band of a $(D_2O)_6$ cluster centered in the 15 THz (510 cm^{-1}) region. The experimental rotational constants describing the mass distribution in the cluster via the principal moments of inertia extracted from the present VRT spectra agree most closely with those predicted for the prism structure. We find a dramatic librational enhancement in the bifurcation tunneling splittings of the D_2O cluster relative to the ground state, in analogy with other recent cluster studies in this spectral region [1,4,5,41,115,116].

Experimental

Our previous investigations of water dimer, trimer, and pentamer librational motions in the 15 THz region prompted us to search for similar transitions in larger clusters [1,5]. The Berkeley diode laser/supersonic beam spectrometer used in this study has been described in detail elsewhere and only a short description is provided here [47,48].

A helium-cooled spectrometer (Spectra Physics) using lead-salt diodes (Laser Photonics) was used to produce infrared radiation from 509-514 cm^{-1}. The beam was multipassed 18-22 times through a pulsed planar supersonic expansion of a mixture of D_2O and He using a Herriot cell and detected using a helium-cooled (Si:B) photoconductive detector (IR Labs). The supersonic expansion was produced by bubbling pure He gas, with a backing pressure of 1-2 atm through liquid D_2O (Cambridge Labs, 99.96% purity), and then expanding through a 101.6 mm long slit at a repetition rate of 35 Hz into a vacuum chamber maintained at ~200 mTorr by a Roots blower (Edwards 4200) backed by two rotary pumps (E2M 275) [49]. Simultaneously, the fringe spacing of a vacuum-spaced etalon and an OCS reference gas spectra were detected with a liquid He cooled (Cu:Ge) detector (Santa Barbara Research Center) and recorded to enable precise frequency calibration. The observed linewidths of ~ 30-40 MHz full-width half maximum (FWHM) are somewhat larger than the Doppler-limited linewidths extrapolated from earlier experiments using argon expansions. Typical frequency measurement accuracy is 10-20 MHz, limited by both linewidths of the cluster absorptions and laser drift. Spectra were detected in direct absorption using a time-gated phase sensitive signal processing approach [49].

Accessing the 15 THz (500 cm^{-1}) region of the electromagnetic spectrum has generally been notoriously difficult. The spectra reported here required the use of 10 separate laser diodes, each scanned across several modes to cover the specified spectral range. Moreover, large laser gaps are present in the spectra, which causes considerable difficulty in the assignment. Additionally, the spectrum reflects several distinct laser intensity fluctuations across different devices that are apparent in the complete spectra shown in Figure 17. Specifically, between 512.4 cm^{-1} and 513.2 cm^{-1} the laser intensity is enhanced (as was found in a previous study [4]) and between 509.5 cm^{-1} and 510 cm^{-1} the laser intensity is depressed.

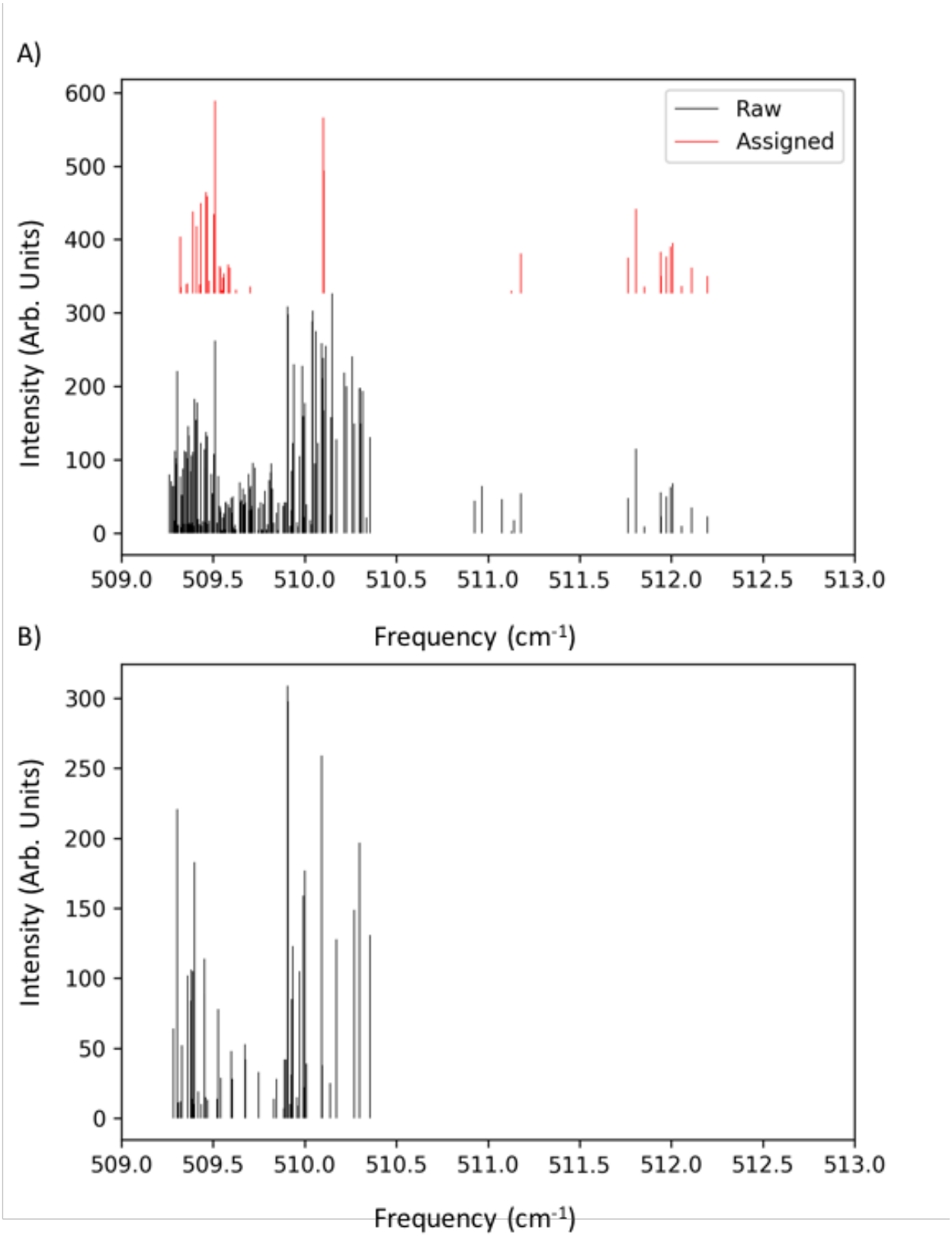

Figure 17: A) All 188 transitions observed in the experimental range examined are shown in black. The 46 remaining unassigned transitions are shown in red. B) Transitions assigned to Subband 3, showing the typical pattern observed in these experiments. Laser gaps prohibited further assignment of the R and P branches.

Results and Analysis

Assignment

We have assigned 142 of the 188 observed transitions in the studied region using the PGOPHER platform [117]. The transitions belong to three distinct a-type ($\Delta K_a=0$) subbands, which are assigned to different tunneling levels of the water hexamer-d_{12} prism isomer. The observed transitions were fit to an S-reduced Watson Hamiltonian. For the assignment, we fixed the ground state constants to those obtained in [116]. Correlation matrices of the fit and a list of all assigned transitions are given in the Supplementary Information.

Anharmonic Excited State Vibrational Calculations

To elucidate the nature of the observed vibration, anharmonic frequencies and rotational constants were calculated by applying generalized second-order vibrational perturbation theory (GVPT2) [118,119] to the second-order Møller–Plesset perturbation theory (MP2) potential energy surface using the Gaussian 09 D.01 package [120]. The geometry of the lowest energy D_2O prism was optimized at the MP2/aug-cc-pVDZ level of theory enforcing 'very tight' convergence criteria, following which a GVPT2 calculation was performed at the same level of theory using the parameters recommended by Temelso and Shields [93]. The Gaussian input file, full list of calculated harmonic and anharmonic frequencies, as well as the rotational constants are listed in the Supplementary Information in Appendix A.

Table 8: Molecular constants for the asymmetric top fit with fixed ground state constants. The uncertainty in the final two digits for each constant is given in parenthesis. The values of the subband origin, A, B, C, and RMS error are given in MHz; all other values are in kHz. Ground state constants were held fixed in the fit, and obtained from Reference [116].

	Fit Constants			
	Subband 1	Subband 2	Subband 3	Ground State
Origin	15277446(17)	15281136(17)	15284328(16)	0
A	1599.33(20)	1601.84(28)	1594.04(24)	1493.9052(12)
B	1257.40(25)	1251.51(56)	1250.01(41)	1218.3566(12)
C	1212.30(26)	1203.86(58)	1214.47(38)	1185.6460(11)
D_K	0.724(15)	-0.466(22)	-0.312(134)	-0.961(63)e-3
D_{JK}	-0.697(11)	0.307(27)	-0.045(20)	1.662(58)e-3
D_J	0.2245(44)	0.0103(87)	0.0476(82)	0.4094(94)e-3
δ_K	0.593(32)	3.005(25)	2.521(97)	-2.92(27)e-3
δ_J	0.0295(15)	0.0140(97)	-0.0664(46)	0.0511(63)e-3
H_K	0.0210(27)	0.1283(20)	0.0769(95)	0
H_{KJ}	-0.0136(30)	-0.1843(30)	-0.1224(14)	0
H_{JK}	-7.7(10)e-4	0.059(12)	0.0452(54)	0
H_J	1.72(31)e-3	-9.1(11)e-4	-2.19(86)e-3	0

RMS (MHz)	39.2	31.0	40.3
Number of Transitions	51	38	53

Fit Analysis

We obtained a good quality fit of the observed transitions; the average RMS of the fit is ~37 MHz as a result of the wavelength accuracy of < 20 MHz and the observed linewidths of 30-40 MHz. We note that the A, B, and C constants of all three bands show good agreement with one another, providing evidence that these bands originate from tunneling sublevels of a common excited state. Additionally, a fit with floating ground state constants yielded good agreement with the observed values from Reference [116], although we have chosen to keep those values fixed in the reported fit.

Tunneling Dynamics

We refer the reader to the recent work of Richardson et al for detailed treatment of the water hexamer prism tunneling dynamics, and instead focus only on the relevant considerations for the fully deuterated cluster [80]. The feasible prism tunneling motions can be described by the complete nuclear permutation inversion (CNPI) subgroup isomorphic to point group D_{2d}. Previous work has shown that the water hexamer prism exhibits two feasible tunneling motions (here we define 'feasible' as "experimentally observed" [35]), which are referred to as P_a and P_g. In CNPI notation, P_a=(A D)(B F)(C E)(1 7)(2 8)(3 11)(4 12)(5 9)(6 10), where the labels correspond to the structure in Figure 1. The motion associated with this element involves a double flip of the free hydrogens, resulting in breaking a single hydrogen bond. Likewise, in CNPI notation, P_g=(A D)(B F)(C E)(1 8 2 7)(3 11)(4 12)(5 9)(6 10) and the motion is described as a double flip accompanied by a bifurcation, which breaks two hydrogen bonds. The character table for this group is given in Table 9.

Table 9: Character table for the point group D_{2d}; group elements correspond to CNPI operations.

D_{2d}	E	$2P_g$	(12)(78)	$2P_a$	2(12)
A_1	1	1	1	1	1
A_2	1	1	1	-1	-1
B_1	1	-1	1	1	-1
B_2	1	-1	1	-1	1
E	2	0	-2	0	0
Γ_{ns}	531441	243	59049	729	177147
Γ_{dip}	3	-1	3	-1	3

The character representation of the nuclear spin wavefunction (Γ_{ns}) and the electric dipole moment (Γ_{dip}) are given at the bottom of Table 9. We can reduce Γ_{ns} to its irreducible representation:

$$118341\ A_1 \oplus 29403\ A_2 \oplus 29646\ B_1 \oplus 117855\ B_2 \oplus 118098\ E.$$

For the fully deuterated hexamer prism, the total spin wavefunction must transform as A_1 which leads to the spin statistical weights: A_1:A_2:B_1:B_2:E of 487:121:122:485:486. The irreducible representation of the electric dipole moment is $A_1 \oplus 2B_2$ and for a-type (ΔK_a=0) transitions, the dipole transforms as B_2. Thus, the expected selection rules are A_1 <-> B_2, A_2 <-> B_1, and E <-> E. These selection rules lead to a "doublet of triplets" pattern with a central doublet, as shown in Figure 18. Richardson et al established that the energy level pattern of the hexamer prism is represented by the eigenvalue of the tunneling matrix shown in Figure 18A [80].

A) Tunneling Hamiltonian

$$\hat{H}=\begin{vmatrix} v & h_g & 0 & h_g & h_a & 0 & 0 & 0 \\ h_g & v & h_g & 0 & 0 & h_a & 0 & 0 \\ 0 & h_g & v & h_g & 0 & 0 & h_a & 0 \\ h_g & 0 & h_g & v & 0 & 0 & 0 & h_a \\ h_a & 0 & 0 & 0 & v & h_g & 0 & h_g \\ 0 & h_a & 0 & 0 & h_g & v & h_g & 0 \\ 0 & 0 & h_a & 0 & 0 & h_g & v & h_g \\ 0 & 0 & 0 & h_a & h_g & 0 & h_g & v \end{vmatrix}$$

B) Energy Level Diagram

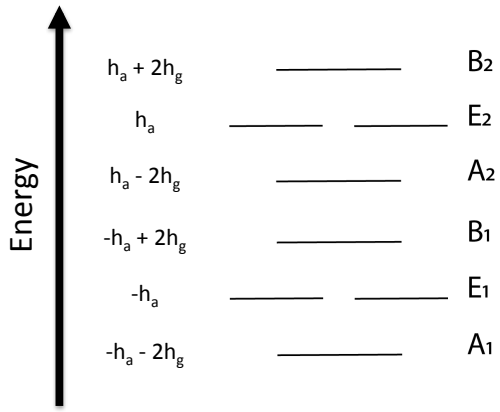

C) Transitions Energy Levels

$B_2 \rightarrow A_1 : E(J,K) - h_a' - h_a'' - 2h_g' - 2h_g''$

$E_2 \rightarrow E_1 : E(J,K) - h_a' - h_a''$

$A_2 \rightarrow B_1 : E(J,K) - h_a' - h_a'' + 2h_g' + 2h_g''$

$E_2 \rightarrow E_2 : E(J,K) + h_a' - h_a''$

$E_1 \rightarrow E_1 : E(J,K) - h_a' + h_a''$

$B_1 \rightarrow A_1 : E(J,K) + h_a' + h_a'' - 2h_g' - 2h_g''$

$E_1 \rightarrow E_2 : E(J,K) + h_a' + h_a''$

$A_1 \rightarrow B_2 : E(J,K) + h_a' + h_a'' + 2h_g' + 2h_g''$

D) Transition Energy Diagram

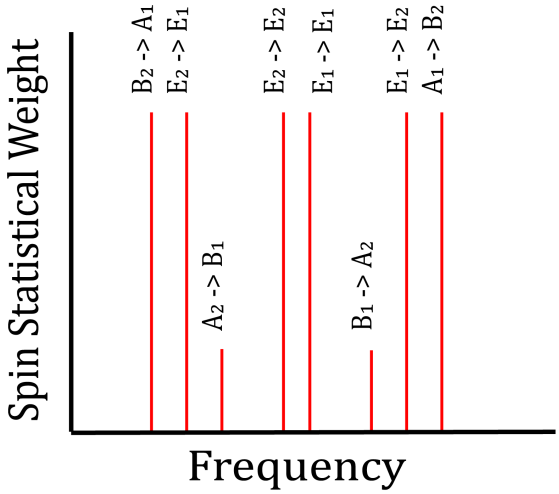

Figure 18: **A)** Tunneling Hamiltonian of the water hexamer prism. The term v represents the band origin. The terms h_g and h_a represent the tunneling splittings associated with group elements P_g and P_a, respectively. **B)** Energy level diagram resulting from the two feasible tunneling motions present in the water prism hexamer (n.b. the subscript on the E symmetry labels merely corresponds to whether the level belongs to the upper (2) or lower (1) triplet). **C)** Energies of the selection rule-allowed tunneling transitions for the prism hexamer. E(J, K) represents the typical rigid rotor energy level.(n.b. E_1 and E_2 energy levels refer to whether the level belongs to the upper or lower energy triplet). **C)** Energy level diagram depicting the level ordering shown in B of this figure. The diagram assumes all tunneling elements are positive and $h_g' < h_g''$, which was an arbitrary choice for the figure.

Based on these considerations, we assign the $B_2 \rightarrow A_1$, $E_2 \rightarrow E_1$, and $A_2 \rightarrow B_1$ transitions to subbands 1, 2, and 3, respectively. This assignment is based on the equal spacing between three subbands and the intensity ratio of 1:1:0.85. While this intensity ratio does not agree quantitatively with the expected ratio (based on spin statistics above), given the large intensity fluctuations of the lasers used, we consider this assignment as the most likely of those possible under parallel selection rules. Based on this assignment, we can estimate the tunneling matrix element, h_g. The separation between subband 1 and subband 2 corresponds to the quantity $2h_g' + 2h_g''$, wherein the prime and double prime represent the values in the excited and ground state, respectively. The separation between subband 2 and 3 corresponds to the same quantity. Given the measured values in the ground state (which are <1 MHz), we can explicitly calculate the value for the excited state (assuming these transitions originate in the ground vibrational state). Based on our fitted values of the band origins, we find the average value of h_g' to be ~1720 MHz, which corresponds to a ca. 1000x enhancement of that tunneling splitting relative to the value for the ground state. This enhancement would be consistent with the enhancement of tunneling splitting observed for the water dimer, trimer, and pentamer upon excitation of a single quantum of 15 Thz librational vibration. We note that using the intensity ratio to assign the observed subbands to the lower triplet is in some ways arbitrary due to the power fluctuations of the diode laser. It can be argued that the subbands could be assigned to the upper triplet just as easily; however, that assignment does not change the analysis of the tunneling enhancement, as both triplets are symmetric. Further experiments are needed to definitively establish which triplet these subbands represent.

Discussion

Vibrational Origin

These experiments were conducted in a He supersonic expansion, which cools the rotational temperature to approximately 10 K, and the vibrational temperature to ca. 100 K. The most likely vibrational origin of the transitions is the ground state. Based on the calculated anharmonic vibrational frequencies and assuming that the transitions observed originate from the absolute ground state, we attempted to assign a vibrational mode to the experimental transitions; however, we note several interesting observations. We find two likely candidates for anharmonic vibrational modes with transition frequencies from the absolute ground state of 505.693 and 539.359 cm^{-1}, both of which lie close to the observed average band origin of 509.7183 cm^{-1}. However, we stress that this experimental band origin corresponds to the average origin of individual tunneling bands and is not the true vibrational band origin. In Table 10 we show a comparison between the observed rotational constants and the predicted values for the 4 closest vibrational modes.

Table 10: Comparison of observed and calculated values of D_2O hexamer prism rotational constants. All values are reported in cm^{-1}.

	Origin	A	B	C	ΔA	ΔB	ΔC
Observed	509.718	0.049831	0.041795	0.040368	0.003486	0.001155	0.000819
Calculated	635.026	0.049008	0.040504	0.039004	-0.000141	-0.000202	-0.000125
	539.359	0.049009	0.040609	0.038967	-0.000140	-0.000097	-0.000162
	505.693	0.049097	0.040533	0.039039	-0.000052	-0.000173	-0.000090
	426.105	0.049251	0.040520	0.039026	0.000102	-0.000186	-0.000103

From the table we can see that the observed values are all larger in magnitude that than the predicted values. The most striking observation in the calculations is that the calculated values of ΔM (where M is A, B, or C) are opposite in sign and about an order of magnitude smaller than what is observed experimentally. Some that disagreement can be attributed to the fact that there is are large perturbations to the excited state, shown by the large higher order terms in the fit results, indicating and very "floppy" excited state. We have previously observed dramatic fluctuation of the centrifugal distortion constants in this experimental region [1,4,5]. Another possibility, would be that the ground state of these transitions is not actually the absolute ground state of this cluster, but rather a "hot band". While this is unlikely, given the strong cooling in a supersonic expansion; there are several vibrational states located within 10 cm^{-1} of the absolute ground state. However, further experimental studies and calculation will be needed to determine a definitive resolution of this disagreement. We also stress that these values represent only the lower triplet of the tunneling pattern, which should be fairly representative of the excited state.

Librational Enhancement of Tunneling

We have previously studied the water dimer, trimer, and pentamer in the 15 Thz librational region, with the most salient observation being the dramatic enhancement of the tunneling splittings in these clusters [1,4,5]. We observe a similar effect here; however, we can only determine the enhancement for the h_g pathway. As described by Richardson et al [80], the h_g pathway motions is characterized by a double flip accompanied by a bifurcation, which involves the breaking of two hydrogen bonds. Studies of the water dimer, trimer, and pentamer tunneling in the 500 cm^{-1}region involve motions which only break a single hydrogen bond [1,4,5]. We observe a 1000x enhancement relative to the observed ground state tunneling for the $(D_2O)_6$ prism from microwave experiments [80]. This observation indicates that the observed enhancement in the librational region does not seem to be influenced by the number of hydrogen bonds broken in the tunneling pathway. Additionally, the reported enhancement is with respect to the observed tunneling in the $(H_2O)_6$ prism reported by Richardson et al [80]. As observations of the tunneling in the fully deuterated ground state do not presently exist, an accurate measure of the enhancement cannot be obtained; however, due to the larger mass-weighted path

for the deuterated species, we can consider the observed 1000x enhancement as a lower bound.

Due to the absence of the higher energy triplet (Figure 18C) in our measured spectra, we cannot presently characterize the h_a tunneling pathway in this excited librational state. The absence of this triplet is most likely a result of the large laser gaps present in the experiment, coupled with the fact that the observed transitions occur near the edge of the available laser coverage.

The results reported here are significant, as the water hexamer represents a transition of the minimum energy structure of water clusters from ring-like forms to a fully 3-D structure. The water prism tunneling motion has been predicted to potentially describe the motions of water in interfacial and confined environments; hence, the results presented here indicate that excitation of librational vibrations have a significant impact on the hydrogen bond dynamics in these macroscopic environments.

Conclusions

We have measured 3 a-type subbands belonging to a common librational vibration of the $(D_2O)_6$ prism cluster. Assigning the transitions to tunneling sublevels allows us to extract a value of ~1720 MHz for the h_g tunneling motion, representing a ca. 1000x enhancement of the tunneling splitting, relative to the ground state splitting observed for the $(H_2O)_6$ cluster. This enhancement is consistent with the dramatic tunneling enhancement observed previously for the water dimer, trimer, and pentamer in the same (15 THz) experimental region.

From comparison to theoretical calculations, we find the observed change in the all rotational constants to be dramatically larger than predicted. This large change indicates a very "floppy" excited state, which would be consistent with the large tunneling splittings observed and the breaking of one or two hydrogen bonds in the tunneling pathway.

Terahertz VRT Spectroscopy of the Water Hexamer-h12 Cage: Dramatic Libration-Induced Enhancement of Hydrogen Bond Tunneling Dynamics

The full details of this section can be found in: Cole, W.T.S., Yönder, Ö., Sheikh, A.A., Fellers, R.S., Viant, M.R., Saykally, R.J., Farrell, J.D., Wales, D.J., J. Phys. Chem. A., ***122*** *(37) 7421 (2018).*

Introduction

The challenge in developing a predictive molecular-scale description of water is essentially that of correctly describing its extended and highly dynamic hydrogen-bonded network [2,28,30,86–88]. High-resolution spectroscopy of water clusters provides a means of systematically untangling its complexities. In this context, the water hexamer is of particular interest, as it is the smallest cluster exhibiting a 3-D hydrogen bond network [77,87,89–101]. Previous studies have revealed the existence of low energy cage, prism, and book hexamer isomers produced in a supersonic expansion [77,79,80,102,121]. It has been established that the cage isomer is the global minimum energy structure [77,103], although the prism lies in close energetic proximity [79,87,104–111]. Additionally, cyclic hexamer clusters have been observed in frozen rare gas matrices [112,113].

The first detailed experimental study of a water hexamer cluster was reported in 1996 by Liu et al, who observed and characterized the cage isomer in a supersonic expansion [77,121]. From those experiments, the cage structure was determined, as shown in Figure 19, along with the "feasible" tunneling motions of the cluster. Liu determined that the tunneling splitting of the cage cluster can be described by the molecular symmetry group G_4, comprising three "feasible" tunneling motions. Two tunneling motions, $ß_1$ and $ß_2$, are described by a switching of the hydrogens of the two single donor- single acceptor (SDA) hydrogen bonded monomers. The third pathway, $ß_3$, is described as the simultaneous exchange of the hydrogens of both doubly hydrogen bonded monomers.

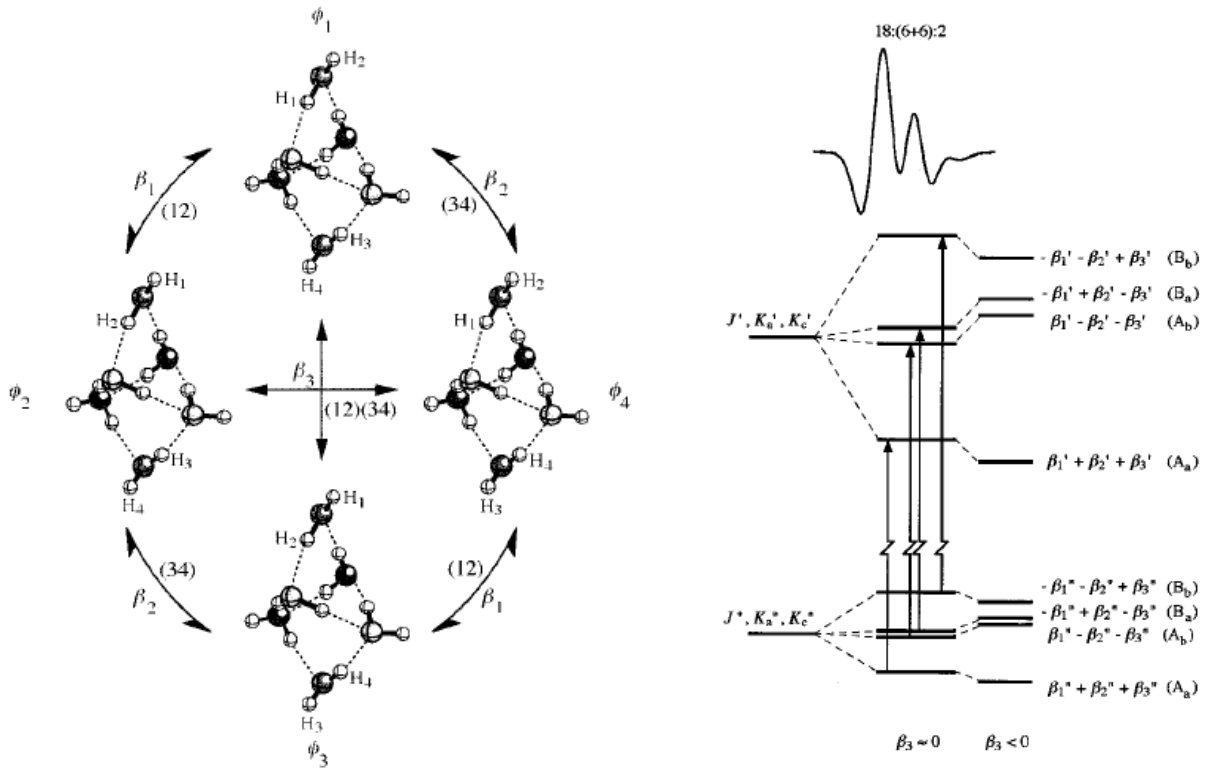

Figure 19: (Left) The structure of the water cage hexamer along with the "feasible" tunneling motions. The labels in parentheses correspond to the group elements of the molecular symmetry group, G_4. (Right) The expected spectral pattern caused by the tunneling of the cluster system. Liu et al observed that the splitting between the $A_b \rightarrow A_b$ and $B_a \rightarrow B_a$ was below the experimental resolution of the experiment indicating that the magnitudes of $ß_1$ and $ß_2$ are quite similar**. Reproduced with permission from Ref. 9.**

More recently, Perez et al observed the cage, prism, and book isomer (in addition to heptamer and nonamer clusters) in a supersonic expansion using broadband microwave spectroscopy [79,80,122]. This study characterized the ground state structures of these isomers at high resolution and provided critical insight into the associated hydrogen bond network tunneling motions.

Most recently, we reported the measurement and analysis of 142 VRT transitions of the fully deuterated hexamer prism in the 15 THz librational band region, which revealed a thousand-fold enhancement in the bifurcation tunneling splitting upon single quantum excitation of this librational vibration[40]. Here, we report the assignment of 176 VRT transitions belonging to four a-type ($\Delta K_a=0$) librational subbands originating from the $(H_2O)_6$ cage structure near 520 cm^{-1}. The tunneling splittings in the excited vibrational state also show a dramatic enhancement, consistent with our previous results for the hexamer-d6, as well as for the water dimer, trimer, and pentamer clusters in this 15 THz librational band region [1,3–5].

Experimental

Our previous investigations of water dimer, trimer, and pentamer librational motions in the 15 THz region prompted us to search for similar transitions in larger clusters [1]. The Berkeley diode laser/supersonic beam spectrometer used in this study has been described in detail elsewhere and only a short description is provided here [47,48].

A helium-cooled spectrometer (Spectra Physics) using lead-salt diodes (Laser Photonics) was used to produce infrared radiation from 515-528 cm^{-1}. The beam was multipassed 18-22 times through a pulsed planar supersonic expansion of a mixture of H_2O and He using a Herriot cell and detected using a helium-cooled (Si:B) photoconductive detector (IR Labs). The supersonic expansion was produced by bubbling pure He gas, with a backing pressure of 1-2 atm through liquid H_2O and then expanding through a 101.6 mm long slit at a repetition rate of 35 Hz into a vacuum chamber maintained at ~200mTorr by a Roots blower (Edwards 4200) backed by two rotary pumps (E2M 275) [49]. The nominal rotational temperature of the expansion is 4-10K. Simultaneously, the fringe spacing of a vacuum-spaced etalon and an OCS reference gas spectra were detected with a liquid He cooled (Cu:Ge) detector (Santa Barbara Research Center) and recorded to enable precise frequency calibration. The observed linewidths of ~ 30-40 MHz full-width half maximum (FWHM) are somewhat larger than the Doppler-limited linewidths extrapolated from earlier experiments using argon expansions. Typical frequency measurement accuracy is 10-20 MHz, limited by both linewidths of the cluster absorptions and laser drift. Spectra were detected in direct absorption using a time-gated phase sensitive signal processing approach.

Accessing the 15 THz (500 cm^{-1}) region of the electromagnetic spectrum has generally been notoriously difficult. The spectra reported here required the use of 10 separate laser diodes, each scanned across several modes to cover the specified spectral range. Moreover, large laser gaps are present in the spectra, which causes considerable difficulty in the assignment. The laser diodes also exhibited intensity fluctuations, which renders the intensities quite arbitrary.

Results

Experimental Assignment

We have assigned 176 of 364 precisely measured transitions in the 515-528 cm^{-1} region to the $(H_2O)_6$ cage cluster. The transitions belong to 4 a-type ($\Delta K_a=0$) type subbands which are determined to originate from tunneling splitting of the rigid rotor energy levels. The transitions were fit to a standard S-reduced Watson Hamiltonian energy level expression using the PGOPHER platform [117,123]. Fixed ground state constants were obtained from the work of Liu et al and Perez et al [79,121] for which we assume the lower intermolecular vibrational state to be the ground state, consistent with the low temperature of the supersonic expansion. The fitted constants for the four measured subbands are given in Table 11. Correlation matrices of the fit and a list of all assigned transitions are given in the Supplementary Information for this article. Figure 20 shows transitions assigned to subband 1, in addition to all observed transitions.

Anharmonic Excited State Vibrational Calculations

To elucidate the nature of the observed vibration, anharmonic frequencies and rotational constants were calculated by applying generalized second-order vibrational perturbation theory (GVPT2)[118,119] to the second-order Moller-Plesset (MP2) perturbation theory potential energy surface using Gaussian 09 D.01 package [120]. The geometry of the lowest energy H_2O cage was optimized at the MP2/aug-cc-pVDZ level of theory, enforcing "very tight" convergence criteria, following which a GVPT2 calculation was performed at the same level of theory using the parameters recommended by Temelso and Shields [93]. The Gaussian input file, the full list of calculated harmonic and anharmonic frequencies, and the rotational constants are listed in the Supplementary Information.

Table 11: Fitted constants for assigned transitions. All values are given in MHz. The uncertainties in the last two significant digits are shown in parentheses. Number of transitions per subband and RMS of the fits are shown below. Values for the ground state are taken from Liu et al and Perez et al [79,121].

	Subband 1	Subband 2	Subband 3	Subband 4	Ground State[a]
Origin	15693333.2(14)	15698512.9(16)	15703420(10)	15708936.3(11)	NA
A	2060.18(88)	2057.62(24)	2058.97(25)	2059.78(84)	2162.12(13)
B	1121.28(139)	1124.67(17)	1121.06(10)	1121.41(78)	1129.07(05)
C	1060.76(13)	1058.67(20)	1060.38(11)	1060.03(68)	1066.88(05)
D_K[b]	-0.039(37)	-0.032(79)	0.022(56)	-0.037(31)	0.0083(15)
D_{JK}	0.020(30)	-0.120(71)	-0.032(29)	0.012(24)	-0.00221(89)
D_J	0.010(10)	0.051(25)	5.0(85)e-3	3.3(62)e-3	0[#]
Δ_K	-1(20)e-4	3.5(36)e-3	-7.8(89)e-4	-2.20(43)e-3	-1.43(46)e-4
Δ_J	-1.5(77)e-3	-0.020(11)	-1.9(24)e-3	-2.4(11)e-3	4.28(92)e-4
H_K	-7.8(18)e-5	-5.2(11)e-3	8.5(36)e-4	-3.3(27)e-4	0[#]
H_{KJ}	-2.0(45)e-4	5.0(18)e-3	-7.3(53)e-4	2.0(14)e-4	-5.36(61)e-5
H_{JK}	1.7(24)e-4	-2.18(82)e-3	9.0(12)e-5	-2.9(83)e-5	5.7(18)e-6
H_J	2.6(45)e-5	4.0(16)e-4	3.0(23)e-7	3.8(18)e-6	0[#]
Number of Transitions	53	34	38	51	
RMS	22.8	16.5	21.5	26.4	

a) **Ground state constants taken from Liu et al and Perez et al [79,121]**

b) **Description of the fit constants can be found in references 21 and 22.**

#) Constants not include in fit

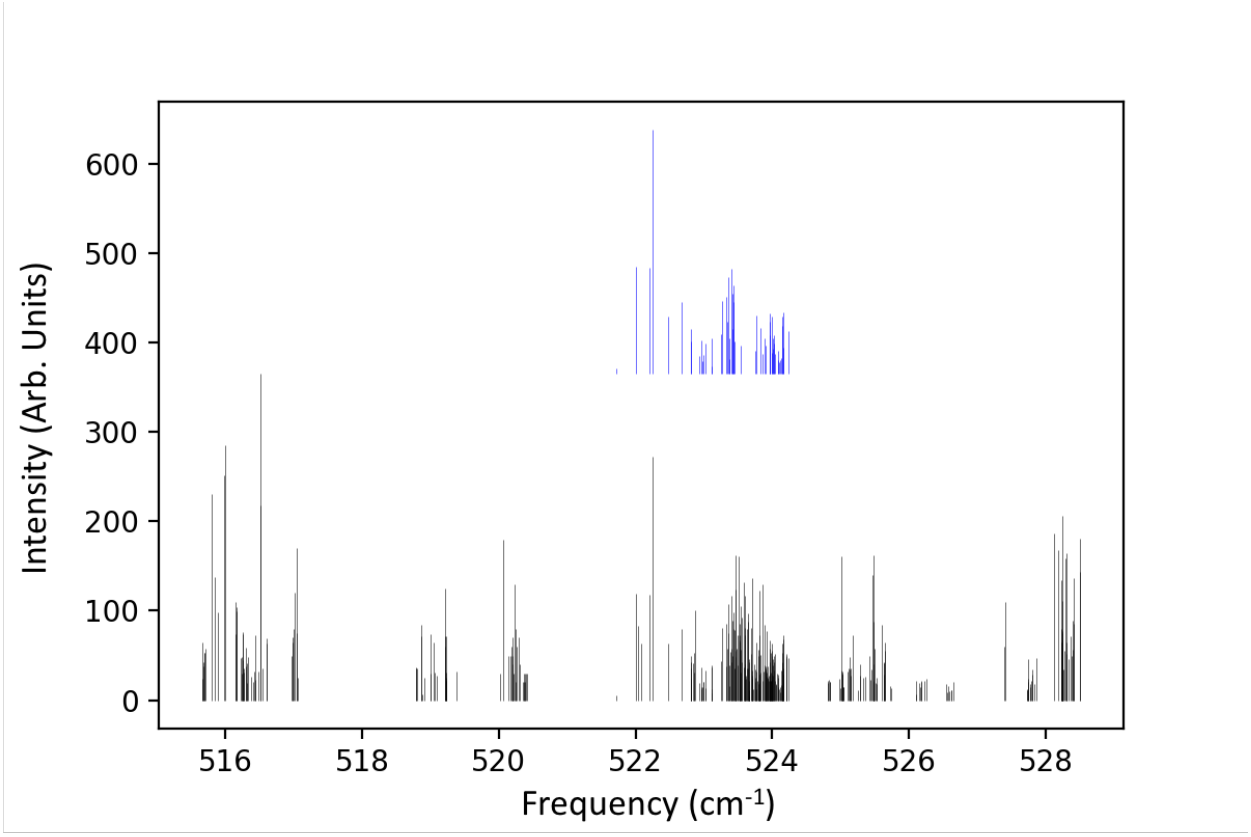

Figure 20: Stick spectrum of all observed transitions is shown in black. Transitions assigned to Subband 1 are shown in blue. The assignment was complicated by large laser gaps, which are apparent across the experimental range.

Fit Analysis

We obtained a high quality fit with an average RMS of 21.8 MHz, which is below the observed linewidth of 30-40 MHz and on the order of the frequency accuracy of the experiment (~20 MHz). The similarity of the rotational constants for the 4 assigned subbands' implies that the transitions originate from a common vibrational state. Additionally, we report the ground state constants from Liu et al [121], which show good agreement with those recently observed by Perez et al [79].

Subband Tunneling Assignment

From Figure 19 we see that the observation of 4 subbands fits with the predicted tunneling pattern of the cage clusters. This pattern is produced by 3 tunneling motions, $ß_1$, $ß_2$, and $ß_3$, with the first two pathways corresponding to permutation of the hydrogens of one of the single donor, single accepter (SDA) water monomers and $ß_3$ is the simultaneous permutation of the hydrogens of both SDA monomers. The predicted spacings between the 4 theoretical subbands are given in Equations 1-3:

$$\Delta(B_b - B_a) = 2\left[-ß_2' + ß_2'' + ß_3' - ß_3''\right] \quad (1)$$

$$\Delta(B_a - A_b) = 2\left[-ß_1' + ß_2' + ß_1'' - ß_2''\right] \quad (2)$$

$$\Delta(A_b - A_a) = 2\left[-ß_2' + ß_2'' - ß_3' + ß_3''\right] \quad (3)$$

Liu et al previously found the magnitude of $ß_3$ to be below experimental resolution in lower energy transitions, as a result of the need to simultaneously break and reform two hydrogen bonds. Also, Liu et al found the relative magnitude of $ß_1$ and $ß_2$ to be nearly identical, resulting in the predicted quartet collapsing to a triplet.

Spin statistics predict the A_a:A_b:B_a:B_b intensity ratio to be 18:6:6:2; but due to laser intensity fluctuations and the large laser gaps, we find an experimental intensity ratio for subbands 1:2:3:4 of 40:55:36:38, which we do not consider realistic due to the above reasons. The four subbands are about equally spaced, with the values of Δ(4-3), Δ(3-2), and Δ(2-1) of 5516.3, 4907.1, and 5179.7 MHz, respectively. The middle two subbands are closer together, and the quartet is asymmetric, which would be expected if $ß_3$ was non-negligible (see Figure 19). It is clear, regardless of the assignment, that the magnitudes of the splitting are greatly enhanced relative to the lower energy states previously measured [77,121]. Hence, we will assume the ground state splittings as being much smaller than the excited state values, which allows us to ignore them and obtain an estimate of the enhanced excited state values. An assumption also has to be made as to whether subband 1 is A_a or B_b, but this only affects the sign of the $ß_3$ term; we arbitrarily assign subband 1 to B_b symmetry, as that makes all of the tunneling motions positive in sign.

Thus, with the assignment of subbands 1/2/3/4 as $B_b/B_a/A_b/A_a$ and assuming $ß_1$", $ß_2$", and $ß_3$" to be ~0, from Equations 1-3 we obtain $ß_1$'= 5127.55 MHz, $ß_2$'= 2674 MHz, and $ß_3$'= 84.15 MHz. This analysis yields several insights; first, the values for $ß_1$ and $ß_2$ are different by nearly a factor of two. This observation would indicate that the local

environments of the two SDA monomers are no longer identical in the excited state. We also see that all of the tunneling motions are indeed greatly(by $>10^3$) enhanced relative to the ground state values, which were previously observed to be ca. 1 MHz [77,121]. This is in keeping with previous observations in this experimental range [1,3–5,28].

Discussion

Vibrational Origin

Since the rotational temperatures of a He supersonic expansion are ~10K, whereas the vibrational temperatures can be somewhat higher, it is reasonable to assume that the observed transitions originate from the vibrational ground state. Upon inspection of the calculated anharmonic vibrational frequencies, we find that there are 3 modes predicted at 497.903, 516.356, and 574.222 cm^{-1}, which lie close to the average band origin of 523.731 cm^{-1}. The 3 bands at 497.903, 516.356, and 574.222 cm^{-1} have the calculated values of ΔA: -10.2, -10.6, and -3.7 MHz, respectively. Our observed value of ΔA is -103.0, nearly an order of magnitude greater than the calculated results. This is similar to our recent results for the fully deuterated water hexamer prism[3] in the same experimental range. This provides more evidence that the intermolecular vibrations of clusters in the 500 cm^{-1} region deviate significantly from the predictions for "semi-rigid" clusters [2–5,88]. Further investigation of this experimental region by theory is warranted.

From the observed changes in rotational constants, we can say that the vibration exhibits significant motion about the A-principal axis, which connects the two SDA water monomers (Figure 19). Any motion about that axis will engender changes in the local environment of those monomers, which, in turn, are expected to affect the barriers of tunneling motions. The higher-order constants of the fit also show an increase in magnitude relative to the ground state, which is consistent with the vibrational motions of a "floppy" cluster molecule.

Librational Tunneling Enhancement

While our analysis of the excited state tunneling dynamics is clearly subject to several assumptions, some observations are significant, viz. the tunneling motions which break/reform the hydrogen bonds are dramatically enhanced relative to the ground state, similar to our previous results for the water dimer, trimer, pentamer, and prism hexamer in this experimental range [1,3–5]. Definitive determinations of the ground state tunneling splittings have not, to our knowledge, been made experimentally, but the earlier observations of Liu et al showed that $(-ß_2'+ß_2'') \sim 0.9$ MHz for an intermolecular vibration near 83 cm^{-1}, and likewise $|ß_3'-ß_3''| < 25$kHz. We find ca. 3 orders of magnitude enhancement for all three tunneling motions, subject to our assumption that the ground state tunneling splittings are negligible. This $\sim 10^3$ enhancement is greater than that observed for the water dimer (40x) and trimer (100x), but similar to that for the pentamer and prism hexamer [1,3–5].

The most interesting observation of this study is this striking libration-induced enhancement in the tunneling splittings, and the finding that $ß_1$ and $ß_2$ are no longer

approximately equal, indicating an asymmetric vibration with respect to the two SDA monomers. While this is supported by the large change in rotational constant A, it would be enlightening to characterize the actual vibrational motion associated with this transition. However, it should be noted that the large observed tunneling splittings combined with the large changes in rotational constants indicates the deviation from a semi-rigid cluster to a more floppy (non-rigid) structure, which provides additional complications for the theory.

Conclusions

In summary, we have assigned 176 transitions to the cage isomer of the H_2O water hexamer near 15 THz (500 cm^{-1}). The tentative tunneling assignment of the transitions indicates a significant enhancement of the hydrogen bond breaking tunneling motions of the cluster, consistent with our previous studies on other water clusters [1,3–6]. As indicated by the rotational constants measured here, the excited states display significant motion about the A-principal axis, which has interesting consequences for the tunneling pathways.

As this cluster is the fifth system to display unusual behavior in the 15 THz region, further detailed study seems warranted; this region obviously contain vital information about the hydrogen bond breaking/reformation dynamics of water clusters, and as such, may provide useful insight into the associated dynamics that occur in the bulk liquid [6,28,30,124]. Of particular interest is the point in which the local dynamics observed in clusters transition to the dynamics more relevant to the liquid [125], and we note that it is the thermal excitation of librational motions that have been invoked as the essential hydrogen bond breaking mechanism in the liquid [50].

Structure and torsional dynamics of the water octamer from THz laser spectroscopy near 215 μm

*The full details of this section can be found in: Cole, W.T.S., Farrell, J.D., Wales, D.J., Saykally, R.J., Science, **352** (6290) 1194, (2016).*

Introduction

Spectroscopic study of water clusters provides accurate benchmarks for detailed characterization of the complex pairwise and many-body forces that operate in bulk water phases, which have proven difficult to adequately capture through bulk experiments or theory [9,28,30,126]. The need to accomplish this goal is underscored by recurring controversies surrounding the fundamental intermolecular structure and dynamics of water [10,30,103]. Clusters ranging from dimer through heptamer, as well as nonamer and decamer [114] have been studied in detail by high precision microwave and terahertz spectroscopy, but the octamer has proven elusive [8,30,79,126,127]. Whereas the most stable structures of smaller clusters evolve with size from quasi-planar rings to 3-D cages, the octamer represents the transition to cuboidal [8] structures formed by stacking quasi-planar 4- and 5-membered rings, a dominant motif in larger systems.

Accordingly, the water octamer has become a benchmark for theory, starting with the early work of Stillinger and David [128], Brink and Glasser [129], and Tsai and Jordan [130]. Many groups have since investigated the structures, melting transitions, and hydrogen bond rearrangement dynamics of the octamer cluster [93,131–146]. However, experimental characterization has been very challenging, with only a few successful mid-IR spectroscopy [147–150] and crystallographic studies [151–153]. The mid-IR results are particularly interesting, revealing two nonpolar low energy structures (Figure 21) formed by stacking of homodromic tetramer rings with the in-plane hydrogen bonds (HBs) directed in either the same (S_4 symmetry) or opposite (D_{2d} symmetry) senses. Both structures possess two distinct monomer environments: single HB donor and double HB donor, with the latter responsible for the association between the two tetramer rings. These structures have subsequently been refined by theory, with several groups calculating the ground state energy difference between the S_4 and the D_{2d} structures to be < 0.1 kJ/mol [93,131,139,140,153]. Given such a small energy difference, both structures should be present even in very low temperature environments, e.g. supersonic beams.

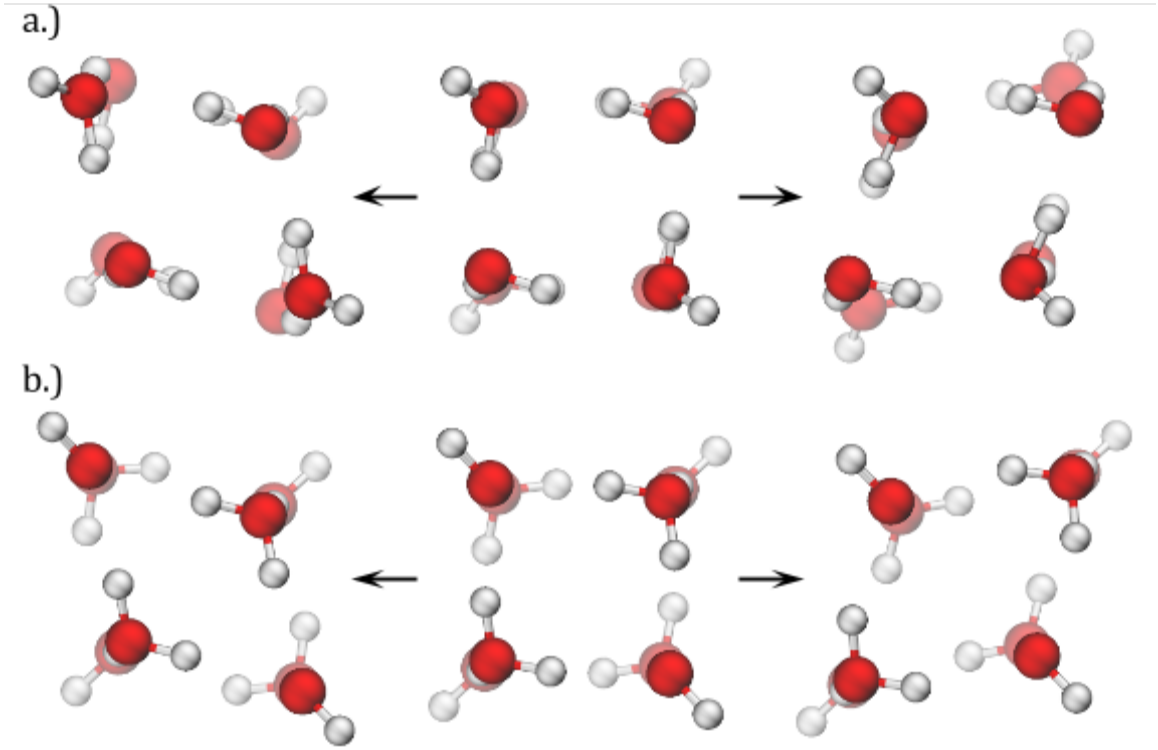

Figure 21: The two lowest energy structures predicted for the water octamer, viewed along the principal axes. Tentatively assigned low frequency vibrational motions are also depicted. a.) The S_4 structure, viewed along the long axis (middle), pictured with displacements along the normal mode on either side; b.) The corresponding D_{2d} structure and displacements, viewed along the short axis. The D_{2d} structure is predicted to be slightly lower in energy, while entropy favors the S_4 structure [140].

Here we present the results of a study of the water h_{16}-octamer by terahertz vibration-rotation-tunneling (VRT) spectroscopy, involving the measurement of a very low frequency torsional vibration in both low-lying isomers. Nearly 100 individual vibration-rotation transitions have been measured to ppm accuracy and fitted to a standard semi-rigid symmetric rotor model, producing rotational constants, which, when combined with theoretical values, characterize the structures and vibrational distortions of the cluster. The results are in good agreement with recent theoretical predictions of the hydrogen bond rearrangement tunneling rates [8] and cluster structures.

In an earlier study, Richardson et al. presented VRT spectra comprising 99 weak transitions measured near 1.4 THz, and assigned to the h_{16}-water octamer cluster on the basis of detailed isotopic dilution studies [8]. Spectral assignment was not possible at that time. In the same study, application of the Ring Polymer Perturbative Instanton Method predicted the hydrogen bond rearrangement tunneling rates for the h_{16}-octamer. Those results indicated that even for the most energetically accessible rearrangement, the magnitude of the tunneling splitting was < 42 Hz, well below our experimental resolution (ca. 1MHz). Subsequently, we have employed a statistical spectral assignment algorithm, which has enabled the detailed assignment of the spectra. A least squares fit of the transitions yielded precise values for the vibrationally-induced changes in the rotational constants of both isomers, which in combination with the earlier results of Gruenloh et al [148,149], provide a good estimate of the excited state rotational constants. Harmonic normal mode analysis predicts a diamond-type vibrational mode, shown in Figure 1, for both isomer structures.

The measurement of VRT spectra and assignment to the h_{16}-water octamer with the Berkeley Terahertz spectrometer is described in detail in [28,30,126] and in Supplementary Material. Because the 99 measured octamer transitions are confined to a very compact region (~350 MHz), it was assumed that the transitions belong to a Q branch. This is consistent with our previous THz VRT results for the similar h_{12}-hexamer, in which the Q branches were observed to have higher intensity than P or R branch transitions. To approach assignment of the very dense observed spectrum, we created a pattern recognition program to search the spectrum for transitions that displayed the energy level pattern characteristic of the D_{2d} and S_4 structures. These patterns are distinct in that the D_{2d} equilibrium structure is an oblate symmetric rotor, whereas the S_4 structure is a prolate symmetric rotor, exhibiting opposite intensity variations with the same J-quantum numbers. Using the output of this program as a starting point facilitated the assignment of 91 transitions to the D_{2d} (60 transitions) and S_4 (31 transitions) structures. The assignment, along with the 8 weak unassigned lines, is shown in Figure 22A. Figure 22 and Figure 22C shows a comparison between the calculated and observed experimental spectrum for a representative Q branch progression of each symmetry. As predicted [8], no evidence for tunneling splittings was observed. Figure 23 shows a measured vibration-rotation absorption feature, compared with the predicted tunneling splitting. We ultimately determined that the assigned transitions belong to two distinct parallel ($\Delta K=0$) bands. The complete collection of assigned transitions is given in Tables S1 and S2.

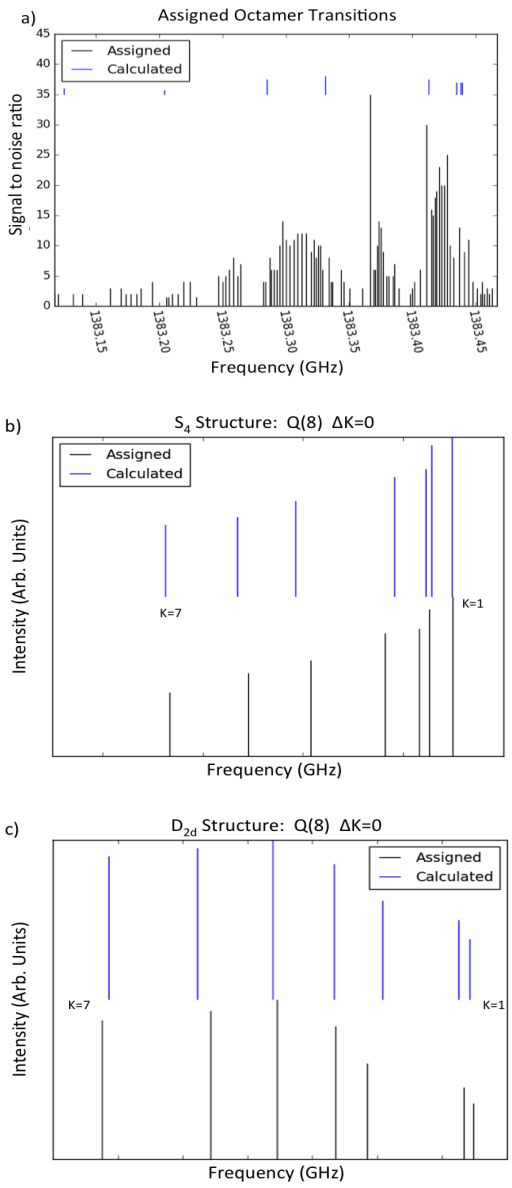

Figure 22: Experimental spectra. **a)** The full assigned spectrum is shown along with the 8 (out of 99) transitions that could not be assigned. **b)** Typical example of an assigned K-progression of transitions calculated from the fitted constants for the S_4 isomer. **c)** Typical example of an assigned K-progression of transitions calculated from the fitted constants for the D_{2d} isomer. Note the opposite intensity variation with K in b) and c) above, which supports assignment of the two bands to prolate and oblate tops, respectively. The intensities of the assigned and calculated branches shown in b) and c) are normalized such that the most intense transition has a value of 1. The associated data are presented in Tables S1 and S2 (Supplementary Material).

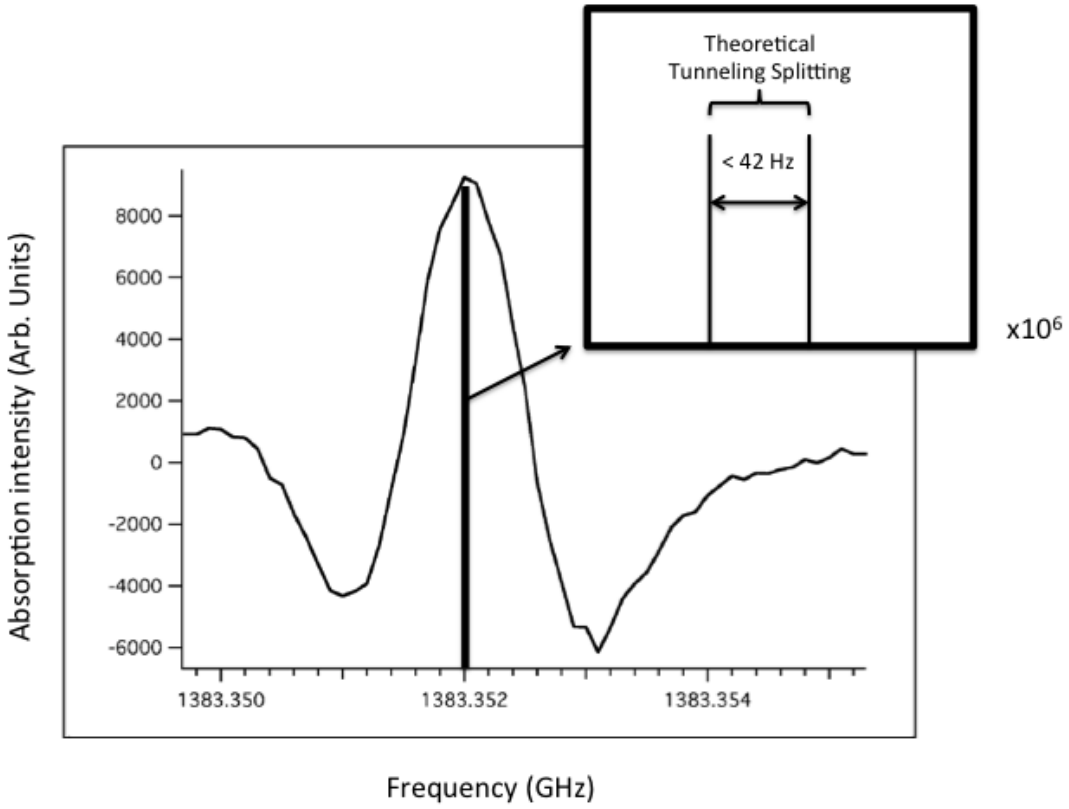

Figure 23: A measured absorption transition showing the characteristic second derivative lineshape observed. The FWHM linewidths are ca. 1 MHz. Tunneling splittings predicted in [8] are well below the experimental resolution, which is determined by the residual Doppler width in the planar supersonic expansion.

After assignment, the transitions were fitted to a standard, semi-rigid rotor energy level expression (eq. 1):

$$E(J,K) = v + \Delta B * J(J+1) + \Delta M * K^2 - \Delta D_J * J^2(J+1)^2 - \Delta D_{JK} * J(J+1)K^2 - \Delta D_K * K^4 \qquad (1)$$

Here v is the band origin, B is the perpendicular rotational constant, and the D terms are the standard centrifugal distortion constants. The band origins are defined with respect to the absolute ground state of the respective cluster structures. All differences are defined as excited state minus ground state. The term ΔM is:

$$\Delta M = (A' - B') - (A'' - B'') \qquad for\ the\ S_4\ octamer$$

$$\Delta M = (B'' - C'') - (B' - C') \qquad for\ the\ D_{2d}\ octamer$$

A and C represent the two remaining rotational constants, and primed values refer to excited state terms, whereas the double primed values are those of the ground state. The difference in the ΔM terms reflects the two octamer structures being different types of symmetric rotors, as previously noted.

A least squares fit of the 91 assigned transitions to eq 1, yielded rms deviations of 2.7 MHz (D_{2d}) and 2.5 MHz (S_4), respectively.

Table 12 Table 12 and Table 13 present the fitted constants of both octamer structures for the ground and excited states, along with the 1σ errors. Correlation matrices for the fits are given in Appendix A. Although a simple symmetric top rigid rotor energy expression produced a good fit of the assigned data, it is well-known that water clusters are actually highly non-rigid complexes, and as such may violate simple selection rules because the projection of rotational angular momentum along the symmetry axis (quantum number, K) is not rigorously conserved [30,154].

Table 12: Fitted constants (in MHz) for the D_{2d} structure based on 60 assigned transitions. Band origin is 46.13503 (cm^{-1}). Root mean square deviation of fit: 2.7 MHz.

Constant	Value	Error
ΔB	4.455	3.0E-02
ΔM	0.881	8.3E-03
ΔD_J	1.03E-02	9.0E-05
ΔD_{JK}	1.74E-02	7.9E-04
ΔD_K	-4.13E-04	4.5E-05
Band Origin	1383093.60	1.6E+00

Table 13: Fitted constants (in MHz) for the S_4 structure based on 31 assigned transitions. Band origin is 46.13951 (cm^{-1}). Root mean square deviation of fit: 2.5 MHz.

Constant	Value	Error
ΔB	2.705	1.3E-01
ΔM	1.960	9.6E-02
ΔD_J	-1.58E-03	3.3E-04
ΔD_{JK}	-1.40E-02	3.3E-03
ΔD_K	4.16E-03	8.6E-04
Band Origin	1383227.90	5.5E-01

Although spectroscopic determination of structural parameters is not possible without R or P branch assignments, the detailed isotope dilution results previously presented in [8] and the absence of any asymmetry splittings, unambiguously identified the spectral carrier as the h_{16}-water octamer.

The observation of two distinct bands (at 46.13503 cm^{-1} and 46.13951 cm^{-1}) can be rationalized in two ways. Either the bands could originate from two different vibrational modes of a single octamer structure; or each could belong to a similar vibration from separate octamer isomers. We argue that the second option is more likely. Two experimental observations support this conclusion. First, the two bands have opposite intensity patterns, one displaying higher K components with lower intensity and the other higher K components with higher intensity, as evident in Figure 22B and Figure 22C. These observations are consistent with the ground state energy level diagrams of prolate and oblate symmetric tops, respectively. We have neglected vibrationally induced dipole changes here, as the transitions within a Q branch can reasonably be assumed not to differ significantly in that regard. Second, the vibrational changes in rotational constants of the two bands are strikingly similar, indicating that the corresponding motions are nearly identical. Moreover, even in molecules of this size, it is unlikely two modes would exist in such extreme proximity (less than 0.005 cm^{-1}) as observed herein. Based on these considerations, we are confident in assigning the two bands to different water octamer isomers, one an oblate symmetric top, and the other a prolate top.

Because the supersonic expansion cools the clusters to about 4 K, we are confident that the two structures are the D_{2d} and S_4 isomers, because they are consistently predicted to be particularly close in energy [93,131,135,138,148], and having prolate (S_4) and oblate (D_{2d}) symmetric rotor eigenstates. On this basis, we assign the two observed bands to the S_4 or D_{2d} water octamer isomers.

The group comprising the energetically accessible permutation-inversion operations for the water octamer (i.e. operations that do not break a covalent bond) contains on the order of $8! \times 2^8 \times 2 = \sim 10^8$ elements. As for previous water clusters [28,30,126,133], the water octamer is expected to display a high degree of nonrigidity. Assuming a rigid system enables us to exploit the corresponding point groups; however, this simplification may fail if the system is significantly nonrigid. A symmetric rotor energy level expression is thus an approximation to the true energy level structure of the complex. As with other water clusters, nonrigidity could lead to tunneling splittings of the simple symmetric top rigid rotor energy levels. While we did not observe any tunneling in the spectra reported herein (in agreement with predictions [8], the system still displays significant nonrigidity in the form of low frequency torsional vibrations and relaxed selection rules. A direct consequence of this non-rigidity is encountered in the description of the vibrational mode observed herein.

The observed transitions belong to parallel bands, implying a change in the dipole moment along the principal rotation axis. This result requires the observed vibration to have B symmetry in the case of the S_4 structure, and B_2 symmetry for the D_{2d} competitor. A normal mode analysis with the MB-pol potential [9,155,156] reveals that the lowest frequency B_2 vibration corresponds to the pattern in Figure 21B, where the tetramers in the perpendicular plane distort to diamond geometries (see SM for methodological details

and harmonic frequencies). The harmonic frequency of this mode is 74.8 cm-1. The next lowest B_2 mode occurs at 204.1 cm-1, involving the antisymmetric compression and expansion of the perpendicular faces. It is unlikely that these modes would reorder upon inclusion of anharmonic effects.

Given that both octamer structures display similar changes in rotational constants, and noting the close proximity of the two bands, it is reasonable to expect that this vibrational motion is similar in the D_{2d} and S_4 isomers. The two lowest B modes of the S_4 structure occur at 69.9 and 76.9 cm-1, the second of which is most similar in frequency to the mode assigned to the D_{2d} vibration, and describes an almost identical displacement (Figure 21A).

We stress that this description of the vibrational motion is but a starting point for future work. Previous studies of water clusters [28,30,80,126,154] have shown that nonrigidity results in vibrational motions that deviate significantly from simple harmonic/rigid rotor approximations. Detailed quantitative analysis of the intermolecular vibrations in the octamer will clearly require further experiments and calculations.
Given the complexity of the nonrigid octamer structures, spectroscopically accurate calculations for the vibrational modes present a major challenge. Furthermore, a simple analysis of the energy landscape using TIPXP water potentials (X=3-5) suggests that the number of minima may increase rapidly in the presence of an electric field [146]. Shields and coworkers [93,135] report the lowest anharmonically corrected *ab initio* intermolecular vibrational frequencies for the octamer as 57.2 (D_{2d}) and 54.7 (S_4) wavenumbers, considerably higher than the experimental values near 46.1 cm^{-1}. Clearly, further theoretical advances are necessary in order to compute such cluster properties reliably, noting that significant progress in this regard has recently been achieved for the water hexamer [80].

Finally, we report evidence in support of calculations showing that the D_{2d} structure is the lowest in energy [131,135,137,146]. If we assume that the transition dipole moment is similar for the competing cuboids, we can use the number and intensities of the observed transitions to infer the relative energetics. For the D_{2d} structure, we observe J values from 2 to 17, with some of the higher J subbands lacking some K value components. For the S_4 structure, we observe J values of only 5 to 10, and again, the higher J subbands are missing some K-value transitions. From this evidence, we infer that the D_{2d} structure is the lowest.

Remaining Unassigned Transitions

Despite our best efforts, not all of the observed could be assigned. In total, 187 H_2O and 46 D_2O transitions were not assigned and those transitions are shown in Figure 24 below. For the H_2O transitions, visual inspection suggests that some structure remains, but our methodology could not find a satisfactory assignment. If an assignment exists for these transitions, it is likely to originate from a larger water cluster as the spacing between adjacent lines is quite small, indicating a small value for rotational constant B. The small number of D_2O line remaining, likewise shown some provocative structure, but attempts at assignment were inhibited by the lack of enough transitions to achieve a satisfactory fit. All unassigned transitions are reported in Appendix A of this thesis.

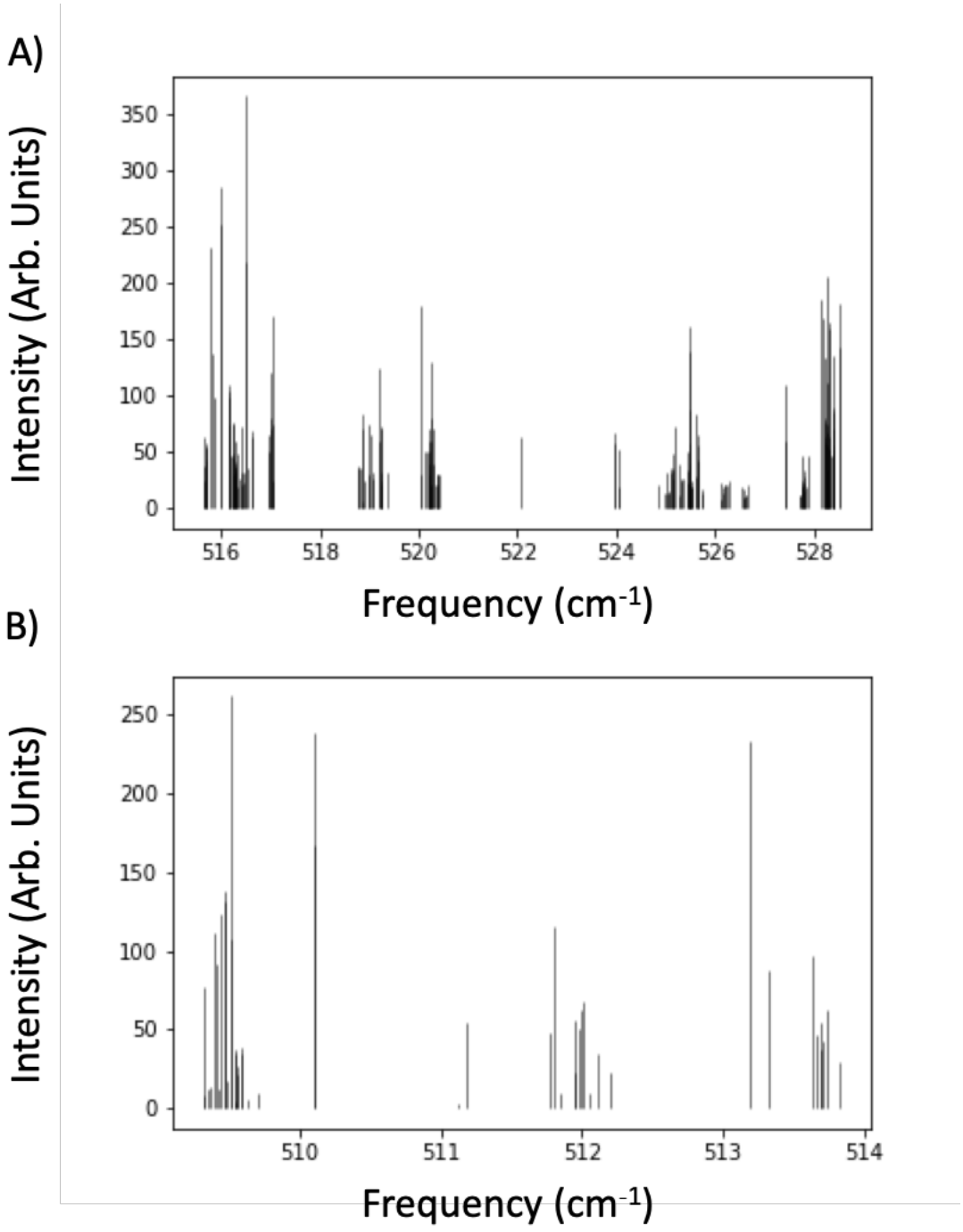

Figure 24: A) Line spectrum of the remaining 187 unassigned H_2O transitions. B) Line spectrum of the remaining 46 unassigned D_2O transitions.

Use of Assignments in Benchmarking Theory

The first studies of gas phase water clusters, and the assignments of rotational-vibration-tunneling transitions, lead to development of some of the earliest water potential models. Anthony Stone potential model, for example, could be parameterized using available water cluster transitions [13]. These early water models proved relatively successful at predicting specific properties of water. Notably, the water dimer proved valuable in elucidating the absorption of solar radiation in the atmosphere [26,157–159]. However, as ab initio method became more powerful and the understanding of many body terms advanced, use of water cluster transitions for the direct development of potential energy surfaces diminish. Currently, the available ab initio models far exceed the capacities of cluster parametrized models [155,160,161]. Thus, the main use of assigned water cluster transitions has been to benchmark new models.

One noticeably shortfall of current theories, is the inability to accurately calculate the transition frequencies in the librational region of water. One reason for this is the large density of states which exists in that region, making it difficult to assign predicted transitions to those observed experimentally. The understanding of the librational region is critical to understanding the nature of the hydrogen bond as Chandler and Luzar have detailed [43,44,61,62]. As ab initio models become more powerful, it is hoped that the transitions assignment herein provide some use for benchmarking and refining the interactions between water molecules.

We have also attempted to extend the usefulness of the large quantity of available assignments by simulating the tunneling dynamics of water clusters as a function of vibrational excitation (detailed in the following section). This is not a new idea, and was originally put forward by Keutsch et al[41] studying tunneling motions which break and reform the hydrogen bond.

Hydrogen Bond Network Rearrangement Dynamics in Water Clusters: Effects of Intermolecular Vibrational Excitation on Tunneling Rates

*The full details of this section can be found in: Cole, W.T.S. and Saykally, R.J., J. Chem. Phys., **147** (6), 064301, (2017).*

Introduction

It is well known that the remarkable properties of water result from the intricacies of the hydrogen bond network (HBN) connecting the individual water monomers [28,43,61,80,162–164]. Understanding details of the processes by which the HBN rearranges is thus essential to understanding and modeling water. Many different experimental techniques have addressed these rearrangement dynamics, but these have generally required extensive interpretation to rationalize the measured properties [42,46,165–169]. In contrast, molecular dynamics (MD) simulations have provided a detailed microscopic picture of many aqueous systems, but are limited as they depend explicitly on the model potentials used in the simulation [43,44,61,163]. More recent work has again indicated that nuclear quantum effects are important for correctly describing hydrogen bond behavior [170,171].

Incoherent neutron scattering experiments of both H_2O and D_2O demonstrate evidence of relaxation processes with two distinct timescales [165]. Similar experiments performed by Cabral et al. on mixtures of H_2O with DMSO showed good agreement with the theoretical results of Luzar and Chandler [165,172], viz. that the "residence" time, defined as the average time in which a molecule remains in a narrow geometric domain wherein a hydrogen bond could form, is 1.8 ± 0.4 ps for pure water and is 6 ± 2ps in the mixture. These neutron scattering experiments supported the theoretical contention that librational motions (hindered rotations) are the primary means of breaking and forming hydrogen bonds in the liquid. Subsequent experiments using coherent quasielastic neutron scattering have provided further refinement of these deductions and also demonstrated that the temperature dependence of hydrogen bond dynamics is curiously weak compared to that of other transport properties of liquid water [165,173,174].

More recently, mid-IR femtosecond pump-probe spectroscopy experiments and photon echo experiments have yielded additional insight into the intramolecular modes associated with HBNR dynamics. Pump-probe spectroscopy experiments on the O-H stretch in HDO:D_2O solutions demonstrate that coupling between the intramolecular OH stretch and a translational intermolecular vibration is essential to understanding the vibrational relaxation in the liquid [42,169,175–178]. Further studies employing femtosecond mid-IR spectroscopy demonstrated coupling between intra- and inter-molecular modes, and also identified two distinct time domains for relaxation processes, viz. sub-picosecond and picosecond [167,179–182]. In photon echo experiments, Stenger et al. demonstrated that there may also be an even longer (5-15 ps) timescale process occurring which must be connected to the hydrogen bond rearrangement, indicating that these dynamics may be much slower than previously thought [183]. Huse et al. then performed ultrafast pump probe experiments on the O-H bending mode and showed that explicit

consideration of the librational excitations is necessary to rationalize ultrafast vibrational relaxation [177].

While the proceeding experiments have provided significant insight into aqueous hydrogen bond dynamics, some authors have argued that they possess a common weakness [61,164], viz. lack of a conclusive connection between the relaxation processes observed and the detailed hydrogen bond dynamics occurring in the bulk. While some measured properties, such as the "residence time" obtained in neutron scattering experiments, have been shown to agree well with the predicted hydrogen bond lifetimes, the connections of other properties to actual bulk phase dynamics is less transparent. Motivated by this history, and mindful of the ambiguities, our group has endeavored to explore the relation of our high-precision terahertz spectroscopy measurements of water cluster intermolecular vibrational modes to the HBNR dynamics of bulk water.

We draw attention to studies suggesting that the behavior of other small water clusters can provide additional insight into the hydrogen bond dynamics of the bulk [32,41,184,185]. In the aforementioned theoretical studies by Luzar and Chandler, the authors found that the dynamics of a particular hydrogen bond were not affected by the neighboring hydrogen bonds [44,61,176,178], i.e. the local environment of a hydrogen bond does not significantly affect the dynamics of the hydrogen bond itself. Furthermore, more recent studies show that even static correlations are insignificant, and this result holds regardless of temperature [185]. Additionally, the spectra of clusters comprising 10-100 molecules resemble the spectra of bulk [46,161].

In the past, we have also shown that the lifetimes associated with breaking of the hydrogen bonds via permutational tunneling in the water trimer librational band show surprisingly good agreement with the accepted hydrogen bond lifetime in liquid water [41,69,72,184]. Recent studies of the water hexamer cluster have revealed tunneling pathways, which involve the concerted breaking of two hydrogen bonds. These motions were suggested to be important in interfacial and confined environments [80]. While the water dimer, trimer, and pentamer do not possess the 3-dimensional HB structures existing in liquid water, insights into the respective HBNR dynamics could similarly elucidate dynamics of water in bulk environments. We wish to emphasize that isolated cluster do not exist in the bulk, and that the dynamics of the bulk are more complicated. The gas phase cluster systems presented herein provide an insight into the dynamics of small hydrogen bonded cluster systems and the effect of cluster size and vibrational motion. Here we present results from applying a simple time evolution method for the water dimer, trimer, and pentamer clusters to extract tunneling lifetimes associated with the different experimentally measured tunneling pathways which break and reform hydrogen bonds.

Figure 25: The feasible tunneling motions of the water dimer (A), trimer (B), and pentamer (C). In this study we limit our focus to those motions, which break and reform a hydrogen bond.

A) Water Dimer Tunneling Pathways: oxygens are colored red, protons 1->4 are labeled grey, blue, green, and purple. Acceptor switching does not involve breaking/reforming a hydrogen bond and is not explicitly considered in this study. The interchange motions results in the acceptor and donor monomer changing roles. Bifurcation results in the free proton of the donor monomer exchanging with the proton involved in the hydrogen bond. The bifurcation proceeds through a transition state in which both protons of the donor monomer are coordinated to the acceptor monomer.

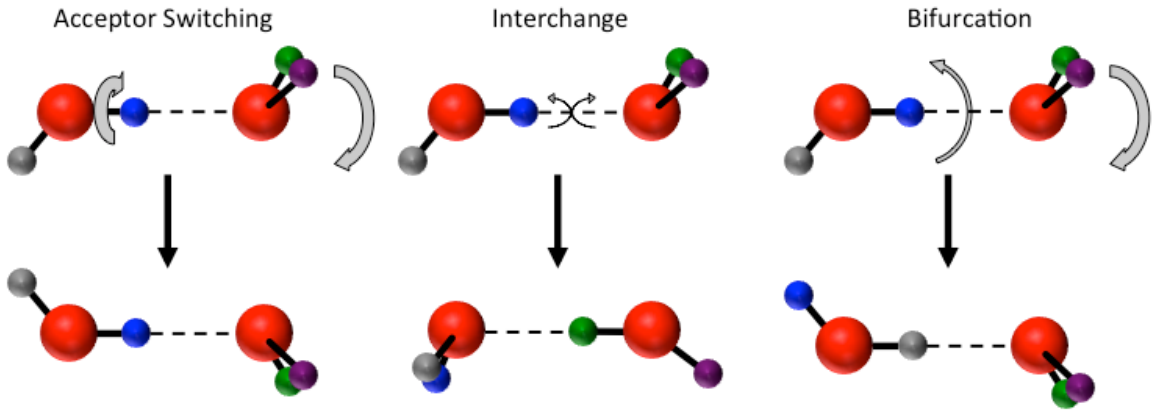

B) Water Trimer Bifurcation Tunneling: oxygens are labeled red, hydrogens unaffected by the tunneling are colored grey, and hydrogens participating in the tunneling are colored purple, green, and blue. The predicted transition state of the bifurcation pathway is also shown.

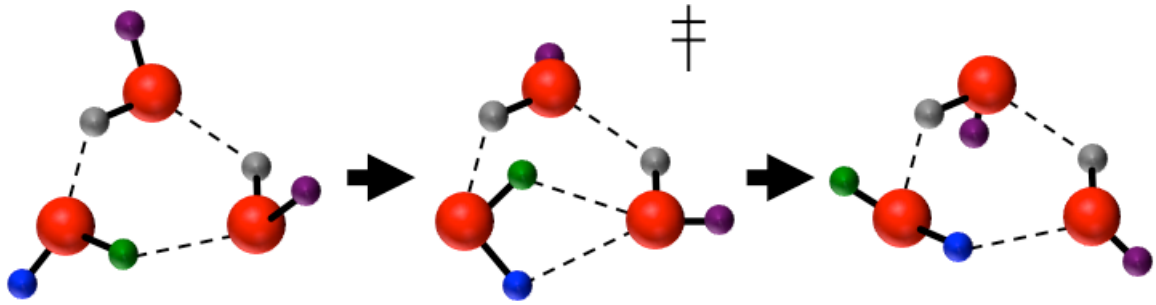

C) Water Pentamer Bifurcation Tunneling: oxygens are labeled red, hydrogens unaffected by the tunneling are colored grey, and hydrogens participating in the tunneling are colored green and blue. The predicted transition state is also shown.

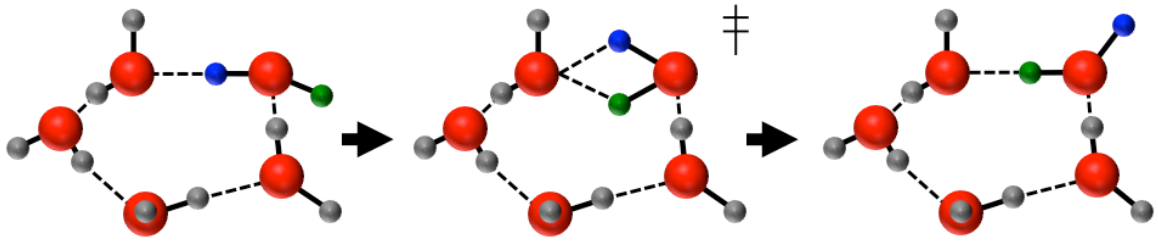

Methods

Tunneling Motions

It is well known that the HBNR tunneling in water clusters can be described in terms of complete nuclear permutational inversion (CNPI) group theory, wherein the tunneling motions are represented by group operations that are termed "feasible". For the purpose of this study, "feasible" will be taken to mean experimentally observed. The basis set becomes the set of permutational isomers which are connected by feasible operations. For the water dimer, it has been shown that there are 8 isomers connected by four tunneling pathways: acceptor switching (AS), geared interchange (G), antigeared interchange (I), and bifurcation (B) shown in Figure 25A. Three of these pathways break and reform the hydrogen bond: G, I, and B. The observed experimental splittings are accounted for by the eigenvalues of the tunneling Hamiltonian (shown in Figure 26A). The 8 permutational isomers (labeled |1> to |8>) that make up the basis set for the dimer are shown in the supplemental information in Appendix A. The term υ represents the vibrational origin.

A) Dimer Hamiltonian

	|1>	|2>	|3>	|4>	|5>	|6>	|7>	|8>
<1|	υ	B	0	AS	G	G	I	I
<2|	B	υ	AS	0	G	G	I	I
<3|	0	AS	υ	B	I	I	G	G
<4|	AS	0	B	υ	I	I	G	G
<5|	G	G	I	I	υ	B	0	A
<6|	G	G	I	I	B	υ	A	0
<7|	I	I	G	G	0	A	υ	B
<8|	I	I	G	G	A	0	B	υ

B) Trimer Hamiltonian

	|1>	|2>	|3>	|4>	|5>	|6>	|7>	|8>
<1|	υ	A	A	A	B	B	B	C
<2|	A	υ	B	B	A	A	C	B
<3|	A	B	υ	B	A	C	A	B
<4|	A	B	B	υ	C	A	A	B
<5|	B	A	A	C	υ	B	B	A
<6|	B	A	C	A	B	υ	B	A
<7|	B	C	A	A	B	B	υ	A
<8|	C	B	B	B	A	A	A	υ

Figure 26: Tunneling Hamiltonians used for the water dimer (A), trimer (B). The labels represent the permutational isomers connected by the feasible tunneling motions. Descriptions of the elements in the matrices can be found in the text. The tunneling matrix for the pentamer can be found in the Supplemental Information in Appendix A.

The water trimer exhibits two feasible tunneling motions: flipping and bifurcation. The flipping motion has been shown to be essentially barrierless, and can thus be neglected within the context of this study. However, the bifurcation pathway, shown in Figure 25B, results in 8 degenerate minima. We can construct the tunneling Hamiltonian by inspection of the group operation that represents bifurcation. As shown by Keutsch et al [31], the tunneling Hamiltonian for the trimer is given in Figure 2B, where A represents a single bifurcation event, B represents two consecutive bifurcation events, and C represents three consecutive bifurcation events. Experimentally, we have only observed single bifurcation events, so we set B=C=0. The term υ represents the vibrational origin. We show the permutational isomers corresponding to the labels |1> to |8> in the Supplemental Information in Appendix A.

The water pentamer also exhibits two feasible tunneling pathways: flipping and bifurcation. Again, the flipping pathway is essentially barrierless, and also can be ignored here. The bifurcation pathway, shown in Figure 25C, results in 32 permutational isomers. A tunneling Hamiltonian can be constructed to account for the experimental splitting pattern, and is shown in the SI. From these simple tunneling Hamiltonians, we can extract a measurement of the tunneling lifetime for each water cluster in turn, using the typical time evolution operator. As a note, the tunneling magnitudes and relative signs were taken from experimental studies [4,5,36–38,41,57,69,71–73] and correspond to the eigenvalues observed. In more sophisticated dynamical tunneling analysis, the relative signs of matrix elements can play an important role in the observed dynamics. Due to the simple approach applied here, a change in relative signs would change the lifetime for an individual pathway, but overall the same lifetimes would be observed. As each pathway represents an essentially identical motion (breaking and reforming the hydrogen bond), further analysis of this change would provide insight into how the different tunneling pathways might interfere with each other. We only use experimentally observed values for the tunneling; though we acknowledge that theoretical values exist for some missing modes.

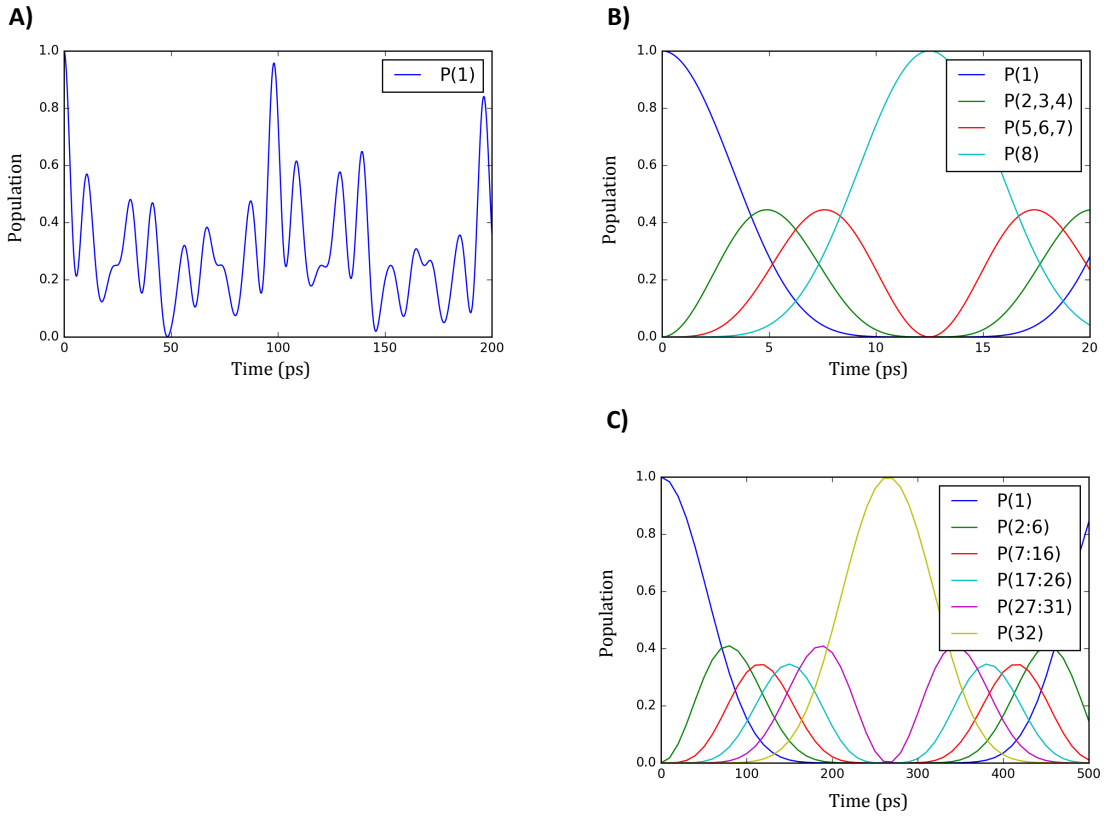

Figure 27: Typical plots of probability to be in a specific minima versus time for the three cluster systems. A) Probability of being in minima |1> of the water dimer when I, G, and B are active for the out-of-plane vibrational state. B) Probability of the 8 degenerate minima of the trimer versus time for the 520 cm^{-1} vibration. The 4 plotted sets correspond to: P(1) -> probability of being in minima |1>, P(2,3,4) -> combined probability of being in minima |2>, |3>, or |4>, P(5,6,7) -> combined probability of being in minima |5>, |6>, or |7>, and P(8) is the probability of being in minima |8>. C) Probability of the 32 degenerate minima of the pentamer versus time for the 512 cm^{-1} vibration. The probability of being in a specific minima, i, is indicated by the sets labeled P(i). Likewise, the combined probability of being in a specific set of minima, i through j, is represented by the sets labeled P(i:j).

Table 14: Tunneling magnitudes and lifetimes for the water dimer. Values are taken from References [4,5,36–38,57,69,71–73].

$(H_2O)_2$

Vibrational Origin (cm^{-1})	Geared Interchange Tunneling (cm^{-1})	Anti-geared Interchange Tunneling (cm^{-1})	Bifurcation Tunneling (cm^{-1})	Lifetime Range (ps)	Shortest Bifurcation Lifetime (ps)	Shortest Interchange Lifetime (ps)
7.6	1.75E-01	-1.26E-02	2.20E-02	44.3-667	758	44.3
87.75	1.02E+00	3.88E-01	5.40E-03	5.93-26.7	3080	5.93
102.8	1.48E+00	1.50E+00	1.38E-01	2.80-476	120	2.80
124.255	1.30E+00	-1.24E+00	8.16E-01	3.29-139	20.4	3.29
151.875	5.48E-01	5.50E-02	6.55E-01	13.3-318	25.4	13.8
531.67	8.46E-01	-1.73E-01	5.19E-01	8.18-109	32.2	8.18

$(D_2O)_2$

Vibrational Origin (cm^{-1})	Geared Interchange Tunneling (cm^{-1})	Anti-geared Interchange Tunneling (cm^{-1})	Bifurcation Tunneling (cm^{-1})	Lifetime Range (ns)	Shortest Bifurcation Lifetime (ns)	Shortest Interchange Lifetime (ns)
4.16	9.38E-03	-3.75E-04	2.40E-04	0.855-22.2	69.4	0.855
65.726	2.66E-01	6.24E-02	-1.23E-03	0.0254-0.134	13.5	0.0254
83.5	1.21E-01	9.71E-03	3.24E-03	0.0637-0.858	5.15	0.0637
89.873	1.09E-01	-1.39E-03	-2.54E-03	0.0753-6.06	6.58	0.0753

Lifetimes for Trimer Tunneling
$(H_2O)_3$

Vibrational Origin (cm^{-1})	Bifurcation Tunneling (cm^{-1})	Shortest Bifurcation Lifetime (ps)
42.9	6.50E-04	8550
65.6	-4.25E-03	1310
87.1	-4.82E-03	1150
520	6.67E-01	8.33

Lifetimes for Pentamer Tunneling
$(H_2O)_5$

Vibrational Origin (cm^{-1})	Bifurcation Tunneling (cm^{-1})	Shortest Bifurcation Lifetime (ps)
89	8.01E-05	41600

$(D_2O)_3$

Vibrational Origin (cm^{-1})	Bifurcation Tunneling (cm^{-1})	Shortest Bifurcation Lifetime (ns)
19.5	1.67E-05	333
28	-1.50E-05	371
41.1	-2.50E-05	222
81.8	4.50E-05	124
89.6	1.00E-04	55.6
98	8.34E-05	66.7
142.8	1.67E-05	333

$(D_2O)_5$

Vibrational Origin (cm^{-1})	Bifurcation Tunneling (cm^{-1})	Shortest Bifurcation Lifetime (ns)
27.3*	1.33E-06	2510
512	3.14E-02	0.106

*This entry represents all of the values of $(D_2O)_5$ where bifurcation tunneling is below experimental resolution: the vibrational origins are: 27.3, 30.2, 45, 45.4, 47.7, 50.7, and 81.2 cm^{-1}.

Results and Discussion

The results of the fit are present in Table 14 and pictorially in Figure 27. We define the tunneling lifetime in these clusters as the time required to break and reform a hydrogen bond, which corresponds to the period of the oscillating cosines in the probability equation. This is similar to the approach employed by Keutsch et al, in their earlier study of dynamics in the water trimer [41].

For the dimer, the presence of multiple tunneling pathways complicates the analysis; in order to isolate interchange and bifurcation, we sequentially set the corresponding matrix elements to 0 in order to isolate the pathway of interest. All the calculated lifetimes are shown with respect to vibrational origin in Figure 28. As a note, we initialized the total wavefunction in the minima labeled |1> for all systems, but this, of course, was an arbitrary choice. Additionally, for the water dimer we report both the range of tunneling lifetimes in addition to the shortest lifetimes for bifurcation and interchange. The shortest lifetimes are reported specifically for comparison with the lifetimes of the trimer and pentamer.

Isotope Effect

Substituting hydrogen by deuterium results in a large decrease in tunneling rates for all studied clusters, as would be expected due to larger mass-weighted pathways. This effect is essentially the same for both the bifurcation and interchange pathways. However, perdeuteration does not seem to negate the tunneling rate enhancement that has been observed for excitations to librational states-particularly for the trimer and pentamer systems.

Cluster Size

We observe that the tunneling lifetimes decrease with increasing cluster size, which is not surprising, as the hydrogen bond strength also increases with cluster size. For the water dimer, it is important to point out that for all observed vibrational states, the interchange lifetimes are shorter that the bifurcation lifetimes, which is again unsurprising, since the lifetimes are inversely related to the tunneling magnitudes. We also find that cluster size is a much more reliable predictor of tunneling lifetimes as compared to isotopic identity, underscoring the importance of cooperativity in the hydrogen bond dynamics of clusters.

Intermolecular Vibrational Excitation

The effect of intermolecular vibrational excitation depends explicitly on the cluster species. The water dimer is relatively unaffected by the nature and frequency of the excited vibration, which indicates that the tunneling pathways are relatively uncoupled to the vibrational motions. For both dimer isotopomers, excitation of *any* intermolecular vibration reduces the tunneling lifetime to a common timescale: picoseconds for $(H_2O)_2$ and 10s of picoseconds for $(D_2O)_2$.

There is a drastic difference between the dynamics of the dimer and those of the trimer and pentamer. For the latter, only excitations of the librational motions reduce the tunneling lifetime, viz. the trimer lifetime reduces to a picosecond timescale (a ~100x decrease relative to the next shortest timescale), and the pentamer reduces to a 100 picosecond timescale (a ~380x decrease). These enhancements in the tunneling rates indicate that librational vibrations are indeed very effective in inducing hydrogen bond breaking in water clusters, similar to predictions for the liquid [43,61].

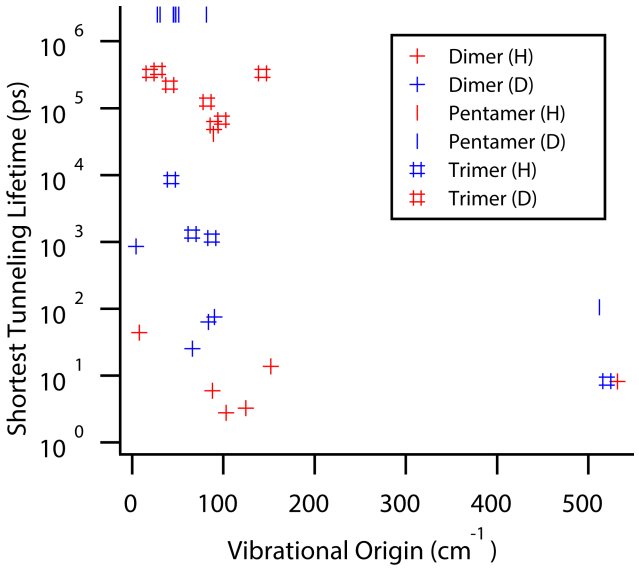

Figure 28: Comparison of the shortest tunneling lifetimes for each cluster studied with respect to vibrational origin. The values are given in Table 1.

Conclusions

The most interesting results extracted from these calculations are that the specific nature of the vibrational excitation does not significantly influence the tunneling lifetime of the water dimer, and that only excitations of a librational vibration affect the water trimer or pentamer tunneling lifetimes significantly, relative to those in the ground state. Previous studies of the hydrogen bond breaking dynamics in the bulk liquid have indicated that such librational motions initiate the HB breaking process [43,61]. Thus, observing and quantifying dynamics related to hydrogen bond breaking/reformation events for these types of vibrations in water clusters supports this prediction. The specific enhancement of tunneling rates in larger clusters relative to the dimer indicates that hydrogen bond cooperativity is a vital element of these cluster dynamics.

The above theoretical studies also indicated that hydrogen bond dynamics in the liquid are essentially uncorrelated with the number of additional hydrogen bonds the two relevant monomers are participating in, i.e. is a very local process. Therefore, we might have expected the water dimer to most closely represent the behavior of the bulk with respect to hydrogen bond dynamics. Indeed, we find that the tunneling lifetimes of the hydrogen bond in the dimer agree quite well with the accepted bulk liquid water hydrogen bond lifetime, which is on the order of a picosecond. However, we also find that the tunneling lifetime for the librationally excited state of the water trimer has a similar timescale. If we compare just the bifurcation pathways, we instead find that the dimer lifetimes are longer compared to those in the excited trimer librational mode. The significance of this being that the bifurcation pathways for all three systems involve breaking and reforming the *same* hydrogen bond (acceptor and donor monomer roles are not exchanged) whereas the interchange pathway of the dimer exchanges the monomer roles of acceptor and donor. We wish to emphasize that isolated clusters do not exist in the bulk, and that the dynamics of the bulk are much more complicated than for these gas phase cluster systems. The possibly coincidental agreement between the tunneling lifetimes observed here with the accepted hydrogen bond lifetime of the bulk warrant further investigation. Specifically, the observation that only excitation of librational vibrations significantly enhance hydrogen bond breaking tunneling motions in larger water clusters. Recent microwave measurements of the water hexamer and octamer indicate that tunneling is greatly quenched in the ground state of those systems [2,80], probably as a result of their high symmetry, which requires more concerted motions of constituent monomers [8].

References:

(1) Keutsch, F. N.; Fellers, R. S.; Viant, M. R.; Saykally, R. J. Far-Infrared Laser Vibration-Rotation-Tunneling Spectroscopy of Water Clusters in the Librational Band Region of Liquid Water. *J. Chem. Phys.* **2001**, *114* (9), 4005–4015.

(2) Cole, W. T. S.; Farrell, J. D.; Wales, D. J.; Saykally, R. J. Structure and Torsional Dynamics of the Water Octamer from THz Laser Spectroscopy near 215 Um. *Science (80-.).* **2016**, *352* (6290), 1194–1197.

(3) Cole, W. T. S.; Farrell, J. D.; Sheikh, A. A.; Yönder, Ö.; Fellers, R. S.; Viant, M. R.; Wales, D. J.; Saykally, R. J. Terahertz VRT Spectroscopy of the Water Hexamer-D12prism: Dramatic Enhancement of Bifurcation Tunneling upon Librational Excitation. *J. Chem. Phys.* **2018**, *148* (9), 094301–094307.

(4) Cole, W. T. S.; Fellers, R. S.; Viant, M. R.; Saykally, R. J. Hydrogen Bond Breaking Dynamics in the Water Pentamer: Terahertz VRT Spectroscopy of a 20 μ m Libration. *J. Chem. Phys.* **2017**, *146* (1), 014306–014316.

(5) Cole, W. T. S.; Fellers, R. S.; Viant, M. R.; Leforestier, C.; Saykally, R. J. Far-Infrared VRT Spectroscopy of the Water Dimer: Characterization of the 20 μ m out-of-Plane Librational Vibration. *J. Chem. Phys.* **2015**, *143* (15), 154306–154324.

(6) Cole, W. T. S.; Saykally, R. J. Hydrogen Bond Network Rearrangement Dynamics in Water Clusters: Effects of Intermolecular Vibrational Excitation on Tunneling Rates. *J. Chem. Phys.* **2017**, *147* (6), 064301–064308.

(7) Cole, W. T. S.; Yönder, Ö.; Sheikh, A. A.; Fellers, R. S.; Viant, M. R.; Saykally, R. J.; Farrell, J. D.; Wales, D. J. Terahertz VRT Spectroscopy of the Water Hexamer-H12 Cage: Dramatic Libration-Induced Enhancement of Hydrogen Bond Tunneling Dynamics. *J. Phys. Chem. A* **2018**, *122* (37), 7421–7426.

(8) Richardson, J. O.; Wales, D. J.; Althorpe, S. C.; McLaughlin, R. P.; Viant, M. R.; Shih, O.; Saykally, R. J. Investigation of Terahertz Vibration-Rotation Tunneling Spectra for the Water Octamer. *J. Phys. Chem. A* **2013**, *117* (32), 6960–6966.

(9) Babin, V.; Leforestier, C.; Paesani, F. Development of a "First Principles" Water Potential with Flexible Monomers: Dimer Potential Energy Surface, VRT Spectrum, and Second Virial Coefficient. *J. Chem. Theory Comput.* **2013**, *9* (12), 5395–5403.

(10) Fellers, R. S.; Leforestier, C.; Braly, L. B.; Brown, M. C.; Saykally, R. J. Spectroscopic Determination of the Water Pair Potential. *Science (80-.).* **1999**, *284* (5416), 945–948.

(11) Hodges, M. P.; Stone, A. J.; Xantheas, S. S. Contribution of Many-Body Terms to the Energy for Small Water Clusters: A Comparison of Ab Initio Calculations and Accurate Model Potentials. *J. Phys. Chem. A* **1997**, *101* (48), 9163–9168.

(12) Mas, E. M.; Wormer, P. E. S.; Szalewicz, K.; van der Avoird, A.; Groenenboom, G. C.; Bukowski, R. Water Pair Potential of near Spectroscopic Accuracy. I. Analysis of Potential Surface and Virial Coefficients. *J. Chem. Phys.* **2002**, *113* (16), 6687–6701.

(13) Millot, C.; Stone, A. J. Towards an Accurate Intermolecular Potential for Water. *Mol. Phys.* **1992**, *77* (3), 439–462.

(14) Goldman, N.; Fellers, R. S.; Brown, M. G.; Braly, L. B.; Keoshian, C. J.; Leforestier, C.; Saykally, R. J. Spectroscopic Determination of the Water Dimer Intermolecular Potential-Energy Surface. *J. Chem. Phys.* **2002**, *116* (23), 10148–10163.

(15) Leforestier, C. Water Dimer Equilibrium Constant Calculation: A Quantum Formulation Including Metastable States. *J. Chem. Phys.* **2014**, *140* (7).

(16) Leforestier, C.; Gatti, F.; Fellers, R. S.; Saykally, R. J. Determination of a Flexible (12D) Water Dimer Potential via Direct Inversion of Spectroscopic Data. *J. Chem. Phys.* **2002**, *117* (19), 8710–8722.
(17) Leforestier, C.; Szalewicz, K.; Van Der Avoird, A. Spectra of Water Dimer from a New Ab Initio Potential with Flexible Monomers. *J. Chem. Phys.* **2012**, *137* (1).
(18) Bukowski, R.; Szalewicz, K.; Groenenboom, G. C.; Van Der Avoird, A. Predictions of the Properties of Water from First Principles. *Science (80-.).* **2007**, *315* (5816), 1249–1252.
(19) Huang, X.; Braams, B. J.; Bowman, J. M.; Kelly, R. E. A.; Tennyson, J.; Groenenboom, G. C.; Van Der Avoird, A. New Ab Initio Potential Energy Surface and the Vibration-Rotation-Tunneling Levels of (H2O)2 and (D2O)2. *J. Chem. Phys.* **2008**, *128* (3), 1–9.
(20) Kelly, R. E. A.; Tennyson, J.; Groenenboom, G. C.; van der Avoird, A. Water Dimer Vibration-Rotation Tunnelling Levels from Vibrationally Averaged Monomer Wavefunctions. *J. Quant. Spectrosc. Radiat. Transf.* **2010**, *111* (9), 1262–1276.
(21) Howard, J. C.; Gray, J. L.; Hardwick, A. J.; Nguyen, L. T.; Tschumper, G. S. Getting down to the Fundamentals of Hydrogen Bonding: Anharmonic Vibrational Frequencies of (HF)2 and (H2O)2 from Ab Initio Electronic Structure Computations. *J. Chem. Theory Comput.* **2014**, *10* (12), 5426–5435.
(22) Howard, J. C.; Tschumper, G. S. Benchmark Structures and Harmonic Vibrational Frequencies near the CCSD(T) Complete Basis Set Limit for Small Water Clusters: (H<inf>2</Inf>O)<inf>n = 2, 3, 4, 5, 6</Inf>. *J. Chem. Theory Comput.* **2015**, *11* (5), 2126–2136.
(23) Tschumper, G. S.; Leininger, M. L.; Hoffman, B. C.; Valeev, E. F.; Schaefer, H. F.; Quack, M. Anchoring the Water Dimer Potential Energy Surface with Explicitly Correlated Computations and Focal Point Analyses. *J. Chem. Phys.* **2002**, *116* (2), 690–701.
(24) Shank, A.; Wang, Y.; Kaledin, A.; Braams, B. J.; Bowman, J. M. Accurate Ab Initio and "Hybrid" Potential Energy Surfaces, Intramolecular Vibrational Energies, and Classical Ir Spectrum of the Water Dimer. *J. Chem. Phys.* **2009**, *130* (14).
(25) Dyke, T. R. Group Theoretical Classification of the Tunneling–Rotational Energy Levels of Water Dimer. *J. Chem. Phys.* **1977**, *66* (492), 492–497.
(26) Goldman, N.; Leforestier, C.; Saykally, R. J. A "first Principles" Potential Energy Surface for Liquid Water from VRT Spectroscopy of Water Clusters. *Philos. Trans. R. Soc. A Math. Phys. Eng. Sci.* **2005**, *363* (1827), 493–508.
(27) Leforestier, C.; Liu, K.; Elrod, M. J.; Saykally, R. J.; Braly, L. B. Fully Coupled Six-Dimensional Calculations of the Water Dimer Vibration-Rotation-Tunneling States with a Split Wigner Pseudo Spectral Approach. II. Improvements and Tests of Additional Potentials. *J. Chem. Phys.* **2002**, *106* (20), 8527–8544.
(28) Mukhopadhyay, A.; Cole, W. T. S.; Saykally, R. J. The Water Dimer I: Experimental Characterization. *Chem. Phys. Lett.* **2015**, *633*, 13–26.
(29) Pugliano, N.; Saykally, R. J. Measurement of the Î½8 Intermolecular Vibration of (D2O)2 by Tunable Far Infrared Laser Spectroscopy. *J. Chem. Phys.* **1992**, *96* (3), 1832–1839.
(30) Keutsch, F. N.; Saykally, R. J. Water Clusters: Untangling the Mysteries of the Liquid, One Molecule at a Time. *Proc. Natl. Acad. Sci.* **2001**, *98* (19), 10533–10540.
(31) Smit, M. J.; Groenenboom, G. C.; Wormer, P. E. S.; Van Der Avoird, A.; Bukowski, R.; Szalewicz, K. Vibrations, Tunneling, and Transition Dipole Moments in the Water Dimer. *J. Phys. Chem. A* **2001**, *105* (25), 6212–6225.

(32) Buckingham, A. D.; Del Bene, J. E.; McDowell, S. A. C. The Hydrogen Bond. *Chem. Phys. Lett.* **2008**, *463* (1–3), 1–10.
(33) Coudert, L. H.; Hougen, J. T. Tunneling Splittings in the Water Dimer: Further Development of the Theory. *J. Mol. Spectrosc.* **1988**, *130* (1), 86–119.
(34) Coudert, L. H.; Hougen, J. T. Analysis of the Microwave and Far Infrared Spectrum of the Water Dimer. *J. Mol. Spectrosc.* **1990**, *277*, 259–277.
(35) Longuet-Higgins, H. C. The Symmetry Groups of Non-Rigid Molecules. *Mol. Phys.* **2002**, *100* (1), 11–20.
(36) Braly, L. B.; Cruzan, J. D.; Liu, K.; Fellers, R. S.; Saykally, R. J. Terahertz Laser Spectroscopy of the Water Dimer Intermolecular Vibrations. I. (D2O)2. *J. Chem. Phys.* **2000**, *112* (23), 10293–10313.
(37) Braly, L. B.; Brown, M. G.; Keutsch, F. N.; Fellers, R. S.; Saykally, R. J. Terahertz Laser Spectroscopy of the Water Dimer Intermolecular Vibrations. II. (H2O)2. *J. Chem. Phys.* **2000**, *112* (23), 10314–10326.
(38) Goldman, N.; Keutsch, F. N.; Saykally, R. J.; Leforestier, C.; Harker, H. A. Complete Characterization of the Water Dimer Vibrational Ground State and Testing the VRT(ASP-W)III, SAPT-5st, and VRT(MCY-5f) Surfaces. *Mol. Phys.* **2004**, *101* (23–24), 3477–3492.
(39) Coudert, L. H.; Lovas, F. J.; Suenram, R. D.; Hougen, J. T. New Measurements of Microwave Transitions in the Water Dimer. *J. Chem. Phys.* **1987**, *87* (11), 6290–6299.
(40) Suenram, R. D.; Fraser, G. T.; Lovas, F. J. Microwave Spectrum of (D20) 2. *J. Mol. Spectrosc.* **1989**, *138*, 440–449.
(41) Keutsch, F. N.; Fellers, R. S.; Brown, M. G.; Viant, M. R.; Petersen, P. B.; Saykally, R. J. Hydrogen Bond Breaking Dynamics of the Water Trimer in the Translational and Librational Band Region of Liquid Water. *J. Am. Chem. Soc.* **2001**, *123* (25), 5938–5941.
(42) Bakker, H. J.; Woutersen, S.; Nienhuys, H. K. Reorientational Motion and Hydrogen-Bond Stretching Dynamics in Liquid Water. *Chem. Phys.* **2000**, *258* (2–3), 233–245.
(43) Luzar, A.; Chandler, D. Structure and Hydrogen Bond Dynamics Mixtures by Computer Simulations. *J. Chem. Phys.* **1993**, *98* (10), 8160–8173.
(44) Luzar, A.; Chandler, D. Effect of Environment on Hydrogen Bond Dynamics in Liquid Water. *Phys. Rev. Lett.* **1996**, *76* (6), 928–931.
(45) Keutsch, F. N.; Cruzan, J. D.; Saykally, R. J. The Water Trimer. *Chem. Rev.* **2003**, *103* (7), 2533–2577.
(46) Goss, L. M.; Brault, J. W.; Blake, T. A.; Sharpe, S. W.; Vaida, V. Direct Absorption Spectroscopy of Water Clusters. *J. Phys. Chem. A* **2002**, *103* (43), 8620–8624.
(47) Blake, G. A.; Laughlin, K. B.; Cohen, R. C.; Busarow, K. L.; Gwo, D. H.; Schmuttenmaer, C. A.; Steyert, D. W.; Saykally, R. J. Tunable Far Infrared Laser Spectrometers. *Rev. Sci. Instrum.* **1991**, *62* (7), 1693–1700.
(48) Blake, G. A.; Laughlin, K. B.; Cohen, R. C.; Busarow, K. L.; Gwo, D. H.; Schmuttenmaer, C. A.; Steyert, D. W.; Saykally, R. J. The Berkeley Tunable Far Infrared Laser Spectrometers. *Rev. Sci. Instrum.* **1991**, *62* (7), 1701–1716.
(49) Liu, K.; Fellers, R. S.; Viant, M. R.; McLaughlin, R. P.; Brown, M. G.; Saykally, R. J. A Long Path Length Pulsed Slit Valve Appropriate for High Temperature Operation: Infrared Spectroscopy of Jet-Cooled Large Water Clusters and Nucleotide Bases. *Rev. Sci. Instrum.* **1996**, *67* (2), 410–416.
(50) Von Puttkamer, K.; Quack, M. High Resolution Interferometric FTIR Spectroscopy of

(HF)2: Analysis of a Low Frequency Fundamental near 400 Cm-1. *Mol. Phys.* **1987**, *62* (5), 1047–1064.
(51) Ceponkus, J.; Engdahl, A.; Uvdal, P.; Nelander, B. Structure and Dynamics of Small Water Clusters, Trapped in Inert Matrices. *Chem. Phys. Lett.* **2013**, *581*, 1–9.
(52) Ceponkus, J.; Nelander, B. Water Dimer in Solid Neon. Far-Infrared Spectrum. *J. Phys. Chem. A* **2004**, *108* (31), 6499–6502.
(53) Ceponkus, J.; Uvdal, P.; Nelander, B. Intermolecular Vibrations of Different Isotopologs of the Water Dimer: Experiments and Density Functional Theory Calculations. *J. Chem. Phys.* **2008**, *129* (19), 1–7.
(54) Ceponkus, J.; Uvdal, P.; Nelander, B. Far-Infrared Band Strengths in the Water Dimer: Experiments and Calculations. *J. Phys. Chem. A* **2008**, *112* (17), 3921–3926.
(55) Saykally, R. J.; Leforestier, C.; Harker, H. A.; Han, J.-X.; Keutsch, F. N.; Scribano, Y. Toward a Precise Determination of the Acceptor Switching Splitting in the Water Dimer. *Mol. Phys.* **2007**, *105* (5–7), 497–512.
(56) Hu, T. A.; Dyke, T. R. Water Dimer Coriolis Resonances and Stark Effects. *J. Chem. Phys.* **1989**, *91* (12), 7348–7354.
(57) Harker, H. A.; Keutsch, F. N.; Leforestier, C.; Scribano, Y.; Han, J. X.; Saykally, R. J. Refinements in the Description of Excited VRT States of the Water Dimer. *Mol. Phys.* **2007**, *105* (5–7), 513–527.
(58) Cole, W. T. S.; Hlavacek, N. C.; Lee, A. W. M.; Kao, T.-Y.; Hu, Q.; Reno, J. L.; Saykally, R. J. A Terahertz VRT Spectrometer Employing Quantum Cascade Lasers. *Chem. Phys. Lett.* **2015**, *638*, 144–148.
(59) Reisler, H.; Bowman, J. M.; Czakó, G.; Mancini, J. S.; Wang, Y.; Samanta, A. K. Experimental and Theoretical Investigations of Energy Transfer and Hydrogen-Bond Breaking in Small Water and HCl Clusters. *Acc. Chem. Res.* **2014**, *47* (8), 2700–2709.
(60) Maréchal, Y. The Molecular Structure of Liquid Water Delivered by Absorption Spectroscopy in the Whole IR Region Completed with Thermodynamics Data. *J. Mol. Struct.* **2011**, *1004* (1–3), 146–155.
(61) Luzar, A. Resolving the Hydrogen Bond Dynamics Conundrum. *J. Chem. Phys.* **2000**, *113* (23), 10663–10675.
(62) Luzar, A.; Chandler, D. Hydrogen-Bond Kinetics in Liquid Water. *Nature* **1996**, *379*, 55–57.
(63) Xantheas, S. S. Ab Initio Studies of Cyclic Water Clusters (H 2 O) n , n =1–6. II. Analysis of Many-body Interactions . *J. Chem. Phys.* **2002**, *100* (10), 7523–7534.
(64) Xantheas, S. S. Ab Initio Studies of Cyclic Water Clusters (H2O)n, n = 1-6. III. Comparison of Density Functional with MP2 Results. *J. Chem. Phys.* **1995**, *102* (11), 4505–4517.
(65) Xantheas, S. S.; Dunning, T. H. Ab Initio Studies of Cyclic Water Clusters (H2O)n, N=1-6. I. Optimal Structures and Vibrational Spectra. *J. Chem. Phys.* **1993**, *99* (11), 8774–8792.
(66) Wales, D. J.; Walsh, T. R. Theoretical Study of the Water Pentamer. *J. Chem. Phys.* **1996**, *105* (16), 6957–6971.
(67) Restrepo, A.; Guerra, D.; Hadad, C. Z.; Ramírez, F.; David, J. Structural Studies of the Water Pentamer. *Chem. Phys. Lett.* **2011**, *507* (4–6), 229–233.
(68) Wales, D. J.; Momen, R.; Xu, T.; Farrell, J.; Xu, Y.; Kirk, S. R.; Jenkins, S. QTAIM and Stress Tensor Interpretation of the (H 2 O) 5 Potential Energy Surface . *J. Comput. Chem.*

2016, *37* (31), 2712–2721.
(69) Liu, K.; Brown, M. G.; Cruzan, J. D.; Saykally, R. J. Vibration-Rotation Tunneling Spectra of the Water Pentamer: Structure and Dynamics. *Science (80-.).* **1996**, *271* (5245), 62–64.
(70) Liu, K.; Brown, M. G.; Cruzan, J. D.; Saykally, R. J. Terahertz Laser Spectroscopy of the Water Pentamer: Structure and Hydrogen Bond Rearrangement Dynamics. *J. Phys. Chem. A* **1997**, *101* (48), 9011–9021.
(71) Brown, M. G.; Keutsch, F. N.; Saykally, R. J. The Bifurcation Rearrangement in Cyclic Water Clusters: Breaking and Making Hydrogen Bonds. *J. Chem. Phys.* **1998**, *109* (22), 9645–9647.
(72) Cruzan, J. D.; Viant, M. R.; Brown, M. G.; Lucas, D. D.; Liu, K.; Saykally, R. J. Terahertz Laser Vibration-Rotation-Tunneling Spectrum of the Water Pentamer-D10. Constraints on the Bifurcation Tunneling Dynamics. *Chem. Phys. Lett.* **1998**, *292* (4–6), 667–676.
(73) Harker, H. A.; Viant, M. R.; Keutsch, F. N.; Michael, E. A.; McLaughlin, R. P.; Saykally, R. J. Water Pentamer: Characterization of the Torsional-Puckering Manifold by Terahertz VRT Spectroscopy. *J. Phys. Chem. A* **2005**, *109* (29), 6483–6497.
(74) Viant, M. R.; Brown, M. G.; Cruzan, J. D.; Saykally, R. J.; Geleijns, M.; Van Der Avoird, A. Quantitative Characterization of the (D2O)3 Torsional Manifold by Terahertz Laser Spectroscopy and Theoretical Analysis. *J. Chem. Phys.* **1999**, *110* (9), 4369–4381.
(75) Wales, D. J. Theoretical Study of Water Trimer. *J. Am. Chem. Soc.* **1993**, *115* (24), 11180–11190.
(76) Graf, S.; Mohr, W.; Leutwyler, S. An Ab Initio Study of the Torsional-Puckering Pseudorotation in the Cyclic Water Pentamer. *J. Chem. Phys.* **1999**, *110* (16), 7893–7908.
(77) Liu, Kun; Brown, M. G.; Carter, C.; Saykally, R.J.; Gregory, J.K.; Clary, D. C. Characterization of a Cage Form of the Water Hexamer. *Nature* **1996**, *381*, 501–503.
(78) Liu, K.; Brown, M. G.; Saykally, R. J. Terahertz Laser Vibration-Rotation Tunneling Spectroscopy and Dipole Moment of a Cage Form of the Water Hexamer. *J. Phys. Chem. A* **1997**, *101* (48), 8995–9010.
(79) Pérez, C.; Muckle, M. T.; Zaleski, D. P.; Seifert, N. A.; Temelso, B.; Shields, G. C.; Kisiel, Z.; Pate, B. H. Structures of Cage, Prism, and Book Isomers of Water Hexamer from Broadband Rotational Spectroscopy. *Science (80-.).* **2012**, *336* (6083), 897–901.
(80) Richardson, J. O.; Pérez, C.; Lobsiger, S.; Reid, A. A.; Temelso, B.; Shields, G. C.; Kisiel, Z.; Wales, D. J.; Pate, B. H.; Althorpe, S. C. Concerted Hydrogen-Bond Breaking by Quantum Tunneling in the Water Hexamer Prism. *Science (80-.).* **2016**, *351* (6279), 1310–1313.
(81) Balasubramanian, K. Nonrigid Group Theory, Tunneling Splittings, and Nuclear Spin Statistics of Water Pentamer: (H2O)5. *J. Phys. Chem. A* **2004**, *108* (26), 5527–5536.
(82) Cruzan, J. D.; Brown, M. G.; Liu, K.; Braly, L. B.; Saykally, R. J. The Far-Infrared Vibration – Rotation – Tunneling Spectrum of the Water Tetramer-d 8. *J. Chem. Phys* **1996**, *105* (July), 6634–6644.
(83) Cruzan, J. D.; Viant, M. R.; Brown, M. G.; Saykally, R. J. Terahertz Laser Vibration - Rotation Tunneling Spectroscopy of the Water Tetramer. *J. Phys. Chem. A* **1997**, *101* (48), 9022–9031.
(84) Gregory, J. K.; Clary, D. C. Tunneling Dynamics in Water Tetramer and Pentamer. *J. Chem. Phys.* **1996**, *105* (16), 6626–6633.
(85) Mandziuk, M. On the Tunneling Splitting in a Cyclic Water Trimer. *Chem. Phys. Lett.*

2016, *661*, 263–268.
(86) Clary, D. C. Quantum Dynamics in the Smallest Water Droplet. *Science (80-.).* **2016**, *351* (6279), 1267–1268.
(87) Babin, V.; Paesani, F. The Curious Case of the Water Hexamer: Cage vs. Prism. *Chem. Phys. Lett.* **2013**, *580*, 1–8.
(88) Paesani, F. Getting the Right Answers for the Right Reasons: Toward Predictive Molecular Simulations of Water with Many-Body Potential Energy Functions. *Acc. Chem. Res.* **2016**, *49* (9), 1844–1851.
(89) Wang, Y.; Bowman, J. M. IR Spectra of the Water Hexamer: Theory, with Inclusion of the Monomer Bend Overtone, and Experiment Are in Agreement. *J. Phys. Chem. Lett.* **2013**, *4* (7), 1104–1108.
(90) Kryachko, E. S. Ab Initio Studies of the Conformations of Water Hexamer: Modelling the Penta-Coordinated Hydrogen-Bonded Pattern in Liquid Water. *Chem. Phys. Lett.* **1999**, *314* (3–4), 353–363.
(91) Samanta, A. K.; Wang, Y.; Mancini, J. S.; Bowman, J. M.; Reisler, H. Energetics and Predissociation Dynamics of Small Water, HCl, and Mixed HCl-Water Clusters. *Chem. Rev.* **2016**, *116* (9), 4913–4936.
(92) Santra, B.; Michaelides, A.; Fuchs, M.; Tkatchenko, A.; Filippi, C.; Scheffler, M. On the Accuracy of Density-Functional Theory Exchange-Correlation Functionals for H Bonds in Small Water Clusters. II. the Water Hexamer and van Der Waals Interactions. *J. Chem. Phys.* **2008**, *129* (19), 194111–194125.
(93) Temelso, B.; Shields, G. C. The Role of Anharmonicity in Hydrogen Bonded Systems: The Case of Water Clusters. *J. Chem. Theory Comput.* **2011**, *7* (9), 2804–2817.
(94) Brown, S. E.; Götz, A. W.; Cheng, X.; Steele, R. P.; Mandelshtam, V. A.; Paesani, F. Monitoring Water Clusters "Melt" Through Vibrational Spectroscopy. *J. Am. Chem. Soc.* **2017**, *139* (20), 7082–7088.
(95) Huang, Y.; Zhang, X.; Ma, Z.; Zhou, Y.; Zheng, W.; Zhou, J.; Sun, C. Q. Hydrogen-Bond Relaxation Dynamics: Resolving Mysteries of Water Ice. *Coord. Chem. Rev.* **2015**, *285*, 109–165.
(96) Pham, C. H.; Reddy, S. K.; Chen, K.; Knight, C.; Paesani, F. Many-Body Interactions in Ice. *J. Chem. Theory Comput.* **2017**, *13* (4), 1778–1784.
(97) Saykally, R. J.; Wales, D. J. Pinning Down the Water Hexamer. *Science (80-.).* **2012**, *336* (May), 814–815.
(98) Guevara-Vela, J. M.; Romero-Montalvo, E.; Mora Gómez, V. A.; Chávez-Calvillo, R.; García-Revilla, M.; Francisco, E.; Pendás, Á. M.; Rocha-Rinza, T. Hydrogen Bond Cooperativity and Anticooperativity within the Water Hexamer. *Phys. Chem. Chem. Phys.* **2016**, *18* (29), 19557–19566.
(99) Losada, M.; Leutwyler, S. Water Hexamer Clusters: Structures, Energies, and Predicted Mid-Infrared Spectra. *J. Chem. Phys.* **2002**, *117* (5), 2003–2016.
(100) Tainter, C. J.; Ni, Y.; Shi, L.; Skinner, J. L. Hydrogen Bonding and Oh-Stretch Spectroscopy in Water: Hexamer (Cage), Liquid Surface, Liquid, and Ice. *J. Phys. Chem. Lett.* **2013**, *4* (1), 12–17.
(101) Tainter, C. J.; Skinner, J. L. The Water Hexamer: Three-Body Interactions, Structures, Energetics, and OH-Stretch Spectroscopy at Finite Temperature. *J. Chem. Phys.* **2012**, *137* (10), 104304–104320.
(102) Gregory, J. K.; Clary, D. C.; Liu, K.; Brown, M. G.; Saykally, R. J. The Water Dipole

Moment in Water Clusters. *Science (80-.).* **1997**, *275*, 814–817.
(103) Wang, Y.; Babin, V.; Bowman, J. M.; Paesani, F. The Water Hexamer: Cage, Prism, or Both. Full Dimensional Quantum Simulations Say Both. *J. Am. Chem. Soc.* **2012**, *134* (27), 11116–11119.
(104) Chen, Y.; Li, H. Intermolecular Interaction in Water Hexamer. *J. Phys. Chem. A* **2010**, *114* (43), 11719–11724.
(105) Bates, D. M.; Tschumper, G. S. CCSD(T) Complete Basis Set Limit Relative Energies for Low-Lying Water Hexamer Structures. *J. Phys. Chem. A* **2009**, *113* (15), 3555–3559.
(106) Head-Gordon, M.; Head-Gordon, T. Analytic MP2 Frequencies without Fifth-Order Storage. Theory and Application to Bifurcated Hydrogen Bonds in the Water Hexamer. *Chem. Phys. Lett.* **1994**, *220* (1–2), 122–128.
(107) Kim, J.; Kim, K. S. Structures, Binding Energies, and Spectra of Isoenergetic Water Hexamer Clusters: Extensive Ab Initio Studies. *J. Chem. Phys.* **1998**, *109* (14), 5886–5895.
(108) Kim, K.; Jordan, K. D.; Zwier, T. S. Low-Energy Structures and Vibrational Frequencies of the Water Hexamer: Comparison with Benzene-(H2O)6. *J. Am. Chem. Soc.* **1994**, *116*, 11568–11569.
(109) Gregory, J. K.; Clary, D. C. Theoretical Study of the Cage Water Hexamer Structure. *J. Phys. Chem. A* **1997**, *101* (36), 6813–6819.
(110) Lee, C.; Chen, H.; Fitzgerald, G. Structures of the Water Hexamer Using Density Functional Methods. *J. Chem. Phys.* **1994**, *101* (5), 4472–4473.
(111) Jin Mhin, B.; Shik Kim, H.; Soon Kim, H.; Woo Yoon, C.; Kim, K. S. Ab Initio Studies of the Water Hexamer: Near Degenerate Structures. *Chem. Phys. Lett.* **1991**, *176* (1), 41–45.
(112) Hirabayashi, S.; Yamada, K. M. T. The Monocyclic Water Hexamer Detected in Neon Matrices by Infrared Spectroscopy. *Chem. Phys. Lett.* **2007**, *435* (1–3), 74–78.
(113) Nauta, K.; Miller, R. E. Formation of Cyclic Water Hexamer in Liquid Helium: Smallest Piece of Ice. *Science (80-.).* **2000**, *287* (January), 293–295.
(114) Pérez, C.; Shields, G. C.; Temelso, B.; Zaleski, D. P.; Seifert, N. A.; Pate, B. H.; Kisiel, Z. Hydrogen Bond Cooperativity and the Three-Dimensional Structures of Water Nonamers and Decamers. *Angew. Chemie Int. Ed.* **2014**, *53* (52), 14368–14372.
(115) Mallory, J. D.; Mandelshtam, V. A. Diffusion Monte Carlo Studies of MB-Pol (H2O)2-6and (D2O)2-6clusters: Structures and Binding Energies. *J. Chem. Phys.* **2016**, *145* (6), 2–6.
(116) Evangelisti, L.; Perez, C.; Lobsiger, S.; Seifert, N. A.; Zaleski, D. P.; Pate, B. H.; Kisiel, Z.; Temelso, B.; Shields, G. C. Deuterated Water Hexamer Observed by Chirped-Pulse Rotational Spectroscopy. In *International Symposium on Molecular Spectroscopy*; 2014.
(117) Western, C. M. PGOPHER: A Program for Simulating Rotational, Vibrational and Electronic Spectra. *J. Quant. Spectrosc. Radiat. Transf.* **2017**, *186*, 221–242.
(118) Barone, V. Anharmonic Vibrational Properties by a Fully Automated Second-Order Perturbative Approach. *J. Chem. Phys.* **2005**, *122* (1), 1–10.
(119) Barone, V. Vibrational Zero-Point Energies and Thermodynamic Functions beyond the Harmonic Approximation. *J. Chem. Phys.* **2004**, *120* (7), 3059–3065.
(120) Frisch, M. J.; Trucks, G. W.; Schlegel, H. B.; Scuseria, G. E.; Robb, M. A.; Cheeseman, J. R.; Scalmani, G.; Barone, V.; Mennucci, B.; Petersson, G. A.; et al. Guassian 09. *Guassian 09*. Guassian, INc.: Wallingford CT 2009.
(121) Liu, K.; Brown, M. G.; Saykally, R. J. Terahertz Laser Vibration - Rotation Tunneling

Spectroscopy and Dipole Moment of a Cage Form of the Water Hexamer. *J. Phys. Chem. A* **1997**, *101*, 8995–9010.
(122) Pérez, C.; Zaleski, D. P.; Seifert, N. A.; Temelso, B.; Shields, G. C.; Kisiel, Z.; Pate, B. H. Hydrogen Bond Cooperativity and the Three-Dimensional Structures of Water Nonamers and Decamers. *Angew. Chemie - Int. Ed.* **2014**, *53* (52), 14368–14372.
(123) Western, C. M.; Billinghurst, B. E. Automatic Assignment and Fitting of Spectra with Pgopher. *Phys. Chem. Chem. Phys.* **2017**, *19* (16), 10222–10226.
(124) Luzar, A.; Chandler, D. C. Hydrogen-Bond Kinetics in Liquid Water. *Nature* **1996**, *379*, 55–57.
(125) Wilkins, D. M.; Manolopoulos, D. E.; Pipolo, S.; Laage, D.; Hynes, J. T. Nuclear Quantum Effects in Water Reorientation and Hydrogen-Bond Dynamics. *J. Phys. Chem. Lett.* **2017**, *8* (12), 2602–2607.
(126) Liu, K.; Cruzan, J. D.; Saykally, R. J. Water Clusters. *Science (80-.).* **1996**, *271* (5251), 929–933.
(127) Pérez, C.; Pate, B. H.; Kisiel, Z.; Lobsiger, S.; Zaleski, D. P.; Temelso, B.; Shields, G. C.; Seifert, N. A. Broadband Fourier Transform Rotational Spectroscopy for Structure Determination: The Water Heptamer. *Chem. Phys. Lett.* **2013**, *571*, 1–15.
(128) Stillinger, F. H.; David, C. W. Study of the Water Octamer Using the Polarization Model of Molecular Interactions. *J. Chem. Phys.* **1980**, *73* (7), 3384–3389.
(129) Brink, G.; Glasser, L. Studies in Hydrogen Bonding: The Octamers of Water. *J. Phys. Chem.* **1984**, *88* (16), 3412–3414.
(130) Tsai, C. J.; Jordan, K. D. Monte Carlo Simulation of (H2O)8: Evidence for a Low-Energy S4 Structure and Characterization of the Solid ↔ Liquid Transition. *J. Chem. Phys.* **1991**, *95* (5), 3850–3853.
(131) Xantheas, S. S.; Aprà, E. The Binding Energies of the D2d and S4 Water Octamer Isomers: High-Level Electronic Structure and Empirical Potential Results. *J. Chem. Phys.* **2004**, *120* (2), 823–828.
(132) Tharrington, A. N.; Jordan, K. D. Parallel-Tempering Monte Carlo Study of (H2O)n = 6-9. *J. Phys. Chem. A* **2003**, *107* (38), 7380–7389.
(133) Wales, D. J.; Ohmine, I. Rearrangements of Model (H 2 O) 8 and (H 2 O) 20 Clusters . *J. Chem. Phys.* **2002**, *98* (9), 7257–7268.
(134) Miyake, T.; Aida, M. H-Bond Patterns and Structure Distributions of Water Octamer (H<inf>2</Inf>O)<inf>8</Inf> at Finite Temperatures. *Chem. Phys. Lett.* **2006**, *427* (1–3), 215–220.
(135) Temelso, B.; Archer, K. A.; Shields, G. C. Benchmark Structures and Binding Energies of Small Water Clusters with Anharmonicity Corrections. *J. Phys. Chem. A* **2011**, *115* (43), 12034–12046.
(136) Gelman-Constantin, J.; Carignano, M. A.; Szleifer, I.; Marceca, E. J.; Corti, H. R. Structural Transitions and Dipole Moment of Water Clusters (H2 O) N=4-100. *J. Chem. Phys.* **2010**, *133* (2).
(137) Maeda, S.; Ohno, K. Structures of Water Octamers (H2O)8: Exploration on Ab Initio Potential Energy Surfaces by the Scaled Hypersphere Search Method. *J. Phys. Chem. A* **2007**, *111* (20), 4527–4534.
(138) Miliordos, E.; Xantheas, S. S. An Accurate and Efficient Computational Protocol for Obtaining the Complete Basis Set Limits of the Binding Energies of Water Clusters at the MP2 and CCSD(T) Levels of Theory: Application to (H2O)m, m = 2-6, 8, 11, 16, and 17.

J. Chem. Phys. **2015**, *142* (23).
(139) Day, M. B.; Kirschner, K. N.; Shields, G. C. Pople's Gaussian-3 Model Chemistry Applied to an Investigation of (H 2O)8 Water Clusters. *Int. J. Quantum Chem.* **2005**, *102* (5 SPEC. ISS.), 565–572.
(140) Morrell, T. E.; Shields, R. M.; Shields, G. C.; Archer, K. A.; Temelso, B. Accurate Predictions of Water Cluster Formation, (H 2 O) n =2−10 . *J. Phys. Chem. A* **2010**, *114* (43), 11725–11737.
(141) Asare, E.; Musah, A. R.; Curotto, E.; Freeman, D. L.; Doll, J. D. The Thermodynamic and Ground State Properties of the TIP4P Water Octamer. *J. Chem. Phys.* **2009**, *131* (18).
(142) Hernández-Rojas, J.; González, B. S.; James, T.; Wales, D. J. Thermodynamics of Water Octamer in a Uniform Electric Field. *J. Chem. Phys.* **2006**, *125* (22), 1–5.
(143) Nigra, P.; Carignano, M. A.; Kais, S. Study of Phase Changes of the Water Octamer Using Parallel Tempering and Multihistogram Methods. *J. Chem. Phys.* **2001**, *115* (6), 2621–2628.
(144) Sun, Y. guang; Gao, E. jun; Wei, D. zhou. Construction of Two-Dimensional Supramolecular Structure Containing Water Tetramer and Octamer. *Inorg. Chem. Commun.* **2007**, *10* (4), 467–470.
(145) Wales, D. J.; Ohmine, I. Structure, Dynamics, and Thermodynamics of Model (H2O) 8 and (H2O)20 Clusters. *J. Chem. Phys.* **1993**, *98* (9), 7245–7256.
(146) James, T.; Wales, D. J.; Hernández Rojas, J. Energy Landscapes for Water Clusters in a Uniform Electric Field. *J. Chem. Phys.* **2007**, *126* (5).
(147) Buck, U.; Ettischer, I.; Melzer, M.; Buch, V.; Sadlej, J. Structure and Spectra of Three-Dimensional (H$_2$O)$_n$ Clusters, n=8,9,10. *Phys. Rev. Lett.* **1998**, *80* (12), 2578–2581.
(148) Gruenloh, C. J.; Wang, Z. Q.; Zweier, J. L.; Samouilov, A.; Macarthur, H.; Misko, T. P.; Currie, M. G.; Cuzzocrea, S.; Sikorski, J. A.; Riley, D. P. Infrared Spectrum of a Molecular Ice Cube: The S4 and D2d Water Octamers in Benzene-(Water)8. *Science (80-.).* **1997**, *276* (5319), 1678–1681.
(149) Gruenloh, C. J.; Fredericks, S. Y.; Wood, J. T.; Jordan, K. D.; Carney, J. R.; Zwier, T. S.; Arrington, C. A.; Hagemeister, F. C. Resonant Ion-Dip Infrared Spectroscopy of the S4 and D2d Water Octamers in Benzene-(Water)8 and Benzene2-(Water)8. *J. Chem. Phys.* **2002**, *109* (16), 6601–6614.
(150) Suitte, B. P.; Belair, S. D.; Francisco, J. S. Spectroscopic Characterization of the Five Possible Orientations of a Hydrogen-Bonded Pair of Water Molecules within the Cubic Water Octamer Framework. *Phys. Rev. A - At. Mol. Opt. Phys.* **2005**, *71* (4), 2–7.
(151) Blanton, W. B.; Gordon-Wylie, S. W.; Clark, G. R.; Jordan, K. D.; Wood, J. T.; Geiser, U.; Collins, T. J. Synthesis and Crystallographic Characterization of an Octameric Water Complex, (H2O)8 [12]. *J. Am. Chem. Soc.* **1999**, *121* (14), 3551–3552.
(152) Hao, H.; Sun, D.; Liu, F.; Huang, R.; Zheng, L. Discrete Octamer Water Cluster and 1D T5 (2) Water Tape Trapped in Hosts : From 2D (4 , 4) Net to 3D 5-Fold Interpenetrated Diamond Network. **2011**, *5* (2), 5475–5482.
(153) Prasad, T. K.; Rajasekharan, M. V. A Novel Water Octamer in Ce(Dipic)$_2$(H$_2$O)$_3$ 4H$_2$O: Crystallographic, Thermal, and Theoretical Studies. *Cryst. Growth Des.* **2006**, *6* (2), 488–491.
(154) Cruzan, J. D.; Braly, L. B.; Liu, K.; Brown, M. G.; Loeser, J. G.; Saykally, R. J. Quantifying Hydrogen Bond Cooperativity in Water: VRT Spectroscopy of the Water

Tetramer. *Science (80-.)*. **1996**, *271* (5245), 59–62.
(155) Babin, V.; Medders, G. R.; Paesani, F. Development of a “First Principles” Water Potential with Flexible Monomers. II: Trimer Potential Energy Surface, Third Virial Coefficient, and Small Clusters. *J. Chem. Theory Comput.* **2014**, *10* (4), 1599–1607.
(156) Medders, G. R.; Babin, V.; Paesani, F. Development of a “First-Principles” Water Potential with Flexible Monomers. III. Liquid Phase Properties. *J. Chem. Theory Comput.* **2014**, *10* (8), 2906–2910.
(157) Goldman, N.; Fellers, R. S.; Leforestier, C.; Saykally, R. J. Water Dimers in the Atmosphere : Equilibrium Constant for Water Dimerization from The. *J. Phys. Chem. A* **2001**, *105* (3), 515.
(158) Scribano, Y.; Goldman, N.; Saykally, R. J.; Leforestier, C. Water Dimers in the Atmosphere III: Equilibrium Constant from a Flexible Potential. *J. Phys. Chem. A* **2006**, *110* (16), 5411–5419.
(159) Goldman, N.; Leforestier, C.; Saykally, R. J. Water Dimers in the Atmosphere II: Results from the VRT(ASP-W)III Potential Surface. *J. Phys. Chem. A* **2004**, *108* (5), 787–794.
(160) Babin, V.; Leforestier, C.; Paesani, F. Erratum: Development of a “ First-Principles ” Water Potential with Flexible Monomers: Dimer Potential Energy Surface, VRT Spectrum, and Second Virial Coe Ffi Cient. *J. Chem. Theory Comput.* **2013**, *9* (4), 5395–5403.
(161) Wang, Y.; Huang, X.; Shepler, B. C.; Braams, B. J.; Bowman, J. M. Flexible, Ab Initio Potential, and Dipole Moment Surfaces for Water. I. Tests and Applications for Clusters up to the 22-Mer. *J. Chem. Phys.* **2011**, *134* (9).
(162) Ohmine, I.; Tanaka, H. Fluctuation, Relaxations, and Hydration in Liquid Water. Hydrogen-Bond Rearrangement Dynamics. *Chem. Rev.* **1993**, *93* (7), 2545–2566.
(163) Stillinger, F. H. Water Revisited. *Science (80-.)*. **1980**, *209* (4455), 451–457.
(164) Teixeira, J.; Luzar, A. Series A: Life Sciences - HYdration Processes in Biology. In *Physics of Liquid Water. Structure and Dynamics*; 1999; p 35.
(165) Cabral, J. T.; Luzar, A.; Teixeira, J.; Bellissent-Funel, M. C. Single-Particle Dynamics in Dimethyl-Sulfoxide/Water Eutectic Mixture by Neutron Scattering. *J. Chem. Phys.* **2000**, *113* (19), 8736–8745.
(166) Conde, O.; Teixeiraj, J. Depolarized Light Scattering of Heavy Water, and Hydrogen Bond Dynamics. *Mol. Phys.* **1984**, *53* (4), 951–959.
(167) Fecko, C. J.; Loparo, J. J.; Roberts, S. T.; Tokmakoff, A. Local Hydrogen Bonding Dynamics and Collective Reorganization in Water: Ultrafast Infrared Spectroscopy of HOD/D 2O. *J. Chem. Phys.* **2005**, *122* (5), 0–18.
(168) Lankhorst, D.; Schriever, J.; Leyte, J. C. Determination of the Rotational Correlation Time of Water by Proton NMR Relaxation in H$_2$17O and Some Related Results. *Ber. Bunsenges. Phys. Chem.* **1982**, *86*, 215–221.
(169) Nienhuys, H.; Woutersen, S.; Santen, R. A. Van; Bakker, H. J.; Woutersen, S. Mechanism for Vibrational Relaxation in Water Investigated by Femtosecond Infrared Spectroscopy Mechanism for Vibrational Relaxation in Water Investigated by Femtosecond Infrared Spectroscopy. *J. Chem. Phys.* **2017**, *1494* (1999), 1494–1500.
(170) Habershon, S.; Markland, T. E.; Manolopoulos, D. E. Competing Quantum Effects in the Dynamics of a Flexible Water Model. *J. Chem. Phys.* **2009**, *131* (2), 1–36.
(171) Michaelides, A. Quantum Nature of the Hydrogen Bond. *Acta Crystallogr. Sect. A Found. Crystallogr.* **2015**, *67* (a1), C195–C195.

(172) Luzar, A. Water Hydrogen-Bond Dynamics Close to Hydrophobic and Hydrophilic Groups. *Faraday Discuss.* **1996**, *103*, 29–40.
(173) Teixeira, J.; Bellissent-Funel, M. C.; Chen, S. H.; Dianoux, A. J. Experimental Determination of the Nature of Diffusive Motions of Water Molecules at Low Temperatures. *Phys. Rev. A* **1985**, *31* (3), 1913–1917.
(174) Teixeira, J.; Luzar, A.; Longeville, S. Dynamics of Hydrogen Bonds: How to Probe Their Role in the Unusual Properties of Liquid Water. *J. Phys. Condens. Matter* **2006**, *18* (36).
(175) Woutersen, S.; Emmerichs, U.; Bakker, H. J. Femtosecond Mid-IR Pump-Probe Spectroscopy of Liquid Water: Evidence for a Two-Component Structure. *Science (80-.).* **1997**, *278* (5338), 658–660.
(176) Auer, B. M.; Skinner, J. L. Water: Hydrogen Bonding and Vibrational Spectroscopy, in the Bulk Liquid and at the Liquid/Vapor Interface. *Chem. Phys. Lett.* **2009**, *470* (1–3), 13–20.
(177) Huse, N.; Ashihara, S.; Nibbering, E. T. J.; Elsaesser, T. Ultrafast Vibrational Relaxation of O-H Bending and Librational Excitations in Liquid H2O. *Chem. Phys. Lett.* **2005**, *404* (4–6), 389–393.
(178) Ni, Y.; Skinner, J. L. IR and SFG Vibrational Spectroscopy of the Water Bend in the Bulk Liquid and at the Liquid-Vapor Interface, Respectively. *J. Chem. Phys.* **2015**, *143* (1), 0–12.
(179) Cowan, M. L.; Bruner, B. D.; Huse, N.; Dwyer, J. R.; Chugh, B.; Nibbering, E. T. J.; Elsaesser, T.; Miller, R. J. D. Ultrafast Memory Loss and Energy Redistribution in the Hydrogen Bond Network of Liquid H2O. *Nature* **2005**, *434* (7030), 199–202.
(180) De Marco, L.; Thämer, M.; Reppert, M.; Tokmakoff, A. Direct Observation of Intermolecular Interactions Mediated by Hydrogen Bonding. *J. Chem. Phys.* **2014**, *141* (3).
(181) Ramasesha, K.; De Marco, L.; Mandal, A.; Tokmakoff, A. Water Vibrations Have Strongly Mixed Intra- and Intermolecular Character. *Nat. Chem.* **2013**, *5* (11), 935–940.
(182) Fecko, C. J.; Eaves, J. D.; Loparo, J. J.; Tokmakoff, A.; Geissler, P. L. Ultrafast Hydrogen-Bond Dynamics in the Infrared. *Science (80-.).* **2003**, *301* (September), 1698–1702.
(183) Stenger, J.; Madsen, D.; Hamm, P.; Nibbering, E. T. J.; Elsaesser, T. A Photon Echo Peak Shift Study of Liquid Water. *J. Phys. Chem. A* **2002**, *106* (10), 2341–2350.
(184) Keutsch, F. N.; Saykally, R. J.; Wales, D. J. Bifurcation Tunneling Dynamics in the Water Trimer. *J. Chem. Phys.* **2002**, *117* (19), 8823–8835.
(185) Luzar, A. Extent of Inter-Hydrogen Bond Correlations in Water. Temperature Effect. *Chem. Phys.* **2000**, *258* (2–3), 267–276.

Chapter III: Angle-Resolved Second Harmonic Scattering Spectroscopy of Colloidal Solutions

Introduction to Second Harmonic Scattering

Understanding the detailed behavior of molecules at aqueous interfaces is of fundamental importance to current research topics, including cloud formation, water purification, ocean chemistry, and catalysis [1–17]. The first step towards understanding the behavior of a molecule at an interface is determining the thermodynamics of molecular partitioning from the bulk to the interface. Quantification of, for example, the free energy of adsorption requires a technique that is both surface-specific and specific to the selected molecule [5,10,12,18–21]. Second-order nonlinear spectroscopies exhibit high surface specificity under the dipole approximation and are molecule-specific if a resonant molecular transition exists at either the fundamental or a second-order frequency [21,22].

The two most widely employed second-order techniques, second harmonic generation (SHG) and sum frequency generation (SFG), are normally implemented in reflection geometry [1,2,17]. This geometry is advantageous when studying liquid-vapor interfaces [1,2,23], and second-order techniques can be extended to liquid-solid interfaces in two ways: First, the surface of a prism in contact with liquid can be probed through the prism; the prism surface in contact with the liquid can be functionalized as desired [24–27]. The second possibility, and that employed herein, is to utilize a scattering geometry on a colloidal sample [3,6,28–31]. Specifically, second harmonic scattering (SHS) has been demonstrated on systems of colloidal polystyrene beads (PSB) [3,19,32], nanoparticles [5,33–36], oil-water droplets [37–41], and biopolymers [6,30,42,43]. By exploiting the constructive interference of dipole radiation from particles with a diameter similar to the relevant light wavelength, surface-sensitive measurements of a colloidal solution are possible [18,22]. Using a dye with a resonantly-enhanced hyperpolarizability at the second harmonic frequency in solution, one can determine the thermodynamics of dye molecule adsorption to the solid surface by SHS [4,32,44].

To extend this technique to molecules without an accessible molecular transition, Eisenthal and coworkers developed a simple displacement methodology, wherein a resonant dye molecule adsorbed to a solid surface was competitively displaced by the molecule of interest; that technique later extended by other groups [9,15,28,29]. The resulting decay of the SHS signal can then be fit to a competitive adsorption model, and the adsorption behavior of the displacing molecule quantified. In addition to characterizing the adsorption thermodynamics of the subject molecule, the molecular orientation can also be determined if the full angle-resolved scattering pattern can be recorded with polarization control of the input and output light [4,19,31,45–47]. Several theoretical formalisms have been developed to extract this orientational information, exploiting Mie scattering theory or Rayleigh-Gans-Debye (RGB) scattering theories [19]. Orientation information is particularly valuable for experiments in the vibrational region, wherein vibrational transitions can extract a detailed picture of the chemical structure of an interface [18,37,48,49].

Experimental Setup

Our Angle Resolved Second Harmonic Scattering (AR_SHS) spectrometer consists of a pulsed Ti-Sapphire laser (Spectra Physics Tsunami) operated at 800 nm with a repetition rate of 80 MHz. Each pulse had an average duration of 100 fs and peak energy of ~9 nJ. The input beam was directed through a Faraday isolator (Electo-Optics Technology, Inc.) and a half-waveplate to control the input polarization, and then directed through an 800 nm bandpass filter to remove any nonlinear frequency components. The input beam was then focused to a beam waist of 50 µm using a microscope objective and directed through the glass sample vial (4mm diameter). The SH output was measured by a collection arm with a maximum angle of acceptance of 2˚, and comprising the following optics in series: an aperture, a focusing optic (f = 38.1 mm), 400 nm bandpass filter, a polarizer, and a final focusing optic (f = 75.6 mm). This arm was attached to a rotating stage with a movement range of 100˚ to either side of the transmission geometry. After the collection arm, SH light was directed into a spectrograph (Acton SpectroPro 2500i) *via* a fiber and into a PMT (Hamamatsu R212) operating in photon counting mode. All reported scans were collected with a counting time of 400 ms and represent the average of 20 separate collections with 2.5˚ steps from -90˚ to 90˚, where 0˚ is defined as transmission geometry. For the remainder of the paper, polarization schemes will be labeled with the input polarization followed by the output polarization (*e.g.*, a polarization of SP corresponds to an input polarization of S and an output polarization of P). Scans were subjected to background subtraction and normalization by the water signal as outlined in the Supplemental information presented in Appendix A of this thesis. A cartoon of the experimental setup is shown in Figure 1.

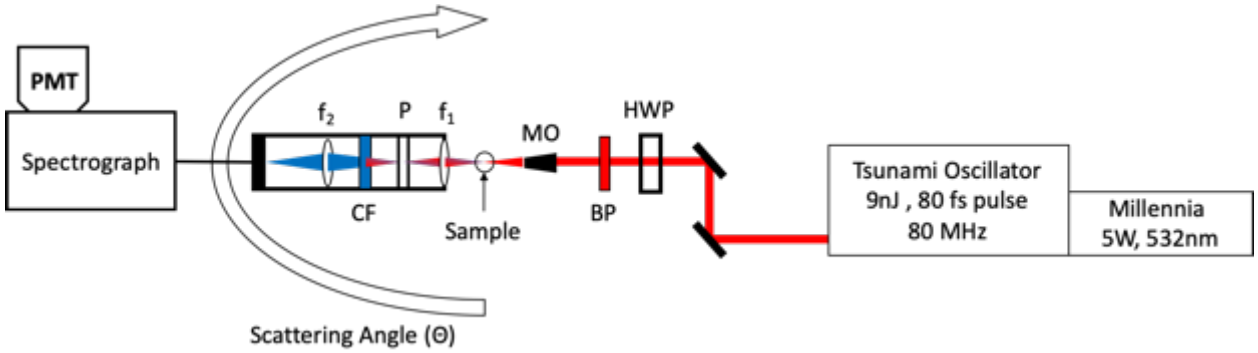

Figure 1: A cartoon of the AR-SHS setup. The beam path is described in detail in the text. Briefly, 800 nm fundamental light is output from a Ti-Sapphire oscillator passing though a half wave plate (HWP) and 800 nm bandpass filter (BP) before being focused onto the sample by a microscope objective (MO). The scattered second harmonic light is collected as a function of angle and passes through two focusing optics (f_1 and f_2), a polarizer (P), and a 400 nm cutoff filter (CF). The collected light is then sent to a PMT for photon counting via a fiber optics cable. The signal is digitized and sent to a computer for analysis.

The following section presents two studies of adsorption dynamics to colloidal samples. In both studies, a calibration curve of a resonant dye molecule is first collected and fit to a first order Langmuir isotherm in order to obtain a value for the Gibbs free energy of adsorption, ΔG_{Ads}. This value along with others from the fit are then used to analyze the SHS intensity decay at a fixed dye concentration as the concentration of a non-resonant, competitor molecule is increased. From this decay, a value of ΔG_{Ads} for the non-resonant molecule can be obtained. Additional information is contained in the measured scattering pattern, but will not be discussed in this thesis.

Adsorption to Polystyrene Beads

The first system investigated with this system was polystyrene beads (PSBs) with a negatively charged surface (nPSB) and a positively charged surface (pPSB). The surface groups responsible for the charge in each case were sulfate groups and amine groups for nPSB and pPSB respectively. PSBs were chosen as a model system due to their relative chemical inertness as well as their previous study in the literature. We also hoped that this surface would provide a more hydrophobic interface that the surface previously studied in our group [2,17].

Adsorption of Resonant Dye Molecules

The adsorption of two resonant dye molecules, Malachite Green (MG) and Naphthol Yellow S (NYS), were probed on nPSB and pPSB, respectively. Figure 2 shows the corresponding scattering patterns. There is a significant surface enhancement of the SHS signal relative to the background for both the aqueous dyes and the PSB alone. It is important to point out that the background from the dye arises from hyper-Rayleigh scattering, as its scattering pattern peaks at 0˚ (transmission geometry). In contrast, the surface-sensitive signal has a scattering pattern that peaks away from 0˚ and is a result of the molecular orientation of the dye molecules at the PSB surface [45]. The background contribution was subtracted from the scans to isolate the surface-sensitive signal, and the scans were normalized by the water signal to correct for differences in scattering volume, as has been described in the literature [3].

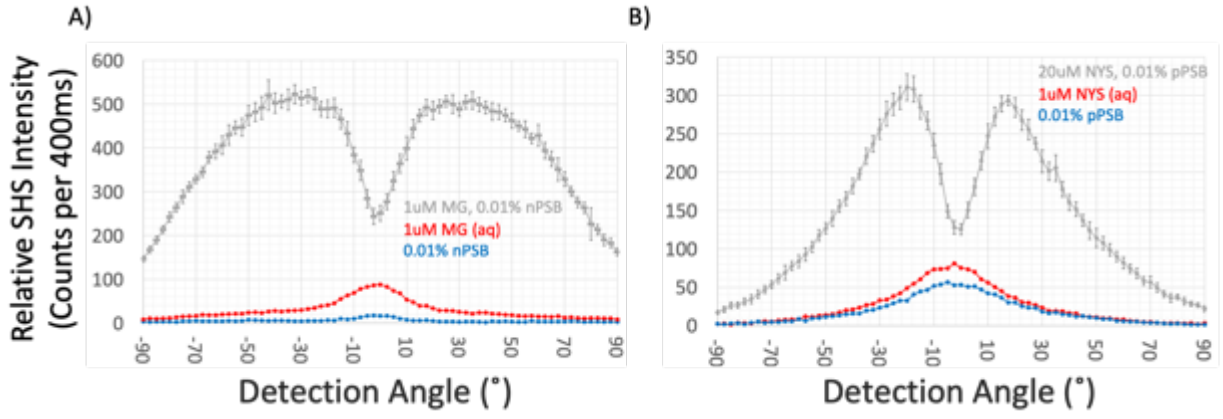

Figure 2: The scattering patterns for malachite green (MG) adsorbed on negative polystyrene (nPSB) (A) and naphthol yellow S (NYS) on positive polystyrene (pPSB) (B). The intensities represent the number of second harmonic photons recorded over a period of 400 ms; each point is the average of 20 measurements at a fixed angle. Error bars are the standard deviation of the arithmetic mean value. The patterns are recorded over an angular range of 180˚ with a resolution of 2.5˚. The data shown have not been subjected to background subtraction or normalization and represent the raw output of the experiment. For both scans,

the signal from the dye in solution with the PSB is shown in grey. The background signal from an aqueous solution of the dye is shown in red and the background of the pure PSB in blue.

In order to minimize flocculation, the pH was adjusted to 2 and 4 for pPSB and nPSB suspensions, respectively. The nPSB suspensions were more stable at higher pH, as the threshold PSB concentration at which the particles begin to flocculate is higher for higher pH. However, the resonance of MG shifts away from the second harmonic frequency of the experiment to longer wavelengths at pH higher than 9 [9,15,27] Additionally, previous studies on MG were performed at pH 4 [9,15], so we also performed our experiments at pH 4 to enable comparison with previously reported data. To determine the free energy of adsorption, the SHS intensity patterns were fit to a modified Langmuir isotherm as described by Wang et al [9,15]

$$I_{SHS} = B + \left[b + a * \theta_D * e^{i\emptyset}\right]^2 \qquad (1)$$

where *B* describes contributions from the constant, non-resonant background, *b* is the bulk contribution from the PSB sample, *a* is a fit constant describing the relative signal from the dye molecules at the surface of the bead, θ_D is the fractional coverage of the dye molecule, and Ø is a phase factor correspond to the difference between the PSB signal and the dye signal. All constants in the above equation are taken to be unitless due to the SHS intensity being normalized, unitless values as described in the supplemental. This version of the Langmuir isotherm is the typical first-order model modified to account for the decrease in bulk dye concentration due to adsorption to the surface [15].
The fractional coverage, θ_D, of the dye molecule is given by Equation 2:

$$\theta_D = \frac{\left[\left(C_D + N_m^D + \frac{55.5}{K_D}\right) - \left\{\left(C_D + N_m^D + \frac{55.5}{K_D}\right)^2 - 4C_D N_m^D\right\}^{1/2}\right]}{2N_m^D} \qquad (2)$$

here C_D is the concentration of the dye molecule in M, N_m^D is the maximum surface number density of the dye molecule in M, and K_D is the equilibrium constant for adsorption and has units M^{-1}, given by the equilibrium:

$$D + S \Leftrightarrow DS$$

here D represents a dye molecule, S represents a site, and DS is a site with a dye molecule adsorbed. Values of N_m^D and K_D can be obtained by fitting SHS signal intensity data to Equations 1 and 2 over a range of dye concentrations, C_D, for MG and NYS adsorption on nPSB and pPSB, respectively. Calculation of ΔG_{Ads} follows directly from the K_D value using a temperature of 25˚C. The results of these fits are shown in Figure 3. Figure 4 shows the fractional coverage calculated from Equation 2 for both MG and NYS on PSB. All constant values determined by the fits shown in Figure 3 are given in Table 1. The correlation matrices for each fit are shown in Appendix A.

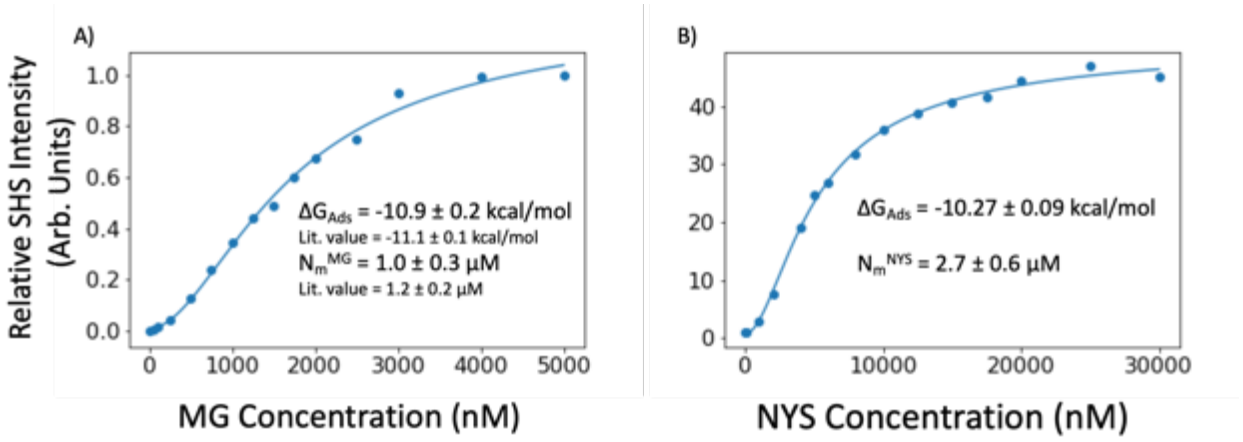

Figure 3: The fits of concentration series of MG adsorbed to (A) nPSB and (B) NYS adsorbed to pPSB to Equation 1. The values of ΔG_{Ads} and N_m^D are shown in the figure insets. Literature values for ΔG_{Ads} and N_m^D in (A) are taken from Wang et al[15]. The given uncertainties represent one standard deviation. The data points in Figure 2 represent the average of a sum over the angles of maximum scattering, defined as 30 to 70˚ for MG/nPSB and 15-60˚ for NYS/pPSB.

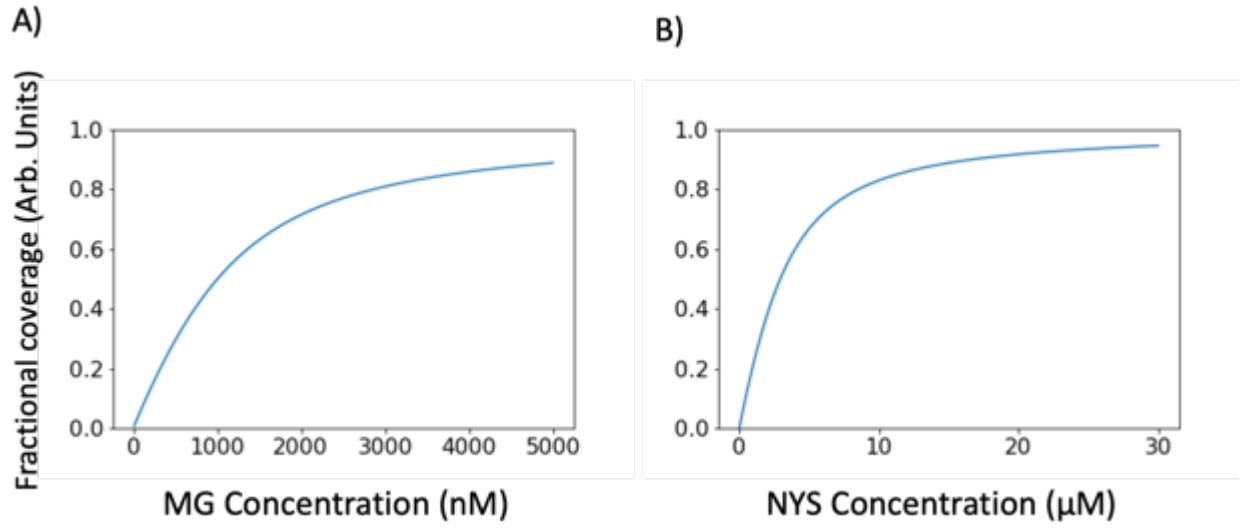

Figure 4: Plots of the fractional coverage of A) MG on nPSB and B) NYS on pPSB. Fractional coverages are calculated from Equation 2 using the constants obtained from the performed fit.

The adsorption of MG to nPSB has been studied previously [6,9,15] and serves as a convenient benchmark for our experimental methodology. We obtained a ΔG_{Ads} value of -11.0 ± 0.2 kcal/mol, which is comparable to values presented previously in the literature. Wang et al reported the ΔG_{Ads} for MG adsorption to 1μm diameter nPSB to be -11.2 ± 0.1 kcal/mol [15], and later studies reported values in the range -11.1 to -12.7 kcal/mol [4,9,32,43,44]. Schürer and Peukert reported a ΔG_{Ads} value of -11.8 ± 0.5 kcal/mol for polydisperse (controlled mixtures of 0.54 and 1.1 μm diameter) suspensions of nPSB [3]. Additionally, we find similar agreement between our value of 1.0 ± 0.3 μM for N_m^D and a reported value of 1.2 ± 0.2 μM [15].

To our knowledge, the adsorption of NYS to pPSB has not been reported prior to this study. We determined a ΔG_{Ads} value of -10.27 ± 0.09 kcal/mol at pH 2 and a N_m^D value of 2.7 ± 0.6 μM. It is interesting that NYS adsorption to pPSB is similar to MG adsorption to nPSB since NYS is divalent, although direct comparison is difficult due to the difference in surface charge density between the two PSB samples. Nevertheless, determination of ΔG_{Ads} and N_m^D values facillitate displacement studies of non-resonant molecules.

Displacement Studies

To obtain adsorption thermodynamics for non-resonant, competitor molecules, we utilized a displacement methodology first employed by Wang et al[9] to study competitive surfactant adsorption with MG on PSB. For a system in which two molecules compete for surface adsorption, the fractional coverage of the dye molecule becomes:

$$\theta_D = \frac{x}{1 + x + y} \qquad (3)$$

$$x = K_D * \frac{(C_D - N_m^D)}{55.5} \qquad (4)$$

$$y = K_C * \frac{(C_C - N_m^C)}{55.5} \qquad (5)$$

Here K_C, C_C, and N_m^C correspond to the competitor molecule ·and represent the same physical quantities as their counterparts K_D, C_D, and N_m^D and thus, have the same units; Equation 3 is derived from Equations 5a and 5b in Wang et al [9]. Equation 1 of this paper still describes the relationship between SHS intensity and the concentrations of the dye molecule and the competitive adsorber.

Two important assumptions of this method are that the surface sites can accommodate either a dye molecule or a competitor, and that all surface sites are chemically equivalent. While these assumptions prevent a detailed characterization of the chemical nature of the surface sites, this method nevertheless provides a route to determination of the relevant adsorption thermodynamics.

Using the determined K_D and N_m^D values for the dye molecule, we performed displacement studies on a variety of competitor molecules over a range of molecular sizes. Table 1 summarizes the results of these studies.

While it is possible to extract an N_m^C value as described by Wang et al [9], relatively high concentrations of the competitor were needed to induce displacement of the dye molecule due to large differences in adsorption ΔG_{Ads} values between the dye and competitors. As a result, the numerator in Equation 5 approaches the value C_C and therefore N_m^C cannot be fit independently from K_C. We elected to fix N_m^C to the value of N_m^D in order to obtain meaningful value for K_C. Any error in introduced to ΔG_{Ads} from this assumption should be negligible due to the magnitude difference between C_C and N_m^C; a similar method was used to extract ΔG_{Ads} values for biopolymers by Eisenthal and coworkers [6].

Table 1: Collection of fit constants.
Constants for Malachite Green and Naphthol Yellow S were obtained from Equations 1 and 2, while all other constants were obtained from Equations 1, 3-5 as explained in the text. B and a are fit constants without units, while the units of N_m^D and $-\Delta G_{Ads}$ are given in parentheses. The uncertainties provided represent one standard deviation.

		nPSB				pPSB			
Molecule	Structure	B	a	N_m^D (μM)	$-\Delta G_{Ads}$ (kcal/mol)	B	a	N_m^D (μM)	$-\Delta G_{Ads}$ (kcal/mol)
Malchite Green		0.01 ± 0.02	1.14 ± 0.05	1.0 ± 0.3	10.9 ± 0.2	NA	NA	NA	NA
Naphthol Yellow S		NA	NA	NA	NA	0.8 ± 0.6	7.2 ± 0.1	2.7 ± 0.6	10.27 ± 0.09
CTAB		0.006 ± 0.03	8.8 ± 0.4	NA	10.02 ± 0.04	0.001 ± 0.05	3.7 ± 0.9	NA	9.3 ± 0.3
Triton X		0.14 ± 0.02	10.7 ± 0.3	NA	9.38 ± 0.06	0.67 ± 0.06	0.76 ± 0.08	NA	7.5 ± 0.3
Caffeine		0.17 ± 0.04	12.1 ± 0.3	NA	4.43 ±0.08	0.22 ± 0.02	1.09 ± 0.01	NA	5.11 ± 0.05
Pentoxifylline		0.001 ± 0.04	13.7 ± 0.3	NA	4.17 ±0.09	0.004 ± 0.02	1.21 ± 0.01	NA	5.05 ± 0.04
Ascorbic Acid		0.21 ± 0.03	12.0 ± 0.2	NA	4.2 ± 0.1	0.28 ± 0.03	1.04 ± 0.02	NA	4.06 ± 0.07

Discussion

Inspecting the values for ΔG_{Ads} in Table 1, it is surprising to note that ΔG_{Ads} for MG to nPSB is so similar to that of NYS to pPSB. NYS is divalent, and it was expected that its adsorption would be enhanced relative to the monovalent MG. A possible explanation would be that the adsorption geometry of NYS to pPSB permits only one of the charged groups to interact with the surface charge. The excellent fit obtained from the first order Langmuir model used herein suggests that a single charge group of NYS interacts with one surface site, though further experiments would be needed to confirm this hypothesis.

Given that only 5-10% of the PSB surfaces are charged (according to manufacturer specification), van der Waals interactions are likely to be a significant adsorption driving force. A small effect of the surface charge is evident in the adsorption of CTAB to the two polymer surfaces, with adsorption of the positively charged surfactant to the negatively charged surface being favorable relative to adsorption to the positively charged surface. Although we expected the adsorption of pentoxifylline to the positive/negative surface to be more favorable than that of caffeine, these adsorptions were essentially identical. As the only structural difference between these two molecules is the 5-carbon ketone group on pentoxifylline, this observation may indicate that the present experiment is not suitable for separating the adsorption behavior of very similar molecules; however, a more detailed experiment would be needed to confirm this hypothesis.

Another unexpected observation was the difference in Triton X adsorption to nPSB and pPSB. Triton X is an uncharged surfactant, and we therefore expected similar adsorption behavior between both PSB surfaces. In our experiments, ΔG_{Ads} was significantly more negative (~1.5 kcal/mol) for adsorption to nPSB than for adsorption to pPSB. Additionally, caffeine and pentoxifylline were more likely to be adsorbed to the positive surface, while ascorbic acid exhibited no surface preference. As noted in the Results section, the solution pH of the nPSB samples was 4, while that of the pPSB samples was 2. This pH difference is small enough that pKa effects of the competitors are expected to be negligible. For the studied molecules, only ascorbic acid has a pKa (4.17) which is near the experimental pH. Based on the similar ΔG_{Ads} values of ascorbic acid to pPSB and to nPSB, we conclude that the pH difference is not a significant factor in the adsorption behavior of these molecules. These results suggest that the surface sites of the two PSB samples are slightly different, as evidenced by the different ΔG_{Ads} values obtained for caffeine and pentoxifylline. More detailed future studies could explore the adsorption of molecules as a function of pH and salt concentration to explicitly determine the contribution of surface charge to adsorption for each PSB sample. While other methods, such as UV absorption spectroscopy and adiabatic calorimetry, have been used to probe organic adsorption to polymeric surfaces [11,15], those methods have suffered from large uncertainties in ΔG_{Ads} (on the order of 1-2 kcal/mol). Our results show that SHS can be effective in probing the adsorption of non-resonant molecules to hydrophobic surfaces, which could enable the study of non-resonant molecules on more exotic surfaces than PSB presented herein. In addition, the resultant ΔG_{Ads} values have greater precision than those determined with other techniques. For example, the ΔG_{Ads} values measured by Gustafaon et al[11] for various organic molecules to polymer surfaces was 1-2 kcal/mol. Maity et al[14] reported uncertainties in the range of ~8%, in comparison the highest uncertainty reported here is 4%. Additionally, interpretation of the scattering pattern of resonant molecules has been shown to provide important details about the

molecular orientation of the adsorbate [45]. Studying the effect of competitive adsorption on molecular orientation could yield important insight into the fundamental adsorption process.

To our knowledge, this study comprises the first use of NYS as a resonant dye for SHS. Previous studies [44] have shown that MG adsorbs to pPSB; however, in our experiments we found the signal from MG adsorbed to pPSB to be dominated by aqueous MG background signal, which led to experimental inconsistency. By utilizing NYS, this problem was eliminated, as the NYS concentrations were below the threshold concentration where the second harmonic signal from the solution becomes relevant (see Figure 1).

Conclusions from Polystyrene Bead Studies

In summary, we report the extension of a displacement methodology first developed by Wang and coworkers[9,15] for the study of organic surfactant and micropollutant adsorption to polystyrene surfaces. We find that the adsorption behavior is dictated primarily by van der Waals interactions, with polymer surface charge having no observable effect in this experiment. The experimentally determined ΔG_{Ads} values show good agreement with previous studies and excellent precision. The ability to probe non-resonant molecules using SHS suggests that this technique could be extended to studying the adsorption of molecules to a diverse range of surfaces. Applying this technique to study practical polymer systems, e.g. those used in water purification, could yield valuable molecular insight about the adsorption process in those materials.

MG Adsorption to Silica

Following the successful proof-of-concept experiment described above, we sought to extend our studies to silica nanoparticles. This system provides a useful starting point for future studies, in which the surface of silica can be functionalized with polymer membranes emulating "real-world" , e.g. desalination, polymers.

Adsorption of MG Dye

Following the procedure outlined above for PSB samples, the adsorption of MG dye onto bare silica nanoparticles (SNPs) was performed. Importantly, the silica beads are larger than the PSBs, viz. 1μm compared to ~100nm; this results in a scattering maximum closer to transmission geometry, as can be seen in the raw scattering patterns in Appendix A. Additionally, the SNP samples were pH-controlled to pH = 9 in order to prevent their flocculation in solution. The results for this calibration are shown in Figure 5 along with a plot of the fractional coverage with respect to dye concentration.

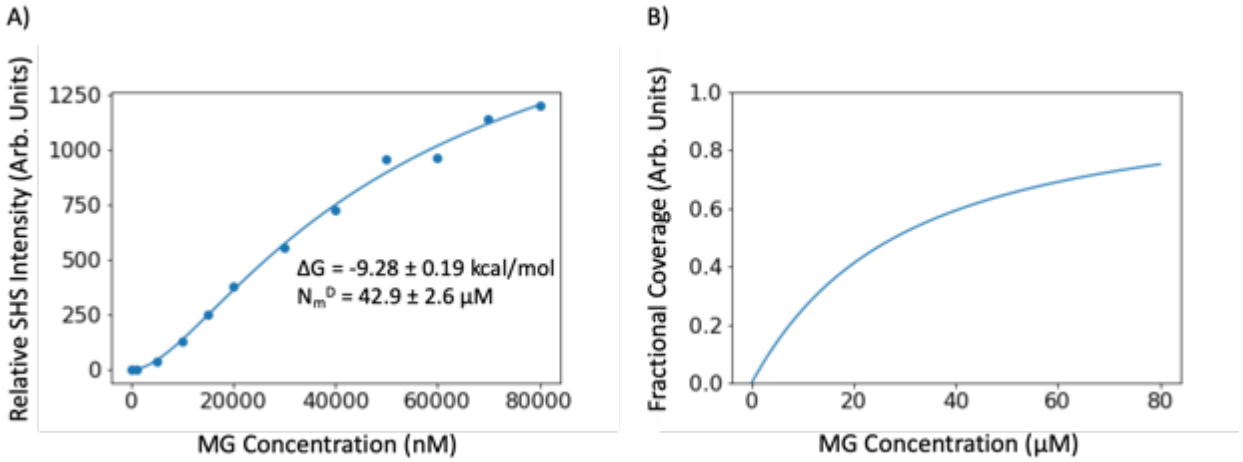

Figure 5: A) Plot of SHS intensity versus MG concentration. The plotted solid line represents a fit to the model outlined in the preceding section (see Equations 1 and 2); the obtained values for ΔG and N_m^D are shown in the inset. B) Plot of fractional coverage (see Equation 2) against MG concentration.

To our knowledge, this is the first determination of MG adsorption to silica beads. It is worthwhile to compare MG adsorption to both nPSB and SNP. as both samples have a negative surface charge; the nPSB samples have sulfate groups at the surface whereas on SNP there are silanol groups at the surface. We can see from inspection of Figure 3 and Figure 5 that MG adsorption is slightly (~1kcal/mol) more favorable for nPSB than for SNP. This difference may be due to different surface charge densities on the surface. This surface charge could be determined using the χ^3 method developed by Eisenthal and coworkers[28,43,47] using the current experimental setup, however, that experiment was not performed here.

Using the determined values of ΔG_{Ads} and N_m^D for MG adsorption on SNP, we can perform the displacement experiment analogous to that performed for the PSB samples. As a note, Triton X was not used as a competitor molecule for SNP; this was a result of strong interactions between SNP and Triton X to the point where the MG signal could not be observed. It would be then reasonable to assume the ΔG_{Ads} for Triton X to SNP is extremely favorable, but unfortunately, this is not measurable in this experiment.

Table 2: Fit constants from displacement experiments on SNP. Structures of molecules are given in Table 1.

Uncertainties are one standard deviation

Molecule	B	a	N_m^D (μM)	$-\Delta G_{Ads}$ (kcal/mol)
Malchite Green	0.00 ± 0.51	39.6 ± 1.9	42.9 ± 2.6	9.28 ± 0.19
Caffeine	0.00 ± 0.23	1.7 ± 0.1	N/a	4.22 ± 0.21
Pentoxifylline	0.47 ± 0.09	1.2 ± 0.1	N/a	4.72 ± 0.32
Ascorbic Acid	0.00 ± 0.11	0.98 ± 0.11	N/a	8.07 ± 0.35
CTAB	0.00 ± 0.16	0.71 ± 0.20	N/a	9.83 ± 0.12

Two key deductions can be made from inspection of Table 2; the first is that ascorbic acid (AA) is dramatically enhanced at the SNP interface compared to the PSB interface. The second is that pentoxifylline is slightly more surface active than caffeine, which is a reversal from the PSB results.

The enhancement of ascorbic acid is particularly unusual, as the pH of the solution (pH = 9 for SNP trials) is much higher than that of either PSB trial (pH = 2 for pPSB and pH = 4 for nPSB). AA ($pK_a = 4.17$) is expected to be deprotonated at pH = 9 and thus be negatively charged. This negative charge was expected to lead to a depletion at the negatively charged interface. The fact that ascorbic acid is more favorable to be at the SNP interface could be the result of several factors. The first is an extension of our results for PSB, where it was determined that van der Waals (vdW) interactions were primarily responsible for the majority of adsorption. If AA is negatively charged and adsorbs strongly to a negatively charged surface, it would seem to indicate that vdW interactions dominate the adsorption dynamics. However, a contradiction arises in the fact that we see vastly different ΔG_{Ads} values for AA compared to caffeine and pentoxifylline despite all three molecules being of a similar size and molecular weight. If increased vdW interactions were the driving force behind the enhancement of AA at the SNP interface, we would expect to also see an enhancement of caffeine and pentoxifylline, but in experiment we observe similar values for ΔG_{Ads} for caffeine and pentoxifylline on both SNP and PSB. Another possible explanation for the enhancement of AA is some type of ion-pairing interaction between negatively charged AA and MG. The only other experiment wherein a charged competitor could have interacted with the dye molecule is the competitive displacement of NYS on pPSB by CTAB. In that experiment, it was assumed that the very favorable measured ΔG_{Ads} value was a result of the large size, and hence large vdW interactions, of the CTAB molecule. This is seemingly supported by observation that the ΔG_{Ads} value for CTAB adsorption to nPSB is similar to its value for adsorption to pPSB. However, a direct comparison between CTAB and AA is not straightforward due to the large size difference between the molecules. It is expected that a charge, similar in magnitude, would have a more pronounced effect on a smaller molecule than a larger one, unless the charge is strongly localized, and thus we cannot completely rule out the effect of the charge of AA. Further studies on AA adsorption to SNP, wherein the pH is varied will hopefully elucidate this enhancement.

The second observed result of competitive adsorption to SNP is that pentoxifylline (PF) was slightly more favorable compared to caffeine. This is the reverse of the trend observed for the PSB trials; however, it should be noted that the difference in ΔG_{Ads} for PF and caffeine in the PSb trials was < 0.2 kcal/mol, whereas for SNP the difference is ~0.5kcal/mol. It is possible that the difference is simply not significant, instead being a result of the larger uncertainties in the values for ΔG_{Ads} observed for SNP. If further studies reveal the result to be statistically significant, the explanation is not straightforward. Caffeine and PF differ in structure by a 5-carbon ketone chain and such a small structural difference would seem unlikely to result in a ~0.5 kcal/mol deviation in ΔG_{Ads} , especially given that the surface of SNP is expected to comprise mainly -(SiO_2)- chains. It may be possible that some steric consideration results in the difference. This hypothesis would imply that the surface sites of SNP are significantly different from those of PSB, and while that seems intuitively obvious, having a system to possibly characterize that difference would be significant.

Conclusions and Future Directions

These initial trials demonstrate that the displacement methodology employed for PSB will also work for SNP, as expected. This trial on bare silica will serve as the starting point for future experiments on coated silica particles. In the immediate future, experiments will be conducted on SNP coated with water purification membranes of various thicknesses. These experiments should elucidate the conditions, under which the adsorption behavior of the nanoparticles might change. Understanding how adsorption changes as a function of surface coating is the ultimate goal of this project, and these upcoming experiments should prove vital for that end. Additionally, there has been some interest in examining the silica surface in different solvents to determine what changes there are to adsorption behavior.

References:

(1) Rizzuto, A. M.; Irgen-Gioro, S.; Eftekhari-Bafrooei, A.; Saykally, R. J. Broadband Deep UV Spectra of Interfacial Aqueous Iodide. *J. Phys. Chem. Lett.* **2016**, *7* (19), 3882–3885.

(2) Mizuno, H.; Rizzuto, A. M.; Saykally, R. J. Charge-Transfer-to-Solvent Spectrum of Thiocyanate at the Air/Water Interface Measured by Broadband Deep Ultraviolet Electronic Sum Frequency Generation Spectroscopy. *J. Phys. Chem. Lett.* **2018**, *9* (16), 4753–4757.

(3) Schürer, B.; Peukert, W. In Situ Surface Characterization of Polydisperse Colloidal Particles by Second Harmonic Generation. *Part. Sci. Technol.* **2010**, *28* (5), 458–471.

(4) Yang, N.; Angerer, W. E.; Yodh, A. G. Angle-Resolved Second-Harmonic Light Scattering from Colloidal Particles. *Phys. Rev. Lett.* **2001**, *87* (10), 1–4.

(5) Gassin, P. M.; Bellini, S.; Zajac, J.; Martin-Gassin, G. Adsorbed Dyes onto Nanoparticles: Large Wavelength Dependence in Second Harmonic Scattering. *J. Phys. Chem. C* **2017**, *121* (27), 14566–14571.

(6) Eckenrode, H. M.; Dai, H. L. Nonlinear Optical Probe of Biopolymer Adsorption on Colloidal Particle Surface: Poly-L-Lysine on Polystyrene Sulfate Microspheres. *Langmuir* **2004**, *20* (21), 9202–9209.

(7) Jen, S. H.; Dai, H. L. Probing Molecules Adsorbed at the Surface of Nanometer Colloidal Particles by Optical Second-Harmonic Generation. *J. Phys. Chem. B* **2006**, *110* (46), 23000–23003.

(8) Wang, H. F.; Troxler, T.; Yeh, A. G.; Dai, H. L. Adsorption at a Carbon Black Microparticle Surface in Aqueous Colloids Probed by Optical Second-Harmonic Generation. *J. Phys. Chem. C* **2007**, *111* (25), 8708–8715.

(9) Wang, H.; Troxler, T.; Yeh, A. G.; Dai, H. L. In Situ, Nonlinear Optical Probe of Surfactant Adsorption on the Surface of Microparticles in Colloids. *Langmuir* **2000**, *16* (6), 2475–2481.

(10) Gonella, G.; Dai, H. L. Second Harmonic Light Scattering from the Surface of Colloidal Objects: Theory and Applications. *Langmuir* **2014**, *30* (10), 2588–2599.

(11) Gustafson, R. L.; Albright, R. L.; Heisler, J.; Lirio, J. A.; Reid, O. T. Adsorption of Organic Species by High Surface Area Styrene-Divinylbenzene Copolymers. *Ind. Eng. Chem. Prod. Res. Dev.* **1968**, *7* (2), 107–115.

(12) Dadap, J. I.; De Aguiar, H. B.; Roke, S. Nonlinear Light Scattering from Clusters and Single Particles. *J. Chem. Phys.* **2009**, *130* (21).

(13) Snyder, S. A.; Adham, S.; Redding, A. M.; Cannon, F. S.; DeCarolis, J.; Oppenheimer, J.; Wert, E. C.; Yoon, Y. Role of Membranes and Activated

Carbon in the Removal of Endocrine Disruptors and Pharmaceuticals. *Desalination* **2007**, *202* (1–3), 156–181.
(14) Maity, N.; Payne, G. F.; Ernest, M. V.; Albright, R. L. Caffeine Adsorption from Aqueous Solutions onto Polymeric Sorbents. The Effect of Surface Chemistry on the Adsorptive Affinity and Adsorption Enthalpy. *React. Polym.* **1992**, *17* (3), 273–287.
(15) Wang, H.; Yan, E. C. Y.; Liu, Y.; Eisenthal, K. B. Energetics and Population of Molecules at Microscopic Liquid and Solid Surfaces. *J. Phys. Chem. B* **1998**, *102* (23), 4446–4450.
(16) Miller, D. J.; Dreyer, D. R.; Bielawski, C. W.; Paul, D. R.; Freeman, B. D. Surface Modification of Water Purification Membranes. *Angew. Chemie - Int. Ed.* **2017**, *56* (17), 4662–4711.
(17) McCaffrey, D. L.; Nguyen, S. C.; Cox, S. J.; Weller, H.; Alivisatos, A. P.; Geissler, P. L.; Saykally, R. J. Mechanism of Ion Adsorption to Aqueous Interfaces: Graphene/Water vs. Air/Water. *Proc. Natl. Acad. Sci.* **2017**, *114* (51), 201702760.
(18) Roke, S.; Roeterdink, W. G.; Wijnhoven, J. E. G. J.; Petukhov, A. V.; Kleyn, A. W.; Bonn, M. Vibrational Sum Frequency Scattering from a Submicron Suspension. *Phys. Rev. Lett.* **2003**, *91* (25), 1–4.
(19) Wunderlich, S.; Schürer, B.; Sauerbeck, C.; Peukert, W.; Peschel, U. Molecular Mie Model for Second Harmonic Generation and Sum Frequency Generation. *Phys. Rev. B - Condens. Matter Mater. Phys.* **2011**, *84* (23), 1–9.
(20) Gonella, G.; Dai, H. L. Determination of Adsorption Geometry on Spherical Particles from Nonlinear Mie Theory Analysis of Surface Second Harmonic Generation. *Phys. Rev. B - Condens. Matter Mater. Phys.* **2011**, *84* (12), 1–5.
(21) De Beer, A. G. F.; De Aguiar, H. B.; Nijsen, J. F. W.; Roke, S. Detection of Buried Microstructures by Nonlinear Light Scattering Spectroscopy. *Phys. Rev. Lett.* **2009**, *102* (9), 6–9.
(22) Gonella, G.; Lütgebaucks, C.; De Beer, A. G. F.; Roke, S. Second Harmonic and Sum-Frequency Generation from Aqueous Interfaces Is Modulated by Interference. *J. Phys. Chem. C* **2016**, *120* (17), 9165–9173.
(23) Otten, D. E.; Shaffer, P. R.; Geissler, P. L.; Saykally, R. J. Elucidating the Mechanism of Selective Ion Adsorption to the Liquid Water Surface. *Proc. Natl. Acad. Sci.* **2011**, *109* (8), 701–705.
(24) Konek, C. T.; Musorrafiti, M. J.; Al-Abadleh, H. A.; Bertin, P. A.; Nguyen, S. B. T.; Geiger, F. M. Interfacial Acidities, Charge Densities, Potentials, and Energies of Carboxylic Acid-Functionalized Silica/Water Interfaces Determined by Second Harmonic Generation. *J. Am. Chem. Soc.* **2004**, *126* (38), 11754–11755.
(25) Malin, J. N.; Hayes, P. L.; Geiger, F. M. Interactions of Ca, Zn, and Cd Ions

at Buried Solid/Water Interfaces Studied by Second Harmonic Generation. *J. Phys. Chem. C* **2009**, *113* (6), 2041–2052.
(26) Hayes, P. L.; Malin, J. N.; Konek, C. T.; Geiger, F. M. Interaction of Nitrate, Barium, Strontium and Cadmium Ions with Fused Quartz/Water Interfaces Studied by Second Harmonic Generation. *J. Phys. Chem. A* **2008**, *112* (4), 660–668.
(27) Geiger, F. M. Second Harmonic Generation, Sum Frequency Generation, and $\chi^{(3)}$: Dissecting Environmental Interfaces with a Nonlinear Optical Swiss Army Knife. *Annu. Rev. Phys. Chem.* **2009**, *60* (1), 61–83.
(28) Wang, H.; Yan, E. C. Y.; Borguet, E.; Eisenthal, K. B. Second Harmonic Generation from the Surface of Centrosymmetric Particles in Bulk Solution. *Chem. Phys. Lett.* **1996**, *259* (1–2), 15–20.
(29) Salafsky, J. S.; Eisenthal, K. B. Protein Adsorption at Interfaces Detected by Second Harmonic Generation. *J. Phys. Chem. B* **2000**, *104* (32), 7752–7755.
(30) Liu, J.; Subir, M.; Nguyen, K.; Eisenthal, K. B. Second Harmonie Studies of Ions Crossing Liposome Membranes in Real Time. *J. Phys. Chem. B* **2008**, *112* (48), 15263–15266.
(31) Schürer, B.; Wunderlich, S.; Sauerbeck, C.; Peschel, U.; Peukert, W. Probing Colloidal Interfaces by Angle-Resolved Second Harmonic Light Scattering. *Phys. Rev. B - Condens. Matter Mater. Phys.* **2010**, *82* (24), 1–4.
(32) Jen, S. H.; Dai, H. L.; Gonella, G. The Effect of Particle Size in Second Harmonic Generation from the Surface of Spherical Colloidal Particles. II: The Nonlinear Rayleigh-Gans-Debye Model. *J. Phys. Chem. C* **2010**, *114* (10), 4302–4308.
(33) Gonella, G.; Gan, W.; Xu, B.; Dai, H. L. The Effect of Composition, Morphology, and Susceptibility on Nonlinear Light Scattering from Metallic and Dielectric Nanoparticles. *J. Phys. Chem. Lett.* **2012**, *3* (19), 2877–2881.
(34) Khebbache, N.; Maurice, A.; Djabi, S.; Russier-Antoine, I.; Jonin, C.; Skipetrov, S. E.; Brevet, P. F. Second-Harmonic Scattering from Metallic Nanoparticles in a Random Medium. *ACS Photonics* **2017**, *4* (2), 262–267.
(35) Gan, W.; Xu, B.; Dai, H. L. Activation of Thiols at a Silver Nanoparticle Surface. *Angew. Chemie - Int. Ed.* **2011**, *50* (29), 6622–6625.
(36) Haber, L. H.; Kwok, S. J. J.; Semeraro, M.; Eisenthal, K. B. Probing the Colloidal Gold Nanoparticle/Aqueous Interface with Second Harmonic Generation. *Chem. Phys. Lett.* **2011**, *507* (1–3), 11–14.
(37) Vaécha, R.; Rick, S. W.; Jungwirth, P.; De Beer, A. G. F.; De Aguiar, H. B.; Samson, J. S.; Roke, S. The Orientation and Charge of Water at the Hydrophobic Oil Droplet - Water Interface. *J. Am. Chem. Soc.* **2011**, *133* (26), 10204–10210.
(38) De Aguiar, H. B.; De Beer, A. G. F.; Strader, M. L.; Roke, S. The Interfacial

Tension of Nanoscopic Oil Droplets in Water Is Hardly Affected by SDS Surfactant. *J. Am. Chem. Soc.* **2010**, *132* (7), 2122–2123.
(39) De Aguiar, H. B.; Strader, M. L.; De Beer, A. G. F.; Roke, S. Surface Structure of Sodium Dodecyl Sulfate Surfactant and Oil at the Oil-in-Water Droplet Liquid/Liquid Interface: A Manifestation of a Nonequilibrium Surface State. *J. Phys. Chem. B* **2011**, *115* (12), 2970–2978.
(40) Zhong, Q.; Baronavski, A. P.; Owrutsky, J. C. Reorientation and Vibrational Energy Relaxation of Pseudohalide Ions Confined in Reverse Micelle Water Pools. *J. Chem. Phys.* **2003**, *119* (17), 9171–9177.
(41) Zhong, Q.; Steinhurst, D. A.; Carpenter, E. E.; Owrutsky, J. C. Fourier Transform Infrared Spectroscopy of Azide Ion in Reverse Micelles. *Langmuir* **2002**, *18* (20), 7401–7408.
(42) Srivastava, A.; Eisenthal, K. B. Kinetics of Molecular Transport across a Liposome Bilayer. *Chem. Phys. Lett.* **1998**, *292* (3), 345–351.
(43) Liu, Y.; Yan, E. C. Y.; Eisenthal, K. B. Effects of Bilayer Surface Charge Density on Molecular Adsorption and Transport across Liposome Bilayers. *Biophys. J.* **2001**, *80* (2), 1004–1012.
(44) Eckenrode, H. M.; Jen, S. H.; Han, J.; Yeh, A. G.; Dai, H. L. Adsorption of a Cationic Dye Molecule on Polystyrene Microspheres in Colloids: Effect of Surface Charge and Composition Probed by Second Harmonic Generation. *J. Phys. Chem. B* **2005**, *109* (10), 4646–4653.
(45) De Beer, A. G. F.; Roke, S. Obtaining Molecular Orientation from Second Harmonic and Sum Frequency Scattering Experiments in Water: Angular Distribution and Polarization Dependence. *J. Chem. Phys.* **2010**, *132* (23).
(46) Chen, Y.; Okur, H. I.; Liang, C.; Roke, S. Orientational Ordering of Water in Extended Hydration Shells of Cations Is Ion-Specific and Is Correlated Directly with Viscosity and Hydration Free Energy. *Phys. Chem. Chem. Phys.* **2017**, *19* (36), 24678–24688.
(47) Ong, S.; Zhao, X.; Eisenthal, K. B. Polarization of Water Molecules at a Charged Interface: Second Harmonic Studies of the Silica/Water Interface. *Chem. Phys. Lett.* **1992**, *191* (3–4), 327–335.
(48) Okur, H. I.; Chen, Y.; Smolentsev, N.; Zdrali, E.; Roke, S. Interfacial Structure and Hydration of 3D Lipid Monolayers in Aqueous Solution. *J. Phys. Chem. B* **2017**, *121* (13), 2808–2813.
(49) Yang, N.; Angerer, W. E.; Yodh, A. G. Second-Harmonic Microscopy of Single Micrometer-Size Particles on a Substrate. *Phys. Rev. A - At. Mol. Opt. Phys.* **2001**, *64* (4), 4.

Appendix A: Supplemental Information

Supplementary Information for:

Far-Infrared VRT Spectroscopy of the Water Dimer: Characterization of the 20 um Out-of-Plane Librational Vibration

The correlation matrices for the fits are presented below. Labels on parameters are always 0, 1, and 2 and correspond to the position of the level in the triplet. 0 is the upper level, 1 is the middle level, and 2 is the bottom level.

K_a=0; 1's levels
Order of parameters is: Band origin, interchange tunneling, bifurcation tunneling, $B^{(i)}$, $D^{(i)}$; where i=0,1,2

1.0	-0.131	0.248	-0.297	-0.233	-0.607	-0.495	-0.335	-0.262
-0.131	1.0	0.131	-0.484	-0.381	0.0	0.0	0.547	0.427
0.248	0.131	1.0	0.297	0.233	-0.607	-0.495	0.335	0.262
-0.297	-0.484	0.297	1.0	0.949	0.0	0.0	0.0	0.0
-0.233	-0.381	0.233	0.949	1.0	0.0	0.0	0.0	0.0
-0.607	0.0	-0.607	0.0	0.0	1.0	0.964	0.0	0.0
-0.495	0.0	-0.495	0.0	0.0	0.964	1.0	0.0	0.0
-0.335	0.547	0.335	0.0	0.0	0.0	0.0	1.0	0.963
-0.262	0.427	0.262	0.0	0.0	0.0	0.0	0.963	1.0

K_a=1; Non-Coriolis coupled 2's Levels

Order of parameters is: and origin, interchange tunneling, bifurcation tunneling, $B^{(i)}$, $D^{(i)}$, $d^{(i)}$, $[(B-C)/4]^{(i)}$; where i=0,1,2.

1.0	-0.038	-0.335	-0.313	-0.262	-0.071	-0.084	-0.633	-0.524	-0.163	-0.183	-0.313	-0.238
	-0.008	0.016										
-0.038	1.0	-0.038	-0.543	-0.455	-0.122	-0.146	-0.0	0.0	0.0	0.0	0.543	0.413
	0.014	-0.028										
-0.335	-0.038	1.0	-0.313	-0.262	-0.071	-0.084	0.633	0.524	0.163	0.183	-0.313	-0.238
	-0.008	0.016										
-0.313	-0.543	-0.313	1.0	0.955	0.312	0.377	0.0	0.0	0.0	0.0	0.0	0.0
	0.0	0.0										
-0.262	-0.455	-0.262	0.955	1.0	0.375	0.473	0.0	0.0	0.0	0.0	0.0	0.0
	0.0	0.0										
-0.071	-0.122	-0.071	0.312	0.375	1.0	0.94	0.0	0.0	0.0	0.0	0.0	0.0
	0.0	0.0										
-0.084	-0.146	-0.084	0.377	0.473	0.94	1.0	0.0	0.0	0.0	0.0	0.0	0.0
	0.0	0.0										
-0.633	-0.0	0.633	0.0	0.0	0.0	0.0	1.0	0.958	0.293	0.341	0.0	0.0
	0.0	0.0										
-0.524	-0.0	0.524	0.0	0.0	0.0	0.0	0.958	1.0	0.332	0.391	0.0	0.0
	0.0	0.0										
-0.163	-0.0	0.163	0.0	0.0	0.0	0.0	0.293	0.332	1.0	0.951	0.0	0.0
	0.0	0.0										
-0.183	-0.0	0.183	0.0	0.0	0.0	0.0	0.341	0.391	0.951	1.0	0.0	0.0
	0.0	0.0										
-0.313	0.543	-0.313	0.0	0.0	0.0	0.0	0.0	0.0	0.0	0.0	1.0	0.942
	-0.146	-0.252										
-0.238	0.413	-0.238	0.0	0.0	0.0	0.0	0.0	0.0	0.0	0.0	0.942	1.0
	-0.264	-0.378										
-0.008	0.014	-0.008	-0.0	0.0	0.0	0.0	0.0	0.0	0.0	0.0	-0.146	-0.264
	1.0	0.943										
0.016	-0.028	0.016	0.0	0.0	0.0	0.0	0.0	0.0	0.0	0.0	-0.252	-0.378
	0.943	1.0										

K_a=1; Coriolis Coupled 2's Levels

Order of parameters is: and origin, interchange tunneling, bifurcation tunneling, $B^{(i)}$, $D^{(i)}$, $d^{(i)}$, $[(B-C)/4]^{(i)}$; where i=0,1,2.

1.0	-0.059	-0.264	-0.335	-0.316	0.068	0.024	-0.605	-0.522	0.014	0.06	-0.324	-0.273
	-0.215	-0.222										
-0.059	1.0	-0.059	-0.551	-0.521	0.113	0.039	0.0	0.0	0.0	0.0	0.535	0.449
	0.354	0.365										
-0.264	-0.059	1.0	-0.335	-0.316	0.068	0.024	0.605	0.522	-0.014	-0.06	-0.324	-0.273
	-0.215	-0.222										
-0.335	-0.551	-0.335	1.0	0.99	-0.313	-0.164	0.0	0.0	0.0	0.0	0.0	0.0
	0.0	0.0										
-0.316	-0.521	-0.316	0.99	1.0	-0.263	-0.112	0.0	0.0	0.0	0.0	0.0	0.0
	0.0	0.0										
0.068	0.113	0.068	-0.313	-0.263	1.0	0.973	0.0	0.0	0.0	0.0	0.0	0.0
	0.0	0.0										
0.024	0.039	0.024	-0.164	-0.112	0.973	1.0	0.0	0.0	0.0	0.0	0.0	0.0
	0.0	0.0										
-0.605	0.0	0.605	0.0	0.0	0.0	0.0	1.0	0.975	0.018	-0.089	0.0	0.0
	0.0	0.0										
-0.522	0.0	0.522	0.0	0.0	0.0	0.0	0.975	1.0	-0.045	-0.155	0.0	0.0
	0.0	0.0										
0.014	0.0	-0.014	0.0	0.0	0.0	0.0	0.018	-0.045	1.0	0.97	0.0	0.0
	0.0	0.0										
0.06	0.0	-0.06	-0.0	0.0	0.0	0.0	-0.089	-0.155	0.97	1.0	0.0	0.0
	0.0	0.0										
-0.324	0.535	-0.324	-0.0	0.0	0.0	0.0	0.0	0.0	0.0	0.0	1.0	0.978
	0.902	0.918										
-0.273	0.449	-0.273	-0.0	0.0	0.0	0.0	0.0	0.0	0.0	0.0	0.978	1.0
	0.943	0.97										
-0.215	0.354	-0.215	-0.0	0.0	0.0	0.0	0.0	0.0	0.0	0.0	0.902	0.943
	1.0	0.987										
-0.222	0.365	-0.222	0.0	0.0	0.0	0.0	0.0	0.0	0.0	0.0	0.918	0.97
	0.987	1.0										

K_a=2; Non-Coriolis coupled 2's Levels

Order of parameters is: and origin, interchange tunneling, bifurcation tunneling, $B^{(i)}$, $D^{(i)}$, $[(B-C)/4]^{(i)}$; where i=0,1,2.

1.0	-0.181	0.308	-0.255	-0.198	-0.045	-0.634	0.362	-0.404	-0.37	-0.317	-0.102
-0.181	1.0	0.181	-0.433	-0.337	-0.077	0.0	0.0	0.0	0.629	0.538	0.174
0.308	0.181	1.0	0.255	0.198	0.045	-0.634	0.362	-0.404	0.37	0.317	0.102
-0.255	-0.433	0.255	1.0	0.956	0.356	0.0	0.0	0.0	0.0	0.0	0.0
-0.198	-0.337	0.198	0.956	1.0	0.485	0.0	0.0	0.0	0.0	0.0	0.0
-0.045	-0.077	0.045	0.356	0.485	1.0	0.0	0.0	0.0	0.0	0.0	0.0
-0.634	0.0	-0.634	0.0	0.0	0.0	1.0	-0.626	0.699	0.0	0.0	0.0
0.362	0.0	0.362	0.0	0.0	0.0	-0.626	1.0	-0.995	0.0	0.0	0.0
-0.404	0.0	-0.404	0.0	0.0	0.0	0.699	-0.995	1.0	0.0	0.0	0.0
-0.37	0.629	0.37	0.0	0.0	0.0	0.0	0.0	0.0	1.0	0.972	0.404
-0.317	0.538	0.317	0.0	0.0	0.0	0.0	0.0	0.0	0.972	1.0	0.481
-0.102	0.174	0.102	0.0	0.0	0.0	0.0	0.0	0.0	0.404	0.481	1.0

K_a=2; Coriolis coupled 2's Levels

Order of parameters is: and origin, interchange tunneling, bifurcation tunneling, $B^{(i)}$, $D^{(i)}$, $[(B-C)/4]^{(i)}$; where i=0,1,2.

1.0	-0.175	0.12	-0.303	-0.228	-0.085	-0.55	-0.15	0.078	-0.347	-0.248	-0.13
-0.175	1.0	0.175	-0.457	-0.344	-0.128	0.0	0.0	0.0	0.524	0.374	0.196
0.12	0.175	1.0	0.303	0.228	0.085	-0.55	-0.15	0.078	0.347	0.248	0.13
-0.303	-0.457	0.303	1.0	0.936	0.548	0.0	0.0	0.0	0.0	0.0	0.0
-0.228	-0.344	0.228	0.936	1.0	0.758	0.0	0.0	0.0	0.0	0.0	0.0
-0.085	-0.128	0.085	0.548	0.758	1.0	0.0	0.0	0.0	0.0	0.0	0.0
-0.55	0.0	-0.55	0.0	0.0	0.0	1.0	0.557	0.106	0.0	0.0	0.0
-0.15	0.0	-0.15	0.0	0.0	0.0	0.557	1.0	0.869	0.0	0.0	0.0
0.078	0.0	0.078	0.0	0.0	0.0	0.106	0.869	1.0	0.0	0.0	0.0
-0.347	0.524	0.347	0.0	0.0	0.0	0.0	0.0	0.0	1.0	0.954	0.766
-0.248	0.374	0.248	0.0	0.0	0.0	0.0	0.0	0.0	0.954	1.0	0.901
-0.13	0.196	0.13	0.0	0.0	0.0	0.0	0.0	0.0	0.766	0.901	1.0

Supplemental Information for:

Hydrogen Bond Breaking Dynamics in the Water Pentamer: Terahertz VRT Spectroscopy of a 20μm Libration

This supplemental information contains the correlation matrices for the fits of the transitions in Table S1. All assigned transitions are presented in Table S2.

Table S1: Correlation matrices for fit labeled by subband. Prime values correspond to the excited state labels and double primes are those of the lower state.

Subband 1

v	1										
B'	-0.475	1									
C'	-0.208	0.540	1								
D_j'	-0.361	0.183	0.359	1							
D_{jk}'	0.021	0.037	0.263	-0.458	1						
D_k'	0.047	-0.110	0.282	0.329	-0.113	1					
B"	-0.270	0.955	0.530	0.193	0.140	-0.192	1				
C"	-0.090	0.418	0.963	0.299	0.171	0.391	0.398	1			
D_j"	-0.209	0.194	0.370	0.942	-0.315	0.203	0.196	0.283	1		
D_{jk}"	-0.002	0.006	0.242	-0.484	0.950	-0.077	0.069	0.188	-0.415	1	
D_k"	0.044	-0.094	0.264	0.345	-0.104	0.967	-0.177	0.380	0.242	-0.122	1

Subband 2

v	1										
B'	-0.367	1									
C'	-0.178	0.518	1								
D_j'	-0.344	0.142	0.231	1							
D_{jk}'	0.044	-0.036	0.546	-0.420	1						
D_k'	-0.009	-0.074	0.338	0.123	-0.307	1					
B"	-0.176	0.964	0.563	0.159	0.054	-0.092	1				
C"	-0.080	0.468	0.974	0.189	0.502	0.383	0.517	1			
D_j"	-0.171	0.171	0.331	0.943	-0.278	0.067	0.172	0.286	1		
D_{jk}"	0.001	-0.006	0.524	-0.363	0.943	-0.265	0.045	0.509	-0.284	1	
D_k"	0.019	-0.147	0.315	0.015	-0.238	0.899	-0.166	0.396	-0.029	-0.273	1

Subband 3

v	1										
B'	-0.343	1									
C'	-0.178	0.551	1								
D_j'	-0.344	0.172	0.337	1							
D_{jk}'	0.075	-0.013	0.486	-0.312	1						
D_k'	-0.022	-0.190	0.148	-0.015	-0.497	1					
B"	-0.168	0.970	0.564	0.121	0.036	-0.201	1				
C"	-0.054	0.514	0.962	0.290	0.477	0.113	0.529	1			
D_j"	-0.163	0.147	0.361	0.948	-0.237	-0.043	0.070	0.310	1		
D_{jk}"	0.057	-0.068	0.400	-0.372	0.896	-0.456	-0.064	0.445	-0.388	1	
D_k"	-0.015	-0.096	0.154	0.103	-0.451	0.845	-0.106	0.150	0.113	-0.278	1

Subband 4

v	1										
B'	-0.211	1									
C'	-0.025	0.406	1								
D_j'	-0.248	0.171	0.222	1							
D_{jk}'	0.102	-0.101	0.571	-0.352	1						
D_k'	0.023	-0.223	0.281	-0.048	-0.276	1					
B"	-0.016	0.965	0.425	0.102	-0.041	-0.236	1				
C"	0.103	0.388	0.968	0.201	0.531	0.287	0.415	1			
D_j"	-0.041	0.156	0.255	0.938	-0.270	-0.089	0.177	0.238	1		
D_{jk}"	0.070	-0.087	0.541	-0.334	0.928	-0.223	-0.070	0.541	-0.332	1	
D_k"	0.046	-0.188	0.234	0.006	-0.296	0.859	-0.201	0.271	-0.007	-0.365	1

Subband 5

v	1										
B'	-0.277	1									
C'	-0.194	0.401	1								
D_j'	-0.293	0.118	0.208	1							
D_{jk}'	0.042	-0.069	0.469	-0.431	1						
D_k'	-0.037	-0.186	0.216	0.132	-0.126	1					
B"	-0.078	0.958	0.391	0.123	0.015	-0.254	1				
C"	-0.045	0.345	0.953	0.171	0.407	0.283	0.335	1			
D_j"	-0.096	0.128	0.221	0.926	-0.301	0.005	0.138	0.170	1		
D_{jk}"	0.014	-0.071	0.458	-0.403	0.924	-0.445	-0.041	0.450	-0.372	1	
D_k"	0.012	-0.161	0.199	0.134	-0.181	0.911	-0.217	0.293	0.051	-0.103	1

Subband 6

v	1										
B'	-0.372	1									
C'	-0.182	0.497	1								
D_j'	-0.343	0.132	0.301	1							
D_{jk}'	0.068	-0.048	0.534	-0.384	1						
D_k'	-0.024	-0.086	0.225	0.212	-0.449	1					
B"	-0.137	0.943	0.515	0.133	0.048	-0.127	1				
C"	-0.038	0.468	0.964	0.284	0.496	0.241	0.490	1			
D_j"	-0.141	0.107	0.339	0.935	-0.281	0.161	0.124	0.319	1		
D_{jk}"	0.030	-0.012	0.481	-0.372	0.931	-0.433	0.035	0.477	-0.347	1	
D_k"	-0.008	-0.040	0.226	0.301	-0.405	0.849	-0.102	0.279	0.264	-0.510	1

Table S2: All assigned transitions labeled by subband. Prime values correspond to the excited state labels and double primes are those of the lower state.

Subband 1						
Transition (cm^{-1})	Residual (cm^{-1})	J'	K'	J"	K"	ΔK
512.919111	4.20E-04	4	0	3	1	-1
513.032815	-4.10E-04	4	2	3	3	-1
513.581429	1.10E-03	7	5	6	6	-1
512.530142	1.50E-03	7	1	7	2	-1
511.760931	-5.90E-04	6	2	7	3	-1
513.646959	8.80E-04	8	4	7	5	-1

512.479436	-1.40E-03	8	0	8	1	-1
513.540676	-2.00E-04	9	0	8	1	-1
513.597376	-1.60E-04	9	1	8	2	-1
511.768959	-1.16E-03	7	4	8	5	-1
513.797160	5.00E-04	11	0	10	1	-1
512.732769	1.60E-04	10	4	10	5	-1
511.228560	4.40E-04	11	2	12	3	-1
511.357169	-2.00E-04	12	6	13	7	-1
510.977502	-4.30E-04	14	3	15	4	-1
511.037141	1.34E-03	14	4	15	5	-1
513.079718	-7.10E-04	15	9	15	10	-1
513.181061	1.30E-04	15	11	15	12	-1
513.226329	1.50E-04	15	12	15	13	-1
510.983268	-1.10E-04	19	13	20	14	-1
511.984244	9.50E-04	2	2	3	1	1
512.703246	1.02E-03	4	4	3	3	1
511.923839	-7.00E-04	3	1	4	0	1
513.177128	-1.43E-03	7	2	6	1	1
512.299868	-2.70E-04	6	3	6	2	1
513.302723	-1.27E-03	8	2	7	1	1
512.424569	-5.70E-04	8	1	8	0	1
513.429780	-6.40E-04	9	2	8	1	1
512.211856	5.10E-04	8	5	8	4	1
512.107637	1.50E-04	8	7	8	6	1
513.203155	9.90E-04	11	11	10	10	1
513.761160	0.00E+00	12	3	11	2	1
513.707940	2.20E-04	12	4	11	3	1
513.328335	-5.30E-04	12	11	11	10	1
512.096945	7.20E-04	12	8	12	7	1
513.624489	-1.30E-04	13	8	12	7	1
513.642296	-2.70E-04	14	10	13	9	1
510.247150	1.06E-03	13	12	14	11	1
510.319151	1.21E-03	14	9	15	8	1
510.262440	1.23E-03	14	10	15	9	1
510.202343	-7.00E-05	14	11	15	10	1
510.006687	-2.90E-04	14	14	15	13	1
512.312739	-3.20E-04	16	5	16	4	1
510.326739	1.25E-03	15	7	16	6	1
510.270053	-8.30E-04	15	8	16	7	1
510.157277	-6.60E-04	15	10	16	9	1
510.035674	-7.10E-04	15	12	16	11	1

509.970059	-7.20E-04	15	13	16	12	1
509.899733	-1.25E-03	15	14	16	13	1
509.826199	3.00E-05	15	15	16	14	1
512.330117	7.40E-04	17	5	17	4	1
510.054082	-1.28E-03	16	10	17	9	1
509.932016	-4.70E-04	16	12	17	11	1
509.864831	-1.30E-03	16	13	17	12	1
509.796578	1.06E-03	16	14	17	13	1
511.787411	-8.40E-04	17	14	17	13	1
509.719555	-2.70E-04	16	15	17	14	1
509.638017	-1.60E-04	16	16	17	15	1
510.013143	1.25E-03	17	9	18	8	1
509.893145	3.80E-04	17	11	18	10	1
509.690815	2.70E-04	17	14	18	13	1
509.613515	-4.00E-04	17	15	18	14	1
509.442067	3.90E-04	17	17	18	16	1
512.139770	4.70E-04	19	9	19	8	1
509.726501	8.00E-05	18	12	19	11	1
509.585822	-1.90E-04	18	14	19	13	1
509.509048	6.50E-04	18	15	19	14	1
509.425242	5.40E-04	18	16	19	15	1
509.924076	-1.60E-03	19	7	20	6	1
509.751650	1.70E-04	19	10	20	9	1
509.403778	5.50E-04	19	15	20	14	1

Subband 2						
Transition (cm^{-1})	Residual (cm^{-1})	J'	K'	J"	K"	ΔK
512.258011	-6.00E-04	1	0	2	1	-1
512.144346	1.40E-04	2	0	3	1	-1
512.612990	6.50E-04	3	2	3	3	-1
513.090907	-7.30E-04	5	0	4	1	-1
512.674930	-5.90E-04	4	3	4	4	-1
511.917934	-9.60E-04	4	0	5	1	-1
513.387853	-1.80E-04	6	3	5	4	-1
512.571455	-1.70E-04	6	1	6	2	-1
512.807973	1.43E-03	6	5	6	6	-1
513.705896	1.30E-04	9	2	8	3	-1
512.704356	3.00E-05	8	3	8	4	-1
513.775515	-1.40E-04	10	1	9	2	-1
512.890402	-7.80E-04	9	6	9	7	-1

512.667722	9.90E-04	10	2	10	3	-1
511.842121	1.18E-03	9	8	10	9	-1
513.017173	-3.60E-04	10	8	10	9	-1
511.896416	-1.02E-03	9	9	10	10	-1
511.269678	-3.20E-04	10	0	11	1	-1
511.165016	-5.60E-04	11	0	12	1	-1
512.634451	4.20E-04	12	1	12	2	-1
513.200379	1.12E-03	12	11	12	12	-1
512.648119	4.00E-04	13	1	13	2	-1
511.175009	-8.20E-04	12	2	13	3	-1
512.821434	6.70E-04	13	4	13	5	-1
513.209188	-6.20E-04	13	11	13	12	-1
513.267490	1.40E-04	14	12	14	13	-1
513.308701	-8.90E-04	14	13	14	14	-1
510.913341	-1.16E-03	14	1	15	2	-1
513.131687	2.20E-04	15	9	15	10	-1
513.233466	8.40E-04	15	11	15	12	-1
513.356094	-2.70E-04	15	14	15	15	-1
512.750912	4.90E-04	16	2	16	3	-1
513.289861	6.00E-05	16	12	16	13	-1
513.341791	2.50E-04	17	13	17	14	-1
513.010625	-4.90E-04	18	6	18	7	-1
510.953663	-9.60E-04	17	7	18	8	-1
513.067170	5.70E-04	18	7	18	8	-1
513.435398	3.20E-04	18	16	18	17	-1
513.325420	-7.80E-04	19	12	19	13	-1
513.363802	-5.10E-04	19	13	19	14	-1
511.067264	5.90E-04	19	14	20	15	-1
512.034043	4.00E-05	2	2	3	1	1
512.859169	1.50E-04	4	2	3	1	1
511.975123	-1.90E-04	3	1	4	0	1
513.037009	1.04E-03	5	1	4	0	1
512.981208	-1.60E-04	5	2	4	1	1
512.339730	1.13E-03	4	3	4	2	1
512.927176	-6.00E-04	5	3	4	2	1
512.286422	5.00E-04	4	4	4	3	1
513.104463	-3.40E-04	6	2	5	1	1
512.344169	-8.00E-05	5	3	5	2	1
511.752152	-1.50E-04	5	1	6	0	1
512.458787	-4.80E-04	6	1	6	0	1
513.283074	-8.40E-04	7	1	6	0	1

513.229617	3.50E-04	7	2	6	1	1
512.195179	8.50E-04	6	6	6	5	1
513.408750	-6.80E-04	8	1	7	0	1
513.301114	1.10E-04	8	3	7	2	1
513.247074	-9.80E-04	8	4	7	3	1
512.477349	1.24E-03	8	1	8	0	1
513.536698	7.70E-04	9	1	8	0	1
512.422402	9.80E-04	8	2	8	1	1
512.210275	-2.00E-05	8	6	8	5	1
512.157550	-7.90E-04	8	7	8	6	1
513.663353	-2.00E-05	10	1	9	0	1
512.431853	4.90E-04	9	2	9	1	1
513.609446	8.30E-04	10	2	9	1	1
512.271119	-8.10E-04	9	5	9	4	1
512.114383	-6.90E-04	9	8	9	7	1
513.790839	-8.80E-04	11	1	10	0	1
513.629125	-5.30E-04	11	4	10	3	1
513.577482	6.00E-04	11	5	10	4	1
512.509736	7.40E-04	11	1	11	0	1
512.346100	-7.50E-04	11	4	11	3	1
513.758721	1.40E-04	12	4	11	3	1
513.651874	-1.03E-03	12	6	11	5	1
513.599765	-3.30E-04	12	7	11	6	1
512.148220	9.40E-04	12	8	12	7	1
513.620266	-6.50E-04	13	9	12	8	1
513.382947	5.60E-04	13	13	12	12	1
512.266792	2.20E-04	13	6	13	5	1
512.213574	2.20E-04	13	7	13	6	1
513.439828	-6.40E-04	14	14	13	13	1
512.281099	7.70E-04	14	6	14	5	1
513.762916	-3.10E-04	15	11	14	10	1
513.636337	1.00E-04	15	13	14	12	1
512.402272	1.90E-04	15	4	15	3	1
510.313243	1.00E-03	14	10	15	9	1
512.074371	7.20E-04	15	10	15	9	1
510.191331	-3.10E-04	14	12	15	11	1
510.126403	-1.90E-04	14	13	15	12	1
511.886465	-3.90E-04	15	13	15	12	1
511.818223	1.02E-03	15	14	15	13	1
512.310296	3.40E-04	16	6	16	5	1
510.209166	2.70E-04	15	10	16	9	1

510.149314	-6.00E-05	15	11	16	10	1
510.087403	3.30E-04	15	12	16	11	1
510.020977	-3.40E-04	15	13	16	12	1
511.827687	-4.00E-05	16	14	16	13	1
509.876466	8.00E-05	15	15	16	14	1
513.744488	0.00E+00	17	15	16	14	1
512.214462	-1.22E-03	17	8	17	7	1
510.046330	2.70E-04	16	11	17	10	1
509.983909	8.40E-04	16	12	17	11	1
509.916804	2.40E-04	16	13	17	12	1
509.845006	-7.90E-04	16	14	17	13	1
509.688714	5.40E-04	16	16	17	15	1
510.338447	-2.00E-05	17	4	18	3	1
510.284473	2.80E-04	17	5	18	4	1
510.118262	-1.18E-03	17	8	18	7	1
509.878970	-6.20E-04	17	12	18	11	1
509.740485	-1.80E-04	17	14	18	13	1
509.663361	-5.40E-04	17	15	18	14	1
509.580705	-4.20E-04	17	16	18	15	1
509.491044	-3.60E-04	17	17	18	16	1
510.349657	5.10E-04	18	2	19	1	1
510.294796	5.30E-04	18	3	19	2	1
510.184776	-3.20E-04	18	5	19	4	1
510.129452	-9.10E-04	18	6	19	5	1
510.074250	-9.00E-04	18	7	19	6	1
509.901809	-7.40E-04	18	10	19	9	1
512.129448	-2.50E-04	19	10	19	9	1
509.777739	1.18E-03	18	12	19	11	1
512.003959	1.17E-03	19	12	19	11	1
509.709642	1.21E-03	18	13	19	12	1
511.933674	-4.50E-04	19	13	19	12	1
509.635527	-3.70E-04	18	14	19	13	1
509.473994	-3.40E-04	18	16	19	15	1
509.384104	6.00E-04	18	17	19	16	1
510.251775	4.40E-04	19	2	20	1	1
510.196072	-2.40E-04	19	3	20	2	1
510.141315	-1.50E-04	19	4	20	3	1
510.032309	8.00E-04	19	6	20	5	1
509.862273	9.70E-04	19	9	20	8	1
509.738818	-4.20E-04	19	11	20	10	1
509.531245	-1.90E-04	19	14	20	13	1

509.367616	-1.30E-04	19	16	20	15	1

Subband 3						
Transition (cm^{-1})	Residual (cm^{-1})	J'	K'	J''	K''	ΔK
512.543656	1.00E-04	2	0	2	1	-1
512.954058	4.00E-05	3	1	2	2	-1
512.547259	2.50E-04	3	0	3	1	-1
512.080267	2.00E-04	3	0	4	1	-1
513.141293	3.80E-04	5	0	4	1	-1
512.136855	1.00E-05	3	1	4	2	-1
512.194543	-8.00E-05	3	2	4	3	-1
512.252939	-3.50E-04	3	3	4	4	-1
512.724604	-1.70E-04	4	3	4	4	-1
511.967771	-2.00E-04	4	0	5	1	-1
513.264811	4.50E-04	6	0	5	1	-1
513.320948	-1.60E-04	6	1	5	2	-1
512.672220	4.50E-04	5	2	5	3	-1
513.378790	-4.00E-05	6	2	5	3	-1
512.730775	4.10E-04	5	3	5	4	-1
511.913546	-2.00E-04	5	1	6	2	-1
513.445230	-3.50E-04	7	1	6	2	-1
512.678697	1.90E-04	6	2	6	3	-1
513.502941	-3.10E-04	7	2	6	3	-1
512.736859	-1.80E-04	6	3	6	4	-1
513.561832	9.00E-05	7	3	6	4	-1
513.514546	1.90E-04	8	0	7	1	-1
511.803582	-3.20E-04	6	1	7	2	-1
513.571473	4.20E-04	8	1	7	2	-1
512.686328	2.00E-05	7	2	7	3	-1
512.744462	-3.00E-04	7	3	7	4	-1
512.803798	-4.00E-05	7	4	7	5	-1
513.745627	-4.70E-04	8	4	7	5	-1
512.863097	-1.80E-04	7	5	7	6	-1
512.922643	-1.20E-04	7	6	7	7	-1
513.640636	-1.80E-04	9	0	8	1	-1
512.637394	-1.60E-04	8	1	8	2	-1
512.695051	-9.00E-05	8	2	8	3	-1
511.929146	-4.20E-04	7	5	8	6	-1
511.988825	-1.50E-04	7	6	8	7	-1
511.821606	1.10E-04	8	5	9	6	-1

512.881006	-2.10E-04	9	5	9	6	-1
512.601378	-3.50E-04	10	0	10	1	-1
512.715453	-3.40E-04	10	2	10	3	-1
512.773456	-5.00E-04	10	3	10	4	-1
513.123377	5.30E-04	10	9	10	10	-1
513.019324	-4.00E-04	11	7	11	8	-1
513.077121	1.00E-04	11	8	11	9	-1
511.893732	5.40E-04	10	10	11	11	-1
512.740357	1.90E-04	12	2	12	3	-1
512.914984	1.00E-05	12	5	12	6	-1
513.031480	2.10E-04	12	7	12	8	-1
511.732999	2.90E-04	11	9	12	10	-1
512.640066	1.00E-04	13	0	13	1	-1
511.167199	-1.40E-04	12	1	13	2	-1
513.155737	5.20E-04	13	9	13	10	-1
513.207892	-3.30E-04	13	10	13	11	-1
511.778096	-1.40E-04	12	12	13	13	-1
511.064285	-4.20E-04	13	1	14	2	-1
512.711041	2.30E-04	14	1	14	2	-1
511.121797	-5.00E-05	13	2	14	3	-1
512.767797	-1.10E-04	14	2	14	3	-1
511.296122	3.40E-04	13	5	14	6	-1
513.112762	2.00E-05	14	8	14	9	-1
510.963011	5.00E-05	14	1	15	2	-1
512.782816	-1.00E-04	15	2	15	3	-1
511.192905	-4.00E-04	14	5	15	6	-1
513.070666	4.40E-04	15	7	15	8	-1
513.028112	8.00E-05	16	6	16	7	-1
511.205559	-1.00E-05	15	7	16	8	-1
513.293132	-7.00E-05	16	11	16	12	-1
513.338318	1.50E-04	16	12	16	13	-1
512.702281	4.10E-04	17	0	17	1	-1
510.990796	1.40E-04	16	5	17	6	-1
513.098817	-4.10E-04	17	7	17	8	-1
513.389401	-3.00E-04	17	13	17	14	-1
512.888433	-2.30E-04	18	3	18	4	-1
513.002273	-2.60E-04	18	5	18	6	-1
513.058945	3.00E-05	18	6	18	7	-1
513.114728	2.80E-04	18	7	18	8	-1
511.057602	3.50E-04	17	8	18	9	-1
513.168979	2.80E-04	18	8	18	9	-1

511.110153	1.40E-04	17	9	18	10	-1
513.221324	1.70E-04	18	9	18	10	-1
513.400481	-3.30E-04	18	13	18	14	-1
513.462391	1.70E-04	18	15	18	16	-1
512.905597	-2.00E-04	19	3	19	4	-1
513.129891	-1.80E-04	19	7	19	8	-1
513.331292	-6.00E-05	19	11	19	12	-1
511.148173	2.50E-04	18	12	19	13	-1
511.186312	-2.00E-04	18	13	19	14	-1
513.411879	-1.90E-04	19	13	19	14	-1
513.471362	-1.10E-04	19	15	19	16	-1
511.159428	4.00E-05	19	16	20	17	-1
512.602285	-1.00E-05	1	1	0	0	1
512.485144	-4.10E-04	1	1	1	0	1
512.721135	-2.10E-04	2	1	1	0	1
512.488002	1.40E-04	2	1	2	0	1
512.433470	2.10E-04	2	2	2	1	1
512.908648	4.40E-04	4	2	3	1	1
512.441746	4.80E-04	4	2	4	1	1
512.924033	-1.50E-04	5	4	4	3	1
512.501718	1.30E-04	5	1	5	0	1
512.393834	5.30E-04	5	3	5	2	1
513.100364	4.00E-05	6	3	5	2	1
513.047056	-4.50E-04	6	4	5	3	1
512.508019	-3.70E-04	6	1	6	0	1
513.332896	-2.60E-04	7	1	6	0	1
513.278021	-4.50E-04	7	2	6	1	1
512.400010	-2.00E-05	6	3	6	2	1
513.172332	4.80E-04	7	4	6	3	1
513.119598	-2.00E-05	7	5	6	4	1
512.461825	2.60E-04	7	2	7	1	1
512.355117	2.10E-04	7	4	7	3	1
512.302727	1.00E-04	7	5	7	4	1
513.245140	3.20E-04	8	5	7	4	1
512.251210	4.60E-04	7	6	7	5	1
513.192782	-7.00E-05	8	6	7	5	1
512.524739	-4.40E-04	8	1	8	0	1
513.530727	3.70E-04	9	2	8	1	1
512.416965	3.10E-04	8	3	8	2	1
512.310940	-3.10E-04	8	5	8	4	1
513.371101	1.40E-04	9	5	8	4	1

511.316757	-3.60E-04	7	6	8	5	1
512.154968	1.00E-05	8	8	8	7	1
512.480830	4.70E-04	9	2	9	1	1
513.604043	2.50E-04	10	3	9	2	1
512.216153	-3.30E-04	9	7	9	6	1
512.164071	1.10E-04	9	8	9	7	1
513.232284	-1.70E-04	10	10	9	9	1
513.732258	3.20E-04	11	3	10	2	1
512.384184	1.20E-04	10	4	10	3	1
513.573162	-2.00E-04	11	6	10	5	1
512.226499	-1.20E-04	10	7	10	6	1
512.503329	2.80E-04	11	2	11	1	1
511.101016	-8.00E-05	10	4	11	3	1
512.342705	-1.30E-04	11	5	11	4	1
512.289844	-4.10E-04	11	6	11	5	1
513.701368	-4.40E-04	12	6	11	5	1
513.595354	-4.20E-04	12	8	11	7	1
513.429033	3.50E-04	12	11	11	10	1
512.408416	2.60E-04	12	4	12	3	1
513.777735	-1.80E-04	13	7	12	6	1
513.724145	-2.00E-04	13	8	12	7	1
513.669981	1.30E-04	13	9	12	8	1
511.000524	2.80E-04	12	2	13	1	1
510.946224	1.30E-04	12	3	13	2	1
512.475200	1.00E-04	13	3	13	2	1
512.368318	5.00E-05	13	5	13	4	1
512.315080	-1.40E-04	13	6	13	5	1
512.261648	-3.80E-04	13	7	13	6	1
512.207897	-4.30E-04	13	8	13	7	1
513.798982	3.40E-04	14	9	13	8	1
513.741862	-4.00E-04	14	10	13	9	1
513.623227	4.40E-04	14	12	13	11	1
513.489441	-4.40E-04	14	14	13	13	1
512.329006	1.50E-04	14	6	14	5	1
512.166581	3.70E-04	14	9	14	8	1
510.346046	4.20E-04	13	12	14	11	1
510.281199	-1.10E-04	13	13	14	12	1
511.925013	-3.00E-05	14	13	14	12	1
513.685192	-2.60E-04	15	13	14	12	1
511.855804	-4.50E-04	14	14	14	13	1
513.616593	3.30E-04	15	14	14	13	1

512.558404	-3.70E-04	15	2	15	1	1
510.240932	5.00E-04	14	12	15	11	1
512.001235	2.00E-05	15	12	15	11	1
511.935432	-4.60E-04	15	13	15	12	1
510.106308	-8.00E-05	14	14	15	13	1
511.866392	0.00E+00	15	14	15	13	1
513.668061	1.00E-04	16	15	15	14	1
512.412161	1.50E-04	16	5	16	4	1
510.069853	-3.40E-04	15	13	16	12	1
513.794313	3.70E-04	17	15	16	14	1
512.645997	-1.50E-04	17	1	17	0	1
512.591354	3.80E-04	17	2	17	1	1
512.374188	5.30E-04	17	6	17	5	1
512.318949	-1.50E-04	17	7	17	6	1
510.212509	4.00E-05	16	9	17	8	1
510.154975	3.40E-04	16	10	17	9	1
512.088647	-1.10E-04	17	11	17	10	1
511.958985	2.60E-04	17	13	17	12	1
509.894686	-1.10E-04	16	14	17	13	1
512.662852	-3.40E-04	18	1	18	0	1
512.553576	4.40E-04	18	3	18	2	1
512.389525	-1.70E-04	18	6	18	5	1
510.110587	-2.30E-04	17	9	18	8	1
512.221928	-3.00E-05	18	9	18	8	1
511.898278	-3.80E-04	18	14	18	13	1
509.630696	2.00E-04	17	16	18	15	1
511.738530	9.00E-05	18	16	18	15	1
512.625462	5.00E-05	19	2	19	1	1
512.406135	-4.00E-05	19	6	19	5	1
512.350895	1.10E-04	19	7	19	6	1
512.294411	-1.20E-04	19	8	19	7	1
509.950535	-1.50E-04	18	10	19	9	1
512.177877	3.00E-04	19	10	19	9	1
511.747810	2.20E-04	19	16	19	15	1
510.078857	-6.00E-05	19	6	20	5	1
509.966575	-3.10E-04	19	8	20	7	1
509.848927	-4.80E-04	19	10	20	9	1
509.787765	4.20E-04	19	11	20	10	1
509.722616	3.60E-04	19	12	20	11	1
509.501361	-3.50E-04	19	15	20	14	1

Subband 4						
Transition (cm^{-1})	Residual (cm^{-1})	J'	K'	J''	K''	ΔK
512.593885	5.10E-04	1	0	1	1	-1
512.828952	-2.20E-04	2	0	1	1	-1
512.359388	-4.90E-04	1	0	2	1	-1
512.595469	-2.00E-04	2	0	2	1	-1
512.651758	-7.10E-04	2	1	2	2	-1
512.245311	-1.20E-04	2	0	3	1	-1
512.656320	4.20E-04	3	1	3	2	-1
512.712961	-7.50E-04	3	2	3	3	-1
512.604337	6.60E-04	4	0	4	1	-1
513.249752	-2.00E-05	5	1	4	2	-1
513.366281	9.00E-05	5	3	4	4	-1
512.609447	9.00E-05	5	0	5	1	-1
513.549249	4.90E-04	6	4	5	5	-1
511.908810	-2.40E-04	5	0	6	1	-1
511.966249	4.60E-04	5	1	6	2	-1
513.555087	-2.50E-04	7	2	6	3	-1
512.848537	2.00E-04	6	4	6	5	-1
513.672522	-4.90E-04	7	4	6	5	-1
512.623280	-7.20E-04	7	0	7	1	-1
512.738216	-1.40E-04	7	2	7	3	-1
511.972122	2.00E-05	6	3	7	4	-1
513.738741	-4.40E-04	8	3	7	4	-1
512.091251	4.50E-04	6	5	7	6	-1
512.915515	1.00E-04	7	5	7	6	-1
512.689389	-2.00E-04	8	1	8	2	-1
511.805239	4.50E-04	7	2	8	3	-1
512.747861	6.80E-04	8	2	8	3	-1
511.863152	-6.00E-05	7	3	8	4	-1
512.805059	-5.10E-04	8	3	8	4	-1
511.922638	3.80E-04	7	4	8	5	-1
511.982091	4.30E-04	7	5	8	6	-1
512.642774	-7.00E-05	9	0	9	1	-1
512.699119	-3.70E-04	9	1	9	2	-1
512.757355	3.30E-04	9	2	9	3	-1
511.756060	6.50E-04	8	3	9	4	-1
511.814854	5.30E-04	8	4	9	5	-1
511.872961	-6.10E-04	8	5	9	6	-1
512.992573	9.00E-05	9	6	9	7	-1

511.992116	3.80E-04	8	7	9	8	-1
512.049618	-2.30E-04	8	8	9	9	-1
512.653578	-2.00E-04	10	0	10	1	-1
512.826061	4.00E-05	10	3	10	4	-1
511.765892	-6.10E-04	9	5	10	6	-1
511.941831	-2.10E-04	9	8	10	9	-1
511.998509	-3.00E-05	9	9	10	10	-1
513.175682	5.10E-04	10	9	10	10	-1
512.896106	-1.10E-04	11	4	11	5	-1
511.835597	4.40E-04	10	8	11	9	-1
511.891289	-2.00E-05	10	9	11	10	-1
513.239254	2.00E-05	11	10	11	11	-1
513.025658	9.00E-05	12	6	12	7	-1
513.195733	-3.10E-04	12	9	12	10	-1
513.300077	-4.70E-04	12	11	12	12	-1
512.692860	6.80E-04	13	0	13	1	-1
513.095556	-2.90E-04	13	7	13	8	-1
511.783760	3.60E-04	12	11	13	12	-1
512.877407	-4.60E-04	14	3	14	4	-1
512.994013	1.40E-04	14	5	14	6	-1
513.108321	-6.10E-04	14	7	14	8	-1
513.272134	-2.00E-04	14	10	14	11	-1
510.958910	3.00E-05	14	0	15	1	-1
512.778145	-2.70E-04	15	1	15	2	-1
511.071896	-4.00E-04	14	2	15	3	-1
512.835445	5.00E-05	15	2	15	3	-1
512.892235	-6.20E-04	15	3	15	4	-1
513.008217	-1.50E-04	15	5	15	6	-1
513.457664	5.00E-05	15	14	15	15	-1
512.794096	-3.20E-04	16	1	16	2	-1
513.023964	4.20E-04	16	5	16	6	-1
511.258117	1.30E-04	15	7	16	8	-1
513.391733	7.50E-04	16	12	16	13	-1
512.867952	1.10E-04	17	2	17	3	-1
512.925453	5.30E-04	17	3	17	4	-1
510.986134	1.80E-04	16	4	17	5	-1
511.264685	-1.00E-04	16	9	17	10	-1
513.310114	-5.50E-04	17	10	17	11	-1
513.442255	-4.90E-04	17	13	17	14	-1
513.477003	-5.30E-04	17	14	17	15	-1
513.507021	7.10E-04	17	15	17	16	-1

512.885604	6.00E-04	18	2	18	3	-1
513.324945	5.90E-04	18	10	18	11	-1
511.305002	3.60E-04	17	12	18	13	-1
513.454026	0.00E+00	18	13	18	14	-1
513.487229	-6.50E-04	18	14	18	15	-1
513.535756	-6.30E-04	18	16	18	17	-1
512.790264	1.40E-04	19	0	19	1	-1
512.901796	-9.20E-04	19	2	19	3	-1
513.072893	3.10E-04	19	5	19	6	-1
513.128264	-2.50E-04	19	6	19	7	-1
510.954783	-5.10E-04	18	7	19	8	-1
513.384152	-6.00E-04	19	11	19	12	-1
513.427439	7.00E-05	19	12	19	13	-1
511.240081	4.90E-04	18	13	19	14	-1
513.498639	2.50E-04	19	14	19	15	-1
511.300522	2.90E-04	18	15	19	16	-1
513.525373	2.80E-04	19	15	19	16	-1
512.537945	2.60E-04	1	1	1	0	1
512.785037	-4.50E-04	3	3	2	2	1
512.076847	3.90E-04	3	1	4	0	1
513.082927	2.60E-04	5	2	4	1	1
511.969010	7.30E-04	3	3	4	2	1
512.439572	-1.90E-04	4	3	4	2	1
511.964211	-1.20E-04	4	1	5	0	1
513.206008	-8.00E-05	6	2	5	1	1
512.392453	-1.80E-04	5	4	5	3	1
512.560643	2.00E-04	6	1	6	0	1
511.798490	-2.20E-04	5	2	6	1	1
513.330805	2.70E-04	7	2	6	1	1
512.398597	-6.80E-04	6	4	6	3	1
513.223825	-1.30E-04	7	4	6	3	1
513.068468	2.20E-04	7	7	6	6	1
511.743524	1.00E-05	6	1	7	0	1
512.568545	2.50E-04	7	1	7	0	1
512.513288	-3.20E-04	7	2	7	1	1
513.456052	5.00E-05	8	2	7	1	1
512.460260	3.90E-04	7	3	7	2	1
513.402846	6.20E-04	8	3	7	2	1
512.354009	-7.10E-04	7	5	7	4	1
513.296365	-5.70E-04	8	5	7	4	1
512.522356	-1.30E-04	8	2	8	1	1

513.582860	4.30E-04	9	2	8	1	1
512.468965	2.70E-04	8	3	8	2	1
512.362831	-4.90E-04	8	5	8	4	1
513.422469	-6.10E-04	9	5	8	4	1
513.213771	3.70E-04	9	9	8	8	1
513.764602	2.00E-05	10	1	9	0	1
513.710459	6.60E-04	10	2	9	1	1
513.656202	3.20E-04	10	3	9	2	1
513.602253	-4.60E-04	10	4	9	3	1
512.372681	-2.40E-04	9	5	9	4	1
512.321452	7.10E-04	9	6	9	5	1
512.598028	-4.00E-05	10	1	10	0	1
513.730969	1.90E-04	11	4	10	3	1
513.465688	-6.80E-04	11	9	10	8	1
512.117781	1.90E-04	10	10	10	9	1
513.411238	-7.00E-05	11	10	10	9	1
513.353509	-8.50E-04	11	11	10	10	1
511.152923	-2.00E-04	10	4	11	3	1
513.648220	1.80E-04	12	8	11	7	1
513.538706	2.10E-04	12	10	11	9	1
513.481330	2.10E-04	12	11	11	10	1
513.722918	7.10E-04	13	9	12	8	1
513.666770	4.40E-04	13	10	12	9	1
513.608247	-2.30E-04	13	11	12	10	1
513.484479	1.50E-04	13	13	12	12	1
510.998109	-9.00E-05	12	3	13	2	1
512.366872	-5.90E-04	13	6	13	5	1
513.736675	2.90E-04	14	11	13	10	1
513.675428	4.00E-05	14	12	13	11	1
513.611396	3.30E-04	14	13	13	12	1
512.541816	1.20E-04	14	3	14	2	1
512.380946	-2.50E-04	14	6	14	5	1
512.162069	2.00E-05	14	10	14	9	1
512.103069	-3.90E-04	14	11	14	10	1
512.042307	1.00E-04	14	12	14	11	1
510.333295	-4.40E-04	13	13	14	12	1
511.977963	3.50E-04	14	13	14	12	1
512.611440	1.60E-04	15	2	15	1	1
512.556368	-4.70E-04	15	3	15	2	1
512.449711	4.60E-04	15	5	15	4	1
512.174422	-4.00E-04	15	10	15	9	1

510.292281	-5.40E-04	14	12	15	11	1
510.159422	4.90E-04	14	14	15	13	1
512.682180	-2.00E-04	16	1	16	0	1
512.627938	6.70E-04	16	2	16	1	1
512.572964	2.50E-04	16	3	16	2	1
512.519079	5.00E-04	16	4	16	3	1
512.465195	5.00E-04	16	5	16	4	1
512.410649	-1.60E-04	16	6	16	5	1
512.066382	5.00E-04	16	12	16	11	1
512.589120	-1.30E-04	17	3	17	2	1
510.321010	-2.70E-04	16	8	17	7	1
512.316186	-5.00E-04	17	8	17	7	1
510.264688	-3.90E-04	16	9	17	8	1
512.202266	2.40E-04	17	10	17	9	1
512.078357	-4.00E-05	17	12	17	11	1
510.017432	-6.20E-04	16	13	17	12	1
512.011803	1.60E-04	17	13	17	12	1
509.947362	-1.30E-04	16	14	17	13	1
509.872124	2.30E-04	16	15	17	14	1
510.331270	6.30E-04	17	6	18	5	1
512.442965	5.00E-05	18	6	18	5	1
510.275592	-3.00E-04	17	7	18	6	1
509.980808	-1.70E-04	17	12	18	11	1
511.951746	-8.00E-05	18	14	18	13	1
511.791156	-5.80E-04	18	16	18	15	1
509.594372	2.80E-04	17	17	18	16	1
512.733998	-4.00E-04	19	1	19	0	1
510.340368	-1.20E-04	18	4	19	3	1
512.514970	3.10E-04	19	5	19	4	1
512.403781	-5.60E-04	19	7	19	6	1
510.120403	3.10E-04	18	8	19	7	1
510.003156	-6.10E-04	18	10	19	9	1
509.942805	4.10E-04	18	11	19	10	1
512.169870	6.20E-04	19	11	19	10	1
509.878286	2.10E-04	18	12	19	11	1
512.036704	6.30E-04	19	13	19	12	1
509.577241	4.10E-04	18	16	19	15	1
511.800692	-4.00E-04	19	16	19	15	1
509.486055	-2.90E-04	18	17	19	16	1
510.297744	5.30E-04	19	3	20	2	1
510.132496	-1.00E-05	19	6	20	5	1

510.020089	-3.00E-04	19	8	20	7	1
509.840125	-5.90E-04	19	11	20	10	1
509.707544	7.60E-04	19	13	20	12	1
509.633514	-1.00E-05	19	14	20	13	1
509.554794	-2.40E-04	19	15	20	14	1

Subband 5						
Transition (cm^{-1})	Residual (cm^{-1})	J'	K'	J''	K''	ΔK
512.405161	-5.80E-04	1	0	2	1	-1
512.698116	-1.70E-04	2	1	2	2	-1
513.052742	8.40E-04	3	1	2	2	-1
512.759525	1.00E-05	3	2	3	3	-1
512.822756	5.00E-05	4	3	4	4	-1
512.770473	7.70E-04	5	2	5	3	-1
511.954130	-9.10E-04	5	0	6	1	-1
512.719537	7.80E-04	6	1	6	2	-1
513.543767	3.30E-04	7	1	6	2	-1
512.069362	-1.10E-04	5	2	6	3	-1
512.775849	-6.00E-04	6	2	6	3	-1
513.659971	3.60E-04	7	3	6	4	-1
512.187297	2.00E-05	5	4	6	5	-1
513.718697	-5.00E-05	7	4	6	5	-1
512.726463	-1.60E-04	7	1	7	2	-1
513.726869	3.20E-04	8	2	7	3	-1
513.784926	-4.00E-05	8	3	7	4	-1
511.736002	-5.60E-04	7	0	8	1	-1
511.794133	9.00E-04	7	1	8	2	-1
512.911274	7.90E-04	8	4	8	5	-1
512.026845	-8.60E-04	7	5	8	6	-1
512.146276	1.00E-05	7	7	8	8	-1
511.859956	-4.80E-04	8	4	9	5	-1
511.979893	9.50E-04	8	6	9	7	-1
512.755788	-6.60E-04	10	1	10	2	-1
512.813116	-7.90E-04	10	2	10	3	-1
511.753575	-4.00E-05	9	4	10	5	-1
512.990707	9.40E-04	10	5	10	6	-1
511.871220	-5.40E-04	9	6	10	7	-1
513.049620	9.10E-04	10	6	10	7	-1
512.044013	-7.10E-04	9	9	10	10	-1
513.000409	-7.30E-04	11	5	11	6	-1

511.824600	6.50E-04	10	7	11	8	-1
511.881435	-4.00E-05	10	8	11	9	-1
511.938289	6.80E-04	10	9	11	10	-1
511.717635	-7.90E-04	11	7	12	8	-1
512.909551	-4.10E-04	13	3	13	4	-1
513.253936	-6.00E-05	13	9	13	10	-1
511.829855	-1.10E-04	12	11	13	12	-1
512.810230	6.60E-04	14	1	14	2	-1
512.866609	-6.00E-05	14	2	14	3	-1
511.278549	2.80E-04	13	3	14	4	-1
513.210761	-9.50E-04	14	8	14	9	-1
511.771771	7.10E-04	13	12	14	13	-1
512.824400	-5.60E-04	15	1	15	2	-1
511.119072	1.20E-04	14	2	15	3	-1
512.882139	1.80E-04	15	2	15	3	-1
513.279458	7.00E-05	15	9	15	10	-1
513.380850	2.60E-04	15	11	15	12	-1
511.133299	1.00E-05	15	4	16	5	-1
513.344737	3.20E-04	16	10	16	11	-1
513.478717	3.00E-05	16	13	16	14	-1
512.800817	-8.70E-04	17	0	17	1	-1
511.090334	-4.00E-05	16	5	17	6	-1
513.406368	5.30E-04	17	11	17	12	-1
513.450267	1.70E-04	17	12	17	13	-1
513.552661	-6.70E-04	17	15	17	16	-1
513.336116	-7.30E-04	19	9	19	10	-1
513.433179	4.70E-04	19	11	19	12	-1
511.287712	-4.00E-05	18	13	19	14	-1
513.546151	-1.70E-04	19	14	19	15	-1
512.582847	-6.80E-04	1	1	1	0	1
512.818876	-4.20E-04	2	1	1	0	1
512.765093	3.70E-04	2	2	1	1	1
512.585769	-6.00E-05	2	1	2	0	1
512.180729	-3.50E-04	2	2	3	1	1
512.534027	-6.70E-04	3	2	3	1	1
513.007175	1.04E-03	4	2	3	1	1
513.074373	-5.20E-04	5	3	4	2	1
513.022062	-1.10E-04	5	4	4	3	1
512.969355	-8.00E-04	5	5	4	4	1
512.010170	-1.40E-04	4	1	5	0	1
513.306551	0.00E+00	6	1	5	0	1

511.955516	-1.90E-04	4	2	5	1	1
512.545246	3.10E-04	5	2	5	1	1
511.902818	7.00E-04	4	3	5	2	1
513.198958	6.90E-04	6	3	5	2	1
513.093853	4.70E-04	6	5	5	4	1
513.041010	-7.10E-04	6	6	5	5	1
512.605468	-8.90E-04	6	1	6	0	1
513.375865	-5.20E-04	7	2	6	1	1
513.270398	5.70E-04	7	4	6	3	1
513.218008	3.80E-04	7	5	6	4	1
511.789421	-1.40E-04	6	1	7	0	1
512.615084	8.40E-04	7	1	7	0	1
513.447778	-3.30E-04	8	3	7	2	1
513.394570	-5.90E-04	8	4	7	3	1
513.291309	4.00E-04	8	6	7	5	1
512.296226	-9.20E-04	7	7	7	6	1
513.682350	-7.00E-04	9	1	8	0	1
513.627638	-6.80E-04	9	2	8	1	1
513.522261	8.00E-04	9	4	8	3	1
513.469319	3.00E-04	9	5	8	4	1
513.416232	-6.90E-04	9	6	8	5	1
512.306116	6.60E-04	8	7	8	6	1
513.313069	6.10E-04	9	8	8	7	1
512.578824	3.90E-04	9	2	9	1	1
512.471957	4.40E-04	9	4	9	3	1
513.492317	7.70E-04	10	7	9	6	1
513.438001	-8.90E-04	10	8	9	7	1
512.325539	6.10E-04	10	7	10	6	1
513.618721	-3.40E-04	11	7	10	6	1
511.096324	8.00E-04	9	8	10	7	1
512.272362	1.80E-04	10	8	10	7	1
513.565515	-6.20E-04	11	8	10	7	1
511.041536	-6.00E-04	9	9	10	8	1
513.513257	9.00E-04	11	9	10	8	1
512.494073	9.00E-05	11	4	11	3	1
512.335538	-4.80E-04	11	7	11	6	1
512.229493	4.10E-04	11	9	11	8	1
513.584315	-1.90E-04	12	10	11	9	1
512.454399	7.90E-04	12	5	12	4	1
510.936973	3.60E-04	11	7	12	6	1
513.767626	-7.40E-04	13	9	12	8	1

512.185431	7.40E-04	12	10	12	9	1
513.654820	3.30E-04	13	11	12	10	1
512.466885	-2.00E-05	13	5	13	4	1
512.361574	8.50E-04	13	7	13	6	1
513.587768	-5.40E-04	14	14	13	13	1
511.051377	1.10E-04	13	1	14	0	1
512.696975	-4.50E-04	14	1	14	0	1
513.714386	-5.30E-04	15	14	14	13	1
512.549428	-7.00E-05	15	4	15	3	1
512.333535	-5.50E-04	15	8	15	7	1
512.728743	-3.20E-04	16	1	16	0	1
512.673802	-1.60E-04	16	2	16	1	1
512.619564	1.40E-04	16	3	16	2	1
512.457291	-3.30E-04	16	6	16	5	1
512.175946	7.10E-04	16	11	16	10	1
511.976183	1.00E-05	16	14	16	13	1
510.024457	-3.00E-04	15	15	16	14	1
511.900426	-3.20E-04	16	15	16	14	1
511.910580	-4.50E-04	17	15	17	14	1
509.836583	-3.40E-04	16	16	17	15	1
512.708400	1.30E-04	18	2	18	1	1
512.490332	2.40E-04	18	6	18	5	1
512.379888	5.00E-04	18	8	18	7	1
512.322732	3.60E-04	18	9	18	8	1
510.091232	-7.20E-04	17	11	18	10	1
510.028013	-3.60E-04	17	12	18	11	1
512.071643	7.90E-04	18	13	18	12	1
509.812082	-9.30E-04	17	15	18	14	1
511.921070	-5.10E-04	18	15	18	14	1
509.730758	4.60E-04	17	16	18	15	1
511.748963	1.01E-03	18	17	18	16	1
512.617654	9.90E-04	19	4	19	3	1
512.561867	-1.40E-04	19	5	19	4	1
510.279002	3.10E-04	18	6	19	5	1
510.224236	6.50E-04	18	7	19	6	1
512.337203	-7.50E-04	19	9	19	8	1
510.050402	-1.00E-03	18	10	19	9	1
509.989639	-4.00E-04	18	11	19	10	1
512.152922	9.40E-04	19	12	19	11	1
511.931546	-7.80E-04	19	15	19	14	1
509.624071	9.00E-05	18	16	19	15	1

509.533928	7.20E-04	18	17	19	16	1
510.344119	-5.80E-04	19	3	20	2	1
510.180725	5.80E-04	19	6	20	5	1
510.067894	-2.70E-04	19	8	20	7	1
510.011152	8.00E-04	19	9	20	8	1
509.887845	-7.90E-04	19	11	20	10	1
509.754684	1.00E-05	19	13	20	12	1
509.518432	5.10E-04	19	16	20	15	1

Subband 6						
Transition (cm^{-1})	Residual (cm^{-1})	J'	K'	J''	K''	ΔK
512.232990	-3.70E-04	4	2	3	3	-1
513.417613	-4.40E-04	3	0	4	1	-1
512.717135	-7.10E-04	6	0	5	1	-1
513.286485	-5.00E-05	6	2	5	3	-1
513.532758	-1.09E-03	6	3	5	4	-1
513.658411	-5.00E-04	6	4	5	5	-1
511.907439	-6.90E-04	6	0	6	1	-1
510.973000	1.06E-03	7	2	6	3	-1
513.004103	1.13E-03	7	3	6	4	-1
513.590300	1.41E-03	5	4	6	5	-1
513.716985	-1.43E-03	7	4	6	5	-1
512.917407	7.40E-04	6	4	7	5	-1
511.750249	-7.50E-04	6	5	7	6	-1
512.928413	1.03E-03	7	2	8	3	-1
511.333486	6.00E-05	9	3	9	4	-1
510.930757	-5.10E-04	9	5	9	6	-1
513.650108	1.40E-03	9	8	9	9	-1
512.244127	-2.60E-04	9	3	10	4	-1
513.773557	2.60E-04	10	3	10	4	-1
512.133464	1.15E-03	9	4	10	5	-1
511.810414	0.00E+00	9	6	10	7	-1
512.191479	-1.00E-04	9	7	10	8	-1
513.034802	-1.02E-03	10	7	11	8	-1
513.110460	9.00E-05	10	9	11	10	-1
513.125134	6.80E-04	11	9	11	10	-1
511.927317	3.00E-04	11	7	12	8	-1
510.901629	1.39E-03	11	9	12	10	-1
511.985819	-7.90E-04	12	9	13	10	-1
511.878476	-3.80E-04	12	10	13	11	-1

511.774288	2.90E-04	13	12	13	13	-1
513.212470	-4.60E-04	13	3	14	4	-1
511.993102	-1.23E-03	13	10	14	11	-1
513.287905	-5.00E-05	15	5	15	6	-1
511.888185	0.00E+00	15	9	15	10	-1
511.780613	1.01E-03	14	12	15	13	-1
513.334727	-3.80E-04	16	5	16	6	-1
511.834264	-5.50E-04	16	2	17	3	-1
511.728299	-9.90E-04	17	15	17	16	-1
513.460266	-3.90E-04	17	3	18	4	-1
511.721589	1.80E-04	18	12	18	13	-1
513.516701	6.20E-04	19	2	19	3	-1
513.606840	2.00E-04	19	15	19	16	-1
513.626450	1.10E-04	19	16	19	17	-1
513.645884	-8.60E-04	19	6	20	7	-1
513.557830	9.40E-04	4	4	3	3	1
511.956738	-5.90E-04	4	3	5	2	1
511.846440	-6.00E-05	4	4	5	3	1
512.956448	4.10E-04	6	4	5	3	1
511.904491	7.00E-05	5	3	6	2	1
513.201754	-6.90E-04	6	4	6	3	1
512.500121	-2.70E-04	5	5	6	4	1
513.451531	-2.40E-04	8	2	7	1	1
513.704457	2.80E-04	8	4	7	3	1
512.563426	-1.70E-04	8	5	7	4	1
512.575566	-1.17E-03	8	5	8	4	1
511.741099	2.70E-04	9	6	8	5	1
513.398690	-4.50E-04	10	4	9	3	1
512.463869	1.33E-03	10	5	9	4	1
513.653580	1.60E-04	9	7	9	6	1
510.994334	-4.00E-04	9	8	9	7	1
512.566901	-4.00E-04	10	8	9	7	1
510.288355	-1.14E-03	11	7	10	6	1
513.473220	1.06E-03	11	9	10	8	1
510.233614	0.00E+00	12	9	11	8	1
512.370458	-6.50E-04	11	11	11	10	1
513.673968	9.90E-04	12	4	12	3	1
512.317324	1.11E-03	13	11	12	10	1
513.494448	-1.10E-04	13	13	12	12	1
512.375865	-2.80E-04	13	4	13	3	1
510.123607	7.50E-04	12	5	13	4	1

513.569352	2.40E-04	14	8	14	7	1
513.695941	-7.00E-05	15	14	14	13	1
510.166151	-4.40E-04	16	16	15	15	1
510.309183	3.90E-04	16	5	16	4	1
510.206508	-5.00E-05	16	10	17	9	1
512.171364	-9.30E-04	16	14	17	13	1
513.711422	7.30E-04	16	15	17	14	1
510.145991	-3.30E-04	16	16	17	15	1
510.081789	-5.60E-04	17	16	17	15	1
513.585784	-6.60E-04	17	10	18	9	1
510.015557	-4.80E-04	17	11	18	10	1
509.912665	-1.09E-03	17	12	18	11	1
509.808322	-1.60E-04	17	13	18	12	1
513.770482	-5.90E-04	18	14	18	13	1
510.048276	-7.10E-04	17	15	18	14	1
512.052478	1.74E-03	17	16	18	15	1
509.735067	1.53E-03	18	9	19	8	1
509.974213	7.30E-04	18	13	19	12	1
509.866914	6.80E-04	18	15	19	14	1
509.762712	-3.50E-04	18	16	19	15	1
509.655704	-4.10E-04	18	17	19	16	1
513.740947	-6.40E-04	19	5	20	4	1
509.891485	-3.50E-04	19	6	20	5	1
511.883097	1.69E-03	19	8	20	7	1
509.786746	-1.20E-04	19	13	20	12	1
509.678063	-1.10E-04	19	14	20	13	1
509.587379	-9.40E-04	19	15	20	14	1
509.481587	1.37E-03	19	17	20	16	1

Supplemental Information for:

Terahertz VRT Spectroscopy of the Water Hexamer-d_{12} Prism: Dramatic Enhancement of Bifurcation Tunneling by Librational Excitation

Table of Figures

Table S3: List of assigned transition frequencies. All transition frequencies and residuals are in units of MHz. All transitions have $\Delta K_a = 0$. Primed values correspond to the excited state and double primed values correspond to the ground state. The column labeled "Obs-Calc" is the value of the residual.

Subband 1

Observed	Obs-Calc	J'	Ka'	Kc'	J"	Ka"	Kc"
15270400.96	-33.6	2	0	2	3	0	3
15268237.03	16.5	3	0	3	4	0	4
15282465.51	24.6	2	0	2	1	0	1
15292877.99	-39.5	6	0	6	5	0	5
15298497.39	19.0	8	0	8	7	0	7
15272739.64	-9.4	1	1	0	2	1	1
15272779.72	-25.0	1	1	1	2	1	2
15270510.15	43.3	2	1	1	3	1	2
15268365.64	44.7	3	1	3	4	1	4
15277701.75	31.6	3	1	3	3	1	2
15277763.65	12.9	4	1	4	4	1	3
15278908.59	-3.1	5	1	4	5	1	5
15285031.88	4.4	3	1	3	2	1	2
15287629.94	7.6	4	1	4	3	1	3
15290560.81	47.9	5	1	4	4	1	3
15290299.00	45.2	5	1	5	4	1	4
15295920.82	-64.3	7	1	6	6	1	5
15298879.45	56.0	8	1	7	7	1	6
15270684.33	-24.9	2	2	0	3	2	1
15268420.26	-63.5	3	2	1	4	2	2
15268506.00	-2.5	3	2	2	4	2	3
15277929.41	0.6	2	2	1	2	2	0
15278021.15	-87.5	3	2	2	3	2	1
15280516.56	-0.6	10	2	9	10	2	8
15290689.51	-10.5	5	2	3	4	2	2
15290601.88	-49.7	5	2	4	4	2	3
15296208.78	-0.1	7	2	5	6	2	4
15278787.36	50.1	4	3	1	4	3	2
15279006.65	-28.3	5	3	2	5	3	3
15278968.07	-60.5	5	3	3	5	3	2
15279454.18	79.6	6	3	3	6	3	4
15280834.49	-39.4	9	3	6	9	3	7

15291096.38	34.8	5	3	2	4	3	1
15293700.47	-102.9	6	3	4	5	3	3
15299492.31	24.9	8	3	5	7	3	4
15267182.54	-28.5	4	4	1	5	4	2
15279268.73	32.0	4	4	1	4	4	0
15279542.38	-9.5	5	4	1	5	4	2
15280357.19	46.6	7	4	3	7	4	4
15280789.85	1.8	8	4	5	8	4	4
15291598.24	20.7	5	4	1	4	4	0
15297156.93	6.0	7	4	4	6	4	3
15280228.49	13.8	5	5	1	5	5	0
15280591.54	11.6	6	5	2	6	5	1
15280908.00	-81.9	7	5	2	7	5	3
15281834.06	-29.0	7	6	1	7	6	2
15282358.96	47.7	8	6	3	8	6	2
15282863.81	-3.4	9	6	3	9	6	4
15318410.15	0.3	12	9	3	11	9	2
15321694.64	-1.0	12	10	3	11	10	2
15271617.43	0.4	11	11	0	12	11	1

Subband 2

Observed	Obs-Calc	J'	Ka'	Kc'	J"	Ka"	Kc"
15276350.70	-31.0	1	0	1	2	0	2
15271819.16	-40.5	3	0	3	4	0	4
15267575.96	-11.6	5	0	5	6	0	6
15283585.86	-5.1	1	0	1	0	0	0
15291248.17	-4.5	4	0	4	3	0	3
15276450.17	20.4	1	1	0	2	1	1
15276539.18	46.8	1	1	1	2	1	2
15274118.06	2.2	2	1	1	3	1	2
15274274.97	68.9	2	1	2	3	1	3
15269600.19	-62.4	4	1	3	5	1	4
15269780.27	-24.0	4	1	4	5	1	5
15267681.24	-11.2	5	1	5	6	1	6
15281279.35	-23.8	1	1	0	1	1	1
15293940.10	13.1	5	1	5	4	1	4
15274338.83	-54.1	2	2	0	3	2	1
15270022.14	47.9	4	2	3	5	2	4
15267905.55	36.9	5	2	4	6	2	5
15281781.20	6.3	3	2	1	3	2	2

15289025.81	41.8	3	2	1	2	2	0
15288975.50	-6.0	3	2	2	2	2	1
15270342.83	10.7	4	3	1	5	3	2
15268152.19	-35.8	5	3	2	6	3	3
15282220.70	45.3	3	3	1	3	3	0
15282624.70	-5.5	5	3	3	5	3	2
15283365.67	-49.5	7	3	5	7	3	4
15282927.43	-15.8	4	4	1	4	4	0
15283192.84	41.6	5	4	1	5	4	2
15283940.52	22.9	7	4	3	7	4	4
15269510.19	21.1	5	5	1	6	5	2
15283878.55	-40.7	5	5	1	5	5	0
15284074.56	-40.6	6	5	1	6	5	2
15298559.63	14.4	6	5	2	5	5	1
15268289.67	14.8	6	6	1	7	6	2
15285105.75	-3.5	6	6	0	6	6	1
15285902.84	2.8	8	6	3	8	6	2
15317187.08	-0.5	12	6	6	11	6	5
15323630.37	-0.5	12	9	3	11	9	2
15292318.40	0.1	10	10	1	10	10	0

Subband 3

Observed	Obs-Calc	J'	Ka'	Kc'	J"	Ka"	Kc"
15281891.56	-32.4	0	0	0	1	0	1
15270896.94	53.2	5	0	5	6	0	6
15268712.20	-12.9	6	0	6	7	0	7
15279602.34	-12.1	1	1	0	2	1	1
15279706.64	20.1	1	1	1	2	1	2
15277359.35	-66.4	2	1	2	3	1	3
15275112.71	43.1	3	1	2	4	1	3
15275286.02	62.0	3	1	3	4	1	4
15272982.14	-88.9	4	1	4	5	1	5
15270748.45	-22.8	5	1	4	6	1	5
15270987.36	42.2	5	1	5	6	1	6
15284405.92	-23.2	1	1	1	1	1	0
15289444.23	33.6	2	1	1	1	1	0
15289364.30	2.1	2	1	2	1	1	1
15294606.38	-48.8	4	1	3	3	1	2
15300079.67	-1.4	6	1	5	5	1	4

15277542.08	-24.6	2	2	0	3	2	1
15273056.64	-68.5	4	2	2	5	2	3
15273155.72	-46.4	4	2	3	5	2	4
15271032.35	61.8	5	2	3	6	2	4
15271161.36	57.1	5	2	4	6	2	5
15269025.84	-23.4	6	2	5	7	2	6
15284823.62	34.8	2	2	1	2	2	0
15285983.51	43.8	6	2	4	6	2	5
15292192.85	7.6	3	2	1	2	2	0
15297555.17	30.0	5	2	3	4	2	2
15275723.24	14.9	3	3	1	4	3	2
15273575.19	37.1	4	3	2	5	3	3
15271373.49	-47.8	5	3	2	6	3	3
15269314.00	-42.6	6	3	3	7	3	4
15267276.61	-41.6	7	3	4	8	3	5
15286566.13	-32.9	7	3	5	7	3	4
15287323.17	0.5	9	3	7	9	3	6
15272020.92	82.0	5	4	2	6	4	3
15267946.14	12.9	7	4	4	8	4	5
15286073.33	-3.7	4	4	1	4	4	0
15286330.79	-40.7	5	4	2	5	4	1
15286672.95	-75.6	6	4	2	6	4	3
15287241.62	58.4	7	4	3	7	4	4
15288118.16	6.2	9	4	5	9	4	6
15298404.57	7.3	5	4	2	4	4	1
15272539.20	-61.9	5	5	1	6	5	2
15268579.69	-27.4	7	5	2	8	5	3
15287044.99	13.8	5	5	1	5	5	0
15287442.93	59.7	6	5	1	6	5	2
15271311.94	-30.1	6	6	1	7	6	2
15288211.33	34.8	6	6	0	6	6	1
15288565.75	-25.6	7	6	1	7	6	2
15289211.95	22.6	8	6	2	8	6	3
15289674.62	-10.5	9	6	3	9	6	4
15270246.33	6.8	7	7	1	8	7	2
15292270.34	-0.3	9	9	1	9	9	0
15293565.21	-0.1	10	9	1	10	9	2

Table S4: Correlation matrices for each fit.

Subband 1													
Origin	1.000												
A	-0.434	1.000											
B	-0.486	-0.046	1.000										
C	-0.364	0.217	0.143	1.000									
DK	0.161	0.193	-0.293	-0.277	1.000								
DJK	-0.076	0.256	-0.047	0.031	-0.677	1.000							
DJ	-0.632	0.040	0.692	0.736	-0.202	-0.237	1.000						
deltaK	0.336	-0.049	-0.453	-0.458	0.767	-0.596	-0.508	1.000					
deltaJ	0.019	-0.116	0.689	-0.448	-0.265	0.204	0.079	-0.362	1.000				
HK	0.310	0.074	-0.469	-0.465	0.786	-0.523	-0.540	0.970	-0.337	1.000			
HKJ	-0.343	-0.013	0.499	0.491	-0.594	0.337	0.632	-0.828	0.328	-0.763	1.000		
HJK	0.315	0.185	-0.553	-0.489	0.141	0.294	-0.816	0.546	-0.192	0.644	-0.790	1.000	
HJ	-0.546	0.007	0.643	0.698	-0.214	-0.225	0.979	-0.553	0.089	-0.597	0.702	-0.588	1.000
Subband 2													
Origin	1.000												
A	-0.467	1.000											
B	-0.246	-0.225	1.000										
C	-0.294	0.082	-0.618	1.000									
DK	0.028	-0.074	0.604	-0.643	1.000								
DJK	0.023	0.478	-0.780	0.446	-0.624	1.000							
DJ	-0.386	-0.354	0.603	0.187	0.270	-0.395	1.000						
deltaK	-0.230	0.581	-0.298	0.256	-0.423	0.566	-0.294	1.000					
deltaJ	0.052	-0.193	0.854	-0.874	0.738	-0.720	0.247	-0.435	1.000				
HK	-0.344	0.506	0.013	0.207	-0.386	0.357	0.060	0.821	-0.187	1.000			
HKJ	0.333	-0.473	0.118	-0.358	0.526	-0.460	-0.046	-0.825	0.344	-0.784	1.000		
HJK	-0.290	0.435	-0.361	0.582	-0.716	0.628	-0.028	0.781	-0.595	0.883	-0.652	1.000	
HJ	0.065	-0.380	0.752	-0.693	0.865	-0.780	0.371	-0.628	0.850	-0.552	0.678	-0.456	1.000
Subband 3													
Origin	1.000												
A	-0.510	1.000											
B	-0.331	-0.156	1.000										
C	-0.334	0.094	-0.324	1.000									
DK	-0.091	0.042	0.428	-0.253	1.000								
DJK	0.110	0.449	-0.725	0.082	-0.741	1.000							
DJ	-0.446	-0.207	0.770	0.279	0.429	-0.623	1.000						
deltaK	0.074	-0.357	0.179	-0.028	-0.271	-0.124	0.161	1.000					
deltaJ	0.025	-0.118	0.792	-0.751	0.437	-0.505	0.328	0.116	1.000				
HK	0.013	-0.255	0.294	-0.091	-0.272	-0.113	0.212	0.952	0.247	1.000			
HKJ	-0.021	0.245	-0.172	-0.005	0.424	-0.022	-0.129	-0.745	-0.100	-0.584	1.000		
HJK	0.041	-0.065	-0.213	0.188	-0.698	0.422	-0.189	0.781	-0.274	0.804	-0.593	1.000	
HJ	-0.268	-0.176	0.830	-0.133	0.690	-0.404	0.844	-0.084	0.650	-0.034	0.176	-0.568	1.000

Table S5: List of calculated vibrational frequencies for the $(D_2O)_6$ prism structure. All values are given in cm^{-1}. A, B, and C correspond to the rotational constants of the structure.

Harmonic	Anharmonic	A	B	C	(B+C)/2	Intensity (Harm.)	Intensity (Anharm.)
2835.248	2730.061	0.049283	0.040773	0.039159	0.039966	80.691	40.416
2831.264	2727.554	0.049276	0.040755	0.039175	0.039965	70.106	52.827
2825.959	2722.765	0.049241	0.040754	0.039181	0.039968	59.856	25.982
2780.181	2689.57	0.049484	0.040763	0.039196	0.03998	112.188	19.562
2760.938	2653.235	0.049359	0.04089	0.039173	0.040032	220.283	12.149
2737.529	2627.762	0.049373	0.04072	0.039373	0.040047	64.001	22.279
2657.983	2559.138	0.04914	0.04073	0.039369	0.04005	124.777	68.061
2646.099	2552.269	0.049234	0.040888	0.039203	0.040046	76.948	50.392
2584.586	2482.369	0.049521	0.041065	0.039138	0.040102	251.722	167.214
2562.466	2466.655	0.049404	0.041174	0.039072	0.040123	116.790	107.131
2495.53	2419.17	0.049658	0.040866	0.039498	0.040182	367.449	214.836
2325.921	2204.404	0.049601	0.041221	0.039588	0.040405	439.106	321.824
1244.05	1228.641	0.049219	0.040733	0.039158	0.039946	35.029	18.498
1232.822	1211.298	0.04921	0.040755	0.039142	0.039949	45.331	28.256
1220.993	1200.751	0.04921	0.040739	0.039183	0.039961	10.294	13.046
1207.169	1188.888	0.049295	0.040752	0.039149	0.039951	31.704	31.496
1201.065	1182.334	0.049255	0.04075	0.039168	0.039959	20.275	111.124
1194.579	1178.49	0.049229	0.040748	0.039199	0.039974	90.494	64.139
746.691	692.751	0.049008	0.040504	0.039004	0.039754	36.529	0.041
649.073	597.084	0.049009	0.040609	0.038967	0.039788	35.732	8.054
618.761	563.418	0.049097	0.040533	0.039039	0.039786	18.643	3.597
533.008	483.83	0.049251	0.04052	0.039026	0.039773	182.588	23.097
503.649	460.317	0.049188	0.040623	0.038991	0.039807	59.197	7.720
468.354	396.601	0.048997	0.040598	0.039197	0.039898	122.018	21.640
454.815	393.785	0.049078	0.04056	0.039088	0.039824	98.922	15.367
400.067	352.15	0.049089	0.040683	0.039065	0.039874	12.851	201.898
397.661	360.013	0.049087	0.040667	0.039086	0.039877	87.308	38.797
354.852	308.554	0.049043	0.040669	0.039094	0.039882	31.603	24.754
339.787	304.494	0.049125	0.040687	0.039075	0.039881	28.243	3.266
314.743	284.365	0.049133	0.040641	0.039103	0.039872	45.352	33.150
309.581	280.085	0.049133	0.040652	0.039069	0.039861	17.846	26.154
283.68	257.492	0.04911	0.04067	0.039045	0.039858	36.285	29.885
265.492	238.256	0.049132	0.04067	0.039107	0.039889	16.826	11.699
252.501	225.532	0.049248	0.040704	0.039016	0.03986	10.887	6.299
239.064	215.294	0.049125	0.040626	0.03904	0.039833	19.633	16.606
224.758	190.071	0.049052	0.040532	0.039096	0.039814	39.015	47.968
217.911	197.748	0.049154	0.0407	0.039104	0.039902	24.366	5.032
211.113	194.002	0.049142	0.040676	0.039079	0.039878	30.860	24.336
200.41	183.652	0.049091	0.040559	0.039124	0.039842	4.549	2.723
176.721	161.642	0.04923	0.040649	0.039103	0.039876	13.684	12.987
160.16	143.567	0.049288	0.040642	0.039107	0.039875	2.397	6.836
156.997	144.471	0.048944	0.040637	0.039013	0.039825	6.804	9.859
135.446	117.802	0.049107	0.040647	0.039087	0.039867	1.899	2.797
90.081	90.2	0.048964	0.040775	0.038963	0.039869	1.022	4.973
81.293	60.036	0.049007	0.040909	0.039014	0.039962	0.817	4.020
71.974	60.316	0.049419	0.040697	0.039231	0.039964	1.158	0.451
67.602	58.071	0.049129	0.040712	0.039016	0.039864	0.095	0.176
59.067	57.725	0.049149	0.040706	0.039129	0.039918	1.875	3.699

Figure S1: Input file for Gaussian calculation.

Gaussian input file
%mem=16GB
%nprocshared=8
%chk=gaussian.prism.mp2.aug-cc-pVDZ.0.chk
#p mp2/aug-cc-pVDZ opt=verytight
freq=(vibrot,anharmonic,readanharm,Step=50)

D2O prism hexamer optimization/frequencies mp2/aug-cc-pVDZ basis; structure 0

0 1
O -1.878977 -0.912104 0.744635
H(iso=2,spin=1) -1.015729 -1.305507 1.015327
H(iso=2,spin=1) -2.556622 -1.366750 1.253438
O 0.761614 1.286754 -1.677960
H(iso=2,spin=1) 0.420698 0.366268 -1.804315
H(iso=2,spin=1) 0.915273 1.642610 -2.557092
O 0.789410 -1.796634 1.049467
H(iso=2,spin=1) 1.223297 -0.900372 1.099955
H(iso=2,spin=1) 1.356733 -2.401697 1.536296
O 1.696318 0.796716 0.986875
H(iso=2,spin=1) 1.755722 1.001229 0.032267
H(iso=2,spin=1) 0.869185 1.257144 1.251681
O -0.911741 1.816031 0.671940
H(iso=2,spin=1) -1.408705 0.977434 0.719677
H(iso=2,spin=1) -0.498049 1.816408 -0.211316
O -0.254719 -1.306873 -1.589006
H(iso=2,spin=1) -1.104339 -1.170431 -1.128038
H(iso=2,spin=1) 0.310535 -1.705756 -0.898653

PT2model=GVPT2

Supplemental Information for:

Terahertz VRT Spectroscopy of the Water Hexamer-h12 Cage: Dramatic Libration-Induced Enhancement of Hydrogen Bond Tunneling Dynamics

Table of Figures

Table S6: List of assigned transition frequencies. All transition frequencies and residuals are in units of MHz. All transitions have $\Delta K_a = 0$. Primed values correspond to the excited state and double primed values correspond to the ground state. The column labeled "Obs-Calc" is the value of the residual.

Subband 1

Calculated	Obs-Calc	J'	Ka'	Kc'	J"	Ka"	Kc"
15640691	3.0783	14	14	0	15	14	1
15649540.8	7.9124	14	10	4	15	10	5
15655336.4	-0.0262	14	6	8	15	6	9
15656547	27.5915	13	7	6	14	7	7
15663689.3	-12.5628	10	7	3	11	7	4
15669123.6	25.5775	9	4	6	10	4	7
15673276.5	-22.4326	8	0	8	9	0	9
15673309.5	6.3457	8	1	8	9	1	9
15677157.3	29.7024	6	2	4	7	2	5
15677826.2	3.2753	6	1	6	7	1	7
15678605.7	-10.3699	13	12	2	13	12	1
15679067	-27.4974	5	3	2	6	3	3
15679666.3	-21.5497	5	1	4	6	1	5
15682649.3	-0.038	13	10	4	13	10	3
15686514	27.3589	2	1	1	3	1	2
15687325.6	-28.3052	13	7	6	13	7	7
15688769.3	20.7041	1	1	0	2	1	1
15689384.8	-9.8895	8	6	2	8	6	3
15689631.6	-13.175	6	6	0	6	6	1
15690268.7	-6.6279	9	5	4	9	5	5
15690415.5	29.5233	8	5	4	8	5	3
15691393.2	15.6889	7	4	4	7	4	3
15691504.7	27.4989	6	4	2	6	4	3
15691598.4	-11.7592	5	4	2	5	4	1
15692073.5	13.0329	7	3	4	7	3	5
15692161	-18.2962	6	3	4	6	3	3
15692640.5	-69.476	5	2	4	5	2	3
15695515.2	1.4996	1	0	1	0	0	0
15701757.6	-8.4825	4	1	4	3	1	3
15701945.4	6.098	4	0	4	3	0	3
15703846.6	-19.299	5	1	5	4	1	4

15704896.2	6.3908	7	6	2	6	6	1
15705805	3.8724	6	2	5	5	2	4
15706411.3	12.3385	9	8	2	8	8	1
15707881.6	16.1173	7	2	6	6	2	5
15708141.5	16.3136	7	0	7	6	0	6
15708851.7	-29.0721	8	4	5	7	4	4
15709015.1	16.116	9	6	4	8	6	3
15709176.8	0.8518	12	10	2	11	10	1
15709541	-7.6	8	3	5	7	3	4
15709936.5	32.5469	8	2	7	7	2	6
15710000.4	16.2492	8	1	8	7	1	7
15710472.1	2.2554	11	8	4	10	8	3
15711574.3	-31.4878	9	3	7	8	3	6
15711612.1	14.8753	9	3	6	8	3	5
15712229.8	-4.6348	9	2	7	8	2	6
15712431.7	23.7006	9	1	8	8	1	7
15712947.9	7.9649	10	4	7	9	4	6
15713428.4	-2.0071	15	11	5	14	11	4
15713609.6	-87.0004	10	3	8	9	3	7
15713884.1	-0.1795	12	7	6	11	7	5
15713979.7	8.023	10	2	9	9	2	8
15716401.3	19.2651	11	1	10	10	1	9

Subband 2

Calculated	Obs-Calc	J'	Ka'	Kc'	J"	Ka"	Kc"
15650273.2	0.0445	13	12	2	14	12	3
15673577.6	3.4965	8	7	1	9	7	2
15674870.9	19.5955	9	3	6	10	3	7
15675499.4	-6.8221	9	1	8	10	1	9
15682539	1.0471	6	1	5	7	1	6
15691329.5	1.6735	12	8	5	12	8	4
15692470.9	-4.4025	13	7	7	13	7	6
15693082.7	18.6591	10	7	3	10	7	4
15693242.8	-28.2451	9	7	2	9	7	3
15694242.7	7.1945	10	6	4	10	6	5
15694703.2	14.6979	7	6	2	7	6	1
15694906.9	2.7765	12	5	7	12	5	8
15696987.9	3.0549	9	3	6	9	3	7
15697008.1	14.8178	8	2	7	8	2	6

15697105.7	-7.6755	8	3	5	8	3	6
15697325.7	-1.37	6	3	4	6	3	3
15697638.8	7.4757	4	1	4	4	1	3
15698087.2	5.3176	2	2	0	2	2	1
15698466.1	10.7172	1	1	0	1	1	1
15698567.3	-20.2102	2	1	1	2	1	2
15698714.8	4.6289	3	1	2	3	1	3
15704817.4	-19.8448	3	1	3	2	1	2
15706801.1	-16.8771	4	2	2	3	2	1
15706914.7	0.1317	4	1	4	3	1	3
15709201.4	21.8433	5	0	5	4	0	4
15710528.1	32.3636	6	3	3	5	3	2
15711112.5	-3.1481	7	5	3	6	5	2
15711426.9	39.0803	6	1	5	5	1	4
15712596.6	-39.0198	7	3	5	6	3	4
15713196.2	-8.5292	7	2	5	6	2	4
15713501	-29.764	7	1	6	6	1	5
15713640.2	-0.4907	10	8	3	9	8	2
15715150.7	-7.5658	8	1	8	7	1	7
15715201.3	-14.6513	9	5	5	8	5	4

Subband 3

Calculated	Obs-Calc	J'	Ka'	Kc'	J"	Ka"	Kc"
15673354.1	21.7873	12	1	11	13	1	12
15674200.9	-5.157	12	0	12	13	0	13
15674749.6	-7.0248	9	8	1	10	8	2
15678089.1	-18.4306	10	1	9	11	1	10
15678134.3	-20.2564	10	2	9	11	2	10
15679893.3	-6.6822	9	3	7	10	3	8
15682524.7	23.0321	8	2	6	9	2	7
15693144.3	-0.4142	11	10	2	11	10	1
15695760.1	-1.5926	14	8	7	14	8	6
15696560.3	8.0847	10	8	2	10	8	3
15696598.5	3.9009	2	1	1	3	1	2
15697961.3	7.2909	10	7	4	10	7	3
15698369	1.2981	7	7	0	7	7	1
15698839.5	-4.87	12	6	6	12	6	7
15698854.5	53.2837	1	1	0	2	1	1
15698980.4	-34.9638	1	1	1	2	1	2

15699016	-7.657	1	0	1	2	0	2
15700229.7	-2.2981	10	5	6	10	5	5
15700454.7	2.2447	13	4	10	13	4	9
15700513.4	-12.357	8	5	4	8	5	3
15700913.8	28.9496	11	4	7	11	4	8
15701017.7	-4.7745	12	3	10	12	3	9
15701485.1	-37.3904	7	4	4	7	4	3
15701822.5	-13.6338	9	3	7	9	3	6
15702183.9	29.106	5	1	5	5	1	4
15702260.2	5.7409	6	3	3	6	3	4
15702563.8	-1.727	4	1	4	4	1	3
15702913	6.4309	5	2	3	5	2	4
15702990.2	13.8337	2	2	1	2	2	0
15703096	-4.8251	2	1	2	2	1	1
15703370.8	-20.4822	1	1	0	1	1	1
15703464.5	-55.7524	2	1	1	2	1	2
15709734.1	27.5871	3	1	3	2	1	2
15713330.2	54.882	5	3	3	4	3	2
15713791.4	-11.0645	5	2	4	4	2	3
15713846.4	-13.4376	5	2	3	4	2	2
15734071.9	3.4876	15	1	14	14	1	13
15734219.9	-6.149	15	2	13	14	2	12

Subband 4

Calculated	Obs-Calc	J'	Ka'	Kc'	J"	Ka"	Kc"
15678733.2	10.8725	9	9	0	10	9	1
15682640.1	16.3155	8	8	0	9	8	1
15688876.7	-19.9765	8	0	8	9	0	9
15689857.9	-41.3113	6	6	1	7	6	2
15690654.8	-33.9031	7	1	6	8	1	7
15691169.6	7.2406	7	1	7	8	1	8
15692972.8	14.7763	6	1	5	7	1	6
15693422	1.8943	6	1	6	7	1	7
15693796.1	-0.5362	15	12	3	15	12	4
15694014.3	-5.2967	5	4	1	6	4	2
15694669.2	-12.1639	5	3	2	6	3	3
15694673.4	14.8908	5	3	3	6	3	4
15695087.4	6.5449	5	2	3	6	2	4
15695277.7	-57.0499	5	1	4	6	1	5

15695629	-19.7833	5	0	5	6	0	6
15697385	16.5455	4	2	2	5	2	3
15699848.1	56.5764	3	1	2	4	1	3
15699951.7	6.8039	13	9	5	13	9	4
15700369.7	-17.9544	11	9	3	11	9	2
15703292.7	-4.3935	11	7	5	11	7	4
15703482.6	7.3514	10	7	4	10	7	3
15703548.1	4.4125	15	6	9	15	6	10
15703923.9	-22.7024	7	7	1	7	7	0
15705129.2	30.5708	7	6	2	7	6	1
15705878	-29.2183	9	5	5	9	5	4
15706154.9	-0.4421	7	5	3	7	5	2
15706263.8	-13.3816	6	5	2	6	5	1
15706354.2	9.8467	5	5	1	5	5	0
15706520.6	-17.0199	12	3	10	12	3	9
15706845.3	5.0385	11	3	9	11	3	8
15707001	27.0077	7	4	4	7	4	3
15707199.7	29.8077	5	4	2	5	4	1
15707347.9	21.4549	10	3	7	10	3	8
15707573.5	-37.0132	8	3	5	8	3	6
15708066.7	45.0132	6	2	5	6	2	4
15708078.2	39.6867	4	1	4	4	1	3
15708505.4	4.7157	2	2	1	2	2	0
15708608.6	-7.2562	2	1	2	2	1	1
15708645.9	2.5146	9	2	7	9	2	8
15708759.5	-55.4866	1	1	1	1	1	0
15708883.4	9.3059	1	1	0	1	1	1
15708980	-3.2912	2	1	1	2	1	2
15709123.9	-15.5776	3	1	2	3	1	3
15715424.6	0.0738	3	0	3	2	0	2
15733348.1	64.4218	12	3	9	11	3	8
15733680.1	55.9306	13	5	9	12	5	8
15738502.8	-34.2555	15	4	12	14	4	11
15739182.6	41.4826	15	3	13	14	3	12
15739403	-1.0023	15	0	15	14	0	14
15739746.7	-0.2442	15	1	14	14	1	13
15739835.3	-7.0226	15	2	13	14	2	12

Table S7: Correlation matrices for each fit.

Subband 1	Origin	A	B	C	DK	DJK	DJ	ΔK	ΔJ	HK	HKJ	HJK	HJ
Origin	1												
A	-0.298	1											
B	-0.39	-0.15	1										
C	-0.5	0.041	-0.374	1									
DK	0.041	0.174	-0.053	0.01	1								
DJK	0.185	0.283	-0.253	-0.258	-0.769	1							
DJ	-0.622	-0.137	0.514	0.524	0.231	-0.702	1						
ΔK	0.187	0.163	-0.004	-0.388	0.15	0.135	-0.354	1					
ΔJ	-0.103	0.049	-0.747	0.848	-0.04	-0.002	0.078	-0.307	1				
HK	-0.129	-0.218	-0.009	0.216	-0.789	0.507	-0.048	-0.419	0.231	1			
HKJ	0.097	0.215	-0.002	-0.145	0.913	-0.639	0.131	0.34	-0.181	-0.97	1		
HJK	0.014	-0.047	-0.143	0.027	-0.912	0.827	-0.386	-0.205	0.17	0.893	-0.952	1	
HJ	-0.409	-0.035	0.483	0.265	0.566	-0.841	0.869	-0.101	-0.121	-0.499	0.564	-0.76	1
Subband 2	Origin	A	B	C	DK	DJK	DJ	ΔK	ΔJ	HK	HKJ	HJK	HJ
Origin	1												
A	-0.332	1											
B	-0.457	0.051	1										
C	-0.555	0.002	-0.172	1									
DK	-0.346	0.416	0.416	0.199	1								
DJK	0.332	0.293	-0.521	-0.391	-0.688	1							
DJ	-0.643	0.088	0.62	0.592	0.664	-0.826	1						
ΔK	-0.059	0.052	0.032	0.065	-0.003	0.007	0.085	1					
ΔJ	-0.096	-0.044	-0.704	0.764	-0.134	0.051	0.026	0.026	1				
HK	0.325	-0.506	-0.411	-0.136	-0.704	0.389	-0.597	-0.173	0.174	1			
HKJ	-0.35	0.488	0.455	0.161	0.827	-0.518	0.668	0.135	-0.186	-0.979	1		
HJK	0.379	-0.237	-0.555	-0.248	-0.849	0.763	-0.814	-0.105	0.185	0.88	-0.941	1	
HJ	-0.522	0.219	0.63	0.399	0.769	-0.783	0.938	0.111	-0.121	-0.804	0.862	-0.95	1
Subband 3	Origin	A	B	C	DK	DJK	DJ	ΔK	ΔJ	HK	HKJ	HJK	HJ
Origin	1												
A	-0.256	1											
B	-0.249	-0.377	1										
C	-0.421	-0.238	-0.144	1									
DK	-0.079	0.808	-0.419	-0.275	1								
DJK	-0.106	0.737	-0.275	-0.27	0.266	1							
DJ	-0.405	-0.499	0.61	0.655	-0.485	-0.534	1						
ΔK	0.041	-0.09	0.514	-0.414	-0.072	-0.072	0.073	1					

ΔJ	-0.112	0.102	-0.748	0.722	0.088	0.047	-0.01	-0.677	1				
HK	-0.146	0.1	0.005	0.204	0.139	-0.107	0.255	-0.022	0.073	1			
HKJ	0.035	0.596	-0.324	-0.379	0.684	0.364	-0.587	-0.029	0.004	-0.616	1		
HJK	-0.145	0.015	0.087	0.213	-0.434	0.439	0.182	-0.078	0.083	0.51	-0.666	1	
HJ	-0.352	-0.481	0.638	0.562	-0.425	-0.576	0.982	0.164	-0.106	0.258	-0.547	0.1	1
Subband 4	Origin	A	B	C	DK	DJK	DJ	ΔK	ΔJ	HK	HKJ	HJK	HJ
Origin	1												
A	-0.505	1											
B	-0.574	0.079	1										
C	-0.565	0.158	0.099	1									
DK	0.017	0.162	-0.094	-0.001	1								
DJK	-0.028	0.308	-0.129	-0.123	-0.822	1							
DJ	-0.594	0.057	0.749	0.602	0.181	-0.456	1						
ΔK	0.018	-0.009	-0.085	0.078	0.109	-0.11	0.041	1					
ΔJ	0.056	0.043	-0.689	0.601	0.061	0.015	-0.152	0.207	1				
HK	0.087	-0.087	-0.09	-0.012	0.811	-0.743	0.128	0.103	0.026	1			
HKJ	-0.099	0.277	0.017	0.008	-0.228	0.303	-0.045	-0.039	0.052	-0.739	1		
HJK	-0.018	0.196	-0.082	-0.093	-0.797	0.922	-0.392	-0.117	-0.03	-0.54	-0.049	1	
HJ	-0.498	0.024	0.692	0.526	0.279	-0.552	0.981	0.078	-0.15	0.188	-0.029	-0.51	1

Table S8: List of calculated vibrational frequencies for the $(H_2O)_6$ cage structure. All values are given in cm^{-1}. The columns for dA and dB correspond to the change in rotational constant A and the change in (B+C)/2 respectively.

#cage-cc_pvtz
#Vibrational Energies and Rotational Constants (in cm^-1); energies w.r.t. ground state

# j <-	i	harm	anharm	dA	dB
1	0	3926.34	3750.845	-0.000009	-0.000003
2	0	3918.911	3736.475	0.000051	-0.000002
3	0	3914.944	3736.485	-0.000004	-0.000008
4	0	3912.55	3734.473	-0.000008	-0.000005
5	0	3789.6	3601.984	0.000146	0.000129
6	0	3754.04	3577.061	0.000153	0.000096
7	0	3710.795	3545.345	0.000111	0.000101
8	0	3587.563	3423.33	0.000268	0.000247
9	0	3578.237	3406.591	0.000605	0.000133
10	0	3486.795	3354.952	0.000429	0.000397
11	0	3445.816	3338.496	0.000831	0.000266
12	0	3231.744	3004.57	0.001576	0.000429
13	0	1729.156	1685.621	-0.000156	-0.00002
14	0	1714.5	1681.983	-0.000033	-0.000039
15	0	1703.815	1649.179	-0.000175	0.000029
16	0	1694.562	1640.378	-0.000061	0.000003
17	0	1682.819	1641.187	-0.000046	0.000011
18	0	1669.596	1626.115	0.000016	0.000002
19	0	1054.485	950.885	-0.00046	-0.000314
20	0	915.967	828.961	-0.000475	-0.000217
21	0	863.712	774.411	-0.000168	-0.000271
22	0	826.039	720.489	-0.000445	-0.000189
23	0	759.747	665.363	-0.000386	-0.000162
24	0	732.094	655.348	-0.000588	-0.000099
25	0	656.746	574.222	-0.000123	-0.000224
26	0	608.102	516.356	-0.000353	-0.000081
27	0	556.693	497.903	-0.000339	-0.000165
28	0	500.406	450.131	-0.000266	-0.000054
29	0	475.831	415.121	-0.000334	-0.00014
30	0	462.973	413.866	-0.000324	-0.000086
31	0	425.745	383.016	-0.000173	-0.000099
32	0	397.535	362.592	-0.000129	-0.000095

33	0	313.574	272.429	-0.000203	0.000012
34	0	297.678	269.19	-0.000287	-0.000079
35	0	281.122	232.576	-0.000123	0.000009
36	0	257.782	233.375	-0.000074	-0.000112
37	0	249.011	216.439	-0.000131	-0.00003
38	0	246.545	219.464	-0.000104	-0.000082
39	0	242.445	214.105	-0.000243	-0.000119
40	0	235.834	202.799	-0.000275	-0.000095
41	0	224.277	199.142	-0.000146	-0.000162
42	0	202.552	174.908	-0.00043	-0.000119
43	0	164.62	139.64	-0.000463	-0.000133
44	0	136.549	107.788	-0.000277	-0.000079
45	0	106.898	93.582	-0.000531	-0.000034
46	0	78.243	74.157	0.000059	0.000019
47	0	56.733	37.385	0.00036	-0.000025
48	0	44.549	15.292	-0.000495	-0.000006

Figure S2: Gaussian input file

```
%mem=24GB
%nprocshared=16
%chk=gaussian.cage.chk
#p mp2/cc-pVDZ opt=verytight freq=(vibrot,anharmonic,readanharm)

H2O cage hexamer optimization/frequencies mp2/cc-pVDZ basis

 0  1
O      -1.681646      0.474708     -0.890663
H      -2.528807      0.676345     -1.288020
H      -1.201169      1.302160     -0.917039
O      -0.016601      2.621714     -0.794925
H       0.653139      2.123932     -0.325997
H       0.472159      3.295267     -1.267865
O       0.643490     -1.060535     -1.262691
H       0.518045     -1.785133     -0.649948
H      -0.219429     -0.651975     -1.331107
O       1.645844      0.788161      0.421017
H       2.537050      0.560433      0.685824
```

H	1.405974	0.116190	-0.217065
O	-0.694558	-0.193159	1.641737
H	0.142861	0.240527	1.477798
H	-1.232022	0.027397	0.881001
O	0.102785	-2.673509	0.901262
H	-0.219384	-1.858896	1.287067
H	-0.317429	-3.364315	1.413551

PT2model=GVPT2

Supplemental Material for:

Hydrogen Bond Network Rearrangement Dynamics in Water Clusters: Effects of Intermolecular Vibrational Excitation on Tunneling Rates

Supplemental Material Outline

I. Water Dimer Minima

The minima for the water dimer are given in Figure S3. The hydrogens are labeled 1-4 and the oxygens are labeled a and b. The labels |1> - |8> are given above the structure in additional to the group element for the G_{16} CNPI group needed to arrive at the given structure. By comparison to the Hamiltonian given in Figure 2A of the main text, one can find the acceptor switching tunneling corresponds to structure |1> permuting to structure |4>. Likewise the bifurcation mechanism take structure |1> to |2>, the geared interchange pathway takes |1> to structure |5> or |6>, and the antigeared interchange pathway takes |1> to |7> or |8>.

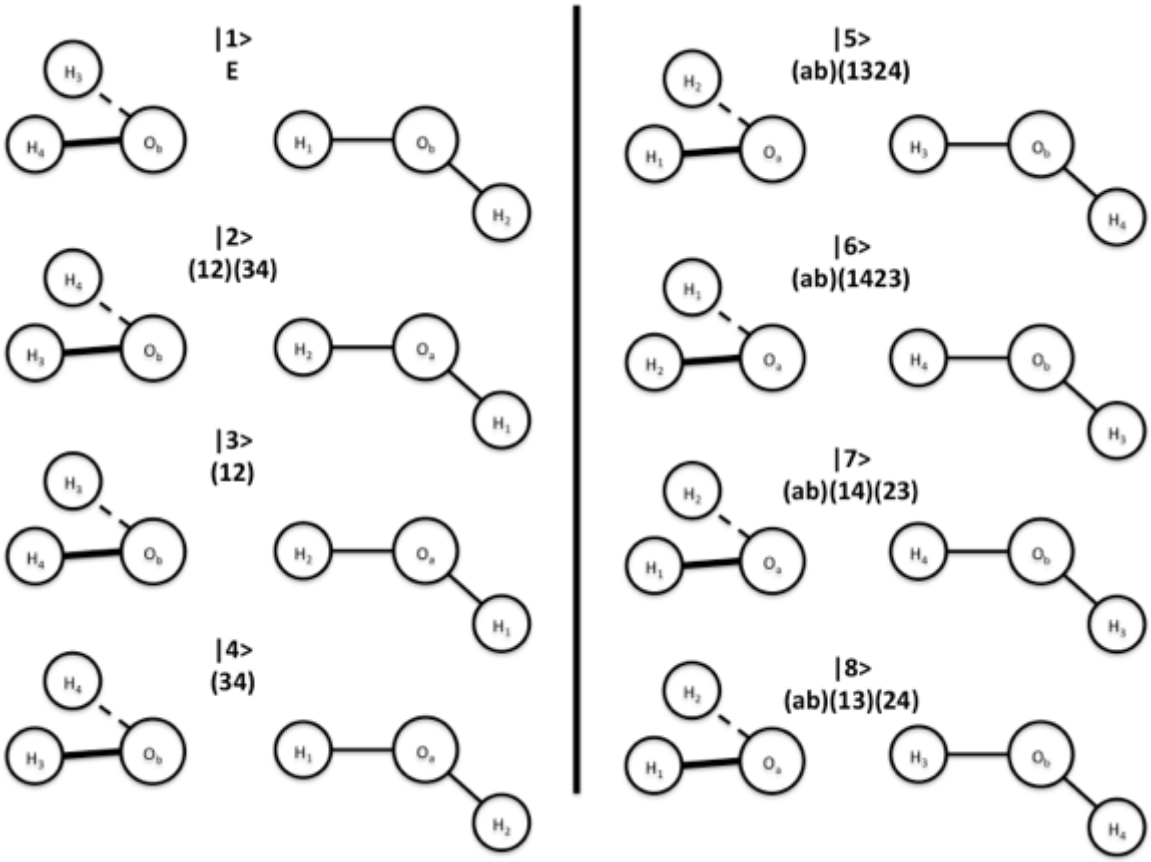

Figure S3: Structures for the 8 degenerate minima of the water dimer.

II. Water Trimer Minima

The 8 degenerate minima of the water trimer are given in Figure S4. The notation for the structures is as follows: the structure is represented as (xyz) where x, y, and z represents each of the monomers, and can have values of 1 or 0 to represent which hydrogen of the monomer is participating in the hydrogen bond. Thus we can represent the bifurcation tunneling motion as flipping the value of x, y, or z (i.e. (010) → (000)). We can neglect considering the orientation of the free hydrogen with respect to the oxygen plane due to the low barrier of the flipping motion in contrast to the bifurcation motion as discussed in the text.

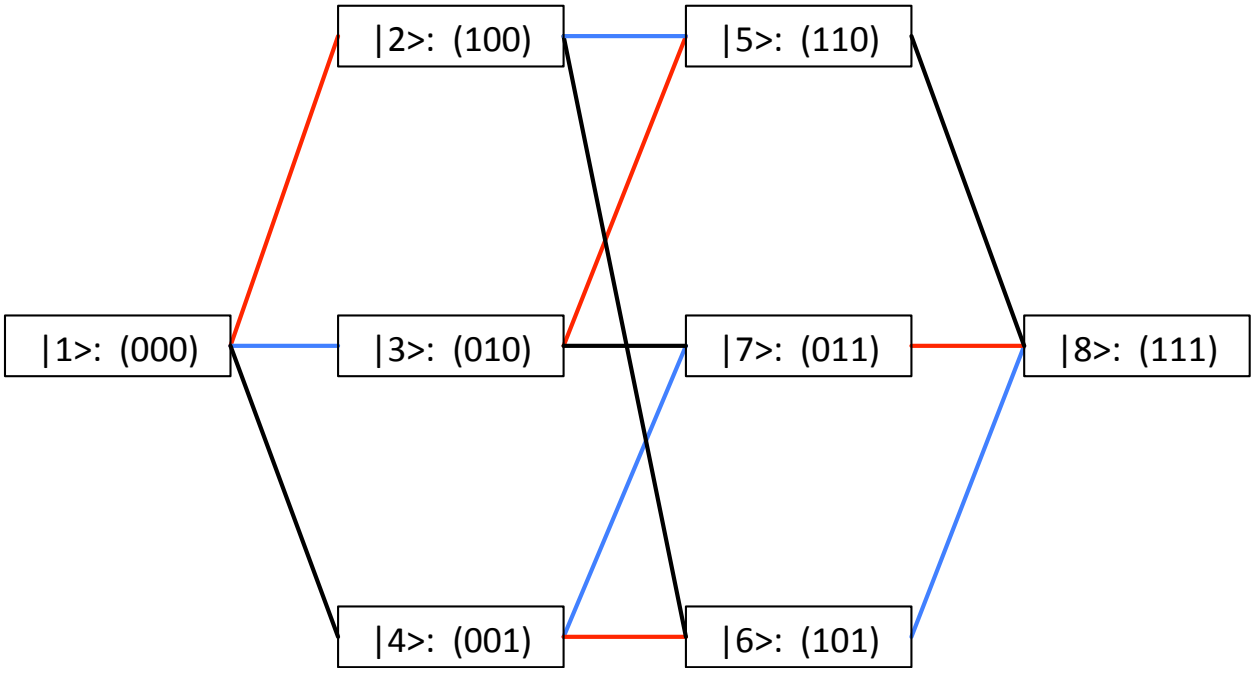

Figure S4: Diagram representing how the 8 degenerate minima of the water trimer are connected by bifurcation. Red lines show bifurcation of the first monomer, blue lines represent bifurcation of the second monomer, and black lines represent bifurcation of the third monomer. The first, second, and third monomers refer to the x,y, and z monomer respectively.

Figure S5: Tunneling Hamiltonian matrix for the water trimer with minima labels

		(000)	(100)	(010)	(001)	(110)	(011)	(101)	(111)
		|1>	|2>	|3>	|4>	|5>	|6>	|7>	|8>
(000)	<1|	O	A	A	A	B	B	B	C
(100)	<2|	A	O	B	B	A	A	C	B
(010)	<3|	A	B	O	B	A	C	A	B
(001)	<4|	A	B	B	O	C	A	A	B
(110)	<5|	B	A	A	C	O	B	B	A
(011)	<6|	B	A	C	A	B	O	B	A
(101)	<7|	B	C	A	A	B	B	O	A
(111)	<8|	C	B	B	B	A	A	A	O

III. Water Pentamer

a. Tunneling Hamiltonian

The tunneling Hamiltonian for the water pentamer is given in Figure S5. Analogous to the trimer's tunneling Hamiltonian, the elements represent consecutive bifurcation events with A representing single bifurcation, B representing two consecutive bifurcation events, and so forth. We neglect the flipping motion as discussed in the main text. In keeping with experimental results we set all elements representing multiple bifurcations to zero (B=C=D=E=0). The tunneling Hamiltonian is constructed in the basis of the 32 degenerate minima described below in Figure S6.

Figure S6: Tunneling Hamiltonian of the water pentamer

		|1> (00000)	|2> (10000)	|3> (01000)	|4> (00100)	|5> (00010)	|6> (00001)	|7> (11000)	|8> (10100)	|9> (10010)	|10> (10001)	|11> (01100)	|12> (01010)	|13> (01001)	|14> (00110)	|15> (00101)	|16> (00011)	|17> (11100)	|18> (11010)	|19> (11001)	|20> (01110)	|21> (01101)	|22> (00111)	|23> (10110)	|24> (10011)	|25> (01011)	|26> (10101)	|27> (11110)	|28> (11101)	|29> (01111)	|30> (10111)	|31> (11011)	|32> (11111)
(00000)	<1|	υ	A	A	A	A	A	B	B	B	B	B	B	B	B	B	B	C	C	C	C	C	C	C	C	C	C	D	D	D	D	D	E
(10000)	<2|	A	υ	B	B	B	B	A	A	A	A	C	C	C	C	C	C	B	B	B	D	D	D	B	B	D	B	C	C	E	C	C	D
(01000)	<3|	A	B	υ	B	B	B	A	C	C	C	A	A	A	C	C	C	B	B	B	B	B	D	D	D	B	D	C	C	C	E	C	D
(00100)	<4|	A	B	B	υ	B	B	C	A	C	C	A	C	C	A	A	C	B	D	D	B	B	B	B	D	D	B	C	C	C	C	E	D
(00010)	<5|	A	B	B	B	υ	B	C	C	A	C	C	A	C	A	C	A	D	B	D	B	D	B	B	B	B	D	C	E	C	C	C	D
(00001)	<6|	A	B	B	B	B	υ	C	C	C	A	C	C	A	C	A	A	D	D	B	D	B	B	D	B	B	B	E	C	C	C	C	D
(11000)	<7|	B	A	A	C	C	C	υ	B	B	B	B	B	B	D	D	D	A	A	A	C	C	E	C	C	C	C	B	B	D	D	B	C
(10100)	<8|	B	A	C	A	C	C	B	υ	B	B	B	D	D	B	B	D	A	C	C	C	C	C	A	C	E	A	B	B	D	B	D	C
(10010)	<9|	B	A	C	C	A	C	B	B	υ	B	D	B	D	B	D	B	C	A	C	C	E	C	A	A	C	C	B	D	D	B	B	C
(10001)	<10|	B	A	C	C	C	A	B	B	B	υ	D	D	B	D	B	B	C	C	A	E	C	C	C	A	C	A	D	B	D	B	B	C
(01100)	<11|	B	C	A	A	C	C	B	B	D	D	υ	B	B	B	B	D	A	C	C	A	A	C	C	E	C	C	B	B	B	D	D	C
(01010)	<12|	B	C	A	C	A	C	B	D	B	D	B	υ	B	B	D	B	C	A	C	A	C	C	C	C	A	E	B	D	B	D	B	C
(01001)	<13|	B	C	A	C	C	A	B	D	D	B	B	B	υ	D	B	B	C	C	A	C	A	C	E	C	A	C	D	B	B	D	B	C
(00110)	<14|	B	C	C	A	A	C	D	B	B	D	B	B	D	υ	B	B	C	C	E	A	C	A	A	C	C	C	B	D	B	B	D	C
(00101)	<15|	B	C	C	A	C	A	D	B	D	B	B	D	B	B	υ	B	C	E	C	C	A	A	C	C	C	A	D	B	B	B	D	C
(00011)	<16|	B	C	C	C	A	A	D	D	B	B	D	B	B	B	B	υ	E	C	C	C	C	A	C	A	A	C	D	D	B	B	B	C
(11100)	<17|	C	B	B	B	D	D	A	A	C	C	A	C	C	C	C	E	υ	B	B	B	B	D	B	D	D	B	A	A	C	C	C	B
(11010)	<18|	C	B	B	D	B	D	A	C	A	C	C	A	C	C	E	C	B	υ	B	B	D	D	B	B	B	D	A	C	C	C	A	B
(11001)	<19|	C	B	B	D	D	B	A	C	C	A	C	C	A	E	C	C	B	B	υ	D	B	D	D	B	B	B	C	A	C	C	A	B
(01110)	<20|	C	D	B	B	B	D	C	C	C	E	A	A	C	A	C	C	B	B	D	υ	B	B	B	D	B	D	A	C	A	C	C	B
(01101)	<21|	C	D	B	B	D	B	C	C	E	C	A	C	A	C	A	C	B	D	B	B	υ	B	D	D	B	B	C	A	A	C	C	B
(00111)	<22|	C	D	D	B	B	B	E	C	C	C	C	C	C	A	A	A	D	D	D	B	B	υ	B	B	B	B	C	C	A	A	C	B
(10110)	<23|	C	B	D	B	B	D	C	A	A	C	C	C	E	A	C	C	B	B	D	B	D	B	υ	B	D	B	A	C	C	A	C	B
(10011)	<24|	C	B	D	D	B	B	C	C	A	A	E	C	C	C	C	A	D	B	B	D	D	B	B	υ	B	B	C	C	C	A	A	B
(01011)	<25|	C	D	B	D	B	B	C	E	C	C	C	A	A	C	C	A	D	B	B	B	B	B	D	B	υ	D	C	C	A	C	A	B

(10101)	<26|	C	B	D	B	D	B	C	A	C	A	C	E	C	C	A	C	B	D	B	D	B	B	B	B	D	υ	C	A	C	A	C	B
(11110)	<27|	D	C	C	C	C	E	B	B	B	D	B	B	D	B	D	D	A	A	C	A	C	C	A	C	C	C	υ	B	B	B	B	A
(11101)	<28|	D	C	C	C	E	C	B	B	D	B	B	D	B	D	B	D	A	C	A	C	A	C	C	C	C	A	B	υ	B	B	B	A
(01111)	<29|	D	E	C	C	C	C	D	D	D	D	B	B	B	B	B	B	C	C	C	A	A	A	C	C	A	C	B	B	υ	B	B	A
(10111)	<30|	D	C	E	C	C	C	D	B	B	B	D	D	D	B	B	B	C	C	C	C	C	A	A	A	C	A	B	B	B	υ	B	A
(11011)	<31|	D	C	C	E	C	C	B	D	B	B	D	B	B	D	D	B	C	A	A	C	C	C	C	A	A	C	B	B	B	B	υ	A
(11111)	<32|	E	D	D	D	D	D	C	C	C	C	C	C	C	C	C	C	B	B	B	B	B	B	B	B	B	B	A	A	A	A	A	υ

b. Minima

The 32 degenerate minima of the water pentamer are given in Figure S7. The notation for the structures is as follows: the structure is represented as (xyzmn) where x, y, z, m, and n represents each of the monomers, and can have values of 1 or 0 to represent which hydrogen of the monomer is participating in the hydrogen bond. Thus we can represent the bifurcation tunneling motion as flipping the value of x, y, z, m, or n (i.e. (01000) → (00000)). We can neglect considering the orientation of the free hydrogen with respect to the oxygen plane due to the low barrier of the flipping motion in contrast to the bifurcation motion as discussed in the text.

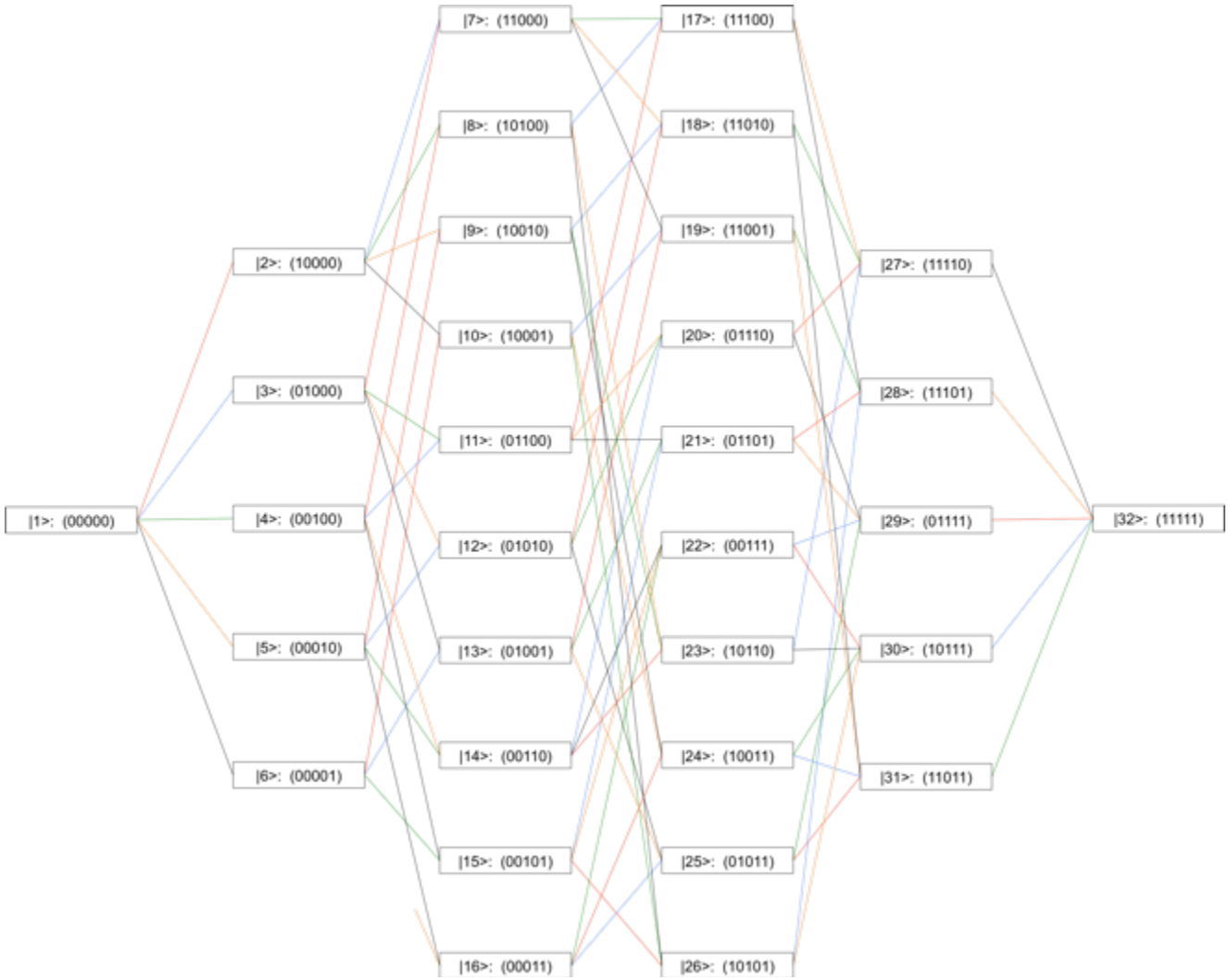

Figure S7: Diagram representing how the 32 degenerate minima of the water pentamer are connected by bifurcation. Red lines show bifurcation of the first monomer, blue lines represent bifurcation of the second monomer, green shows bifurcation of the third monomer, orange shows bifurcation of the fourth monomer, and black lines represent bifurcation of the fifth monomer. The first, second, and third monomers refer to the x, y, z, m, and n monomer respectively.

Figure S8: Tunneling Hamiltonians used with zeroed out elements which are bolded to aid comparison to the full tunneling Hamiltonians. The dimer Hamiltonian has the AS element set to zero. The trimer Hamiltonian has elements B=C=0. The pentamer Hamiltonian has elements B=C=D=E=0. The pentamer is not shown here due to spacing concerns. It can be found in the published manuscript.

A) Dimer Hamiltonian

		1>		2>		3>		4>		5>		6>		7>		8>
<1|	O		B		0		**0**		G		G		I		I
<2|	B		O		**0**		0		G		G		I		I
<3|	0		**0**		O		B		I		I		G		G
<4|	**0**		0		B		O		I		I		G		G
<5|	G		G		I		I		O		B		0		**0**
<6|	G		G		I		I		B		O		**0**		0
<7|	I		I		G		G		0		**0**		O		B
<8|	I		I		G		G		**0**		0		B		O

B) Trimer Hamiltonian

		(000)	1>	(100)	2>	(010)	3>	(001)	4>	(110)	5>	(011)	6>	(101)	7>	(111)	8>
(000)	<1|	O		A		A		A		**0**		**0**		**0**		**0**	
(100)	<2|	A		O		**0**		**0**		A		A		**0**		**0**	
(010)	<3|	A		**0**		O		**0**		A		**0**		A		**0**	
(001)	<4|	A		**0**		**0**		O		**0**		A		A		**0**	
(110)	<5|	**0**		A		A		**0**		O		**0**		**0**		A	
(011)	<6|	**0**		A		**0**		A		**0**		O		**0**		A	
(101)	<7|	**0**		**0**		A		A		**0**		**0**		O		A	
(111)	<8|	**0**		**0**		**0**		**0**		A		A		A		O	

Supplemental Information for:

Structure and Torsional Dynamics of the Water Octamer from Terahertz Laser Spectroscopy near 215 μm^{-1}

This document presents the 91 assigned transitions and the calculated residuals between the observed transitions and those calculated from the fitted rotational constants (Tables S9 and S10). Also included is the correlation matrix for both the D_{2d} and S_4 fits (Figures S9 and S10). A description of the experimental method is provided. Details of the normal mode analysis is provided along with the normal modes for both structures on the MB-pol surface (Tables S11 and S12).

Table S9: Assigned transitions for the D_{2d} Structure. Values for transitions and residuals are given in MHz. The given J and K values refer to the ground state. All assigned transitions belong to Q branch transitions and a parallel-type band.

Exp. line	Obs-Calc	j	k
1383117.2	1.2	2	2
1383119.9	0.9	2	1
1383131.6	-4.2	3	3
1383138.8	-2.4	3	2
1383161.1	2.1	4	4
1383169.2	1.7	4	3
1383173.6	-0.1	4	2
1383177.3	0.0	4	1
1383185.3	2.2	5	5
1383194.5	-1.1	5	4
1383207.1	1.8	5	3
1383209.8	-2.5	5	2
1383214.5	-2.0	5	1
1383205.4	0.5	6	6
1383224.2	1.8	6	5
1383229.1	-7.7	6	4
1383250.3	2.3	6	3
1383252.3	-3.7	6	2
1383258.2	-2.7	6	1
1383219.0	-1.7	7	7
1383246.7	2.4	7	6
1383261.6	-2.9	7	5
1383282.3	1.2	7	4
1383294.9	0.9	7	3
1383300.1	-3.2	7	2
1383315.7	6.9	7	1
1383255.1	-2.0	8	7
1383288.5	4.1	8	6
1383309.1	1.5	8	5
1383327.1	0.4	8	4
1383336.8	-4.8	8	3
1383366.6	1.4	8	2
1383369.7	1.1	8	1

1383292.8	1.0	9	7
1383325.3	2.1	9	6
1383350.2	0.3	9	5
1383372.1	-4.4	9	4
1383384.4	-2.8	9	3
1383398.3	-2.4	9	2
1383406.0	-1.1	9	1
1383181.8	2.6	10	10
1383283.8	1.1	10	8
1383323.6	-2.9	10	7
1383386.0	1.2	10	5
1383415.1	-6.0	10	4
1383427.5	-3.2	10	3
1383444.2	1.2	10	2
1383457.0	-1.1	10	1
1383345.6	-6.1	11	7
1383381.5	-1.1	11	6
1383421.2	0.5	11	5
1383451.3	3.3	11	4
1383411.3	0.3	12	6
1383447.7	1.1	12	5
1383417.8	-0.3	13	6
1383460.8	-1.4	13	5
1383458.8	-0.1	14	5
1383441.2	2.7	15	5
1383453.7	-1.1	16	4
1383432.3	-1.1	17	3

Table S10: Assigned transitions for S_4 Structure. Values for transitions and residuals are given in MHz. The given J and K values refer to the ground

state. All assigned transitions belong to Q branch transitions and a parallel-type transition.

Exp. line	Obs-Calc	j	k
1383264.2	-5.2	5	5
1383287.1	2.3	5	4
1383297.3	1.0	5	3
1383302.8	-1.5	5	2
1383312.3	3.4	5	1
1383290.6	1.1	6	6
1383306.1	-1.3	6	5
1383321.9	0.6	6	4
1383328.8	-2.8	6	3
1383335.7	-3.1	6	2
1383343.6	0.7	6	1
1383320.1	3.3	7	7
1383333.9	-2.7	7	6
1383360.2	0.8	7	5
1383370.7	6.2	7	4
1383375.3	1.9	7	3
1383376.8	-2.8	7	2
1383379.6	-3.6	7	1
1383373.4	-0.9	8	7
1383389.0	-2.2	8	6
1383401.5	-3.0	8	5
1383416.4	1.8	8	4
1383423.2	1.2	8	3
1383425.2	-1.8	8	2
1383429.8	-0.1	8	1
1383399.9	-0.4	9	9
1383419.3	-3.1	9	8
1383436.9	-3.0	9	7
1383455.1	1.5	9	6
1383466.9	2.8	9	5
1383462.7	1.6	10	10

Correlation Matrices

D_{2d} Correlation matrix

Figure S9: Correlation matrix for the D_{2d} octamer fit. For description of constants see main text Equation 1.

	v	ΔB	ΔM	ΔD_j	ΔD_{jk}	ΔD_k
v	1.00	-0.79	0.51	-0.57	-0.58	0.01
ΔB	-0.79	1.00	-0.09	0.86	0.53	-0.32
ΔM	0.51	-0.09	1.00	0.14	-0.61	-0.46
ΔD_j	-0.57	0.86	0.14	1.00	0.11	-0.14
ΔD_{jk}	-0.58	0.53	-0.61	0.11	1.00	-0.35
ΔD_k	0.01	-0.32	-0.46	-0.14	-0.35	1.00

S_4 Correlation Matrix

Figure S10: Correlation matrix for the S_4 octamer fit. For description of constants see main text Equation 1.

	v	ΔB	ΔM	ΔD_j	ΔD_{jk}	ΔD_k
v	1.00	-0.94	-0.34	-0.84	0.30	-0.07
ΔB	-0.94	1.00	0.59	0.97	-0.53	0.22
ΔM	-0.34	0.59	1.00	0.71	-0.87	0.53
ΔD_j	-0.84	0.97	0.71	1.00	-0.70	0.40
ΔD_{jk}	0.30	-0.53	-0.87	-0.70	1.00	-0.86
ΔD_k	-0.07	0.22	0.53	0.40	-0.86	1.00

Experimental

The Berkeley Terahertz spectrometer has been described in detail elsewhere [1,2],and was used in conjunction with a variable field Putley-mode (VFP) detector to locate the water octamer transitions in the region of 1.35 to 1.8 THz. Jet-cooled H_2O clusters were produced by bubbling gaseous argon at a backing pressure of 17-18 psi through a reservoir of distilled room-temperature water, and subsequently expanding the saturated carrier gas though a pulsed planar expansion source described in detail elsewhere [3]. Argon was used as the primary carrier gas in order to maximize the chance of observing tunneling fine structure since the Doppler linewidths are more narrow than for He or Ne. Each data point represents an average over 32 gas pulses [143].

A single far-infrared laser with a center frequency of 1397.1186 GHz (46.6029 cm^{-1} CH_2F_2) was sufficient for observing all of the transitions presented herein. The full-width half-maximum linewidths for the measured transitions are 700 kHz, and are tightly clustered in a region of about 350 MHz. The microwave modulation depth was varied to resolve any possible tunneling splittings, however all observed transitions appeared as singlets with no discernable fine structure.

To determine the identity of the spectral carrier, isotopic dilution experiments were performed as described in references [89,203]. Briefly, specific fractions of D_2O were added in the reservoir and the relative intensity of the transitions was recorded. From these measurements the number of water monomers in the spectral carrier was determined to be eight at 95% confidence. About 2 cm^{-1} was scanned on either side of the reported transitions, but no further octamer lines were found [143].

Table S11: Calculated normal mode frequencies and symmetries for the D_{2d} structure, using the MB-pol potential energy surface. Frequencies are given in cm^{-1}.

Frequency	Symmetry
71.7	A1
74.1	B1
74.8	B2
76.2	E
76.2	E
111.3	A1
168.9	E
168.9	E
169.0	A2
172.9	B1
182.7	A1
204.1	B2
206.9	E
206.9	E
256.2	A1
257.5	A2
257.8	B1
261.9	E
261.9	E
277.7	B2
300.9	E
300.9	E
436.0	A1
444.7	E
444.7	E
486.6	B1
497.4	A2
498.7	B2
540.8	E
540.8	E

564.8	B1
657.4	A2
663.5	E
663.5	E
673.1	E
673.1	E
708.8	B2
831.0	A1
860.9	A2
968.9	E
968.9	E
1032.3	B1
1666.4	E
1666.4	E
1675.7	B2
1677.4	A1
1689.5	E
1689.5	E
1716.7	B2
1736.2	A1
3306.0	A1
3322.2	E
3322.2	E
3358.6	B2
3668.6	E
3668.6	E
3669.0	B2
3685.0	A1
3708.8	B1
3711.3	A2
3749.4	E
3749.4	E
3902.0	E
3902.0	E

3903.1	A1
3903.6	B2

Table S12: Calculated normal mode frequencies and symmetries for the S_4 structure, using the MB-pol potential energy surface. Frequencies are given in cm^{-1}.

Frequency	Symmetry
69.9	B
72.1	A
72.4	E
72.4	E
76.9	B
105.6	A
164.9	E
164.9	E
165.7	A
170.3	B
184.0	A
202.5	B
204.2	E
204.2	E
257.9	A
259.8	B
270.0	E
270.0	E
271.8	A
285.8	E
285.8	E
303.6	B
428.0	A
432.0	B
454.6	E
454.6	E
482.8	B
529.0	E
529.0	E
537.7	A

578.6	A
630.6	B
644.2	E
644.2	E
685.3	E
685.3	E
691.5	B
796.9	A
895.8	E
895.8	E
972.3	A
995.2	B
1662.0	B
1671.1	E
1671.1	E
1679.2	A
1702.2	A
1704.1	E
1704.1	E
1728.0	B
3347.5	A
3360.6	B
3378.8	E
3378.8	E
3683.6	E
3683.6	E
3687.6	B
3699.8	A
3726.0	A
3748.4	E
3748.4	E
3763.6	B
3906.7	A
3907.0	E

3907.0	E
3907.1	B

Computational

Normal mode analysis is performed by transforming the Cartesian coordinates **X** to normal coordinates **Q**,

$$Q_\beta = \sum_{\alpha=1}^{3N} A_{\alpha\beta} X_\alpha \sqrt{M_\alpha}$$

where **M** is the diagonal matrix of atomic masses, and **A** is the matrix of columnwise eigenvectors of the mass-weighted Cartesian Hessian matrix, $\mathbf{M}^{-½}\ \mathbf{H}\ \mathbf{M}^{-½}$, evaluated at the local minimum. The Hessian matrix in normal coordinates is then

$$\mathbf{\Phi} = \mathbf{A}^{T}\ \mathbf{M}^{-½}\ \mathbf{H}\ \mathbf{M}^{-½}\ \mathbf{A}.$$

At the local minimum, **Φ** is a diagonal matrix whose elements are proportional to the squared harmonic vibrational frequencies. The relative harmonic displacements along normal mode γ are obtained from the reverse transformation,

$$X_\alpha = \sum_{\gamma=1}^{3N} A_{\alpha\gamma} Q_\gamma / \sqrt{M_\alpha}$$

in component form.

All calculations are performed using the MB-pol potential energy surface [37,172,173].

Supplemental Information for

Angle-Resolved Second Harmonic Scattering Experiments

Contents

S11: Data Analysis Methodology for SHS Scans

The data analysis methodology follows the standard accepted practice for SHS experiments [3,10]. The contribution from the solvent (with the same input/output polarization scheme), water in this experiment, is subtracted from the scan. The scan is then normalized by S_{in}/S_{out} water scan, which corrects for the change in scattering volume as the angle resolved scattering pattern is recorded [3]. As a result, the intensities reported herein represent a unitless, normalized quantity. Figure S1 shows the application of this analysis to a typical scan from our experiment.

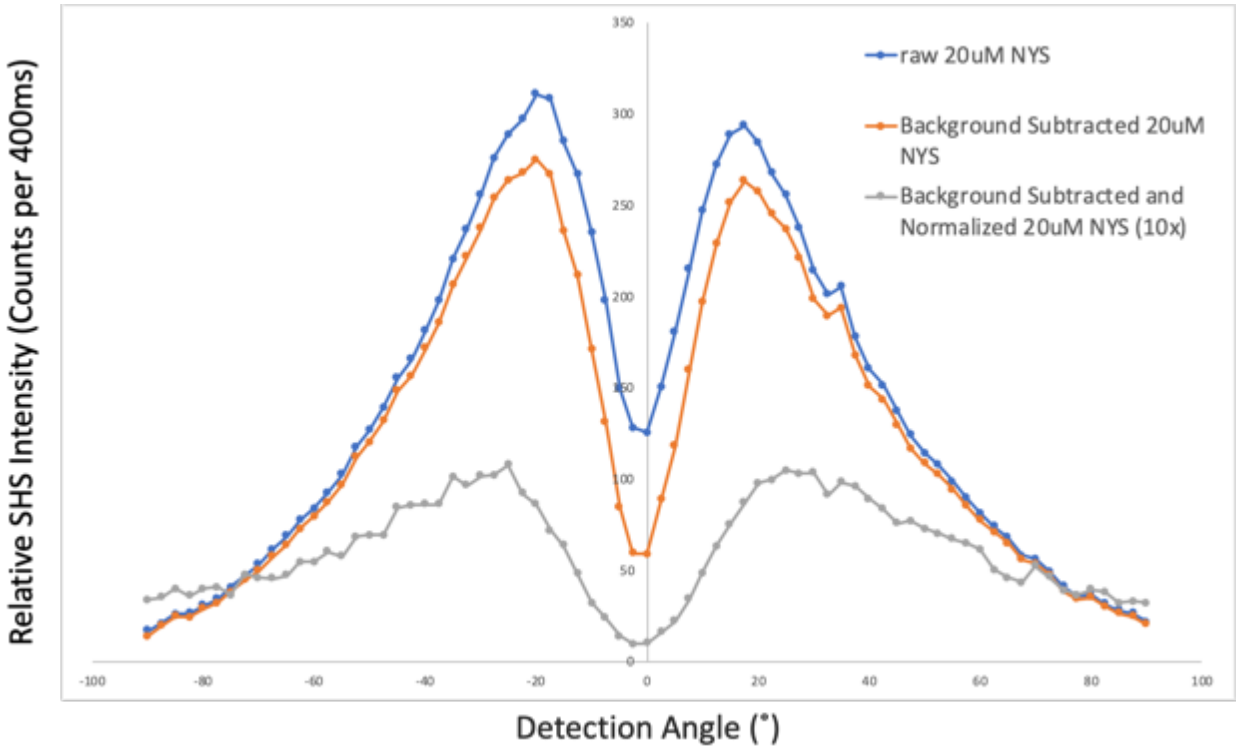

Figure S11: Effect of background subtraction and normalization on the raw signal measured in the experiment.

S12: Fit Correlation Matrices

The correlation matrices for each fit reported in the study are given below.

MG Calibration

1			
-0.402	1		
0.468	-0.876	1	
0.303	-0.96	0.943	1

NYS Calibration

1			
-0.57	1		
0.46	-0.845	1	
0.256	-0.886	0.922	1

MG displaced by Ascorbic Acid

1		
-0.652	1	
0.596	-0.049	1

NYS displaced by Ascorbic Acid

1		
-0.878	1	
0.881	-0.658	1

MG displaced by Caffeine

1		
-0.741	1	
0.811	-0.391	1

NYS displaced by Caffeine

1		
-0.924	1	
0.927	-0.785	1

MG displaced by Pentoxifylline

1		
-0.846	1	
0.849	-0.554	1

NYS displaced by Pentoxifylline

1		
-0.882	1	
0.872	-0.632	1

MG displaced by Triton X

1		
-0.899	1	
0.708	-0.64	1

NYS displaced by Triton X

1		
-0.569	1	
0.66	0.074	1

MG displaced by CTAB

1		
-0.795	1	
-0.594	-0.912	1

NYS displaced by CTAB

1		
0.839	1	
0.872	0.997	1

S13: Plot of SHS intensity v. competitor concentration

<u>nPSB Results</u>

Caffeine

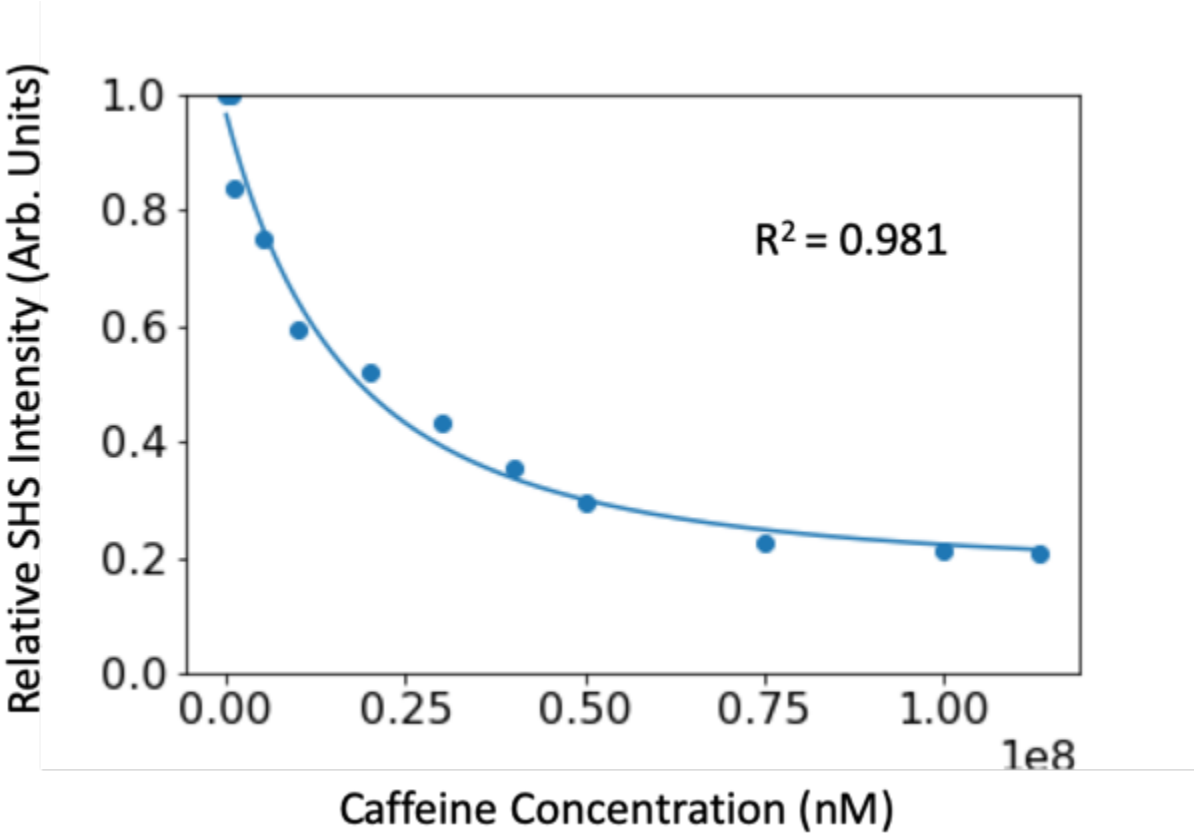

Pentoxifylline

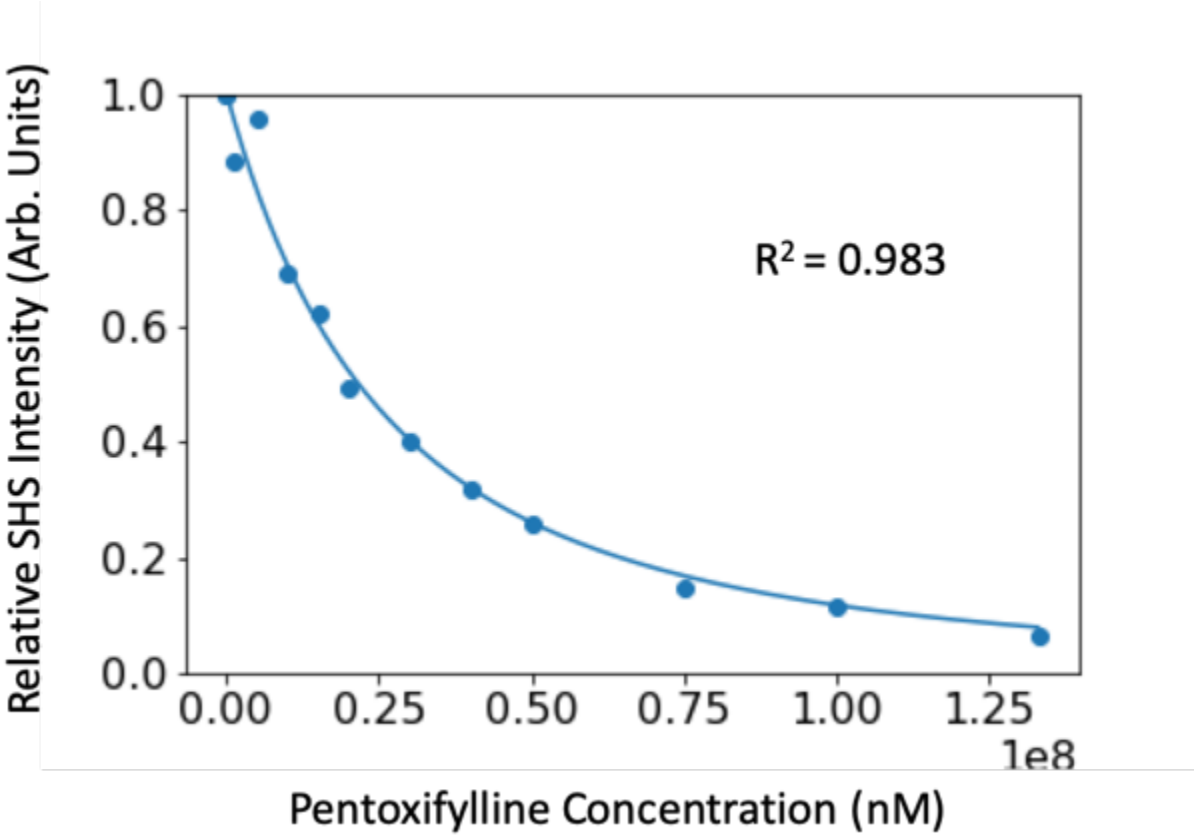

Ascorbic Acid

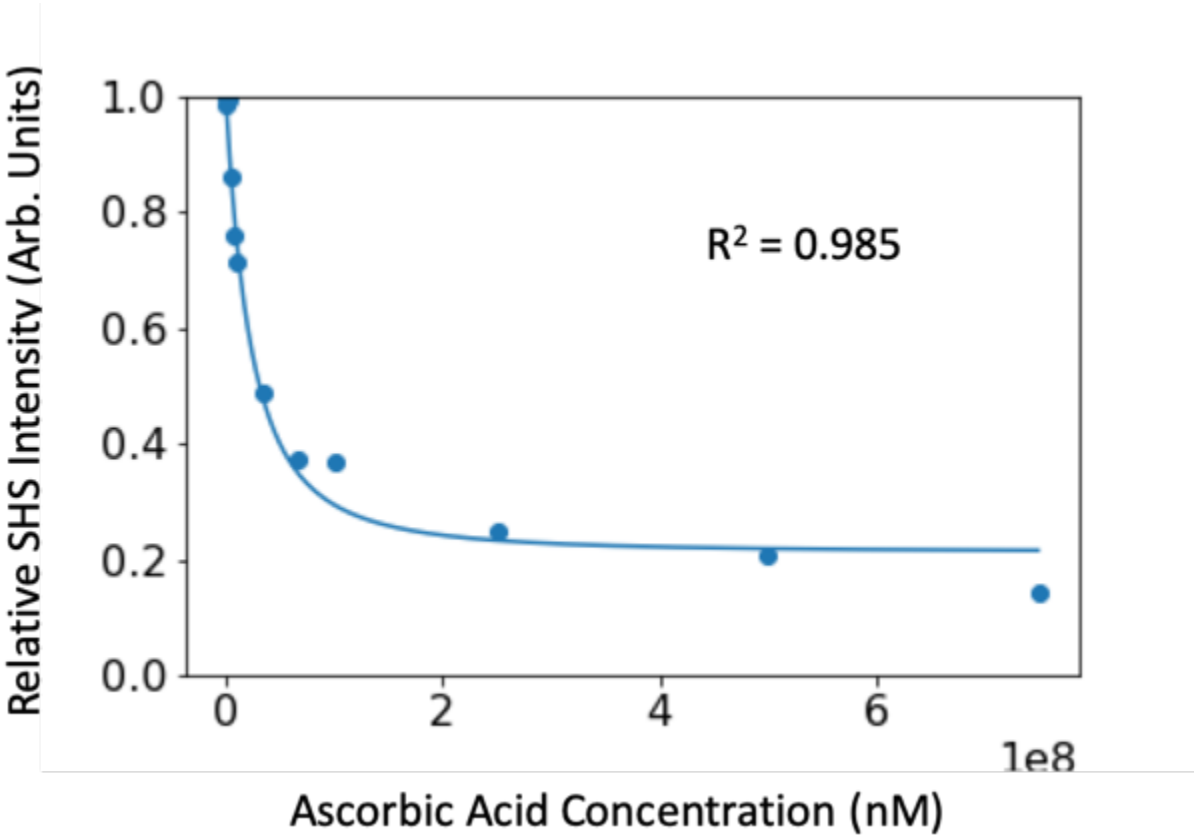
Relative SHS Intensity (Arb. Units)
1.0
0.8
0.6
0.4
0.2
0.0
0
2
4
6
1e8
R² = 0.985
Ascorbic Acid Concentration (nM)

CTAB

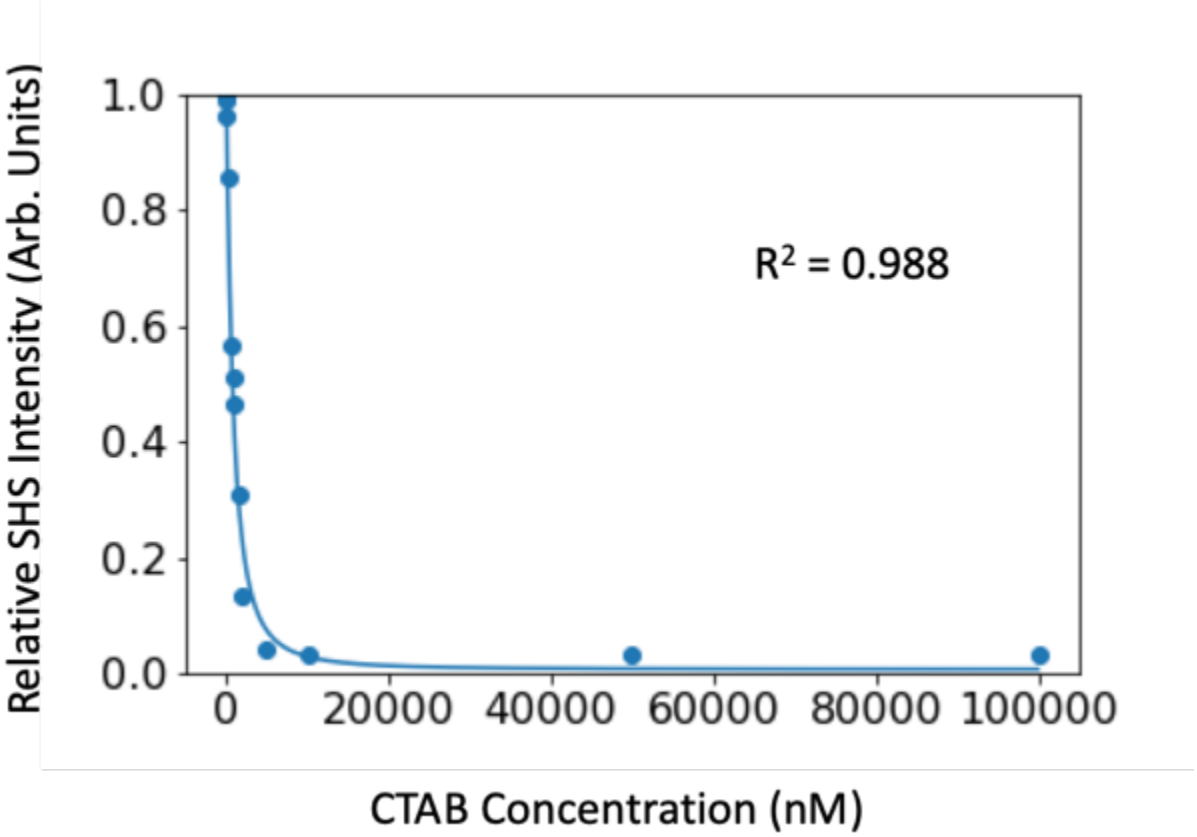
Relative SHS Intensity (Arb. Units)
1.0
0.8
0.6
0.4
0.2
0.0
R^2 = 0.988
0
20000
40000
60000
80000
100000
CTAB Concentration (nM)

TX

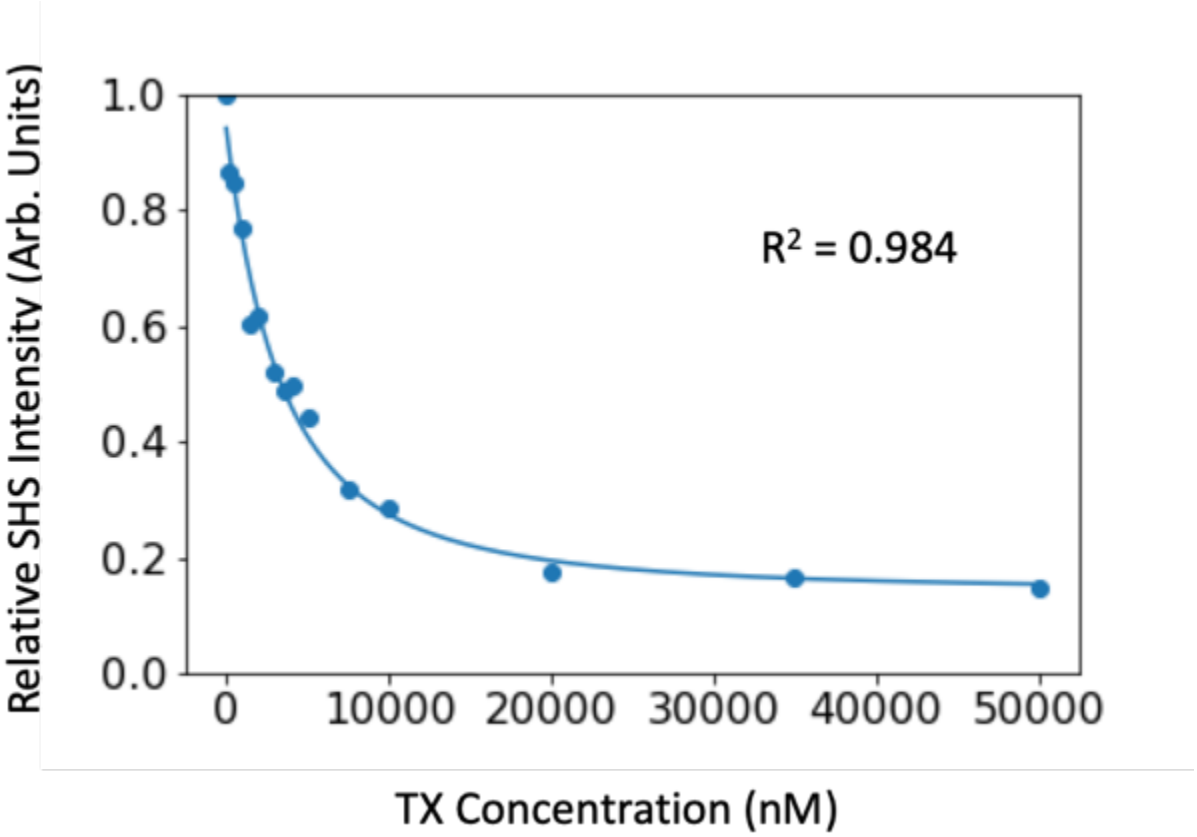

pPSB Results

Caffeine

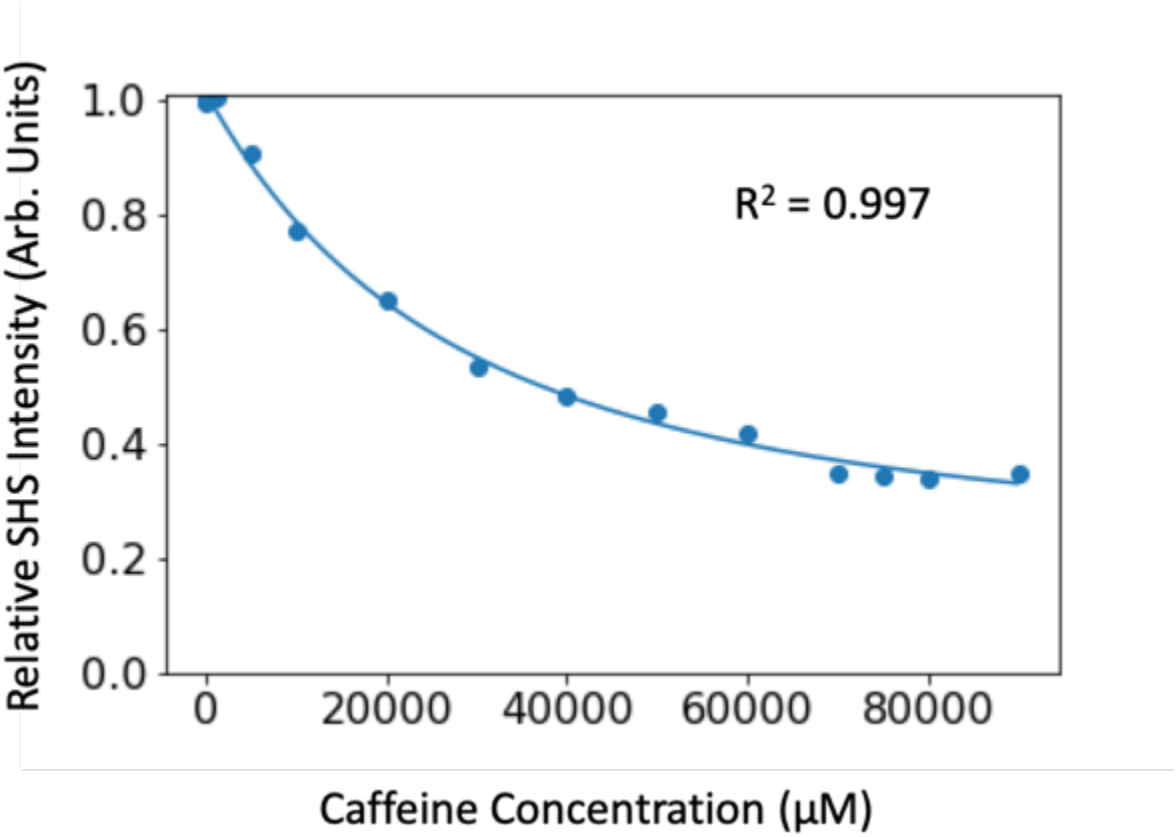

Pentoxifylline

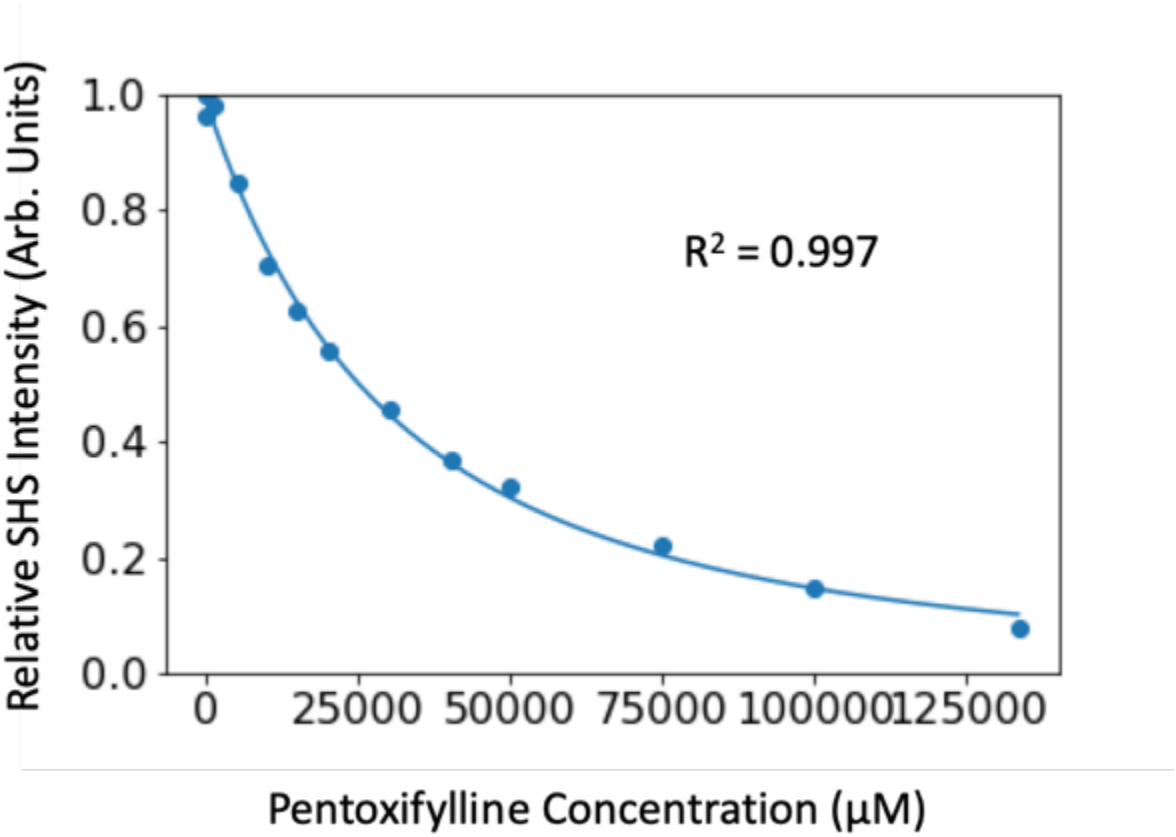

Ascorbic Acid

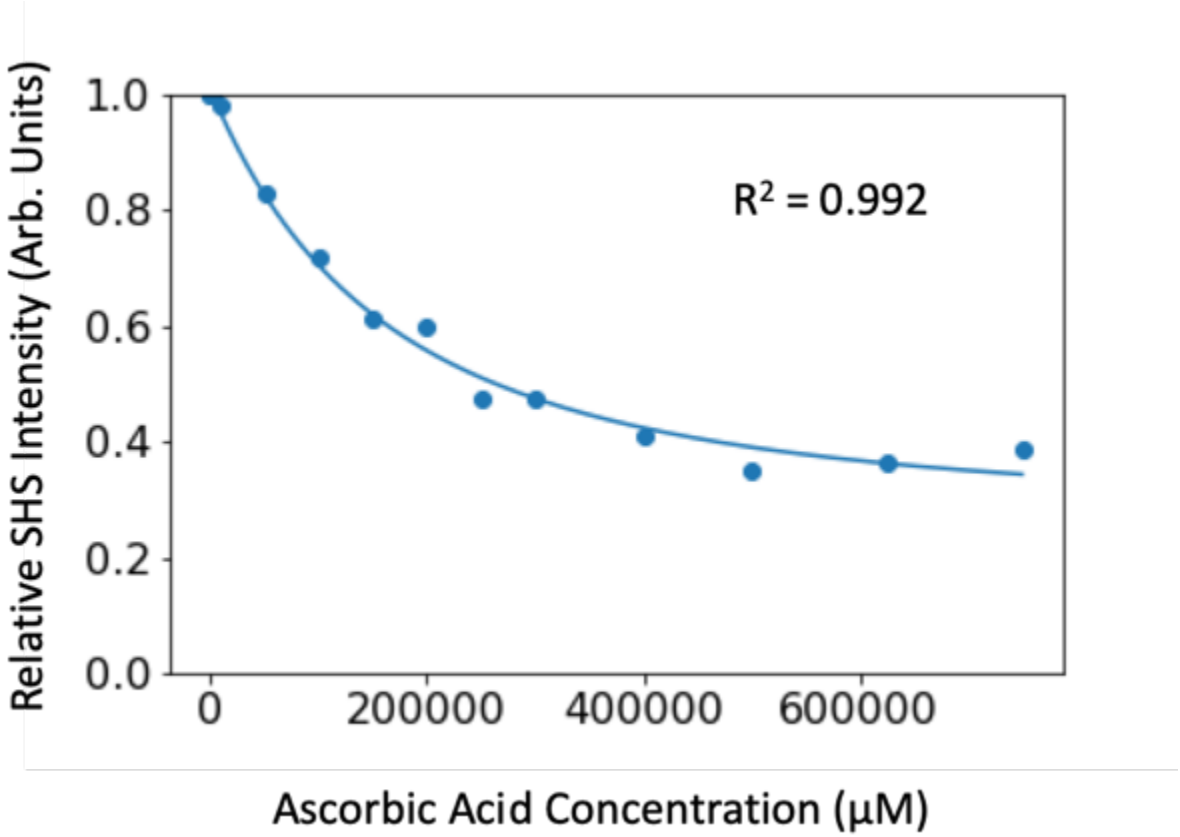
Relative SHS Intensity (Arb. Units)
1.0
0.8
0.6
0.4
0.2
0.0
0
200000
400000
600000
R² = 0.992
Ascorbic Acid Concentration (µM)

CTAB

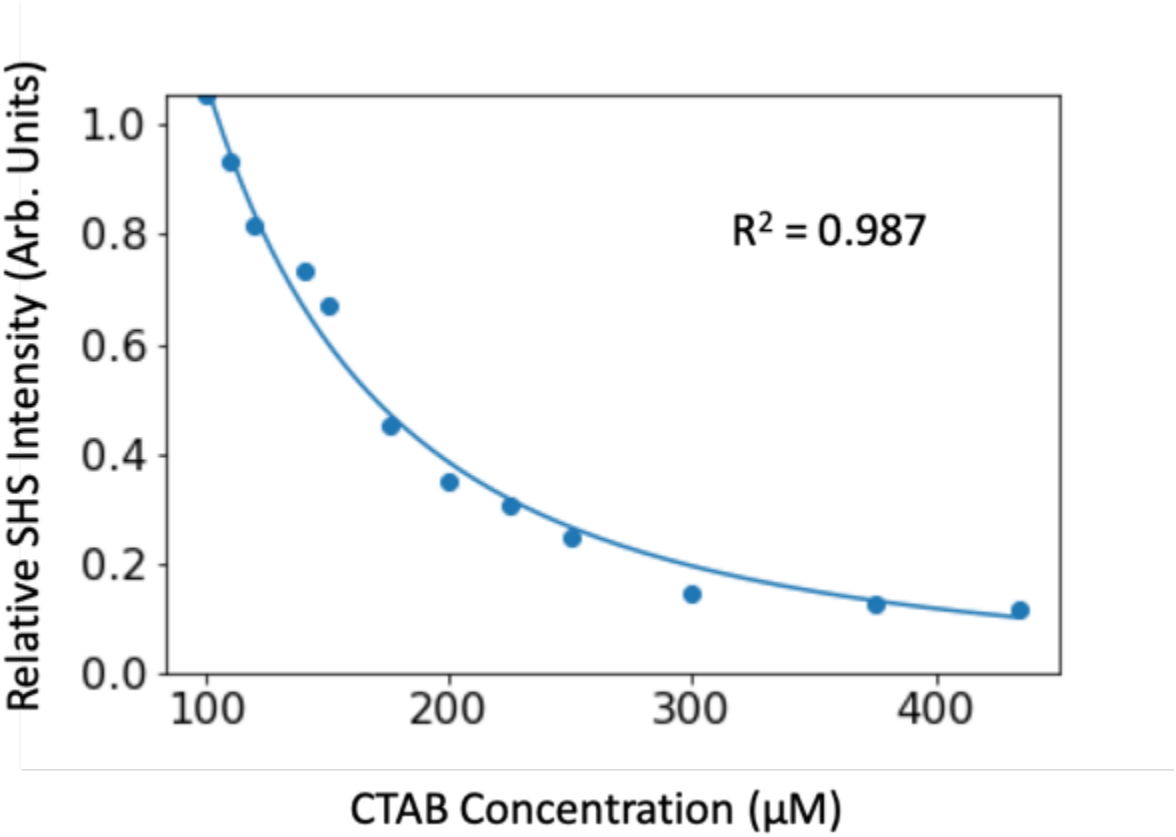
Relative SHS Intensity (Arb. Units)
1.0
0.8
0.6
0.4
0.2
0.0
100
200
300
400
R² = 0.987
CTAB Concentration (μM)

TX

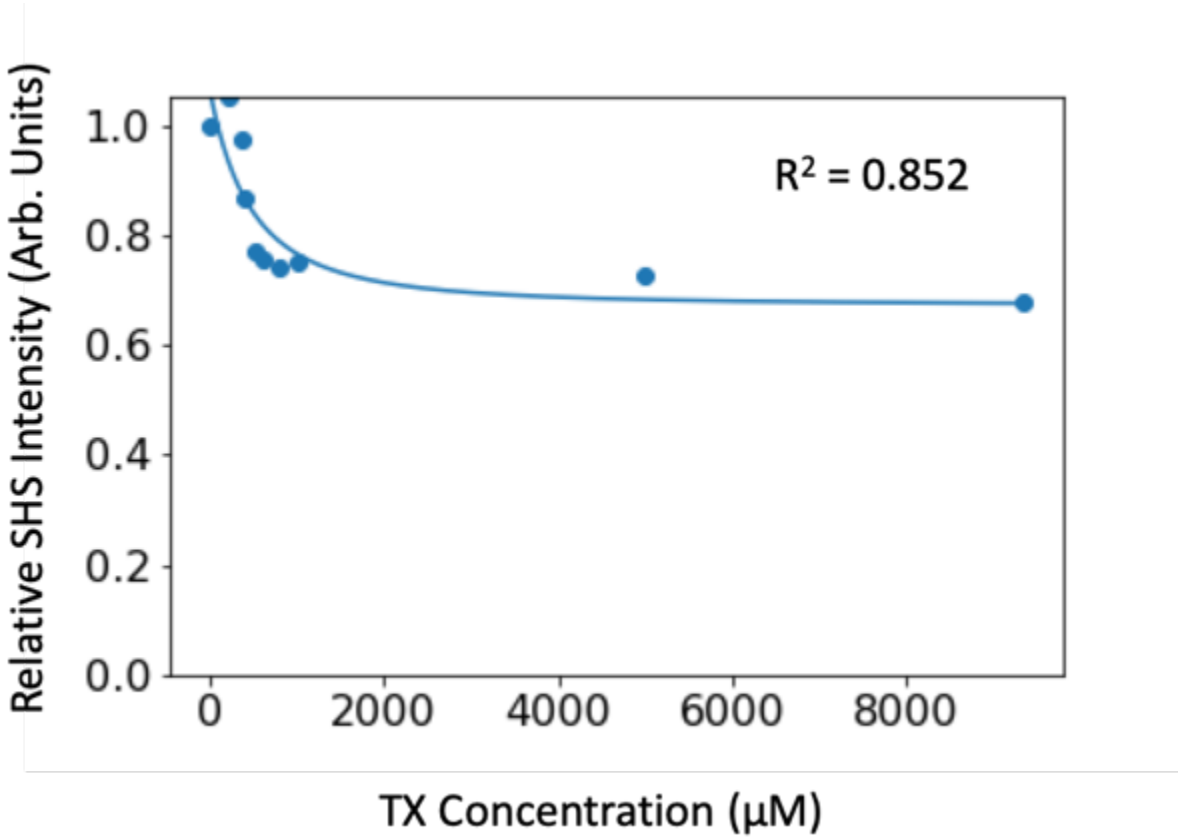
Relative SHS Intensity (Arb. Units)
1.0
0.8
0.6
0.4
0.2
0.0
0
2000
4000
6000
8000
R² = 0.852
TX Concentration (µM)

Appendix B: SHS Operation Guide

The Second Harmonic Scattering experiment location in D36A Hildebrand Hall (at the time of writing this thesis) can be operated as follows.

1. Ensure the pump laser and Ti-saph oscillator are functions according to their manuals. **Note**: The chiller that I used to cool the experiment did not have a flow meter, you need to adjust the temperature on the tower head to be ~ 22˚C when the laser is off and ~26˚C when the laser is on. NOT hotter and NOT colder.
2. The 800nm fundamental passes through the beam path described in Chapter 3 of this thesis. Importantly, the HWP and collection arm are mounted on motorized stages controlled by a Newport X-1000 controller.
    a. This controller sits in the electronics rack beside the experiment and is interfaced with the Labview program that controls the experiment. Should you need to access the control panel of the controller, read the manual for the remote access IP address and use the UN/PW combo: 'Admin'.
3. There is a mechanized beam block that is controlled by a small Keithley power supply. It can be manually controlled by the switch on the laser table by the Ti-saph output.
4. All experiments should currently be conducted with the room lights off as there is a non-negligible contribution at 400nm from them.
5. The experiment is controlled via Labview, the project is "SHG_Scattering_control.lbproj" on the Desktop.
    a. The interface is hopefully self-explanatory, but if not you can open the code and take a look at where things go.